

**Electrical Detection and Actuation of Single
Biological Cells with Application to Deformability
Cytometry for Markerless Diagnostics**

by

Graham Alan Ferrier

A Thesis submitted to the Faculty of Graduate Studies of
The University of Manitoba
in partial fulfillment of the requirements for the degree of

Doctor of Philosophy

Department of Electrical and Computer Engineering
University of Manitoba
Winnipeg, MB, Canada

Copyright © 2011 by Graham Alan Ferrier

Abstract

An all-electrical system is developed to actuate and detect single biological cells in a microfluidic channel for diagnostic applications. Interdigitated electrodes fabricated on the channel floor transfer a high frequency signal for capacitance detection and a low frequency signal for dielectrophoretic actuation. In the fluid-filled channel, a pressure-driven flow propels single biological cells, which induce time-dependent capacitance signatures as they pass over the electrodes. With a sub-attofarad (≈ 0.15 aF RMS, 53 Hz bandwidth) capacitance resolution, this system detects biological cells (e.g., 1 yeast cell ≈ 50 aF) and their deflections ($1 \mu\text{m} \approx 5$ aF) from exerted dielectrophoretic forces (≥ 5 pN). Electrical detection of cell actuation by strong DEP forces provides an avenue for both inducing and monitoring the deformation of viscoelastic cells.

A strong and repulsive dielectrophoretic force can be used to press a biological cell into a channel wall. When this occurs, the mechanical properties of the cell can be investigated by capacitively monitoring the cell-to-wall interaction. The nature of the resulting interaction is shown to depend on the mechanical properties of the cell (surface morphology and viscoelastic properties). Various mammalian cell types such as Chinese Hamster Ovary (CHO) cells, mouse fibroblasts, human blood cells, human breast cells and their tumorigenic phenotypes are investigated using this system. Between these populations, the effective Young's modulus varies widely from 20 Pa (neutrophils) to 1-2 GPa (polystyrene microspheres). The viability and phenotype of a biological cell are known to reflect its mechanical and electrical properties. Consequently, this work investigates whether dielectrophoretically induced cell deformations are correlated with corresponding variations in capacitance, which could be used for discriminating cell phenotypes in the future.

Acknowledgements

*"If I saw further than others, it is because I was standing on the shoulders of giants."
- Sir Isaac Newton*

I feel blessed that my academic journey has been shaped and guided by three terrific advisors: Professors Craig Bennett, Xiaoyi Bao, and Douglas Thomson. Hopefully my future ventures will reflect their collective wisdom in some way.

I wish to thank my Ph.D. advisor, Professor Douglas Thomson, for the opportunity to engage in this multidisciplinary research. With a wonderfully easy-going and balanced character, he has been an exceptional role model for me. He is brilliant, incredibly patient, an engaging and interactive leader, and genuinely concerned about my welfare and progress. I also thank him for giving me opportunities to present at international research conferences, and sending me to nanoelectronics workshops and summer schools sponsored by the Canadian Institute for Advanced Research (CIFAR).

I have enjoyed working with highly skilled colleagues – Chun-Fan Chan, Andre Hladio, Sean Romanuik, Marija Nikolic-Jaric, Szymon Rzeszowski, Tim Cabel, and Elham Salimi. Their incredible work ethic, enthusiasm and fresh perspectives have continually inspired and energized our efforts.

Professor Greg Bridges has essentially been my co-advisor during this project. Like Professor Thomson, he has provided tremendous insight into the physics and engineering of this project, particularly in regard to the RF design. His meticulous approach to editing is also greatly appreciated. Many thanks go to Professor Derek Oliver for regularly sending me relevant literature from the American Physical Society. I wish to thank Professor Mark Freeman and his students for fabricating the

microfluidic channels and electrodes early in this research effort, and for continually providing prompt and valuable feedback regarding the content of our conference and journal articles. Special thanks go to Dan Card for generously offering his extensive design expertise in bringing the system into a much more portable form.

I gratefully acknowledge the University of Manitoba, the National Institute for Nanotechnology (NINT), the Natural Sciences and Engineering Research Council (NSERC), the Canada Foundation for Innovation (CFI), the Canadian Institute for Advanced Research (CIFAR), CMC Microsystems, and Canada Research Chairs for financial support of this research. I specifically thank CMC, Micronit, and NRC-NINT for facilitating the design and fabrication of the microfluidic devices.

For the opportunity to investigate relevant biological systems, I wish to thank group leaders Michael Butler, Francis Lin, Jim Davie, and their exceptional technical staff including Kevin Sunley, Vincent Jung, Catherine Argyiou, Saravanan Nandagopal, Kausik Paul, Cheryl Peltier, and Protiti Khan. They gave me access to the required facilities and prepared the cells for my experiments. Their collective insight into cellular behaviour has been invaluable.

I wish to thank our support staff: Marcia Labiuk, Karin Kroeker, Judy Noble, and Amy Dario! Throughout the course of my studies, they always kept me aware of every deadline in a professional and pleasant manner. Many thanks go to Guy Jonatschick and Mount-First Ng for their computer and network assistance, and to Allan MacKay, Al Symmons, Cory Smit, Dwayne Chrusch, Daryl Hamelin, and James Dietrich for their technical assistance. I'm grateful for my advisory committee - Douglas Thomson, Greg Bridges, and Jim Davie - for our annual progress meetings, and for reviewing my thesis

and providing constructive comments, which allowed me to put my best foot forward. I also wish to thank Professor Chris Backhouse for agreeing to be my external examiner.

For ensuring that I did not become a complete hermit, I wish to thank Yiping Li, Jun Hui Zhao, Karla Kvaternik, Chris Harrower, Nusraat Masood, Kar Mun Cheng, Pommy Patel, Jane Cao, Alireza Motieifar, Arezoo Emadi, Nasim Norouzi, Iman Yahyaie, Mojtaba Safari, Sharmistha Bhadra, Laura Rand, and Vanessa Nowostawski. Thank you all for enduring my often lengthy rants/stories! I wish to thank my landlords, Joan Joos, Gwen Ely, Edwin Rattai, and Robert Rempel and Laverna Eidse for accommodating me over the past decade. To the countless others who have walked beside me in support, I salute you all!

For all its mosquitoes and severe windchills, the city of Winnipeg provides a wonderful multicultural (*Folklorama* is my summer highlight!) and musical atmosphere. For giving me opportunities to musically express myself, share my musical knowledge, and experience music at the highest levels, I sincerely thank Dr. Fraser Linklater, Franco Cianflone, Laureen Reeds, Connie Gitlin, and Naoum Gomon.

Finally, I wish to thank my family for their love and unwavering support during this journey. This thesis is dedicated to them. I love them so much. I wish to thank God for making absolutely everything possible. I'm thankful for my life and abilities, which I always hope will contribute positively to the lives of others.

Table of Contents

Abstract.....	i
Acknowledgements.....	ii
List of Tables.....	viii
List of Figures.....	ix
List of Copyrighted Material for which permission was obtained.....	xvi
Thesis Related Publications.....	xvii
Chapter 1 – Research Motivation and Contributions.....	1
1.1 Optical Methods for Single Cell Analysis	3
1.2 Electrical Methods for Single Cell Analysis	4
1.3 Advantages of Using High Frequencies.....	5
1.4 Scientific Contributions.....	7
1.5 Thesis Outline	10
Chapter 2 – Modelling the Dielectrophoretic Actuation and Capacitive Detection of Biological Cells Flowing Past Coplanar Electrodes in Microfluidic Channels	12
2.1 Dielectric Properties of Aqueous Solutions	13
2.2 Dielectric Properties of Biological Cells.....	21
2.2.1 Polarization mechanisms	22
2.3 Capacitance Change Induced by Single Cells	25
2.3.1 Analytical expression for capacitance change.....	29
2.3.2 Capacitance signatures for particles travelling at a fixed altitude	33
2.4 Dielectrophoresis for Single Cell Actuation	37
2.4.1 Clausius-Mossotti Factor	40
2.4.2 Modelling DEP-induced cell trajectories	50

2.4.3	Determining the empirical lift force constant	54
2.5	Chapter Summary	56
<i>Chapter 3 – Capacitance Detection of Cell Electromanipulation.....</i>		57
3.1	Frequency Modulation [64].....	57
3.2	Microwave Interferometer [65]	66
3.2.1	Sensor calibration.....	73
3.2.2	Operation in high conductivity media	77
3.2.3	Fabrication of microfluidic channel and interdigitated electrodes.....	81
3.2.4	Controlling the fluid flow.....	83
3.2.5	Loading cells into the fluid channel.....	87
3.3	Chapter Summary	89
<i>Chapter 4 – Dielectrophoretically-Induced Compression of Flowing Biological Cells into a Microfluidic Channel Wall.....</i>		91
4.1	Introduction	91
4.2	Linking Cell Deformability to Physiological Functionality.....	95
4.2.1	Structural cell polarization	96
4.3	Biological Cells Are Nonlinear Viscoelastic Materials.....	97
4.4	Methods for Mechanically Probing Cells & Subcellular Structures.....	99
4.5	Impedance Cytometry for Single Cell Characterization	102
4.6	Dielectrophoresis for Cell Electro-deformation	104
4.7	An All-Electrical Approach to Deformability Cytometry	105
4.8	Recap of Interferometric System	106
4.9	Cell Preparation	107
4.10	Data Acquisition & Analysis	108
4.11	Capacitance Signatures from DEP-Actuated Cells	109
4.11.1	Polystyrene spheres as control particles	109
4.11.2	Clausius-Mossotti Factor of 10 μm polystyrene spheres.....	111
4.11.3	Large DEP potentials initiate unique capacitance signatures	113
4.12	Dielectrophoretic Pressing of Blood Cells	116

4.12.1	Experimental neutrophil and red blood cell signatures.....	117
4.12.2	Surveying the detection of structurally polarized T-lymphocytes.....	129
4.12.3	Simulated neutrophil signatures.....	134
4.13	Influence of Electroporation and Electrokinetic Mechanisms on the Flow of Biological Cells Across Interdigitated Electrodes in Microfluidic Channels.....	139
4.13.1	Dielectrophoresis	139
4.13.2	Electroporation	144
4.13.3	AC electrothermal flow.....	150
4.13.4	AC electro-osmotic flow	159
4.13.5	Brief summary of mechanisms.....	159
4.14	Chapter Summary	160
Chapter 5 – Research Highlights & Future Directions.....		162
5.1	Future Work.....	164
Appendix A – Derivation of DEP Equation for Spherical Particles.....		166
Appendix B – Clausius-Mossotti Factor for a Uniform Sphere is a Debye Function.....		171
Appendix C – Preparation of Blood Cells, Breast Cancer Cells, and Fibroblasts		173
C.1	Chinese Hamster Ovary- and Human Blood Cell Preparations	173
C.2	Preparation of 10T1/2 and Ciras-3 Mouse Fibroblasts	173
C.3	Preparation of MCF-7 and MDA-MB-231 Breast Cancer Cells.....	174
C.4	Trypan Blue Staining.....	176
Appendix D – MATLAB Graphical User Interface		177
D.1	MATLAB Code for Plotting Data	180
Bibliography.....		184

List of Tables

Table 2-1: Clausius-Mossotti parameter set.....	48
Table 4-1: Viscoelastic parameters of the SLS model.....	99
Table 4-2: Young's modulus of living cells using force microscopy.....	100

List of Figures

Figure 1-1:	Side view of a suspended cell flowing left-to-right in a parabolic fluid flow.....	7
Figure 2-1:	Permittivity and dielectric loss of water at 25°C mainly due to dielectric (rotational) relaxation and more subtly due to translational vibrations.	16
Figure 2-2:	The low frequency (static) permittivity ratio between salt water and pure water vs. salt concentration.....	20
Figure 2-3:	Dielectric properties of water and PBS.....	20
Figure 2-4:	Dielectric loss for water at 25°C, with the addition of ionic loss.....	21
Figure 2-5:	Membrane-bound cell subject to a uniform electric field at low, intermediate, and high frequencies in a low conductivity medium ($\sigma_{\text{cell}} > \sigma_{\text{medium}}$).	24
Figure 2-6:	Geometry of simulated microfluidic channel..	26
Figure 2-7:	Determining the effective permittivity of a single-shelled sphere.....	28
Figure 2-8:	Side view of scaled model of rectangular parallel plate channel (50 μm x 1 m x 1 m), which is used to verify equation 2-11.	30
Figure 2-9:	Top: Cell permittivity is fixed at 50, while the medium permittivity varies from 10-70. Bottom: The medium permittivity is fixed at 80, and the cell permittivity varies from 10-70.....	32
Figure 2-10:	Simulated capacitance signatures from free-flowing polystyrene spheres (red) accompanied by 5 experimental traces (blue).....	33
Figure 2-11:	Three-electrode configuration. Comparison between energy density and the analytical solution for determining capacitance change of 5.7 μm polystyrene spheres at 5, 10, and 20 μm elevations.	35
Figure 2-12:	Three-electrode configuration. Comparison between energy density and the analytical solution for determining capacitance change.....	36
Figure 2-13:	Fractional change per micron vs. altitude.	36

Figure 2-14: Coaxial electrode geometry, which has an analytical solution for the gradient of the RMS field squared.....	39
Figure 2-15: Comparison between Equations 2-15 (analytical solution) and 2-16 (finite elements) for calculating ∇E_{RMS}^2 in the coaxial geometry (Figure 2-14).....	40
Figure 2-16: CM factor - Viable (TOP) vs. Non-Viable (BOTTOM) Yeast Cells. The medium conductivity varies.....	45
Figure 2-17: CM factor - Viable Yeast – Cytoplasm Conductivity varies.....	46
Figure 2-18: CM factor - Viable Yeast – Cytoplasm Permittivity varies.....	46
Figure 2-19: CM factor - Viable Yeast – Wall Permittivity varies.....	47
Figure 2-20: CM factor - Viable Yeast – Medium Permittivity varies.....	47
Figure 2-21: CM factor - Viable Yeast – Membrane Thickness (and consequently permittivity) varies.....	48
Figure 2-22: Clausius-Mossotti factor vs. frequency using the single-shell model.....	49
Figure 2-23: Side view of a suspended cell flowing left-to-right in a parabolic fluid flow.....	50
Figure 2-24: A single 10 μm polystyrene sphere was translated back and forth approximately 300 times at various speeds to investigate the possibility of a lift force.....	53
Figure 3-1: Experimental apparatus.....	59
Figure 3-2: Transmission spectra of the resonator-channel combination for air-filled and water-filled channels are shifted by 65 MHz. This corresponds to a 45 fF capacitance change.....	60
Figure 3-3: Schematic of the manipulation and detection system.....	61
Figure 3-4: When the resonance frequency increases from f_{r1} to f_{r2} , the voltage difference, V_2-V_1 , increases from zero.....	63
Figure 3-5: Capacitance variations in the channel due to 10 μm polystyrene spheres.....	64
Figure 3-6: Capacitance variations in the channel due to 6 μm yeast cells.....	64

Figure 3-7:	Capacitive detection of the dielectrophoretic trapping and release of yeast cells.	65
Figure 3-8:	A 1.6 GHz microwave interferometer is used to detect single cells flowing in a microfluidic channel past an interdigitated electrode pair [45].	68
Figure 3-9:	Electromagnetic chamber containing the microscope (M), a panel for electrical connections (P), and all the RF electronic components (RF) labelled in Figure 3-8 apart from the RF source and lock-in amplifier, and power sources.	71
Figure 3-10:	Close-up of x-y-z translator (A), which is used to manoeuvre the transmission line resonator (B) above the microfluidic chip (C), which contains four fluid ports (D) and various electrode designs (E).	72
Figure 3-11:	Simulated capacitance signatures from a 6 μm polystyrene sphere passing over the two-gap interdigitated electrodes at constant elevations.	74
Figure 3-12:	From Figure 3-11, we plot the simulated capacitance changes from the green and red dots vs. elevation.	75
Figure 3-13:	By taking the ratio of the simulated capacitance changes in Figure 3-12, the signal valleys and signal peaks corresponding to positions A and B, respectively, one can apply this figure to experimental traces (e.g., Figure 3-14) to determine the particle height above the electrodes.	75
Figure 3-14:	Experimental capacitance signature from a 6 μm polystyrene sphere (TOP) passing over the two-gap interdigitated electrodes as detected using the interferometric system.	76
Figure 3-15:	Examples of capacitance signatures from Chinese Hamster Ovary cells in PBS (TOP), and activated T-cells in RPMI-1640 (BOTTOM).	78
Figure 3-16:	Examples of capacitance signatures from MCF-7 (TOP) and MDA-MB-231 cells (BOTTOM) in D-MEM.	79
Figure 3-17:	Examples of capacitance signatures from 10T $\frac{1}{2}$ (TOP) and Ciras-3 (BOTTOM) mouse fibroblasts in α -MEM.	80
Figure 3-18:	Various electrode designs fabricated across a microfluidic channel containing “cubbies”.	82

Figure 3-19: Micronit microfluidic chip in an H-channel design, used for delivering a differential flow through the intersection, which contains various electrode configurations.....	84
Figure 3-20: Photograph of the MFCS-4C Fluigent pumping system, which operates at a constant external pressure of 500 mbar that is used to control the fluid flow from four 2 ml Fluiwell vials.....	86
Figure 3-21: Graphical user interface provided by Fluigent for controlling the pressure in the microfluidic channel.....	86
Figure 3-22: Velocities of 10 μm polystyrene spheres as they are translated left-to-right and then right-to-left across the electrodes by changing the pressure difference across the channel.....	87
Figure 3-23: Flow velocity vs. pressure differential at different particle elevations.	89
Figure 4-1: A laminar parabolic fluid flow drives the cell from left to right in a microfluidic channel.....	93
Figure 4-2: Members of our group, along with our cell preparation expert, Cheryl Peltier, watch as the system is being prepared to manipulate flowing mouse fibroblasts on site at the Manitoba Institute of Cell Biology.....	108
Figure 4-3: Capacitance changes induced by a 10 μm polystyrene microsphere subjected to a 3 V_{pp} DEP voltage.....	110
Figure 4-4: Capacitance changes induced by a 10 μm polystyrene microsphere subjected to a 4 V_{pp} DEP voltage.....	111
Figure 4-5: Clausius-Mossotti factor for a 10 μm diameter (5 μm radius) polystyrene sphere (PSS) in deionized water (after prolonged exposure to air).....	113
Figure 4-6: Comparison between simulated (Top) and experimental (Bottom) capacitance signatures for a flowing, rigid polystyrene bead subject to a 100 kHz, 10 V_{pp} repulsive DEP signal. The capacitance-induced voltage shift is approx. -0.4 V.....	115
Figure 4-7: Calculated Clausius-Mossotti factor of neutrophils in RPMI-1640 medium using the single- and double shell models.....	116
Figure 4-8: Capacitance signatures from un-actuated neutrophils (N) and red blood cells (RBCs).	117

Figure 4-9:	Capacitance signatures from two RBCs and one neutrophil subject to a 1 V _{pp} applied DEP voltage and 450 kHz frequency.	118
Figure 4-10:	Capacitance signatures from four neutrophils and RBCs subject to a 2 V _{pp} applied DEP voltage and 450 kHz frequency.....	118
Figure 4-11:	Capacitance signatures from five neutrophils and six RBCs subject to an 8 V _{pp} applied DEP voltage and 450 kHz frequency.	119
Figure 4-12:	Capacitance signatures from six neutrophils and two RBCs subject to a 10 V _{pp} applied DEP voltage and 450 kHz frequency.	119
Figure 4-13:	Capacitance signatures from 6 flowing T-lymphocytes experiencing strong nDEP forces from a 2 MHz, 9 V _{pp} DEP signal.....	123
Figure 4-14:	Capacitance signatures from 10 flowing T-lymphocytes experiencing strong nDEP forces from a 2 MHz, 8.5 V _{pp} DEP signal.	124
Figure 4-15:	Top: Observation of T-lymphocyte stretching from 10.8 to 12.3 μm during its transition across the electrode gap. The applied DEP voltage is 9 V _{pp} at 2 MHz. Bottom: Capacitance signature corresponding to the entire transition of the cell across the electrodes.	125
Figure 4-16:	Capacitance signatures from 10T½ mouse fibroblasts DEP-actuated with an 8 V _{pp} , 1 MHz signal.	126
Figure 4-17:	Symmetry of capacitance change versus the entry/exit time ratio of biological cells interacting with the channel wall.....	126
Figure 4-18:	TOP: z-directed fluid velocity across the central 40 μm of channel width for varying elevations (x=10, 12, 14 ... 26, 28, 30 μm). At mid-height (20 μm), the velocity achieves a global maximum at y=0, as expected. At all elevations, the velocities at 20+Δx and 20-Δx elevations are equal at y=0, but begin to deviate across the width due to the curvature of the cross section. BOTTOM: Largest deviations (nearly 8% of y=0 value) occur near the channel ceiling.....	127
Figure 4-19:	Time progression of a T-lymphocyte initially flowing near a channel side wall. The strong DEP force repels the cell, which then encounters the circular ceiling, which funnels the cell toward the channel center.....	128
Figure 4-20:	The capacitance peaks and troughs from rotating polarized T-cells (1 st and 3 rd signatures) are less defined in comparison with	

those generated by un-polarized or non-rotating polarized T-cells (2 nd signature).....	130
Figure 4-21: Free-flowing polarized T-cells that remain parallel with the electrodes during flow generate larger signals than polarized T-cells of similar volume that rotate with a larger “Jeffrey orbit”.....	131
Figure 4-22: Time progression of paired T-lymphocytes experiencing strong negative DEP as they flow left to right over the electrodes.....	132
Figure 4-23: Time progression of a polarized T-lymphocyte experiencing strong negative DEP forces (9 V _{pp} , 2 MHz signal) as it flows left to right over the electrodes.....	133
Figure 4-24: Neutrophil cell elevation vs. horizontal channel position. Note that the electrodes span the range, $-62.5 \mu\text{m} \leq x \leq 62.5 \mu\text{m}$	135
Figure 4-25: Neutrophil cell position vs. time ($V_{\text{DEP}} = 1, 2, 8, 10 \text{ V}_{\text{pp}}$) Top: Position along channel. Bottom: Cell elevation.	137
Figure 4-26: Vertical DEP forces (top) and induced capacitance changes (bottom) of DEP actuated neutrophils.	138
Figure 4-27: Simulated tangential (E_x) and normal (E_y) DEP forces on a 15- μm -diameter CHO cell at various elevations (20 to 37.5 μm - i.e., from mid-channel to 2.5 μm from the ceiling) above the electrode region ($-62.5 \mu\text{m} < x < 62.5 \mu\text{m}$).....	141
Figure 4-28: Simulated Hertz deformation from horizontal ($F_{\text{DEP},x}$) and vertical ($F_{\text{DEP},y}$) DEP forces on CHO cells at various elevations (increasing from 20 to 37.5 μm - i.e., from mid-channel to 2.5 μm from the ceiling) above the electrode gap ($12.5 \mu\text{m} < x < 37.5 \mu\text{m}$).....	142
Figure 4-29: Simulated Hertz deformation from horizontal ($F_{\text{DEP},x}$) and vertical ($F_{\text{DEP},y}$) DEP forces on neutrophils at various elevations (increasing from 20 to 37.5 μm - i.e., from mid-channel to 2.5 μm from the ceiling) above the electrode gap ($12.5 \mu\text{m} < x < 37.5 \mu\text{m}$).....	143
Figure 4-30: Simulated frequency dependence of the transmembrane voltage across a CHO cell immersed in PBS.....	147
Figure 4-31: Simulated electric field amplitude and transmembrane voltage across a CHO cell membrane at elevations ranging from mid-channel height to just 2.5 μm from the channel ceiling (20-37.5 μm).....	148

Figure 4-32: Connected CHO cells are subject to a 9 V _{pp} , 20 kHz DEP signal as they are placed above the central electrode.....	149
Figure 4-33: A) Conductivity and B) relative permittivity of a 5000 ppm saline solution versus temperature.	151
Figure 4-34: Simulated geometry with three domains: 1.1 mm upper borosilicate layer, which contains a 40 μm fluid channel, and a 0.7 mm borosilicate layer.....	153
Figure 4-35: Influence of electrothermally-induced flow on the overall fluid flow.	156
Figure 4-36: Horizontal fluid velocities at fixed elevations (2.5 to 37.5 μm) above the electrodes.	157
Figure 4-37: Joule heating – temperature rise vs. flow rate.	158
Figure D-1: MATLAB graphical user interface for analyzing the capacitance signatures from biological cells.	179

List of Copyrighted Material for which permission was obtained

Figure 2-5 in this thesis reproduces Figure 25 from the journal article, "The Physics of Cell Membranes", written by H.G.L. Coster in the Journal of Biological Physics, volume 29, year 2003, page 363-399, with kind permission from Springer Science and Business Media.

Chapter 3 contains material reprinted with permission from G. A. Ferrier, A. N. Hladjo, D. J. Thomson, G. E. Bridges, M. Hedayatipoor, S. Olson, and M. R. Freeman, "Microfluidic electromanipulation with capacitive detection for the mechanical analysis of cells," *Biomicrofluidics*, vol. 2, no. 4, 044102, 2008. Copyright 2008, American Institute of Physics.

Thesis Related Publications

[Ferrier 2007] G.A. Ferrier, A.N. Hladio, D.J. Thomson, G.E. Bridges, M. Hedayatipoor, S. Olson, and M.R. Freeman, "Microfluidic electromanipulation with capacitive detection for cell diagnostic applications," *Proc. NSTI*, vol. 2, pp. 214-217, 2007.

[Ferrier 2008a] G.A. Ferrier, S.F. Romanuik, D.J. Thomson, G.E. Bridges, and M.R. Freeman, "Capacitance signatures for rapid detection of the polarity of the dielectrophoretic force on single yeast cells," *Proc. NSTI*, vol. 2, pp. 589-592, 2008.

[Ferrier 2008b] G.A. Ferrier, A.N. Hladio, D.J. Thomson, G.E. Bridges, M. Hedayatipoor, S. Olson, and M.R. Freeman, "Microfluidic electromanipulation with capacitive detection for the mechanical analysis of cells," *Biomicrofluidics*, vol. 2, no. 4-044102, pp. 1-13, 2008.

[Ferrier 2009a] G.A. Ferrier, S.F. Romanuik, D.J. Thomson, G.E. Bridges, and M.R. Freeman, "A microwave interferometric system for simultaneous actuation and detection of single biological cells," *Lab on a Chip*, vol. 9, pp. 3406-3412, 2009.

[Ferrier 2009b] G.A. Ferrier, S.F. Romanuik, D.J. Thomson, G.E. Bridges, and M.R. Freeman, "Rapid classification of biological cells based on dielectrophoretic actuation with simultaneous capacitive detection," *Proc. μ TAS*, 2009, Jeju, South Korea.

[Ferrier 2010] G.A. Ferrier, M. Nikolic-Jaric, S. Rzeszowski, T. Cabel, S. Nandagopal, F. Lin, M. Butler, G.E. Bridges, D.J. Thomson and M.R. Freeman, "Dielectrophoretic pressing of biological cells into contact with surfaces: a mechanism for biophysical flow cytometry," *Proc. μ TAS 2010*, Groningen, Netherlands.

[Nikolic-Jaric 2009] M. Nikolic-Jaric, S.F. Romanuik, G.A. Ferrier, G.E. Bridges, M. Butler, K. Sunley, D.J. Thomson, and M.R. Freeman, "Microwave frequency sensor for detection of biological cells in microfluidic channels," *Biomicrofluidics*, vol. 3, no. 3-034103, pp. 1-15, 2009.

[Nikolic-Jaric 2011] M. Nikolic-Jaric, G.A. Ferrier, D.J. Thomson, G.E. Bridges, and M.R. Freeman, "Dielectric response of particles in flowing media: the effect of shear-induced rotation on the variation in particle polarizability," *Phys. Rev. E* (Accepted Feb 17, 2011).

[Nikolic-Jaric 2011b] M. Nikolic-Jaric, T. Cabel, G.A. Ferrier, G.E. Bridges, D.J. Thomson, C.P. Peltier, P. Khan, and J.R. Davie, "All-electronic deformability cytometry for markerless differentiation of cancer cells," *Proc. MicroTAS 2011*, Seattle, USA, October 2-6, 2011 (Accepted).

[Romanuik 2008] S.F. Romanuik, G.A. Ferrier, D.J. Thomson, G.E. Bridges, S. Olson, and M.R. Freeman, "All-electronic detection and actuation of single biological cells for lab-on-a-chip applications," *Proc. IEEE Sensors*, vol. 1, pp. 634-637, 2008.

[Romanuik 2010] S.F. Romanuik, G.A. Ferrier, M. Nikolic-Jaric, D.J. Thomson, G.E. Bridges, and M.R. Freeman, "Dielectrophoretic actuation and simultaneous detection of individual bioparticles," *Advances in Biomedical Sensing, Measurements, Instrumentation, and Systems*, Eds. A. Lay-Ekuakille and S.C. Mukhopadhyay, Springer Verlag, Volume 55, 106-126, 2010.

Chapter 1 – Research Motivation and Contributions

*“Where the telescope ends, the microscope begins. Which of the two has the grander view?”
- Victor Hugo*

There is a great demand for developing portable diagnostic systems that can analyze biological cells [1], [2]. It is important to understand the nature of cells because they contain the necessities for life: water, nutrients, minerals, proteins, enzymes, fats and carbohydrates. Human cells are subject to ever-changing environments due to fluctuations in diet and oxygen intake among other factors.

Extreme and/or prolonged fluctuations in cellular environment can lead to diseases. For instance, when excess low-density lipoprotein (LDL) cholesterol circulates in the blood, it can slowly accumulate on the inner arterial walls and eventually form hard plaques that narrow the artery. If the plaque grows larger and eventually clots the narrowed artery, a heart attack or stroke can result. Smoking encourages the onset of chronic lower respiratory diseases (and lung cancer) by trapping carcinogens from cigarettes in the lungs, and damaging the alveoli (lung air sacs) that are responsible for absorbing oxygen and releasing carbon dioxide. Diabetes results from abnormally high blood sugar levels, while cancer readily occurs in oxygen-deprived cells.

For survival, human cells must be immersed in an extracellular fluid (ECF) that is isotonic to their cytoplasm. Isotonic refers to a solution wherein the cell neither gains nor loses water through osmosis. Unlike plant cells and fungi (e.g., yeast), human cells are not mechanically supported by a rigid cell wall. Only a thin, semipermeable lipid bilayer membrane (~ 10 nm) separates the cytoplasm from its ECF. In addition, there

are a large number of organic molecules dissolved in the cytosol that are not present in the ECF. If this situation is left unchecked, the resulting influx of water would cause the cell to expand and eventually burst. Fortunately, this tragic osmotic imbalance is avoided by pumping sodium ions out of the cell with the Na^+/K^+ ATP-ase, an enzyme located in the plasma membrane that is responsible for maintaining the resting membrane potential and regulating cell volume.

To improve our quality of life and extend our life expectancy, it is important to strive toward properly diagnosing problems related to cells. According to Statistics Canada, the Canadian life expectancy at birth has increased steadily from approximately 60 (from 1920-1922) to 80.4 (in 2005) [3]. Statistics Canada analyst Brigitte Chavez mentions that “improved access to health care, advances in medicine, better diets, and access to clean water all play a role” in this steady increase.

The dream for single cell diagnostics is a lab-on-a-chip device that provides a rapid diagnosis of a patient based on a blood or tissue sample. Ideally, this diagnosis would predict the early onset of diseases for early intervention. For some conditions, this dream is already becoming a reality. Currently, diabetes patients can monitor their blood-glucose levels from a single drop of blood using chemical testing strips [4], and non-invasive procedures that use near-infrared light scattering can monitor oxygen levels in the blood [5].

Cancer is such a dangerous disease because it progresses from the uncontrollable division of only a few cells. As such, experiments that acquire an averaged bulk property from a large heterogeneous cell population will provide misleading

information when a low percentage of cancer cells is included. In addition, when bulk measurements are repeated on the same population, they do not provide the correct distribution of a response, which is needed to develop mathematical descriptions of cellular behaviour [6]. Consequently, optical and electrical *single-cell* analysis approaches are actively being pursued. A new electrical approach to single-cell analysis is the subject of this thesis.

1.1 Optical Methods for Single Cell Analysis

In microfluidic systems, optical tweezers have been successfully used to determine the progression of cancer in breast cells. In particular, Lincoln *et al.* found that metastatic breast cells can be mechanically stretched up to five times more than their healthy counterparts [7]. In such experiments, single cells are trapped between two counter-propagating laser beams via their mutual optical field. Once the cells are trapped, they can be stretched along the optical axis by varying the intensities of the lasers. Finally, the resulting deformation is measured via optical imaging.

However, optical manipulation techniques often have great difficulty in coupling a sufficient amount of light (avoiding stray light) to maintain high signal-to-noise ratios and high sensitivity. Optical components such as lasers, lenses, and photodetectors are expensive, difficult to align and precisely mount, and require a considerable amount of manual work, often done under optical microscopes [8]. Due to the difficulties in integrating these systems, most highly integrated MEMS systems such as accelerometers and gyros now almost exclusively make use of capacitive sensors [9].

1.2 Electrical Methods for Single Cell Analysis

Detecting the presence of single cells near microelectrodes and apertures through changes in electrical impedance has successfully formed the basis of cell counters for several decades [10]. Recently, this technology has been adapted to microfluidic systems and counting rates for polystyrene particles as high as 5000/s have been achieved [11]. Single cell impedance measurements have also emerged as a useful technique for detecting changes in cells and for detecting disease states in cells [12]. Sohn *et al.* have developed a capacitance based cytometer in which cells were detected with a fF capacitance resolution [13].

An all-electrical approach offers the possibility of rapid analysis and the possibility of very high degrees of integration. Romani and co-workers [14] have successfully designed circuits based on CMOS technology for manipulating and capacitively detecting cells in separate stages with a 30 aF capacitance resolution. The interfacial capacitance associated with electrical double layers at electrode surfaces often masks the bulk capacitance of solutions at low frequencies. To help overcome this, one group has successfully measured bacterial growth through changes in the bulk capacitance at low frequencies (below 1 MHz) by confining samples within long narrow geometries, which enhance the bulk resistance and hence the sensitivity to bulk capacitance [15]. Furthermore, capacitance-based sensing systems integrated into gyroscopes have achieved 12 zF resolution [9]. If sensors of this sensitivity were combined with microfluidic systems for transporting cells, highly integrated diagnostic systems would be possible.

At present, the dielectric properties of cells are obtained either from measurements of the bulk properties of a large cell population in suspension, or through parametric fitting of the electrorotation spectra from single cells. Electrorotation occurs when there is a physical displacement between the applied electric field and the induced dipole due to the dipole taking a finite and significant time to respond to the electric field (due to the limit of the relaxation time on dipole formation) [8].

Cell parameters such as cytoplasm permittivity and conductivity, and membrane capacitance have been determined by fitting electrorotation spectra based on shell models [16]. However, even in advanced systems, obtaining dielectric properties of cells via electrorotation is a relatively slow process, requiring several minutes per particle [17]. In addition, one must rely on optical imaging, which has limited spatial resolution along with additional requirements for video acquisition and processing. However, electrorotation has yielded detailed dielectric properties for many types of cells, treated cells and cell phenotypes.

1.3 Advantages of Using High Frequencies

One of the problems associated with using electric fields for probing biological structures involves the often inherent complexity of the response and sensitivity of biological systems to an electrical stimulus. Biological cells have very thin insulating membranes (~ 10 nm) that surround their cytoplasm, nucleus, and other subcellular components. Therefore, for transmembrane potentials exceeding 1-2 V, these cells are subject to electroporation, in which strong transmembrane electric fields (exceeding 10^9 V/m) create nanometer sized pores in the membranes, which can cause cell lysing

(death) [18]. However, if the corresponding frequency is high enough (faster than the inverse relaxation time of the cell membrane), the membrane will not have time to charge up to the electroporation potential and the electric field will pass through the membrane to affect the internal cellular structure. For example, the recent usage of short electrical pulses for killing cancer cells in mice has become a subject of great interest [19].

In this work, high frequencies (GHz) are used for capacitance detection to avoid interference and variability due to effects such as electrical double layers, ionic conduction and other forms of dielectric variation in materials with frequency, which are dominant at frequencies below 200 MHz [20]. The use of high frequencies also opens the door for lower frequencies (kHz-MHz) to be used for other purposes such as simultaneous electromanipulation of biological materials.

Electrical manipulation is possible because the dielectric properties of cells and their surrounding fluid are different [21]. For many biomedical applications, this dielectric difference in combination with non-uniform electric fields can be used to translate cells (dielectrophoresis), or with uniform time-varying fields to rotate cells (electrorotation) [22]. Recently, dielectrophoretic forces have been enhanced with improved control using multi-insulating blocks for manipulating polystyrene microspheres [23]. Parikesit and co-workers recently used insulating structures to enhance dielectrophoretic signals for size-dependent sorting of continuously-flowing DNA molecules [24]. In addition, electric fields can alter the shape of cells through electrostatic pressure [25].

1.4 Scientific Contributions

This thesis describes the operation of an electronic system that simultaneously detects and actuates biological cells flowing in a microfluidic channel (Figure 1-1). In this system, cells are detected via changes in capacitance between coplanar electrodes arranged as an interdigitated pair. Since coplanar electrodes generate non-uniform electric fields (fringing fields), cell actuation can be done using dielectrophoresis (DEP), which arises from the dipole contribution to the electric force that polarizes neutral particles and moves them along the gradient of the electric field intensity.

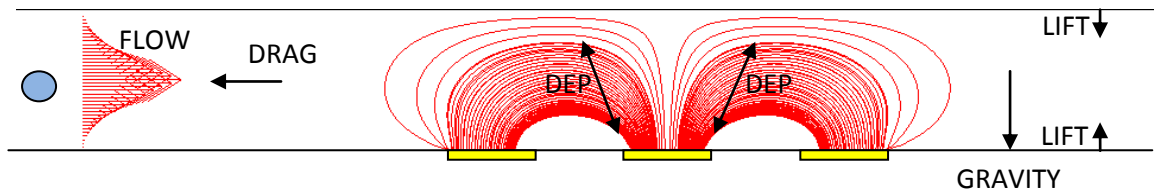


Figure 1-1: Side view of a suspended cell flowing left-to-right in a parabolic fluid flow. Coplanar electrodes generate non-uniform fields that dielectrophoretically-actuate and capacitively detect the cell during its flow over the electrodes. Other forces such as drag, gravity, and lift also influence the cell trajectory (detailed in §2.5).

Two all-electrical experimental approaches were developed to detect the capacitance changes induced by dielectrophoretically actuated biological cells flowing one-by-one in a microfluidic channel. In contrast with other electrical approaches, electrical detection in this work occurs at high frequencies (GHz), which advantageously avoids interference and variability due to effects such as electrical double layers, ionic conduction and other forms of dielectric variation in materials with frequency, which are dominant at frequencies below 200 MHz [20].

High frequency detection also enhances the capacitance sensitivity. This idea has previously been exploited using transmission line resonators, which have been used in the development of scanning capacitance microscopy in which an unprecedented zeptofarad (10^{-21} F) capacitance resolution was achieved [26]. In this thesis, transmission line resonators with high resonance frequencies (1.5 GHz) are used to achieve an RMS capacitance resolution of 0.15 aF (53 Hz BW). With this resolution, we will demonstrate that subtle variations in the cell position can be detected. Under ideal conditions, positional changes of less than 0.1 μm can be detected (see §2.3).

Both the electrical and mechanical properties of a biological cell provide insight into its physiological state. Therefore, this author has proposed an all-electrical approach to deformability cytometry where single cells are dielectrophoretically actuated toward a channel wall. In a flow configuration, the trajectories of free-flowing and DEP-actuated cells are *observed* using capacitance signatures. When repulsive DEP forces are strong enough to press single cells beyond their initial contact with a channel wall, the resulting capacitance signatures include the mechanical effects involved.

For verification, the DEP-induced cell trajectories are modelled by solving the equation of motion, which accounts for DEP, viscous drag, buoyancy, gravity, and a hydrodynamic lift force. Estimates for the mechanical deformation of cells are provided based on calculated DEP forces and direct measurements of the stretching of cells from video files. Comparing the simulations with experimental observations demonstrates that the modelling framework developed in this thesis is capable of predicting the behaviour of particles subject to dielectrophoretic fields with flowing fluids in

microfluidic channels and the capacitance signals from the particles as they flow past the sensing electrodes. Experiments were conducted on many cell types including yeast, Chinese Hamster Ovary cells, mouse fibroblasts, human blood cells, and human breast cells along with their tumorigenic phenotypes.

To facilitate the analysis of thousands of data files, a MATLAB program was written and compiled. This program includes an algorithm that subtracts the background signal variations induced by temperature fluctuations, and incorporates routines for identifying and analyzing cell crossing events.

To summarize, this author's contributions are as follows:

- Primary researcher on the frequency modulation based system
 - All experiments, preliminary modelling
 - First demonstration of simultaneous electrical detection of the dielectrophoretic actuation of single cells
- Developed interferometer-based system in group effort (w/ S.F. Romanuik, M. Nikolic-Jaric, S. Rzeszowski, T. Cabel, E. Salimi, and D. Card). My contributions were:
 - Constructed theoretical framework for calculating cell trajectories considering the forces involved, which reliably predicts trajectories of moderately repelled cells, as well as rigid spheres experiencing strong DEP repulsion, which interact minimally with the wall.
 - Formulated calibration scheme to determine the particle/cell elevation

- First researcher within group to work with mammalian cells, and demonstrated detection in standard high conductivity media such as phosphate buffered saline, D-MEM, etc.
- Proposed all-electrical approach to deformability cytometry
 - Used polystyrene sphere as a model rigid particle. Performed experiments and constructed simulations of the strong DEP repulsion of this particle into a channel wall and found good agreement.
 - Investigated the application of this approach to a number of cell systems including Chinese Hamster Ovary cells, human blood cells, human breast cells, and mouse fibroblasts (and their tumorigenic phenotypes).
 - Demonstrated ability to differentiate between cell types.
 - Carefully investigated several force mechanisms and concluded that DEP was the dominant force for cell actuation.
- Compiled MATLAB GUI to analyze the data collected from thousands of files
 - S.F. Romanuik wrote program in LabVIEW to collect real-time data.
 - T. Cabel followed with a MATLAB program, which collects real-time data and analyzes capacitance responses.

1.5 Thesis Outline

There are 5 chapters in this thesis. In Chapter 2, we describe the polarization mechanisms involved in electrically actuating and detecting dielectric materials such as biological cells. Next, we compute the capacitance changes induced by free-flowing and dielectrophoretically actuated cells. Since dielectrophoresis is exploited in this work to

actuate flowing cells, it is introduced and evaluated versus frequency for a number of cell types. Chapter 3 describes two all-electrical experimental approaches for simultaneously actuating and detecting biological cells. Chapter 4 describes a possible application – all-electronic deformability cytometry – where strong dielectrophoretic signals are used to repel flowing cells temporarily into contact with the channel ceiling. A number of cell systems are investigated and the possible mechanisms involved in the cell-to-wall interaction are explored. Finally, Chapter 5 presents the highlights of this thesis, and outlines some directions for future research. Throughout this thesis, the symbol § denotes thesis sections (§3.2.1 means “section 3.2.1”).

Chapter 2 – Modelling the Dielectrophoretic Actuation and Capacitive Detection of Biological Cells Flowing Past Coplanar Electrodes in Microfluidic Channels

*“Someone told me that each equation I included in the book would halve the sales.”
- Stephen Hawking*

Dielectric properties govern both the electrical actuation and detection of biological cells in their fluid medium. This is because dielectric materials have a finite ability to displace their electrical charges in the presence of an electric field. Depending on the atomic geometry and frequency of the applied field, electrical charges are displaced using one of many mechanisms. For instance, applied electric fields will stretch non-polar molecules, rotate polar molecules (H_2O), separate oppositely charged ions, and deflect positively charged nuclei from their respective electron clouds in dielectric materials. In addition, the movement of free charges, or conduction current, leads to charge separation at the interfaces in heterogeneous materials. These processes collectively alter the dipole moment (charge multiplied by vector separation) between opposing charges, yielding a net dipole moment per unit volume or *polarization* [27]. Consequently, this chapter starts by describing the polarization of biological cells and their fluid environments in terms of the mechanisms involved.

In this research, low- and high-frequency electric fields generated by a pair of coplanar interdigitated electrodes actuate and detect cells flowing through a microfluidic channel. When single cells flowing in suspension interact with the high frequency (GHz) electric field, they induce capacitance changes, which we calculate using an

analytical expression and with finite element analysis. The latter involves drawing the channel and electrode geometries in 3-D using tetrahedral elements (or triangular elements in 2-D), and solving Laplace's equation for the electric fields (and subsequently the capacitances) in the channel. To calculate the induced capacitance change, we must first calculate the permittivity of a heterogeneous cell, which essentially contains many layered shells that have varying dielectric properties. This heterogeneity is handled using a multi-shelled sphere model. In 2-D and 3-D, our analytical expression provides reasonable agreement with the energy density approach, and matches well with experimental traces.

Finally, the well-established electrical phenomenon known as dielectrophoresis (DEP) is introduced as a way to continuously actuate single cells as they flow in suspension over the coplanar electrodes using low-frequency (< 3 MHz) electric fields. Using the example of yeast, we explore the frequency dependence of the dielectrophoretic force, which either actuates cells toward or away from where the largest electric fields exist – i.e., the electrode edges. In this research, we use the same electrodes for DEP actuation and capacitive detection. Therefore, this chapter concludes with a procedure for calculating the DEP-induced cell trajectories, which are influenced by DEP, gravity, buoyancy, viscous drag, and the lift forces from channel walls. Physiological differences in cells are predicted to produce observable dielectrophoretic force variations.

2.1 Dielectric Properties of Aqueous Solutions

Biological cells flowing past coplanar electrodes locally displace the fluid medium to induce capacitance changes and become subject to dielectrophoretic forces. To model

the dielectric behaviour of the system, we start by examining the dielectric behaviour of the background medium. In 1913, Peter Debye [28], [29] introduced a formulation describing the dielectric relaxation response of an ideal, non-interacting population of dipoles to an alternating external electric field:

$$\bar{\epsilon}(f) = \epsilon_{\infty} + \frac{\epsilon_S - \epsilon_{\infty}}{1 + j\omega\tau} \quad (2-1)$$

where $\bar{\epsilon}(f)$ is the frequency-dependent complex permittivity, ϵ_S is the relative permittivity at low frequencies (static region), ϵ_{∞} is the relative permittivity at high frequencies (optical permittivity), ω is the angular frequency ($= 2\pi f$), f is frequency, τ is the characteristic relaxation time, and $j = \sqrt{-1}$.

The bimodal relaxation time distribution involving two such Debye processes is the most appropriate description of the dielectric properties of water in the frequency range $0.2 \leq f(\text{GHz}) \leq 410$ [30]:

$$\bar{\epsilon}(f) = \frac{\epsilon_S - \epsilon_2}{1 + j\omega\tau_1} + \frac{\epsilon_2 - \epsilon_{\infty}}{1 + j\omega\tau_2} + \epsilon_{\infty} \quad (2-2)$$

where ϵ_2 is the intermediate relative permittivity, which represents the transition between the two relaxation processes. Polarization mechanisms with relaxation times, τ_1 and τ_2 , fully manifest at the respective permittivities, ϵ_S and ϵ_2 , which occur at frequencies less than the *characteristic frequencies* f_1 and f_2 , where $f_i = 1/2\pi\tau_i$. In water, the first relaxation time, τ_1 , characterizes the *rotational relaxation* within a hydrogen bonded cluster, and reduces considerably with increasing temperature as hydrogen bonds are weakened and broken.

The rotational relaxation of a molecule with a permanent dipole moment can be modelled by considering the dipoles to be spheres whose rotation in response to the field is opposed by frictional interaction with the surrounding viscous medium. Assuming the dipole is a rigid sphere of radius a , turning in a fluid of macroscopic viscosity η , the relaxation time is $\tau = 4\pi\eta a^3/kT$, where k is Boltzmann's constant and T is absolute temperature. For a molecule of 0.14 nm radius (i.e., half the distance between adjacent oxygen molecules in bulk water) turning in water having a viscosity of $10^{-3} \text{ kg m}^{-1}\text{s}^{-1}$ at 293 K, the relaxation time is 8.5 ps, which is remarkably close to the experimentally determined value of 9.3 ps [31].

The second relaxation time, τ_2 , which is shorter (1.2 ps) and less temperature dependent, is determined primarily by *translational vibrations* within the hydrogen bonded cluster. At frequencies exceeding the highest critical frequency, f_2 , both polarization mechanisms are not fast enough to respond to the electric field, yielding the optical permittivity, $\epsilon_\infty = n^2$ (n = refractive index).

For each Debye process, the maximum dielectric loss occurs at the characteristic frequency where the permittivity is the average value between the lower and upper limits. The *permittivity* and *dielectric loss* relate to the stored energy and dissipation of energy in the medium, respectively, and are simply the real and imaginary components of Equation 2-2:

$$\epsilon_{\text{real}} = \frac{\epsilon_S - \epsilon_2}{1 + (\omega\tau_1)^2} + \frac{\epsilon_2 - \epsilon_\infty}{1 + (\omega\tau_2)^2} + \epsilon_\infty \quad (2-3)$$

$$\epsilon_{\text{imag}} = \frac{(\omega\tau_1)(\epsilon_S - \epsilon_2)}{1 + (\omega\tau_1)^2} + \frac{(\omega\tau_2)(\epsilon_2 - \epsilon_\infty)}{1 + (\omega\tau_2)^2} \quad (2-4)$$

By fitting this bimodal distribution to experimental data at 298.15 K (25°C), Buchner determined the low-, intermediate-, and high-frequency permittivities of water to be 78.32, 6.32, and 4.57, respectively, and the relaxation times (τ_1 and τ_2) to be 9.6 ps and 1.2 ps, respectively [30]. Using this information, we can plot the real and imaginary components of the complex permittivity of water (Figure 2-1). At 16.7 GHz, the real permittivity drops to a value roughly midway between the low- and high-frequency permittivities, and the dielectric loss reaches a maximum value of 36.2. At 1.6 GHz, our frequency of interest, the real permittivity drops from the low-frequency limit (78.32) to 77.67 and the dielectric loss is about 6.84.

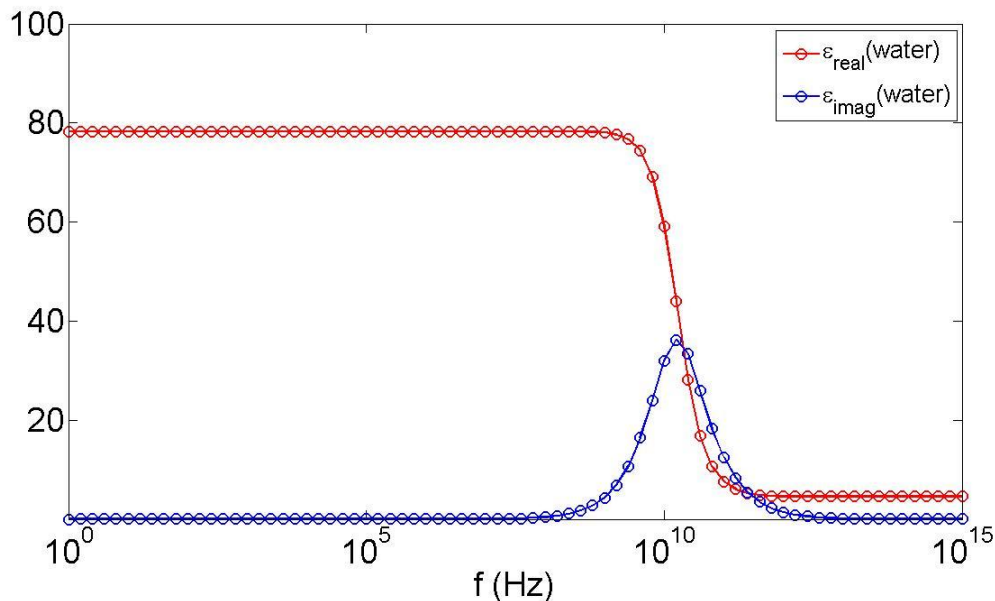


Figure 2-1: Permittivity and dielectric loss of water at 25°C mainly due to dielectric (rotational) relaxation and more subtly due to translational vibrations. At 16.7 GHz, the permittivity transitions from a low frequency value of 78.32 to a minimum value of 4.57, and the loss factor reaches a maximum value of 36.2.

The dielectric loss occurring from *orientation polarization* arises from friction, which occurs as polar molecules endure frictional forces while rotating through a viscous environment, and dissipate the energy as heat. Note that the experimentally determined ($\epsilon_{\infty} = 4.57$, [30]) and theoretical optical permittivity of water ($\epsilon_{\infty} = n^2 = 1.333^2 = 1.78$) vary because experimental data was not collected beyond the THz (10^{12} Hz) frequency range, where additional polarization mechanisms such as atomic and electronic polarization occur ($n_{water} = 1.333 @ 589.2 \text{ nm or } 508.7 \text{ THz}$).

Another loss mechanism known as *ohmic loss* arises in fluids because dissolved substances have a finite ability at a given temperature to dissociate into free positive and negative ions, which become displaced relative to one another. Substances that dissociate into free ions when dissolved in water are called *electrolytes*. Strong electrolytes such as NaCl completely dissociate into Na^+ and Cl^- ions, whereas water itself is a weak electrolyte dissociating to a much lesser extent into H^+ and OH^- ions in bulk water.

The concentration of dissolved ions is proportional to the conductivity, which can vary widely from deionized water ($\sigma = 5.5 \mu\text{S}/\text{m}$) to highly concentrated salt water (sea water; $\sigma \approx 5.0 \text{ S}/\text{m}$). The conductivity, σ , is a measure of how readily electrical current passes through a material, and can be calculated using the following expression, $\sigma = 1000 \sum \Lambda_i C_i$, where Λ_i and C_i are the molar conductivity [$\text{S} \cdot \text{m}^2/\text{mol}$] and molar concentration [mol/L] of the i^{th} ion species. The ohmic loss contribution is determined by adding the effect of conductivity to Equation 2-1:

$$\bar{\epsilon}(f) = \epsilon_{\infty} + \frac{\epsilon_S - \epsilon_2}{1 + j\omega\tau_1} + \frac{\epsilon_2 - \epsilon_{\infty}}{1 + j\omega\tau_2} - j \frac{\sigma}{\omega\epsilon_0} \quad (2-5)$$

Another mechanism known as *ionic polarization* arises from the build-up of charges at electrode surfaces and cell membranes which is addressed in §2.2.

When investigating the properties of non-living particles such as polystyrene beads, deionized water is an appropriate suspension medium. Biological cells, however, require a medium that maintains its pH and ionic concentration within a narrow range in order to live and function. Such a medium is called a *buffer system*, which is a set of chemicals, often a weak acid or base and its salt, that keep the pH of a solution stable by donating and accepting ions that affect pH [32]. For example, our blood is strictly maintained at a pH ranging from 7.3-7.5. Common cell buffers used in experiments described in this thesis include phosphate buffered saline (PBS), Dulbecco's Modified Eagle Medium (D-MEM), Alpha Minimum Essential Medium (α -MEM), and RPMI-1640 (developed at **Roswell Park Memorial Institute**).

In these cell buffers, the presence of NaCl is the main contributor to their conductivity, and it also shifts their low-frequency permittivity. At NaCl molar concentrations exceeding 0.2 mol/L , the low-frequency permittivity of salt water decreases linearly with increasing salinity according to:

$$\epsilon_{salt_water} = \epsilon_{water}(1 - \delta c) \quad (2-6)$$

where ϵ_{water} is the low-frequency permittivity of pure water, c is the molar concentration of NaCl in mol/L , and $\delta = -0.17 [\text{mol/L}]^{-1}$ represents a mean rate of change based on δ values collected by several authors (see [33] and references cited

therein). Data from Nörtemann *et al.* [33] and van Beek [34] suggest that a steeper slope occurs below 0.2 mol/L , leading to the possibility of a permittivity higher than pure water at certain concentrations ($\epsilon_{salt_water} = 1.002\epsilon_{water}$ at 0.051 mol/L), which is assumed to result from “ion atmosphere polarization” effects, but this has not been confirmed. Consequently, for simplicity, we will assume a constant slope of -0.17 , even for concentrations below 0.2 mol/L .

Therefore, our final expression for the complex permittivity is [35]:

$$\bar{\epsilon}(f) = \epsilon_{\infty} + \frac{\epsilon_s(1 - 0.17c) - \epsilon_2}{1 + j\omega\tau_1} + \frac{\epsilon_2 - \epsilon_{\infty}}{1 + j\omega\tau_2} - j\frac{\sigma}{\omega\epsilon_0}. \quad (2-7)$$

The real and imaginary components of this expression give the permittivity (ϵ_{real}) and the dielectric loss (ϵ_{imag}).

The salt concentration in PBS is approximately 0.137 mol/L . Assuming the remaining molecules in PBS, which are present in much lower concentrations, contribute relatively negligibly to the permittivity, the low frequency permittivity drops to 97.5% of the pure water value at 0.137 mol/L (Figure 2-2). The dielectric properties of pure water, and the more conductive ($\sigma = 1.6 \text{ S/m}$) PBS are shown in Figure 2-3. Zooming in near the frequency of interest (Figure 2-4), we see that the ionic loss dominates at medium conductivities above 1 S/m . We also note that at 1.6 GHz , we operate near the local minimum in dielectric/ionic loss. The theoretical permittivity curves shown here compare favourably with measured complex permittivities of PBS and DMEM (page 207 in [36]).

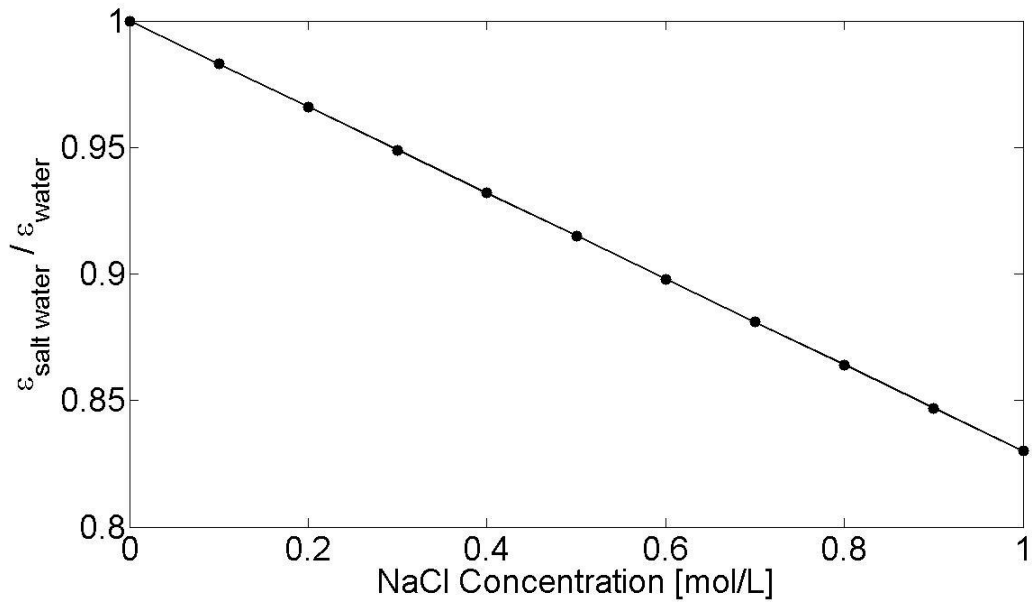


Figure 2-2: The low frequency (static) permittivity ratio between salt water and pure water vs. salt concentration.

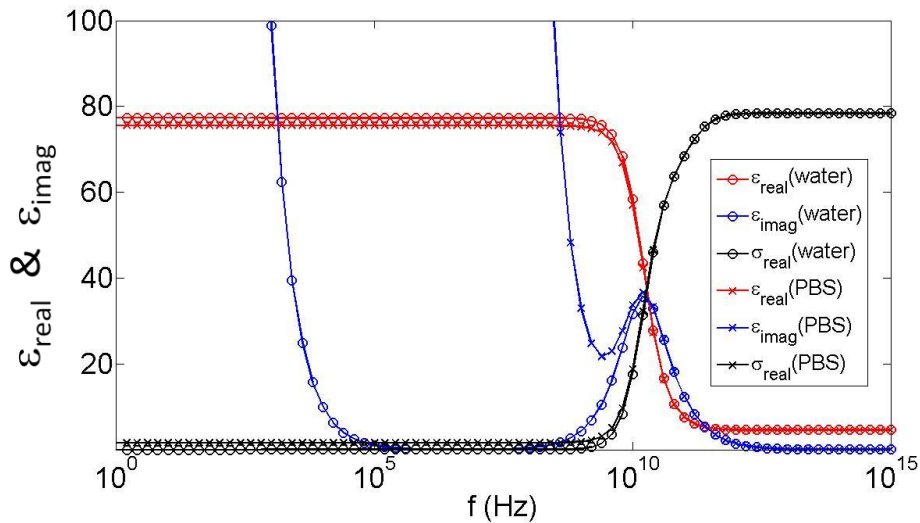


Figure 2-3: Dielectric properties of water and PBS. At low frequencies, adding the strong electrolyte, NaCl, lowers the PBS permittivity and increases the conductivity compared with pure water. At 1.6 GHz, the PBS conductivity is 2.19 S/m compared with 0.60 S/m for pure water. The corresponding dielectric losses are 24.8 and 6.8, respectively.

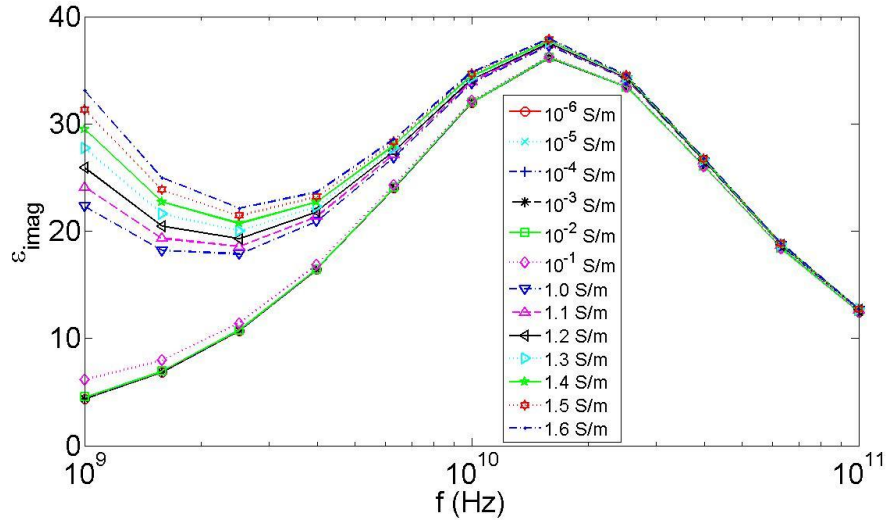


Figure 2-4: Dielectric loss for water at 25 °C, with the addition of ionic loss. The ionic loss is the dominant loss source at medium conductivities above 1.0 S/m. At 1.6 GHz ($10^{9.2}$ Hz), the loss factor in phosphate buffered saline ($\sigma = 1.6$ S/m) is much greater than that of water: $\epsilon_{imag} = \epsilon_{imag}^{dielectric} + \epsilon_{imag}^{ionic} = 6.48 + 18.52 = 25$. N.B.: In the interferometric system described in chapter 3, adding PBS decreases S_{21} by 6 dB compared with that of water, which lowers the Q-factor along with the phase sensitivity.

2.2 Dielectric Properties of Biological Cells

The dielectric properties of healthy eukaryotic cells vary widely throughout their volume. Relative to typical cell buffers (e.g., PBS), the inner cytoplasm is comparably conductive (e.g., ~ 0.2 S/m for yeast [37]) and generally made from water combined with a mixture of salts (K^+ , Na^+) that provides typical relative permittivities of 50-80 [38]. Healthy cells have active systems that maintain their permittivities within a narrow range.

Conversely, the surrounding phospholipid bilayer membrane is extremely thin (10 nm) and insulating (10^{-7} S/m) with a permittivity less than 10. In general, these membrane parameters depend on the osmotic pressure exerted by the suspending solution. This

osmotic pressure is proportional to the *osmolality*, which is the number of osmoles of solute in a kilogram of solvent, where an *osmole* is one mole of any non-dissociable substance (containing 6.02×10^{23} particles). The normal osmolality of body fluids is 280-300 milli-osmoles per kilogram (mOs/kg) [39]. These fluids are *isotonic*, which means that the osmole concentrations in the cytoplasm and the suspending solution are equal. Suspending solutions with lower and higher osmolality values than 280-300 mOs/kg are *hypotonic* and *hypertonic*, respectively. Through osmosis, hypotonic solutions force water into cells, and hypertonic solutions force water out of cells.

Furthermore, this osmotic pressure causes cell contraction or expansion, which is partially controlled by membrane foldings, which provide an excess membrane area that can allow cell deformation without area expansion [40]. Gascoyne *et al.* found that membrane folding was the primary reason for significant variations in *specific membrane capacitance* and *specific membrane conductance* (see §2.4.1) between cancer cells and blood cells [41]. In general, membrane folding includes the additional complexities offered by any morphological feature that increases cell surface area, which includes “villi, microvilli, blebs still attached to the cell body, folds, ridges, and ruffles” [41].

2.2.1 Polarization mechanisms

Three main polarization mechanisms govern the overall electrical behaviour of cells:

1) interfacial polarization, 2) dipolar relaxation (described above) and 3) counter-ion polarization effects [42].

Interfacial polarization, otherwise known as the *Maxwell-Wagner effect*, describes the charging of an interface that depends on its boundary conditions on the fields between phases. *Dipolar relaxation* concerns the equilibrium orientation of an ensemble of independent dipoles that results from a competition between the torque exerted by an external field and random thermal agitation. *Counter-ion polarization* effects arise from ionic diffusion in the electrical double layers adjacent to charged surfaces. In biological systems, counter-ion polarization effects dominate at audio frequencies, Maxwell-Wagner effects dominate in the MHz range, and dipolar relaxation occurs in the GHz range.

Figure 2-5 shows how a uniform electric field interacts with a membrane-bound cell that is immersed in a relatively low conductivity medium (~ 1 mS/m). At low frequencies, the electrical currents are carried largely by ionic currents and the field is excluded from the cell because the cell membrane is a very poor conductor. At mid-frequencies, the membrane capacitance (which has a very large area-specific value because the membrane is very thin) has a relatively low impedance and the field penetrates the cell. Since the cytoplasm is a good electrical conductor (as the ion concentrations in the cytoplasm are relatively large), the field gradients in the cytoplasm are very small. The electric currents are then a mixture of ionic currents and displacement currents. At high frequencies, the currents are largely due to displacement currents and the impedance is determined by the dielectric constants of the cytoplasm and the surrounding solution.

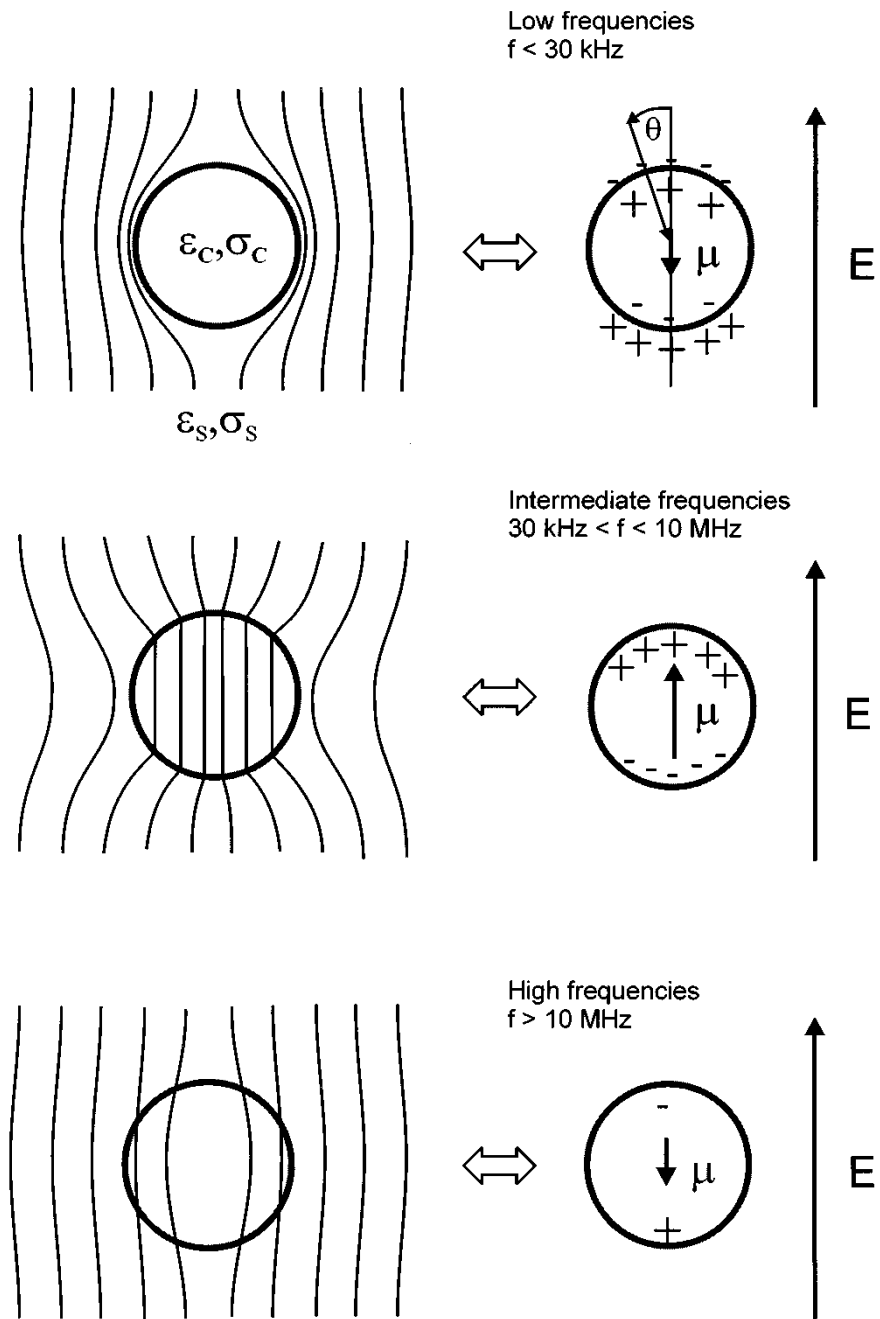


Figure 2-5: Membrane-bound cell subject to a uniform electric field at low, intermediate, and high frequencies in a low conductivity medium ($\sigma_{cell} > \sigma_{medium}$). Reproduced with kind permission from Springer Science and Business Media: Ref. [43].

2.3 Capacitance Change Induced by Single Cells

The dielectric properties of single cells govern the induced capacitance changes as the cells flow over interdigitated electrodes. In this work, capacitance changes are calculated using the time-harmonic quasi-static electromagnetics module in the finite element analysis program, COMSOL Multiphysics®. The electromagnetics module is first used to calculate electric fields in a 3-D microfluidic channel. Electric fields ($E = -\nabla V$, $V =$ position-dependent voltage) in this module have a general dependence on frequency, permittivity, and conductivity through the complex Laplace equation:

$$\nabla \cdot ((\sigma + j\omega\varepsilon_0\varepsilon_r)\nabla V) = 0 \quad (2-8)$$

The model geometry consists of a 3-D microfluidic channel, a spherical cell, and coplanar rectangular electrodes that are modelled as perfect conductors (Figure 2-6). Given that the conductivities of the electrode materials (platinum or gold) are much larger than those of the dielectric materials within the channel ($10^7 \gg 10^{-1}$ S/m), this is a valid approximation. Isotropic etching of the microfluidic channel gives it a flattened semi-circular cross section.

Once the geometry is drawn, we establish the boundary conditions and subdomain properties. Electrode 2 is given a voltage, V_0 , and electrodes 1 and 3 are ground. The remaining boundaries of the microfluidic channel are electrically insulated while the boundary separating the cell from its external fluid environment is given a continuous boundary condition, in which the current densities are equal at the boundary. Specifying the subdomain properties involves noting the permittivities and

conductivities of the corresponding media. For example, deionized water has a relative permittivity of 78 (@ 25°C) and a conductivity of 5.5 $\mu\text{S}/\text{m}$.

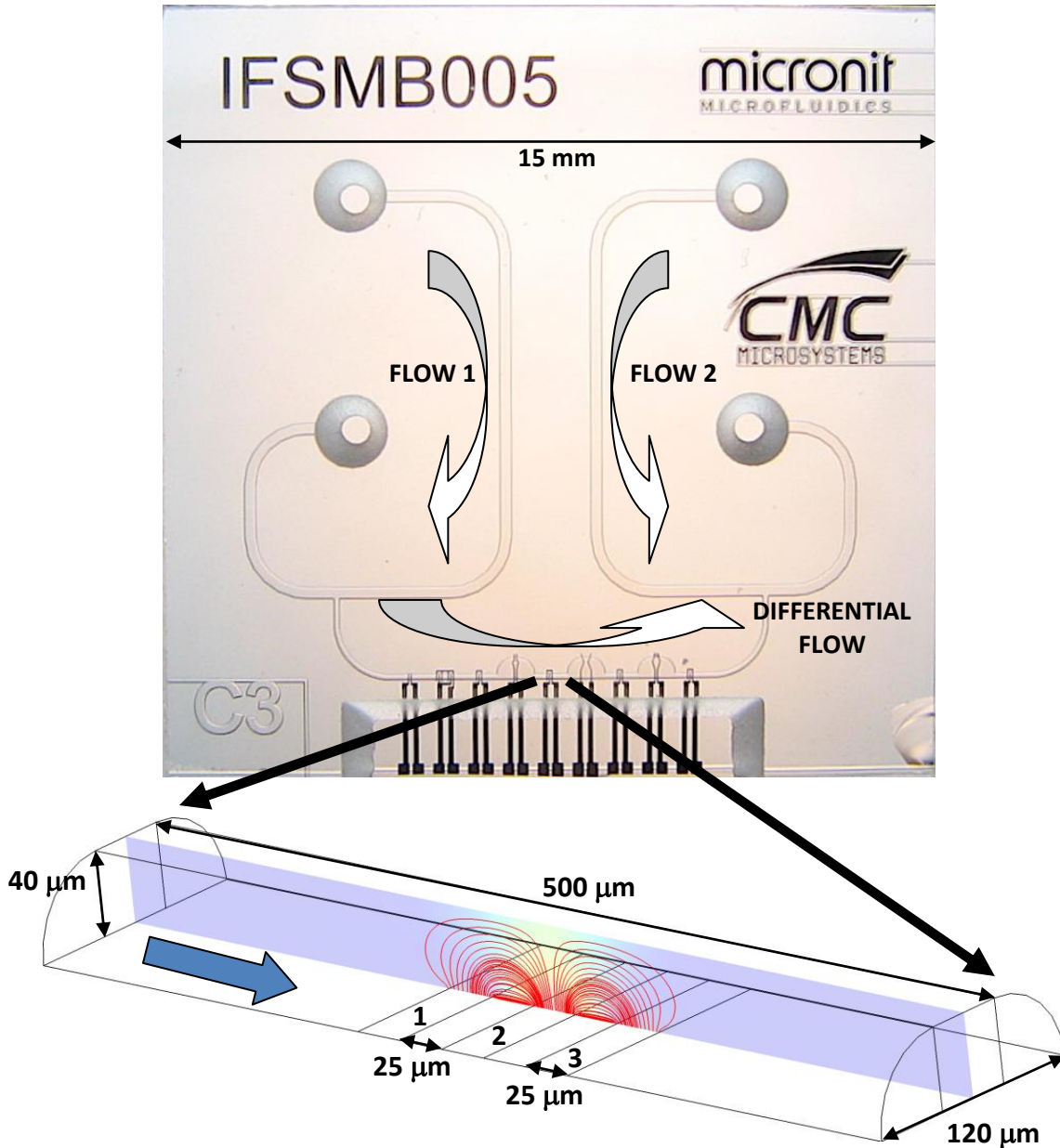


Figure 2-6: Geometry of simulated microfluidic channel. The blue arrow is fluid flow direction. Red contours are electric field lines. Three coplanar electrodes on the floor extend across the width. Electrode 2 is given a potential while electrodes 1 and 3 are grounded. The remaining boundaries are electrically insulating. The electrode widths and spacings are 25 μm each. The channel height, width, and length are 40, 120, and 500 μm , respectively. The experimental channel shown is described thoroughly in §3.2.

Although biological cells contain many different dielectric components, they can often be successfully modelled using a simplified shell approach. Modelling the permittivity of a biological cell using shelled-spheres has been previously described by Jones [44]. As illustrated in Figure 2-7, the procedure involves calculating the effective permittivity of the innermost sphere (ϵ_3) in combination with its nearest outer layer (ϵ_2). The permittivity and conductivity of the surrounding medium are ϵ_1 and σ_1 , respectively. The effective (complex) permittivity for the single-shelled sphere (with ohmic loss) described here is:

$$\bar{\epsilon}'_2 = \bar{\epsilon}_2 \left\{ \frac{\delta^3 + 2 \left(\frac{\bar{\epsilon}_3 - \bar{\epsilon}_2}{\bar{\epsilon}_3 + 2\bar{\epsilon}_2} \right)}{\delta^3 - \left(\frac{\bar{\epsilon}_3 - \bar{\epsilon}_2}{\bar{\epsilon}_3 + 2\bar{\epsilon}_2} \right)} \right\} \quad (2-9)$$

where the prime (') represents an effective quantity, $\bar{\epsilon}_k$ is the complex permittivity of the k^{th} medium, and $\delta = R_{\text{outer}}/R_{\text{inner}}$ (R_{outer} = outer radius; R_{inner} = inner radius). This equation may be used repeatedly (directed from the innermost sphere to outermost layer) to obtain an effective permittivity value for a spherical particle with any number of layers. In general, we add one Maxwell-Wagner relaxation process for each interface. Maxwell-Wagner polarization is governed by the rate of charge accumulation, and consequently charge separation, at the interface between electrically distinct cellular domains [42]. The accumulation rate depends on the permittivities and conductivities of the neighbouring domains.

Once the effective complex permittivity is found, the corresponding scalar values of the effective permittivity and conductivity are

$$\epsilon'_2 = \text{Re}(\bar{\epsilon}'_2) \text{ and } \sigma'_2 = -\omega \text{Im}(\bar{\epsilon}'_2) \quad (2-10)$$

These values are generally dependent on frequency and exhibit Maxwell-Wagner polarization.

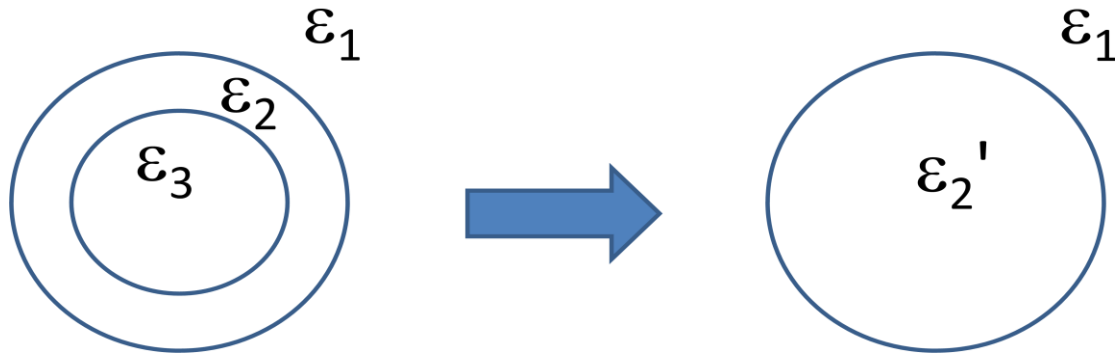


Figure 2-7: Determining the effective permittivity of a single-shelled sphere.

By modelling the biological cell in this way, we can insert one sphere into the model geometry instead of a multi-shelled sphere. This overcomes the practical problems related to the size difference between the cell (10 μm) and its surrounding membrane (10 nm). Specifically, the required resolution of finite elements within the membrane is much smaller than that required in the cell. When the resolutions are customized (larger in the cell, smaller in the membrane), the program has difficulty establishing finite elements along the interface, which often leads to inaccurate or diverging solutions. Therefore, we have chosen to use an effective shell model.

Once the geometry, subdomain properties, and boundary conditions are given, the geometry is meshed and the aforementioned complex Laplace equation is solved to determine the electric potential everywhere in the channel. Since the electric field

equals the negative gradient of the electric potential ($E = -\nabla V$), the electric fields are also solved everywhere.

The corresponding capacitance between the coplanar electrodes in the channel is given by $C = 2W_E/V_{RMS}^2$, where the stored energy, W_E , is found by integrating the time-averaged energy density over the channel volume. Therefore, the capacitance change, ΔC , associated with a cell passing by the electrode array is determined by calculating the capacitance of the channel with and without the cell (requires 2 simulations), and taking the resulting difference in capacitance. To obtain accurate capacitance calculations, the finite elements must be highly concentrated and uniform throughout the channel. However, a high concentration of mesh elements does not significantly (e.g., an improvement from 50000 to 100000 elements would yield less than a 1 aF variation) improve the calculation of the capacitance difference.

2.3.1 Analytical expression for capacitance change

The capacitance change induced by a single cell can also be found analytically using the following expression [45]:

$$\Delta C = 4\pi\epsilon_m a^3 \text{Re}\{K_{CM}\} |\vec{E}_{RMS}|^2 / V_{RMS}^2 \quad (2-11)$$

where ϵ_m is the medium permittivity, a is the cell radius, and the root-mean-squared (RMS) amplitudes of the external electric field and applied voltage are $|\vec{E}_{RMS}|$ and V_{RMS} , respectively. This is a convenient formulation for the capacitance change as the external fields are easily calculated while the induced cell polarization is encompassed in the Clausius-Mossotti factor, K_{CM} , which, for a sphere, is given by:

$$K_{CM}(\omega) = \frac{\bar{\epsilon}_p - \bar{\epsilon}_m}{\bar{\epsilon}_p + 2\bar{\epsilon}_m} \quad (2-12)$$

where $\bar{\epsilon}_p$ and $\bar{\epsilon}_m$ are the complex permittivities of the particle and external medium, each having the general form $\bar{\epsilon} = \epsilon - j\sigma/\omega\epsilon_0$. At high frequencies (GHz), the Clausius-Mossotti expression reduces to a ratio of real permittivities:

$$K_{CM}(\omega) = \frac{\epsilon_p - \epsilon_m}{\epsilon_p + 2\epsilon_m} \quad (2-13)$$

Using a very simple parallel-plate geometry, we can confirm the validity of this equation. Again, using COMSOL Multiphysics, we simulate a 3-D rectangular channel with nominal dimensions 50 m x 1 m x 1 m ($l \times w \times h$) with a cell of radius 0.25 m directly between the electrodes (Figure 2-8). The top electrode is 1 V, and the bottom electrode is ground. The 1 m inter-electrode distance makes $|\vec{E}_{RMS}|^2/V_{RMS}^2 = 1$, and our equation simplifies to $\Delta C = 4\pi\epsilon_m a^3 K_{CM}$.

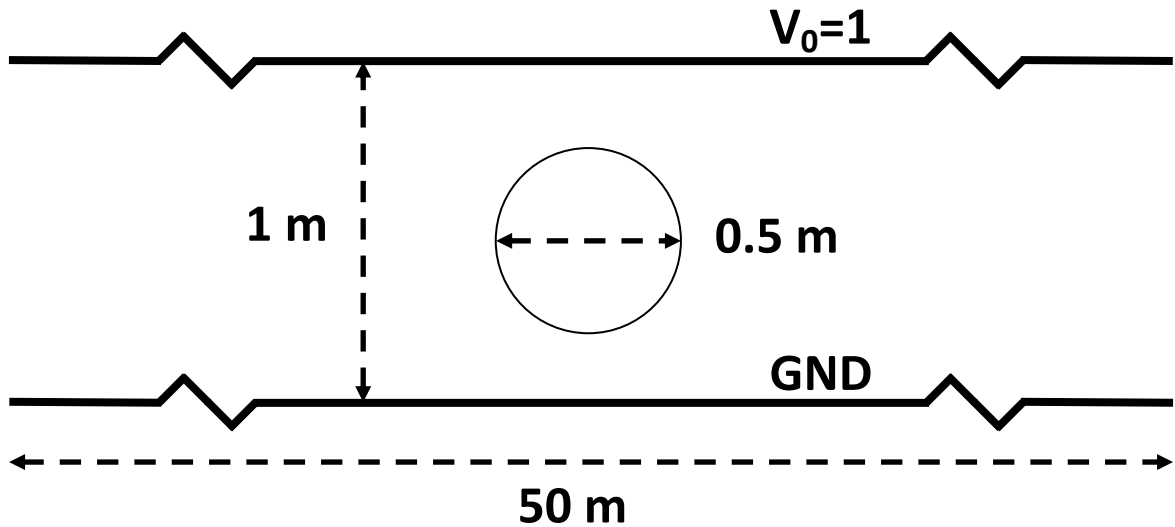


Figure 2-8: Side view of scaled model of rectangular parallel plate channel (50 m x 1 m x 1 m), which is used to verify equation 2-11. Scaling is done here just to simplify the RMS field to voltage ratio to 1.

To compare the *energy density* approach with Equation 2-11, we vary the cell permittivity while fixing the fluid permittivity, and vice versa (Figure 2-9). With a very modest degree of meshing (only ~15000 elements in 3-D simulation), and for practical permittivities, we obtain less than 2% relative error between the two methods. This gives us very good confidence that our formula is correctly derived.

In the next section, we will investigate the effectiveness of the analytical expression in determining the capacitance changes of polystyrene spheres flowing at constant elevations over our coplanar electrode geometry, which generates non-uniform fields.

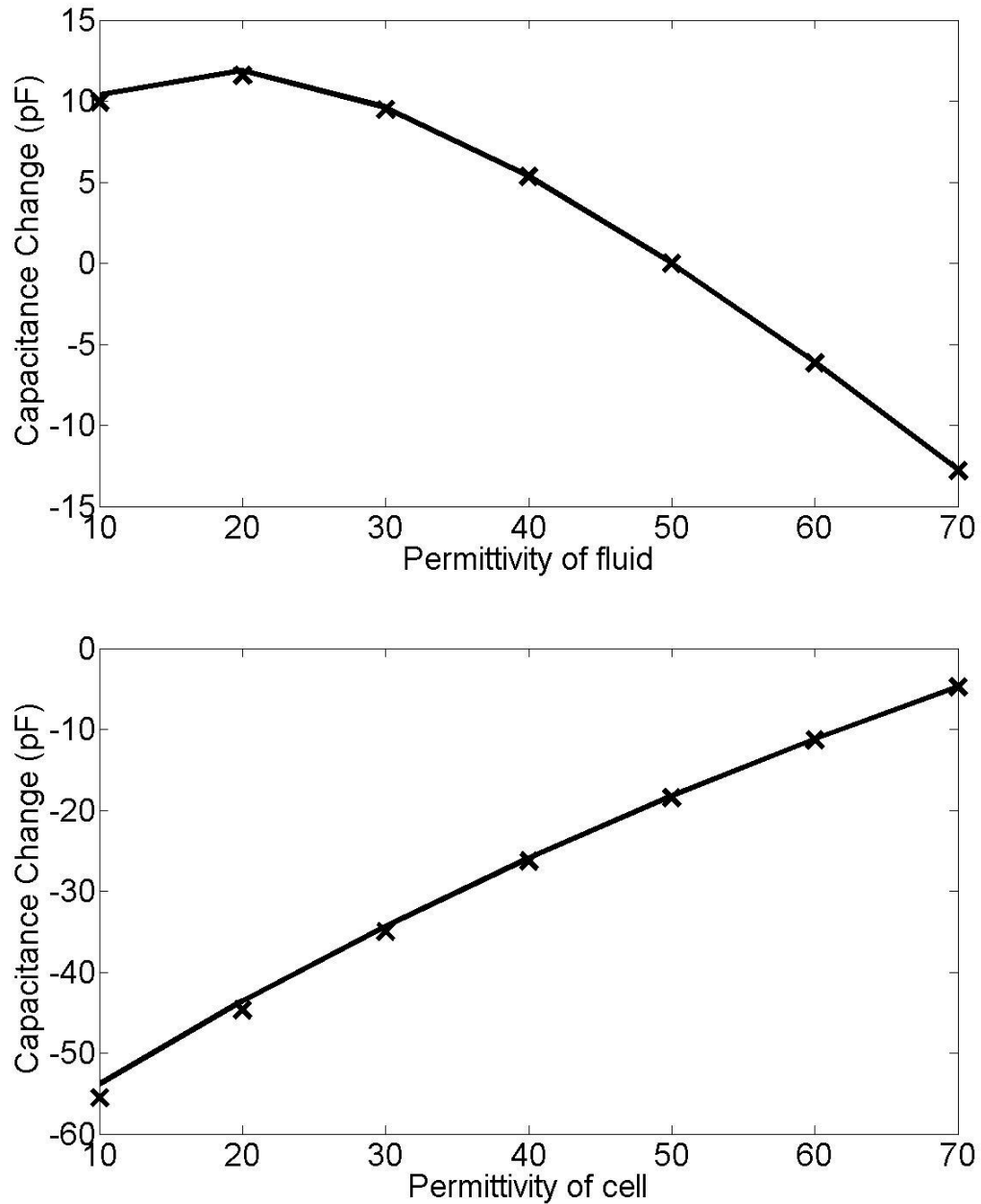


Figure 2-9: **Top:** Cell permittivity is fixed at 50, while the medium permittivity varies from 10-70. **Bottom:** The medium permittivity is fixed at 80, and the cell permittivity varies from 10-70. Through these permittivity ranges, the relative error between the COMSOL calculations (line) and the analytical solution (x) is less than 2%.

2.3.2 Capacitance signatures for particles travelling at a fixed altitude

Figure 2-10 illustrates the capacitance changes induced by uniform 5.7 μm diameter polystyrene spheres as they pass over the electrodes (Figure 2-6) at constant elevations (5, 6, 7, 8, 9, 10, 12, 14, 16, 18, 20 μm). Elevation is defined as the distance from the center of the particle to the bottom surface of the microfluidic channel. As the elevation decreases from 20 to 5 μm , an increase in the magnitude of capacitance change is accompanied by the gradual emergence of double valleys corresponding to the strong electric fields at the electrode edges. For elevations at or higher than mid-channel (20 μm), the largest capacitance changes occur between the electrodes, where the electrode edge effects are not discernible. With this information, the capacitance change profile can be used to calibrate the particle elevation.

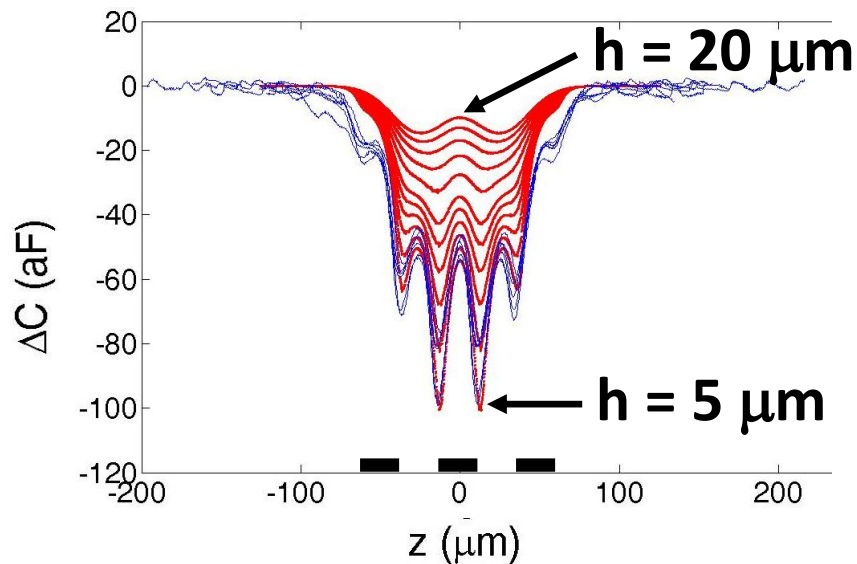


Figure 2-10: Simulated capacitance signatures from free-flowing polystyrene spheres (red) accompanied by 5 experimental traces (blue). Elevation varies from 5 to 20 μm . The lack of agreement between the outermost side-peak results likely reflects the error inherent in using a point-particle approximation, as well as the possibility of elevated edges due to subtle errors in fabrication. Three bars representing 25 μm electrode widths are displayed on the horizontal axis.

In Figures 2-11, and 2-12, the capacitance changes for a 5.7 μm particle diameter travelling at uniform elevations are calculated for the geometry of Figure 2-6. In both cases, we compare the energy density approach with our analytical expression (Equation 2-11) in 2-D and 3-D geometries. The 2-D geometry is simply a 2-D slice through the center of Figure 2-6. In Figure 2-11, we compare the capacitance change induced by a 5.7 μm sphere at 5, 10, and 20 μm elevations.

As expected, the best agreement occurs furthest away from the electrodes, where the fields are most uniform. At low altitudes, the presence of peaks associated with the edge of the electrodes can be observed. At higher altitudes ($h = 10 \mu\text{m}$), only the peaks associated with the maximum field in the electrode gaps are observed. Figure 2-12 considers what happens when the particle elevation remains fixed ($h = 10 \mu\text{m}$), but the particle radius increases. Again, Equation 2-11 deviates for larger particles as they see more field non-uniformities.

If forces act on the particle as it passes over the electrodes, the particle will move toward or away from the electrodes. This movement can be detected by measuring the change in amplitude between two adjacent peaks as the particle passes over. If the force is attractive, the second peak will be larger. If the force is repulsive, the second peak will be smaller.

When particles flow near the electrodes, changes in elevation result in capacitance variations. If we use the peak capacitance, elevation variations of less than 1 μm can be observed. Figure 2-13 reveals the fractional change in the peak amplitude versus particle elevation. For a 6 μm diameter PSS, which typically flows at a 6 μm elevation, a

fractional amplitude change of $0.14/\mu\text{m}$ is predicted. At this elevation, the signal amplitude is 50 aF. Consequently, a $1 \mu\text{m}$ movement causes a 7 aF ($0.14 \times 50 \text{ aF}$) capacitance shift (see §3.2.1).

The noise limit for the measurement system presented in this thesis is 0.15 aF (53 Hz bandwidth). Since a $1 \mu\text{m}$ movement causes a 7 aF shift, the noise limited detection of movement is $0.15/7=0.021 \mu\text{m}$ or 21 nm. The sensitivity to particle elevation decreases as particles move away from the electrodes. Using the calculation from Fig. 2-13, when the elevation increases to $25 \mu\text{m}$, the resulting 0.04 fractional change and 15 aF signal amplitude yield $0.60 \text{ aF}/\mu\text{m}$. Therefore, the limit in this case is $0.15/0.60=0.40 \mu\text{m}$ or 400 nm.

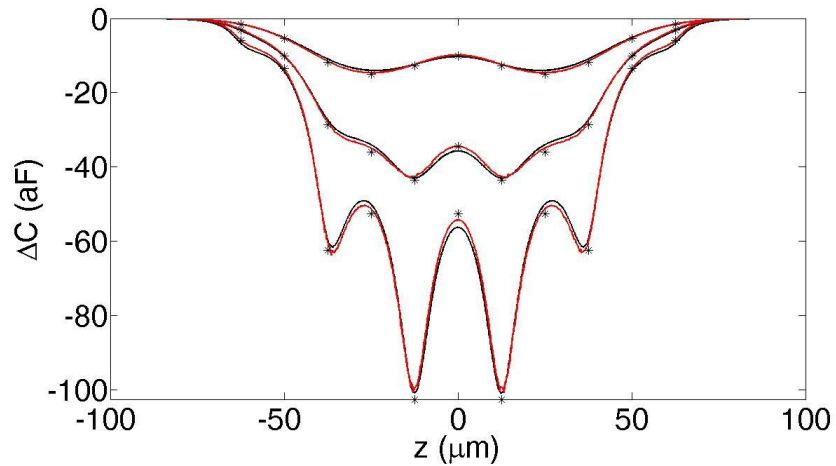


Figure 2-11: Three-electrode configuration. Comparison between energy density and the analytical solution for determining capacitance change of $5.7 \mu\text{m}$ polystyrene spheres at 5, 10, and $20 \mu\text{m}$ elevations. Black and red lines represent the analytical solution in 2D and 3D, respectively. The stars indicate capacitance changes calculated from the energy density (3D). The 3D simulations provide a better fit to the energy density approach, as it accounts for the influence of the rounded cross-section.

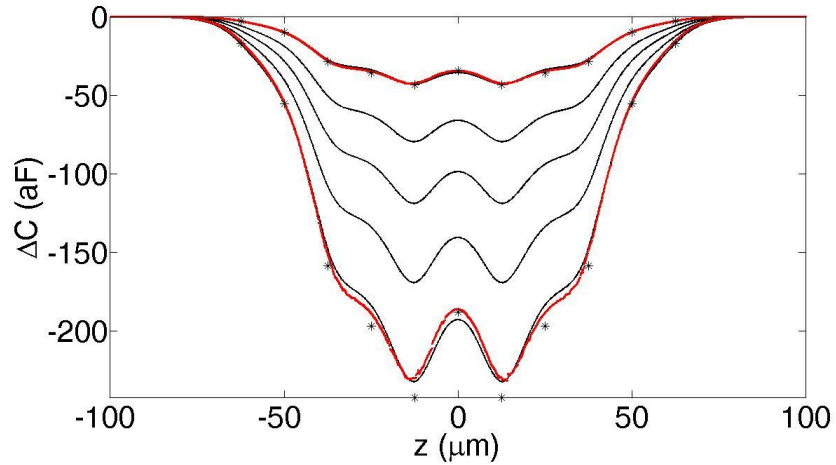


Figure 2-12: Three-electrode configuration. Comparison between energy density and the analytical solution for determining capacitance change. Black and red lines represent analytical solutions for different cell radii (2.85, 3.5, 4.0, 4.5, 5.0 μm) in 2D and 3D, respectively. Stars represent the energy density approach. Again, the 3D data provides a better match to the energy density approach. For a given height ($h=10 \mu\text{m}$), the difference between the analytical solution and the energy density approach increases with cell radius because the field variation across the cell becomes more significant.

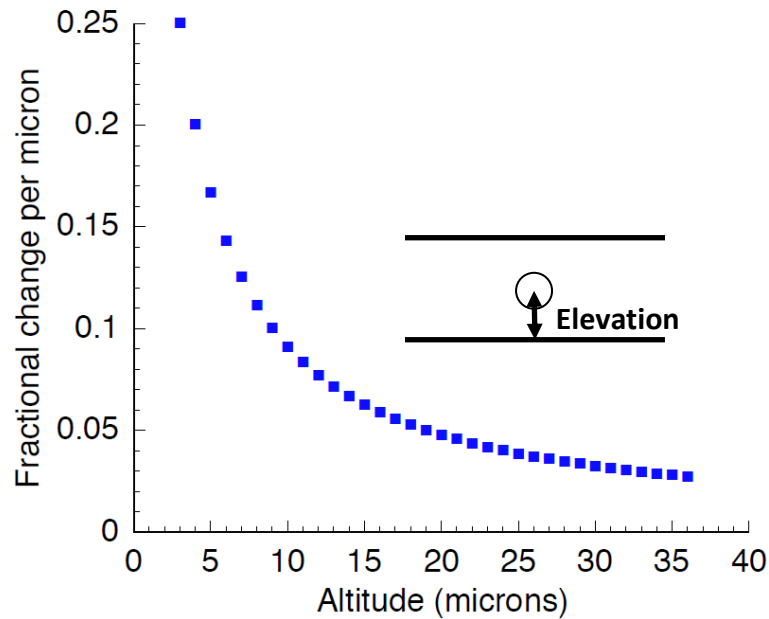


Figure 2-13: Fractional change per micron vs. altitude. The point particle approximation is used in this calculation.

2.4 Dielectrophoresis for Single Cell Actuation

When biological cells flow at constant elevations, their capacitance signatures are symmetric in amplitude and time. However, asymmetric capacitance signatures (§2.5) can be generated using an electrokinetic phenomenon known as dielectrophoresis (DEP). This “dielectric force” actuates cells in spatially non-uniform electric fields along the gradient of the electric field intensity. Coplanar electrodes effectively generate such non-uniform (fringing) fields, and the direction of cell motion depends on which medium, the cell or its surroundings, has the higher effective polarizability.

When the cell has a higher polarizability than the surrounding medium, it moves toward regions of maximum electric field (i.e., the electrode edges). Conversely, when the surrounding medium polarizes more readily, the cell moves away from the electrode edges. The respective scenarios are termed *positive dielectrophoresis* (pDEP) and *negative dielectrophoresis* (nDEP).

In the flow configuration in Figures 1-1 and 2-1, these DEP-induced cell movements are continuous and mainly vertical relative to the electrode plane. Consequently, the induced capacitance changes may continuously increase or decrease depending on whether the cell moves toward or away from the electrode edges, respectively. Such asymmetric capacitance signatures may provide insight into the magnitude and sign of the actuating forces, which may additionally help in determining the electrical properties of the cell. The time-averaged dielectrophoretic force experienced by a uniform dielectric sphere is given by [46], [44], (Appendix A):

$$\langle \vec{F}_{DEP} \rangle = 2\pi r^3 \varepsilon_m \varepsilon_0 \text{Re}\{K_{CM}(\omega)\} \nabla |\vec{E}_{RMS}|^2 \quad (2-14)$$

where r , ε_m , and ε_0 are the particle radius, absolute medium permittivity, and vacuum permittivity, and $\nabla |\vec{E}_{RMS}|^2$ is the gradient of the root-mean-squared (RMS) electric field intensity given by

$$\begin{aligned} \nabla |\vec{E}_{RMS}|^2 &= \nabla (\vec{E}_x^2 + \vec{E}_y^2 + \vec{E}_z^2) \\ &= 2 \left\{ \begin{aligned} &(E_x E_{x,x} + E_y E_{y,x} + E_z E_{z,x}) \hat{x} + (E_x E_{x,y} + E_y E_{y,y} + E_z E_{z,y}) \hat{y} \\ &+ (E_x E_{x,z} + E_y E_{y,z} + E_z E_{z,z}) \hat{z} \end{aligned} \right\} \end{aligned}$$

where $E_{i,j}$ represents the derivative of the i^{th} component of the RMS electric field with respect to j .

To confirm that the gradient of the root-mean-squared electric field intensity is calculated properly, we examine an electrode configuration that provides a known analytical solution. For the coaxial electrode geometry shown in Figure 2-14, the gradient of the RMS electric field squared as a function of distance r_E from the common axis is given by [8]:

$$\nabla |\vec{E}_{RMS}|^2 = \frac{2V_{RMS}^2 \hat{r}}{r_E^3 (\log_e(r_1/r_2))^2} \quad (2-15)$$

where \hat{r} represents the unit vector pointing toward the common axis, r_1 and r_2 represent the radii of the inner and outer surfaces, respectively, and V_{RMS} denotes the RMS potential difference between the inner and outer electrodes. The lines in Figure 2-14 indicate arbitrary arc-lengths over which the fields are calculated. For the

simulation: $r_1 = 0.2 \text{ m}$, $r_2 = 0.5 \text{ m}$, and $r_E = \sqrt{x^2 + y^2}$. The RMS voltage of the inner electrode is $1/\sqrt{2} \text{ V}$, and the outer electrode is ground.

In 2-D, the magnitude of $\nabla|\hat{E}_{RMS}|^2$ along the unit vector \hat{r} is

$$|\nabla|\vec{E}_{RMS}|^2| = 2\sqrt{(E_x E_{x,x} + E_y E_{y,x})^2 + (E_x E_{x,y} + E_y E_{y,y})^2} \quad (2-16)$$

The reliability of Equation 2-16 depends on the precision in calculating the fields, and particularly their derivatives in a region composed of a mesh of finite elements. More elements will give better accuracy. For this example, the maximum spacing between elements is 4 mm. As expected, Figure 2-15 reveals the match between Equations 2-15 (analytical solution) and 2-16 (finite elements). Again, the variations in the data based on Equation 2-16 arise from the limited accuracy in determining the fields and derivative variations between elements.

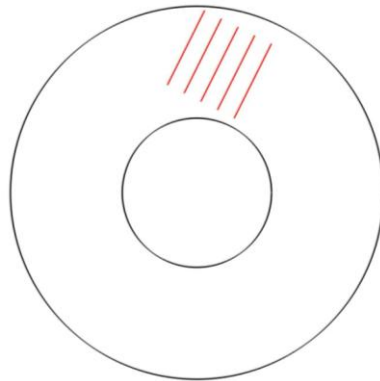


Figure 2-14: Coaxial electrode geometry, which has an analytical solution for the gradient of the RMS field squared. The inner electrode ($r_1 = 0.2 \text{ m}$) and outer ($r_2 = 0.5 \text{ m}$) electrodes are given a 1 V peak amplitude and ground, respectively. The lines represent arbitrary arc-lengths over which the electric fields and derivatives are calculated.

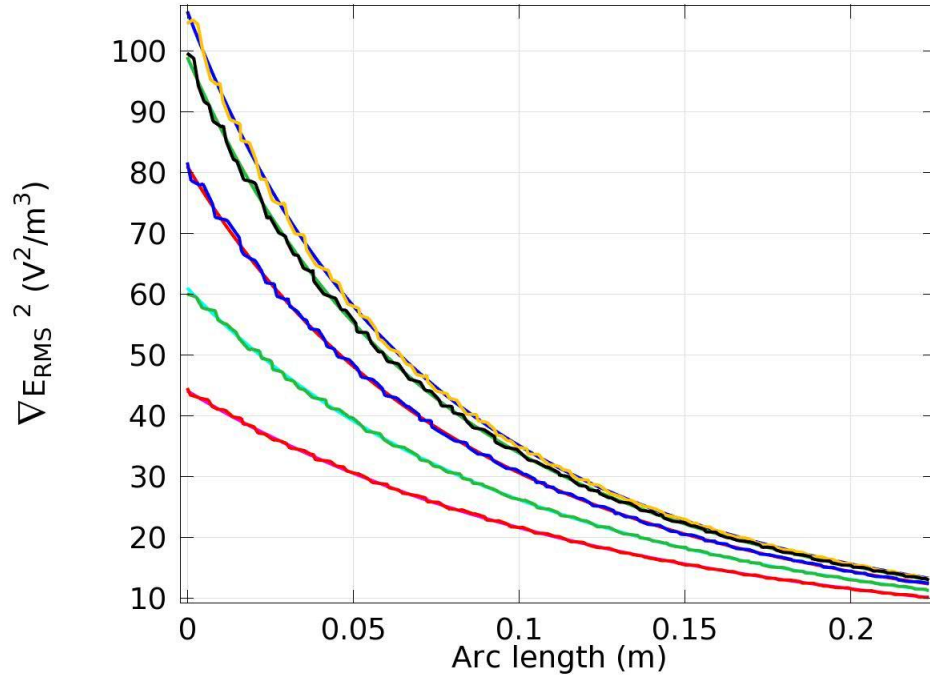


Figure 2-15: Comparison between Equations 2-15 (analytical solution) and 2-16 (finite elements) for calculating $\nabla|E_{RMS}|^2$ in the coaxial geometry (Figure 2-14). For five arbitrary arc-lengths, Equations 2-15 and 2-16 are matched. The subtle fluctuations in the traces generated by Equation 2-16 can be reduced by incorporating more elements per unit distance.

2.4.1 Clausius-Mossotti Factor

The Clausius-Mossotti factor, $K_{CM}(\omega)$, contains both the polarity and entire frequency dependence of the dielectrophoretic force, and is given by:

$$K_{CM}(\omega) = \frac{\bar{\epsilon}_p - \bar{\epsilon}_m}{\bar{\epsilon}_p + 2\bar{\epsilon}_m} \quad (2-17)$$

where $\bar{\epsilon}_p$ and $\bar{\epsilon}_m$ are the complex permittivities of the cell and external medium, each having the general form $\bar{\epsilon} = \epsilon - j\sigma/\omega\epsilon_0$. The vacuum and relative permittivities are ϵ_0

[F/m] and ε , the conductivity is σ [S/m], $j = \sqrt{-1}$, and the angular frequency is $\omega = 2\pi f$ [rad/s], and $f =$ frequency [Hz].

The real part of the Clausius-Mossotti factor (CMF) for a uniform dielectric sphere (with ohmic loss) in fluid is expressed intuitively as a Debye function with a single relaxation time, corresponding to a single Maxwell-Wagner relaxation [47], (Appendix B):

$$\text{Re}\{K_{CM}(\omega)\} = U_h + \frac{\Delta U}{1 + \omega^2 \tau_{MW}^2} \quad (2-18)$$

where $U_h = \frac{\varepsilon_p - \varepsilon_m}{\varepsilon_p + 2\varepsilon_m}$, $\Delta U = \frac{\sigma_p - \sigma_m}{\sigma_p + 2\sigma_m} - \frac{\varepsilon_p - \varepsilon_m}{\varepsilon_p + 2\varepsilon_m}$, and $\tau_{MW} = \frac{\varepsilon_p + 2\varepsilon_m}{\sigma_p + 2\sigma_m}$ is the Maxwell-Wagner relaxation time.

Equation 2-18 clearly shows that the low ($\omega \rightarrow 0$) and high frequency ($\omega \rightarrow \infty$) limits of the CMF are $(\sigma_p - \sigma_m)/(\sigma_p + 2\sigma_m)$ and $(\varepsilon_p - \varepsilon_m)/(\varepsilon_p + 2\varepsilon_m)$, respectively. Therefore, the CMF for a uniform sphere is simply an evolution between these limits that is governed by a single Maxwell-Wagner relaxation process occurring at the cell-fluid interface. Although the difficulty in solving the CMF of shelled-spheres grows rapidly with more shells, one can show that each additional shell simply contributes another Debye term to the Clausius-Mossotti factor [44].

We can show that the CMF is modified by changes in the cell. The following figures reveal the dependence of the CMF on cell viability, medium conductivity, and cytoplasmic conductivity and permittivity for yeast cells (Figures 2-15 to 2-20). Yeast cells are modelled as homogenous cytoplasmic spheres surrounded by spherical shells representing the membrane and the cell wall (recall §2.3).

Unless otherwise stated, the following dielectric properties of yeast are taken from references [37] and [38]. The cytoplasm is given a 4 μm radius, a real absolute permittivity of 50 ϵ_0 , and a conductivity of 200 mS/m. The membrane has an 8 nm thickness, a real absolute permittivity of 6 ϵ_0 , and a conductivity of 250 nS/m. Finally, the cell wall has a 220 nm thickness, a real absolute permittivity of 60 ϵ_0 , and a conductivity of 14 mS/m. For non-viable yeast cells, the cytoplasm, membrane and wall conductivities become 7 mS/m, 1.5 mS/m, and 0.16 mS/m, respectively. The cytoplasm radius and cell wall thickness values were 3.5 μm and 250 nm, respectively. The medium permittivity in all simulations is 78.

Figure 2-16 shows the CMF for viable and non-viable yeast cells. When yeast cells are immersed in low conductivity media (<0.01 S/m) and subject to low-frequency (<100 kHz) DEP signals, viable yeast experiences nDEP while non-viable yeast experiences pDEP. Therefore, dielectrophoretic signals with frequencies below 100 kHz will strongly separate viable from non-viable cells. This effect has been used in DEP-based separation schemes [48], [49], [50]. Note that common high-conductivity cell buffers such as PBS ($\sigma = 1.6$ S/m) yield nDEP over all frequencies.

Viable cells exhibit three frequency dispersions (regions of variation) in the CMF, while non-viable cells exhibit just two. Figure 2-16 reveals the two dispersions caused by the “*cytoplasm-plasma membrane*” and “*plasma membrane-cell wall*” interfaces in viable cells. The third dispersion caused by the “*cell wall-surrounding medium*” interface is effectively “hidden” as the dielectric properties of the corresponding phases are similar yielding minimal dielectric contrast. When the membrane is compromised, the yeast

cells become non-viable and they consequently exhibit one less dispersion. According to data from [37] and [38], the subsequent fluid penetration through the membrane increases its conductivity by a factor of approximately 1000. Furthermore, note that “viable” as discussed here is considered to be a condition where the membrane remains intact.

Finally, note that Figure 2-16 reveals that the low-frequency limit of the CMF increases as the medium conductivity decreases (recall that $CMF|_{f \rightarrow 0} = (\sigma_p - \sigma_m)/(\sigma_p + 2\sigma_m)$). Once the medium conductivity equals the membrane conductivity, the CMF behaves like that from a non-viable cell (i.e., one dispersion/interface removed).

Figures 2-17 to 2-21 evaluate the CMF of viable yeast cells as the dielectric parameters of the cytoplasm, membrane and cell wall vary over typical ranges. Figure 2-17 reveals that the relatively high cytoplasm conductivity (0.2 S/m) has a vital role in establishing the intermediate pDEP frequency regime from ~100 kHz – 100 MHz and its corresponding strength. Larger pDEP strengths and pDEP frequency regimes occur for larger cytoplasm conductivities, which exceed the medium conductivity. However, when the cytoplasm conductivity matches or falls below the medium conductivity, the pDEP regime gradually disappears.

Figure 2-18 reveals that the high frequency limit of the CMF, $(\epsilon_p - \epsilon_m)/(\epsilon_p + 2\epsilon_m)$, increases as the cytoplasm permittivity increases. Typically, the cytoplasm permittivity falls in a regime below that of water ($\epsilon_m = 78$). However, the estimated cytoplasm permittivities of some cells actually exceed that of water [51], perhaps due to the assumption regarding the particular shell model used. Consequently, applying DEP

signals at high frequencies may provide a way of verifying these values, or otherwise confirming that alternative polarization mechanisms must be considered in determining the cytoplasm permittivity [51], [16], [52].

Figures 2-19 and 2-20 reveal small changes in the high frequency limit as the wall and medium permittivities vary. Finally, the low frequency limit is marginally affected by variations in the membrane thickness (Figure 2-21). As mentioned in §2.2, membrane foldings can change the effective membrane thickness depending on the osmotic pressure exerted by the suspending solution.

Table 2-1 and Figure 2-22 outline the dielectric parameters of five cell types examined in this thesis. For each cell type, the average cell radii were measured from the video captures, and the medium conductivities were measured using a conductivity meter. This section can be summarized by observing that physiological changes in the cell results in changes in the electrical properties of the cell.

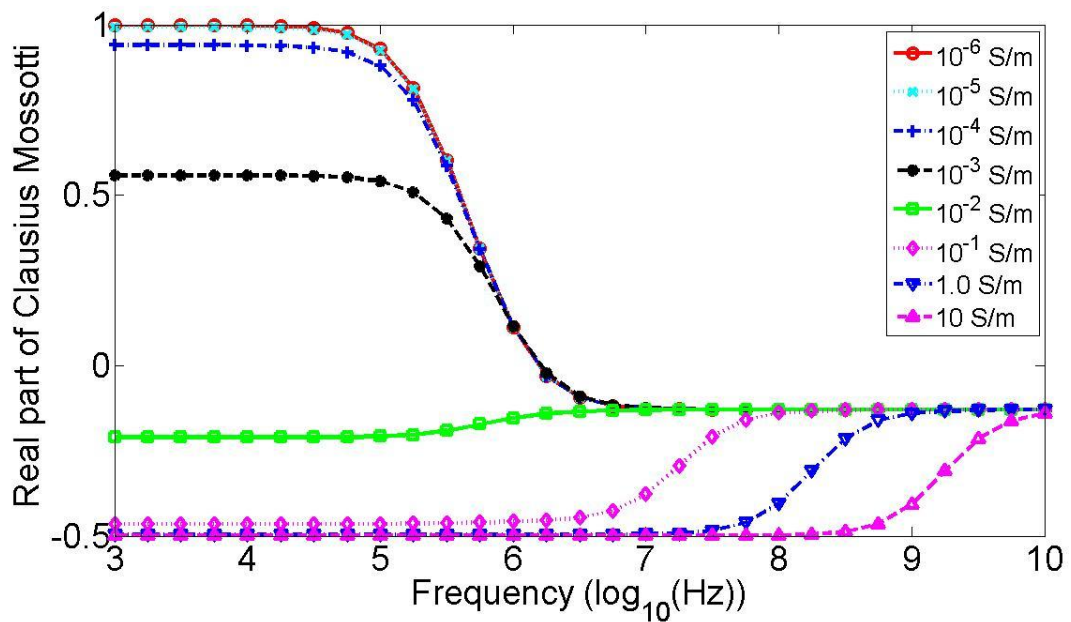
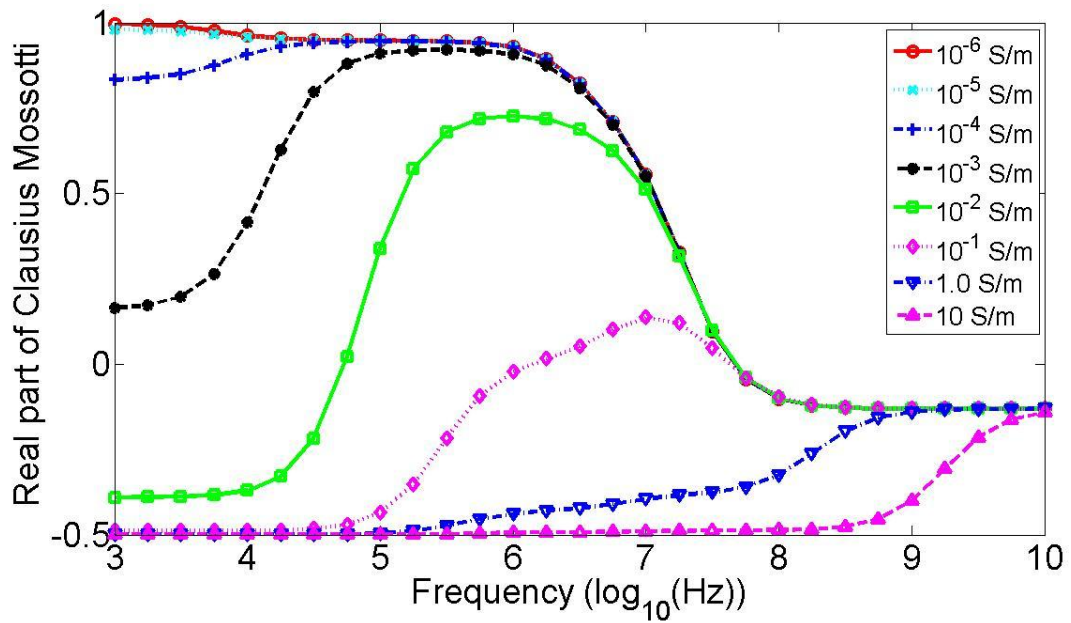


Figure 2-16: CM factor - Viable (TOP) vs. Non-Viable (BOTTOM) Yeast Cells. The medium conductivity varies.

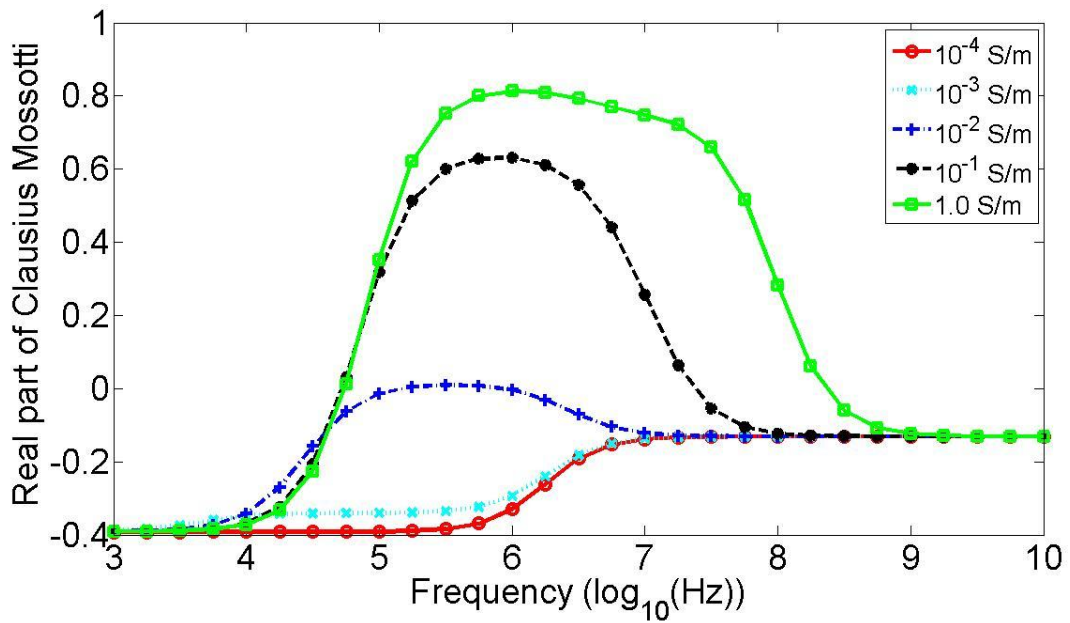


Figure 2-17: CM factor - Viable Yeast – Cytoplasm Conductivity varies. The medium conductivity is 0.01 S/m.

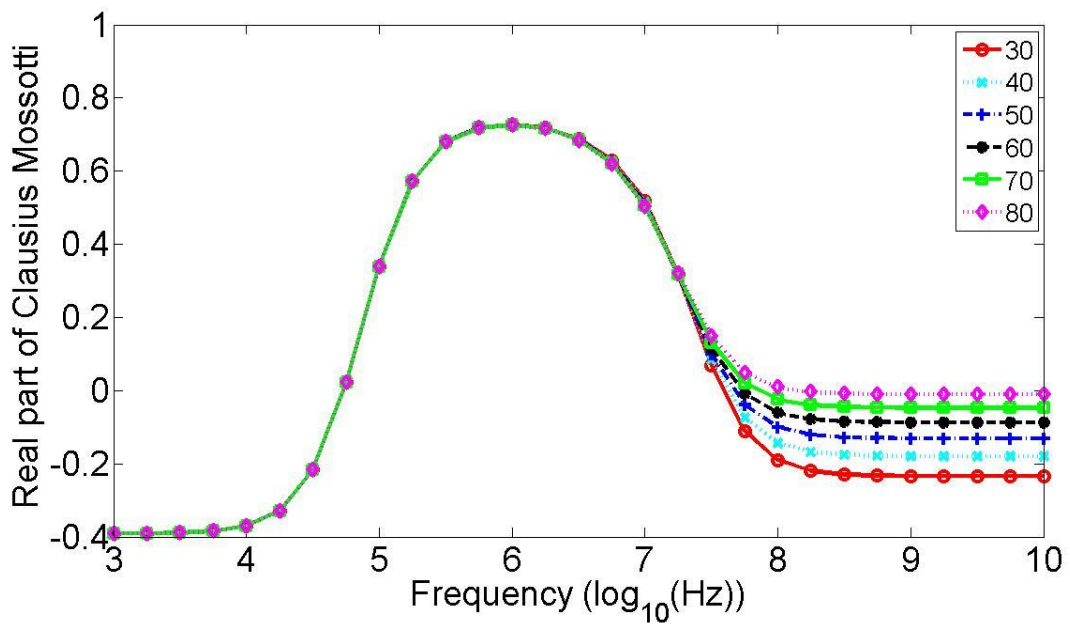


Figure 2-18: CM factor - Viable Yeast – Cytoplasm Permittivity varies. The medium conductivity is 0.01 S/m.

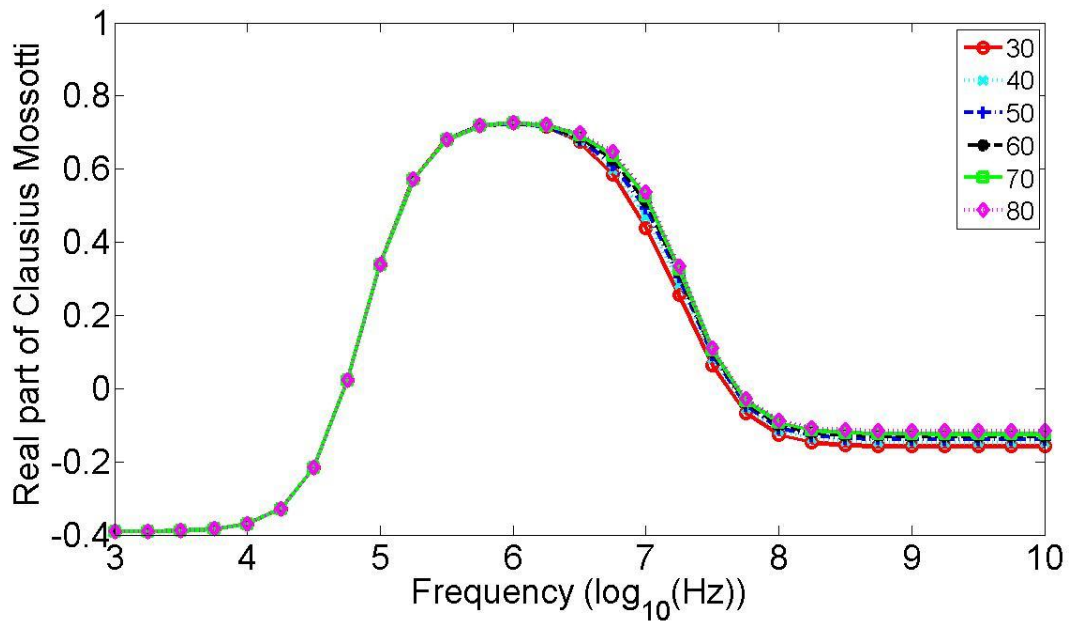


Figure 2-19: CM factor - Viable Yeast - Wall Permittivity varies. The medium conductivity is 0.01 S/m.

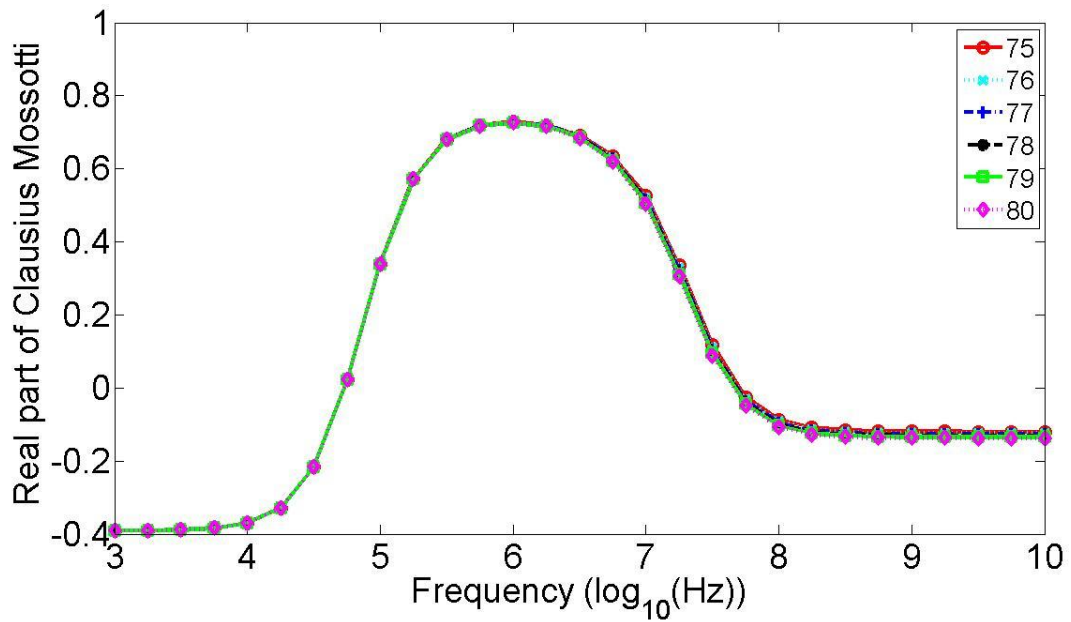


Figure 2-20: CM factor - Viable Yeast - Medium Permittivity varies. The medium conductivity is 0.01 S/m.

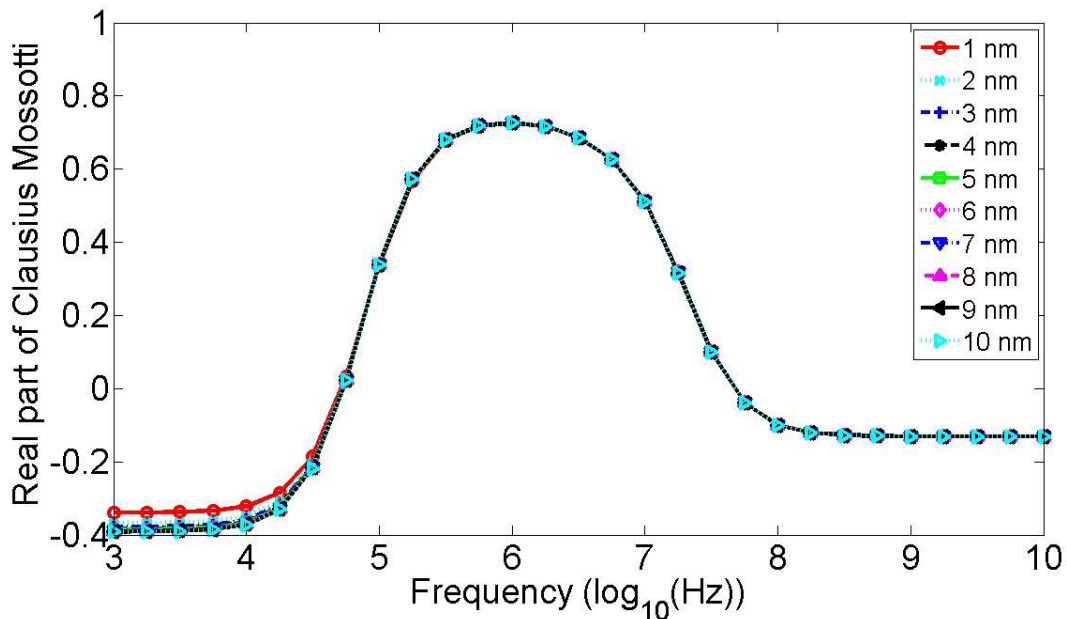


Figure 2-21: CM factor - Viable Yeast – Membrane Thickness (and consequently permittivity) varies. The medium conductivity is 0.01 S/m.

Table 2-1: Clausius-Mossotti parameter set. The membrane conductivities are given directly or evaluated using $\sigma_m = G_m d_m$, where G_m is the specific membrane conductance [S/m^2] and d_m is the membrane thickness. The membrane permittivities are given directly or evaluated using $\epsilon_m = C_m \gamma = C_m d_m / \epsilon_0$, where C_m is the specific membrane capacitance [F/m^2]. MDA-MB-231 and MCF-7 are evaluated in both D-MEM, and D-MEM with 5 mM EDTA. The medium conductivities (bottom row) and cell radii are measured quantities.

	MDA-MB-231	MCF-7	CHO	Neutrophils	T-cells
$r_{cell}(\mu m)$	11	12	7.5	6	6
$d_m(nm)$	10	10	10	8	4.5
$\sigma_m(S/m)$	$320d_m$	$320d_m$	3.2×10^{-6}	1×10^{-12}	$100d_m$
ϵ_m	0.022y	0.0124y	0.01y	6.2	0.0121y
$\sigma_{cyto}(S/m)$	0.7	0.23	0.35	0.3	1.06
ϵ_{cyto}	75	80	60	60	74
Medium	D-MEM	D-MEM	PBS	RPMI-1640	RPMI-1640
References	[53]	[54], [55]	[56], [57]	[58]	[59]
	D-MEM	D-MEM (5 mM EDTA)	PBS	RPMI-1640	α -MEM
	1.344 S/m	1.428 S/m	1.654 S/m	1.196 S/m	1.408 S/m

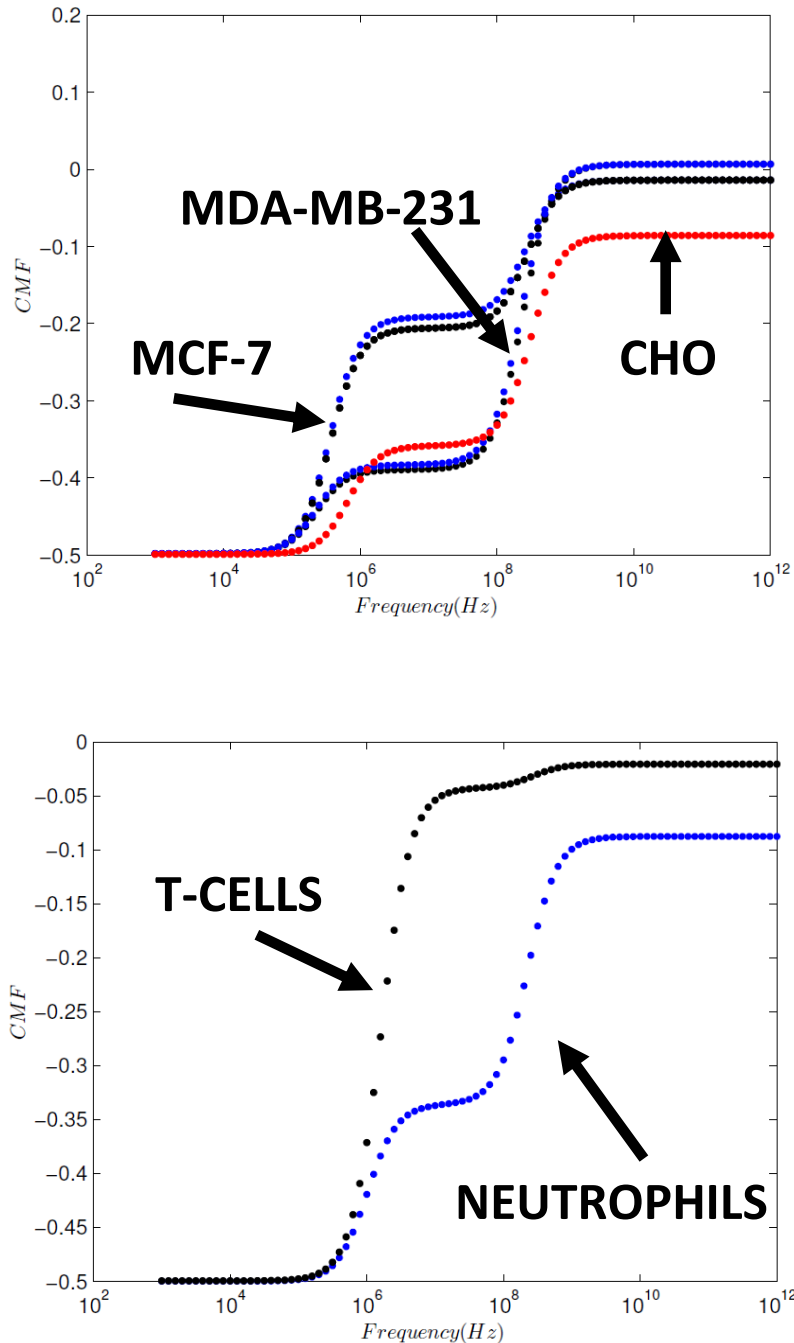


Figure 2-22: Clausius-Mossotti factor vs. frequency using the single-shell model. TOP: MCF-7 and MDA-MB-231 cells in both D-MEM (blue), and D-MEM with 5 mM EDTA (black) added. Little difference is observed between the two media. The red curve corresponds to Chinese Hamster Ovary cells in phosphate buffered saline (PBS). BOTTOM: Neutrophils in RPMI-1640 (blue) and T-lymphocytes in RPMI-1640 (black).

2.4.2 Modelling DEP-induced cell trajectories

The ability to simultaneously manipulate and detect biological cells has opened the door for investigating the electrical properties of biological cells using this approach. For example, by measuring the displacement of flowing cells due to DEP forces, the CMF can be estimated. This in time could be used to determine if cells are viable or non-viable.

In this section, we present the results of experiments and simulations that are done to monitor the displacement of flowing cells caused by DEP, gravitational, drag, and hydrodynamic lift forces (Figure 2-23).

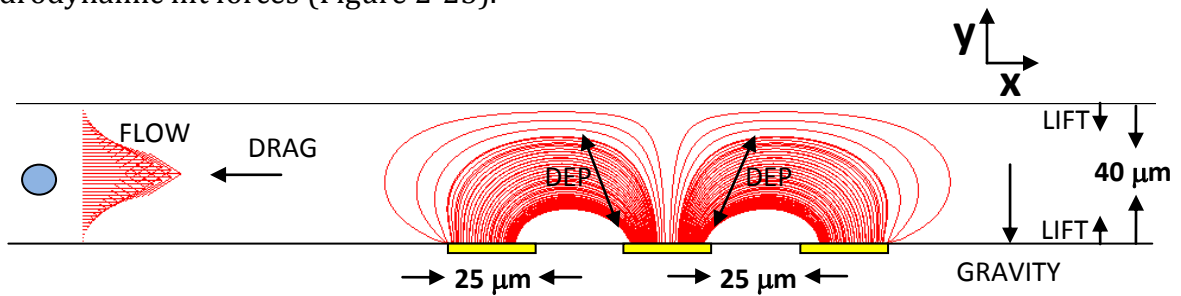


Figure 2-23: Side view of a suspended cell flowing left-to-right in a parabolic fluid flow. Coplanar electrodes generate non-uniform fields that dielectrophoretically-actuate and capacitively detect the cell during its flow over the electrodes. Other forces such as drag, gravity, and lift also influence the cell trajectory. The channel geometry and electrode designs varied over the course of this research, but unless clearly stated, simulations in this thesis focus on the two-gap interdigitated electrode geometry illustrated in Figure 2-6.

In microfluidic channels, the fluid flow is typically laminar, which means that the flow is parabolic [48] about its cross section and characterized by a low Reynolds number ($Re \ll 1$). The parabolic fluid velocity, v_m , is described by Equation 2-19 where $\langle v \rangle$ = mean fluid velocity, H = top-to-bottom wall spacing, and h = distance from the channel

bottom. The fluid velocity is zero at the channel walls ($h = 0$ and $h = H$) and maximum in the center ($h = H/2$).

$$v_m = 6\langle v \rangle (h/H)(1 - h/H) \quad (2-19)$$

Near the channel wall, the parabolic flow initiates shear forces, which act to “lift” the cell away from the wall toward the center. Such forces are called *hydrodynamic lift forces*. More specifically, the uneven velocities experienced by the cell surface cause it to rotate and accelerate toward the center of the channel (region of maximum flow velocity). Although the theory generally predicts higher hydrodynamic lift forces than observed experimentally, we include the lift forces here as they are only approximately an order of magnitude lower than the DEP forces for our fluid velocities ($\sim 300 \mu\text{m/s}$).

In Figure 2-24, we translate a single $10 \mu\text{m}$ PS sphere back and forth approximately 300 times across the electrodes at arbitrary flow rates. The majority of cells traversed the electrodes in 1 s. We observed decreasing capacitance signal amplitudes as the transition times decreased. For transition times up to approximately 5 lock-in amplifier time constants, the time constant ($\tau=30 \text{ ms}$) limits how quickly capacitance changes are detected. Hence, apparently weaker signals are observed. However, above 5 time constants (150 ms), the probable mechanism for decreased capacitance changes is the hydrodynamic lift force. Above transition times of approximately 500 ms (or equivalently, velocities below $250 \mu\text{m/s}$), the lift force is negligible and the spheres essentially roll along the bottom. At faster velocities, one should consider the lift force.

Cell trajectories are calculated by solving the equation of motion, $\Sigma \vec{F} = m\vec{a}$, in the “Particle Tracing” post-processing tab in COMSOL® Multiphysics.

$$\vec{F}_{DEP} + \vec{F}_{lift} + \vec{F}_{gravity} + \vec{F}_{drag} = m\vec{a} \quad (2-20)$$

The Stokes drag force is given by the following expression:

$$\vec{F}_{drag} = 6\pi\eta R(\vec{v}_p - \vec{v}_m) \quad (2-21)$$

where η is medium viscosity, R is cell radius, \vec{v}_p is cell velocity, and \vec{v}_m is the medium velocity. The gravitational force, counter-balanced by a buoyancy force, is given by:

$$\vec{F}_{gravity} = -\frac{4\pi R^3}{3}g(\rho_c - \rho_m)\hat{y} \quad (2-22)$$

where g is the acceleration due to gravity (9.81 m/s²), and the cell and medium densities are ρ_c and ρ_m , respectively. Recall the DEP force given by Equation 2-14:

$$\langle \vec{F}_{DEP} \rangle = 2\pi r^3 \epsilon_m \epsilon_0 \text{Re}\{K(\omega)\} \nabla |\vec{E}_{RMS}|^2$$

Finally, the hydrodynamic lift force acting on a cell near a channel wall is [60], [61], [62]:

$$\vec{F}_{lift} = -C \frac{6\eta R^3 \langle v \rangle \text{sgn}(y)}{H(H/2 - |y| - R)} \hat{y} \quad (2-23)$$

where R is the cell radius, η and $\langle v \rangle$ are the dynamic viscosity and mean velocity of the fluid, H is the channel height, and $h = H/2 - |y|$ ($-H/2 \leq y \leq H/2$) is the distance from a channel wall to the center of the particle. The constant C has previously been empirically determined to be 0.172 for polystyrene spheres.

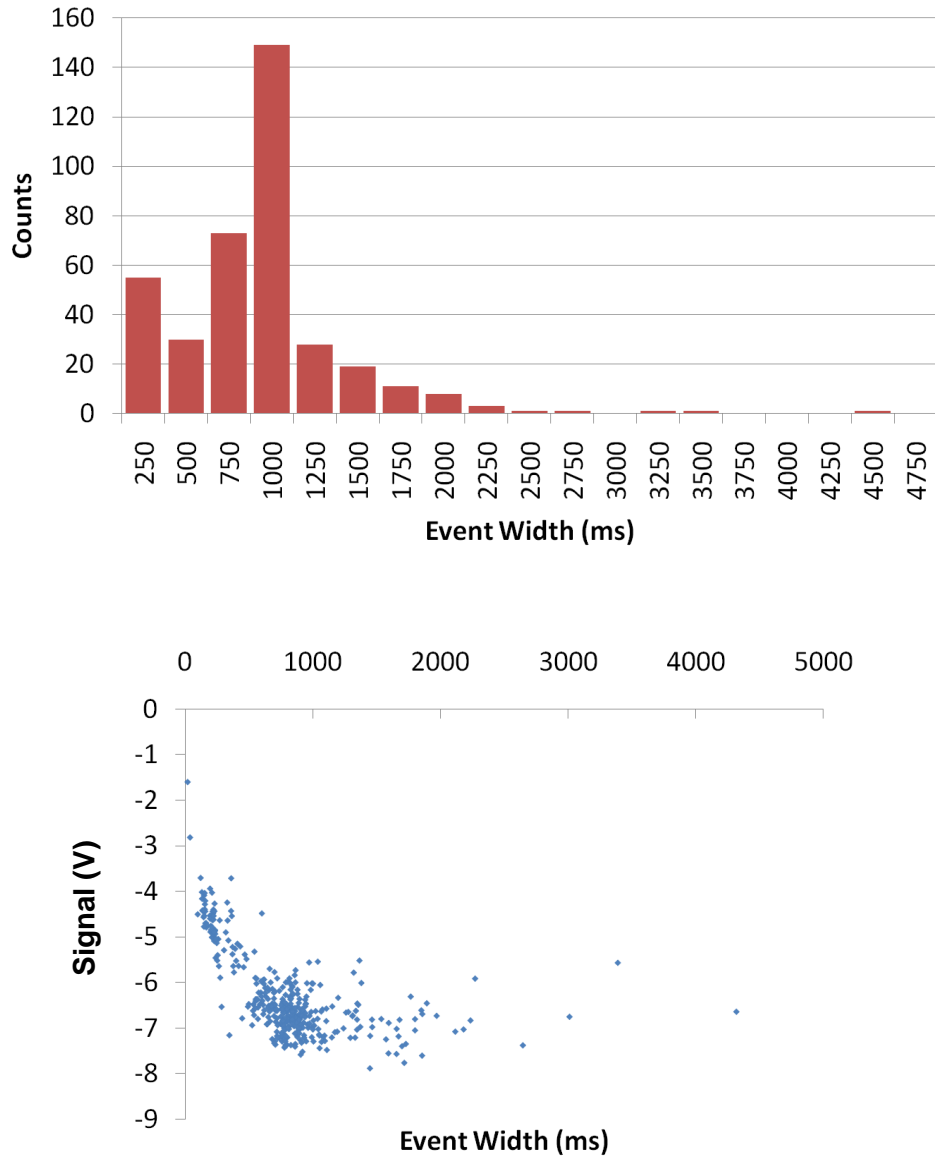


Figure 2-24: A single 10 μm polystyrene sphere was translated back and forth approximately 300 times at various speeds to investigate the possibility of a lift force. For transit times below 500 ms, the signal “amplitude” clearly decreases. The 30 ms time constant accounts for the signal decreases at high velocities (up until approximately 5 time constants), but cannot account for the signal decreases above 5 time constants, which we can attribute to lift forces. That is, the signal amplitude decreases because the particle elevates from the bottom wall due to enhanced shear forces.

2.4.3 Determining the empirical lift force constant

We determine the elevation of a cell freely-flowing at a given velocity by observing its corresponding capacitance signature and evaluating the central peak-to-trough ratio, as outlined in §3.2.1. After moving through the PEEK tubing, transitioning through the 240 μm wide input channel, and finally entering the 120 μm wide sensing channel, cells begin to acquire an equilibrium elevation governed by a balance between the lift and gravitational forces. By equating the lift and gravitational forces, and using a calibrated elevation for a given cell velocity, we can first solve for the empirically determined constant, C :

$$C \frac{6\eta R^3 \langle v \rangle}{H(h - R)} = \frac{4\pi R^3}{3} g(\rho_c - \rho_m) \quad (2-24)$$

Rearranging for C , we get:

$$C = \Delta\rho \frac{4\pi g H(h - R)}{3 \frac{6\eta \langle v \rangle}{H(h - R)}} \quad (2-25)$$

Recall that the fluid flow is parabolic according to Equation 2-19, which can be rearranged for $\langle v \rangle$ to yield:

$$\langle v \rangle = v_m H^2 / 6h(H - h) \quad (2-26)$$

By substituting this expression into Equation 2-25, we solve for C based on the actual velocity rather than the mean velocity.

$$C = \Delta\rho \frac{4\pi g}{3\eta v_m H} (h - R)h(H - h) \quad (2-27)$$

The velocity of free-flowing cells can be estimated by measuring the time between the central minima in a capacitance signature, which are approximately 25 μm apart (channel width). The cell velocity (v_m) of free-flowing and DEP-actuated cells can generally be found using Tracker software [63], which tracks position vs. time in video files on a frame by frame basis. The cell height is again determined from the corresponding capacitance signature. Therefore, for a polystyrene sphere (PSS) having a 2.85 μm radius and 1050 kg/m^3 density flowing in a channel 40 μm in height, which contains a fluid of known viscosity and density ($10^{-3} \text{ Pa} \cdot \text{s}$ and $10^3 \text{ kg}/\text{m}^3$), $C = 0.0775$.

Once the empirical constant C is determined, we can evaluate the equilibrium height of a cell, which becomes the starting point of the particle trajectory simulation. The following cubic polynomial in h solves for the equilibrium height:

$$h^3 - (H + R)h^2 + (H \cdot R)h + \gamma v H^2 / 6 = 0 \quad (2-28)$$

where $\gamma = 9C\eta/(2\pi g H \Delta\rho)$. This formula gives three roots: two are positive and one is negative (non-physical). The first positive root gives a height above mid-channel (again non-physical as gravity acts downward and the lift force acts to centralize the cell), and the second positive root gives a height below mid-channel, which is the value we choose.

2.5 Chapter Summary

This chapter described the primary polarization mechanisms (orientation and Maxwell-Wagner polarization) acting on biological cells and their fluid environments. The dielectric and ohmic losses were evaluated at our frequency of interest (1.5 GHz). The ohmic loss dominates when the conductivity reaches 1 S/m or more, which is typical for common cell buffers such as PBS.

The well-known dielectric spherical shell model was introduced to model the electrical response of heterogeneous cells. The electric fields generated by coplanar interdigitated electrodes were modelled and used to evaluate the capacitance. Although biological cells are considered electrically neutral as a whole, they can be polarized when the electric field is non-uniform. If the fields are slightly non-uniform, the cell can be treated as a dipole, which then experiences a dielectrophoretic force toward or away from the electrode edges where the electric fields are strongest. This dependence is strongly dependent on frequency and the cell's physiological state. The approach described in §2.4.2 is used later in chapter 4 to determine the trajectories of flowing biological cells by balancing the DEP, viscous drag, gravity, and hydrodynamic lift forces.

Chapter 3 – Capacitance Detection of Cell Electromanipulation

*"Any intelligent fool can make things bigger, more complex, and more violent. It takes a touch of genius - and a lot of courage - to move in the opposite direction."
- Albert Einstein*

In Chapter 2, the advantages of using high frequencies for detection were outlined. One significant advantage is that the cell heterogeneity can be averaged out and the sensor response is closely simulated by assuming the cell is a uniform dielectric object. From this assumption, it would seem that the ability to detect physiological changes, which are heterogeneous, has been lost. However, the ability to detect physiological change comes from using this sensitive detection approach in tandem with dielectrophoretic forces, which *are* sensitive to heterogeneous changes within the cell.

This chapter describes two electrical approaches for capacitively detecting the presence and dielectrophoretic actuation of single biological cells flowing in microfluidic channels. The latter interferometric approach described in §3.2 is currently being used as its minimum detectable capacitance change is significantly lower (0.15 aF) than the frequency modulation approach (2 aF). The text in this chapter is largely taken from references [64] and [65].

3.1 Frequency Modulation [64]

The first experimental apparatus used in our laboratory for capacitance measurements is shown in Figure 3-1. An automated syringe pump (New Era Pump Systems Inc., NE-1000) delivers fluid and cells through a tube into the inlet connector of the microfluidic channel. Gold electrodes are fabricated across the channel at 90° relative to the channel flow direction. To exploit the use of high frequencies in obtaining capacitance

variations due to the presence of cells in the channel, a high-Q quarter wavelength cylindrical cavity resonator made of copper is constructed and brought into contact with the gold electrodes. The resonance frequency of the resonator is approximately 2.3 GHz.

To connect the cavity with the gold electrodes, we extend two wires from the cavity, which are far shorter than a quarter wavelength to minimize loading of the resonator. The first extends from the tip of the center conductor of the cavity and the second extends from the ground plane. These wires effectively lengthen the cavity by an amount dependent on the new capacitance between the wire and the ground plane. Next, these wires are placed on the gold electrodes by moving the cavity with an x-y-z translator. Care is taken to ensure that both wires are securely connected to the gold electrodes. Since the electrodes have a much smaller distance between them than the wires, the capacitance of the cavity-channel combination increases further. Consequently, the cavity has an even longer effective length and therefore a reduced resonance frequency. Because the signal now travels a further distance outside the cavity, it will experience significant losses in the glass. As a result, the quality factor, $Q = f_r/\Delta f$ [26], decreases where Δf is the width of the resonance lineshape.

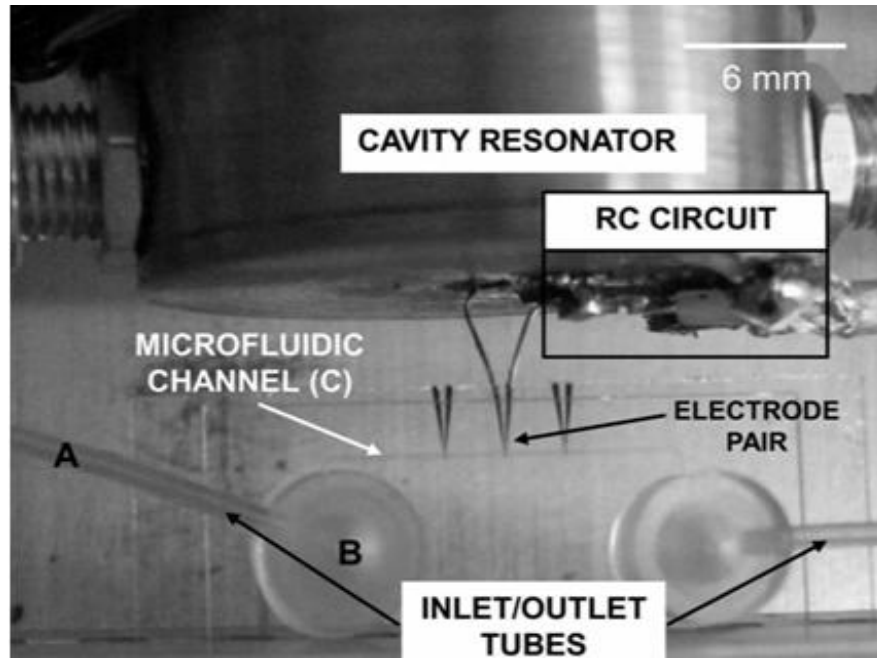


Figure 3-1: *Experimental apparatus. Fluid and cells are delivered through PEEK tubing (A) into inlet connector (B) to the microfluidic channel (C).*

When the resonator contacts the electrodes, subsequent variations in the channel capacitance, for example due to the presence of cells, will vary the effective electrical length of the cavity resonator and hence its resonance frequency f_r . The transmission spectra of the resonator-channel combination when the channel is filled with air and water can be used to calibrate the sensitivity of the sensor (Figure 3-2). The capacitance change associated with water replacing air in the channel is calculated to be approximately 45 fF. Using this value and the measured 65 MHz shift in resonant frequency, the sensitivity of this resonator is estimated to be 1.44 MHz/fF, which is comparable to resonators of similar resonance frequency [26].

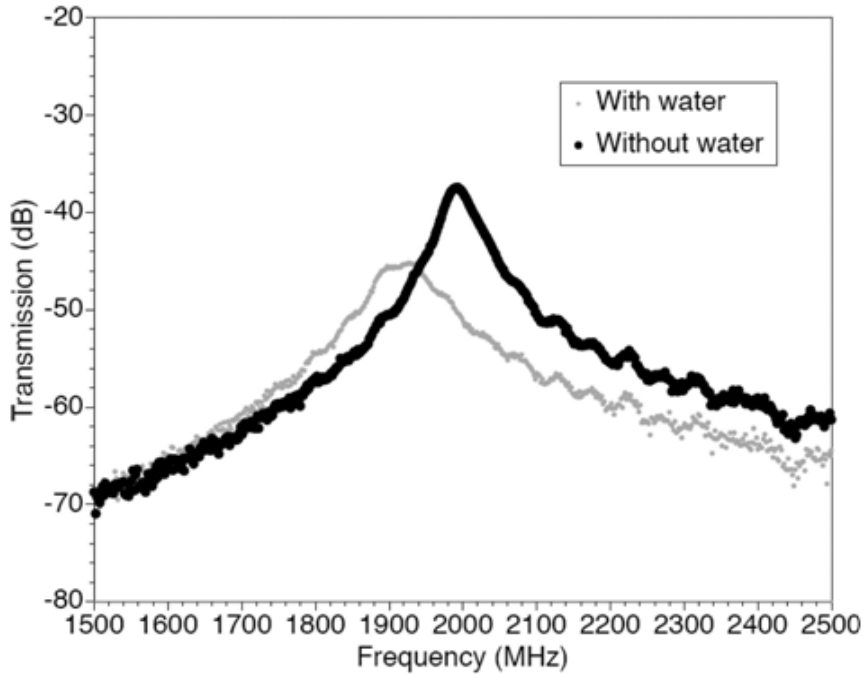


Figure 3-2: Transmission spectra of the resonator-channel combination for air-filled and water-filled channels are shifted by 65 MHz. This corresponds to a 45 fF capacitance change.

A schematic of the manipulation and detection system is shown in Figure 3-3. We measure changes in the resonance frequency of the sensor by square wave modulating the drive frequency of the RF source near the resonant frequency. To optimize the sensitivity to capacitance changes, the modulation frequency f_{mod} is chosen to be the frequency separation between the resonance frequency and the frequency where the steepest gain-frequency slope in the transmission spectrum occurs. For a Lorentzian spectrum, this value occurs when the signal is 82% of the maximum signal.

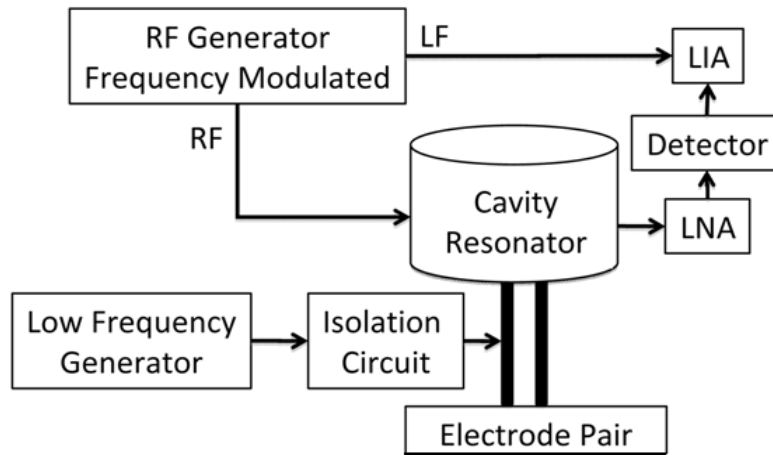


Figure 3-3: Schematic of the manipulation and detection system. A frequency modulated RF signal is delivered to the cavity resonator. The output signal is amplified and sent to the lock-in amplifier. Dielectrophoretic manipulation is achieved using a low frequency generator, which delivers frequencies up to 3 MHz to the fluid channel using an RC isolation circuit.

To make up for the signal lost primarily in the glass, the signal is amplified by 27 dB using a low-noise amplifier. After amplification, the output signal is delivered to a lock-in amplifier, which extracts the signal produced as the source switches between $f_{r1}-f_{mod}$ and $f_{r1}+f_{mod}$ at the reference frequency, f_{ref} . Assuming a symmetric transmission spectrum (see Figure 3-4), the signals at $f_{r1}-f_{mod}$ and $f_{r1}+f_{mod}$ are identical when the transmission spectrum centers at the resonance frequency of the channel-resonator combination, f_{r1} . When the resonance frequency shifts to a new resonance frequency, f_{r2} , due to the passing of cells between the channel electrodes, the signals at $f_{r1}-f_{mod}$ and $f_{r1}+f_{mod}$ become different. Since the lock-in amplifier output represents the signal difference between $f_{r1}+f_{mod}$ and $f_{r1}-f_{mod}$, the output will therefore deviate from zero when the cells pass through the channel.

The signal difference, V_2-V_1 , will either become positive or negative depending on whether the resonance frequency increases or decreases. Because the channel capacitance varies inversely to changes in resonance frequency, this means that V_2-V_1 becomes positive or negative depending on whether the capacitance decreases or increases, respectively. A proportionality factor between voltage and capacitance can be estimated by changing the average frequency of the source by 100 kHz, then measuring the change in the output voltage of the lock-in amplifier and using the sensitivity measured above to find the proportionality factor relating voltage to capacitance. In general, this conversion factor is sensitive to numerous factors, including the sensitivity of the lock-in amplifier. Conversion factors of 50 aF/V and 522 aF/V were used to calculate the capacitance changes from the voltage signals generated from yeast and polystyrene spheres, respectively.

To simultaneously deliver MHz range or below signals in order to manipulate cells using dielectrophoresis and GHz signals for capacitance detection, an RC circuit was built onto the resonant cavity. The circuit is designed to act like an open circuit to the GHz signals but allow the low frequency signals to pass through to the RF ground electrode. Building on previous work [26], we achieved 2 aF sensitivity, at 30 Hz bandwidth, in the water-filled microfluidic channels.

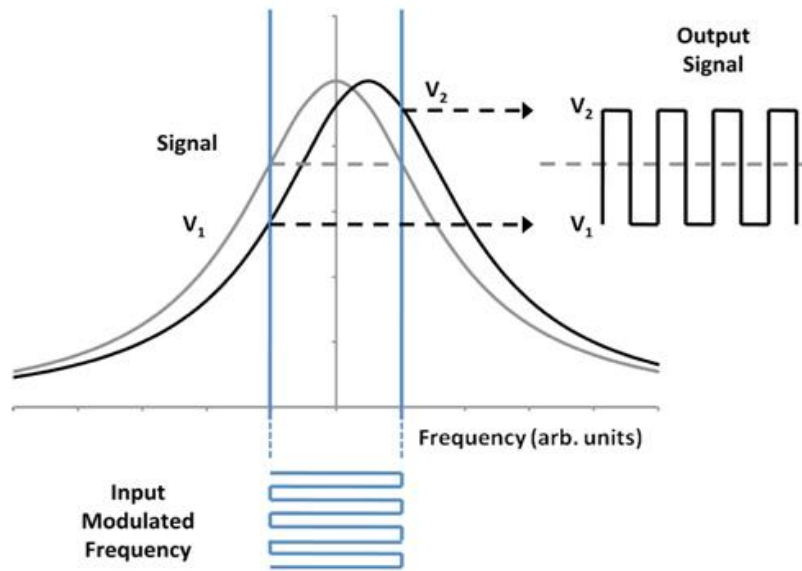


Figure 3-4: When the resonance frequency increases from f_{r1} to f_{r2} , the voltage difference, $V_2 - V_1$, increases from zero. Through calibration, this voltage difference represents the corresponding capacitance shift.

Experimental results from polystyrene spheres and yeast cells are provided in Figures 3-5 and 3-6, respectively. In both cases, we observe a decrease in capacitance because the permittivities of both polystyrene and yeast are less than that of water ($78 \epsilon_0$). The larger capacitance change from polystyrene spheres (~ 100 aF) compared with yeast cells (~ 8 aF) occurs because the polystyrene spheres are larger and have a higher dielectric contrast compared with water. Capacitance differences within each figure arise because different particles pass at different heights above the electrode plane and due to particle size variations.

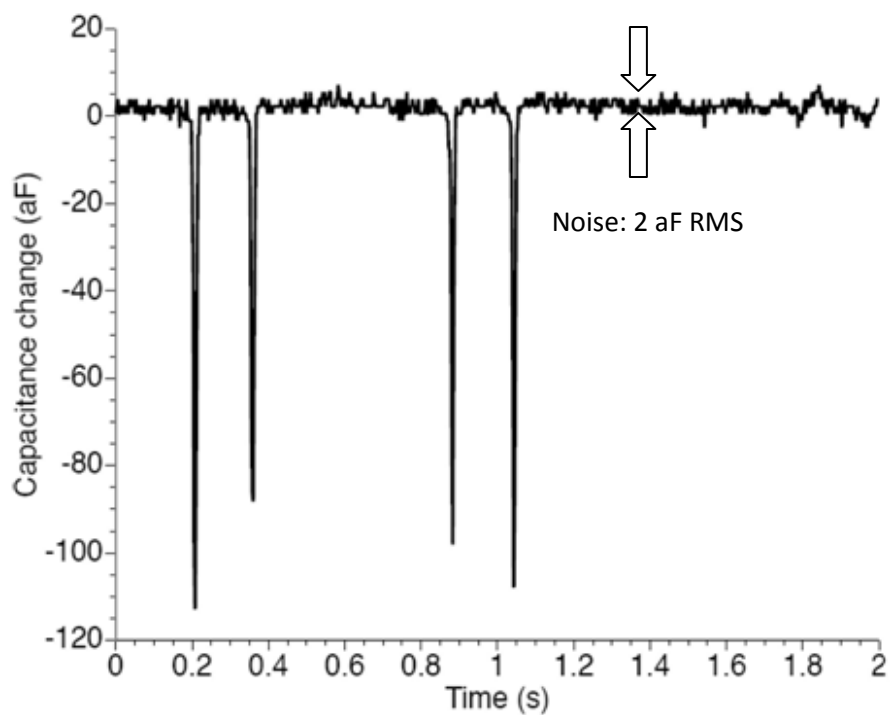


Figure 3-5: Capacitance variations in the channel due to 10 μm polystyrene spheres.

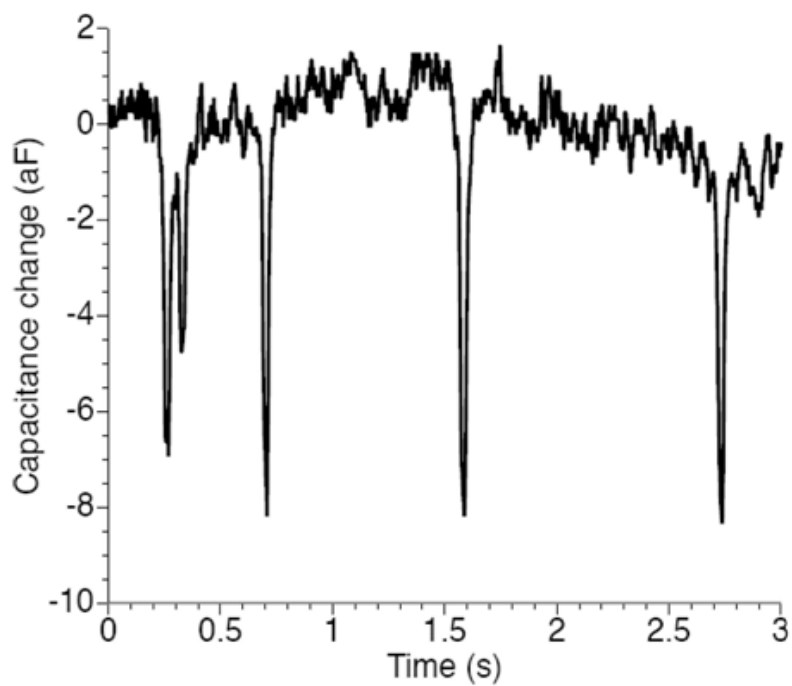


Figure 3-6: Capacitance variations in the channel due to 6 μm yeast cells.

By applying a 3 V_{pp}, 1 MHz frequency signal, we observe the sequential trapping of yeast cells from the fluid flow onto the electrodes. When the trapping potential is removed, the cells are released back into the fluid flow. Smaller capacitance changes are observed as cells flow past the electrodes with the trapping signal off. Figure 3-7 illustrates this effect as a first demonstration of simultaneous electromanipulation and capacitive detection of individual cells in microfluidic channels.

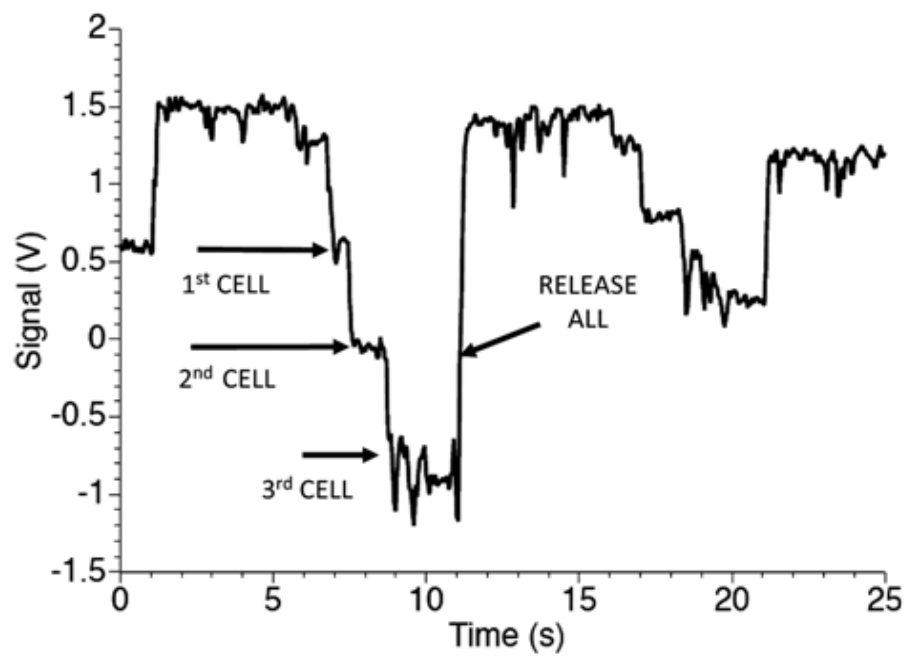


Figure 3-7: Capacitive detection of the dielectrophoretic trapping and release of yeast cells. The trapping signal (3 V / 1 MHz) was turned on and off every 5 s. Three yeast cells were trapped in sequence from 6-11 s, when the trapping signal was on. Smaller signal dips that occur when the trapping signal is off arise from the flow of yeast cells by the electrodes. These events were also observed using optical microscopy.

Each voltage dip represents an event, whether it is a cell passing by the electrode pair or the trapping of an individual cell. As yeast cells flow through the channel, a 1 MHz

trapping signal was turned on and off every 5 s. Giving particular attention to the 6–11 s timeframe, when the trapping signal was on, we observed the sequential trapping of three individual yeast cells. When the trapping signal was turned off at 11 s, the three trapped cells were released. These events were observed both via capacitance and optical detection. During those time frames when the trapping signal was off, the smaller voltage dips corresponded only to the flow of individual yeast cells by the electrode pair.

3.2 Microwave Interferometer [65]

The FM modulated system required improvement as it suffered from rapid drift (Figure 3-6), environmental sensitivity, and inadequate signal to noise. Consequently, a second experimental approach was explored, which monitors the phase differences induced by flowing cells. The *microwave interferometric sensor* is based on a coupled transmission line sensor that has achieved zeptofarad (10^{-21} F) sensitivity in scanning probe microscopes [26].

The origin of the design was work from RCA on a capacitance sensor for the RCA VideoDisc. The RCA capacitance sensor is based on sensing the frequency shift of a resonator and consists of a coupled resonator driven at a fixed frequency (915 MHz), and tuned using a varactor diode connected between the sensor circuit and ground [66]. The present design also uses a fixed frequency, but uses a variable passive phase shifter rather than a tuning varactor for greater stability. In general, the sensor can sense changes to both the real and imaginary parts of the impedance. For the conditions used in this study, it behaves as a capacitance sensor and has achieved a

± 0.15 aF RMS capacitance resolution with a 53 Hz bandwidth. The present design uses coupled transmission line resonators, but operates at a higher frequency (~ 1.6 GHz), thereby achieving greater sensitivity [67].

A schematic diagram of the sensor is shown in Figure 3-8. The complete sensor incorporates an RF source (Agilent E8663B), a signal splitter (Mini-Circuits ZAPDJ-2-S), an adjustable phase delay line (Advanced Technical Materials PNR P1213), a coupled transmission line resonator [26], a low noise amplifier (LNA; Mini-Circuits ZHL-1724MLN), attenuators (Mini-Circuits VAT-3+, VAT-6+, and VAT-10+), a mixer (Mini-Circuits ZEM-4300MH+) and a lock-in amplifier (LIA; Stanford SR830). The signal from the RF source is split equally into a sensing path and a reference path. The sensing path contains a high-isolation switch (Mini-Circuits ZASWA-2-50DR), the microstrip resonator, an adjustable delay line (Advanced Technical Materials PNR P1213), and a low noise amplifier (LNA; Mini-Circuits ZHL-1724MLN). Attenuators (Mini-Circuits VAT-3+, VAT-6+, and VAT-10+) and a match-terminated circulator based isolator (SNT SN20113) are inserted throughout the signal path for isolation. The reference path is coupled directly to the input of the mixer. The resonator shown in Figure 3-8 is milled from copper-clad, low-loss dielectric material (Rogers 5880).

The resonator is a $\frac{1}{4}$ wavelength resonator with the open end being coupled to electrodes in the microfluidic channel using $150 \mu\text{m}$ diameter wire probes soldered to the resonator. The other end of the resonator acts as a short at RF frequencies, but has an RC with 85 pF to ground with 750Ω in series with the low frequency source that allows DC-3 MHz frequencies to be coupled to the center conductor of the resonator.

The resonator has a band-pass filter response, with the design symmetry permitting either port to be used for input/output.

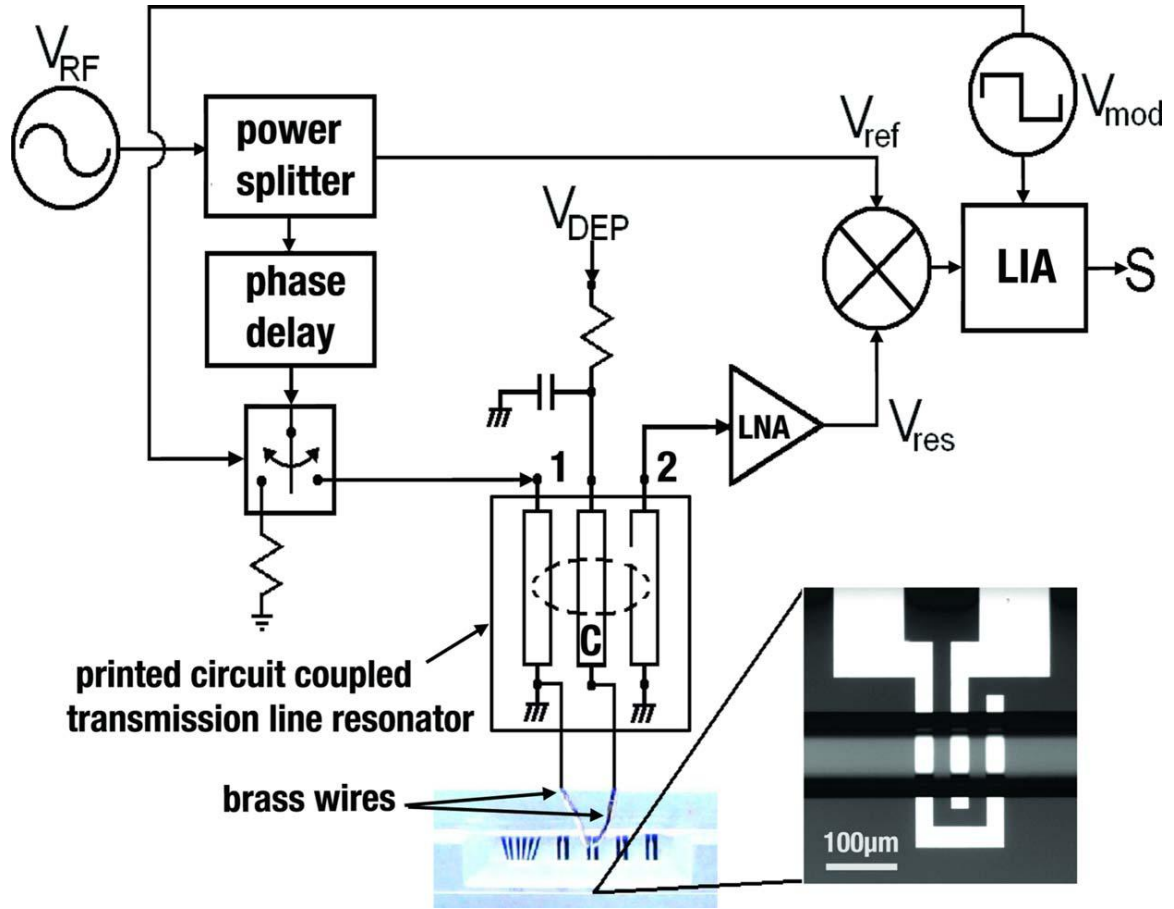


Figure 3-8: A 1.6 GHz microwave interferometer is used to detect single cells flowing in a microfluidic channel past an interdigitated electrode pair [45]. The RF source is evenly split between a reference and a sensing path. The sensing path contains an edge coupled T-line sensor with a resonate line coupled to the electrode pair via wire probes. The sensor output, V_{res} , is mixed with the reference signal, V_{ref} , to yield the interferometer output. The RF signal along the sensing path is toggled on-and-off at 90 kHz so that a LIA can detect the mean interferometer output S within a narrow bandwidth. Using the delay line, the phase is then adjusted to null the interferometer output. As a cell passes over the electrode pair, the load capacitance varies by ΔC , which induces a small phase shift in the sensor output, V_{res} . This phase shift induces a nonzero S response that is proportional to ΔC . An RC LPF is connected to the resonant line, so that a low frequency potential can be superimposed onto the electrode pair to actuate passing cells via dielectrophoresis.

To set up for measurement, the phase shifter is adjusted to null the output signal. Cells passing the electrodes induce a small phase shift in the sensing path RF signal. After mixing with the reference signal, this produces an output signal that is proportional to the magnitude of the phase shift. The RF signal is amplitude modulated so that lock-in detection techniques can be used to reduce the effects of low frequency and out of band noise.

Before coupling the resonator to the electrodes in the microfluidic channel, the resonant frequency of the resonator is ~ 1.9 GHz. After coupling, the frequency shifts to 1.4-1.6 GHz. This is consistent with the addition of ~ 150 -250 fF of capacitance due to the added electrodes. Once the detection system is adjusted, it remains stable for many hours with only minor adjustments in the driving frequency (~ 10 -100 ppm) required to compensate for drifts due to temperature and mechanical induced creep.

During operation, the frequency of the RF source is adjusted to match the resonant frequency of the resonator when its probes are contacting the channel electrodes. The phase delay is then adjusted until the signal out of the mixer is nulled. As a cell passes the electrodes, it causes the resonant frequency of the resonator to shift. This in turn shifts the phase of the signal reaching the mixer and produces an output signal. For small capacitance changes (less than ~ 10 fF), the magnitude of the signal can be estimated using:

$$S_{cell} = GV_{ref}V_{res} \frac{d\theta}{dC} |_{f_r} \Delta C_{cell} \quad (3-1)$$

Here, S_{cell} is the signal resulting from the presence of the cell, G is the gain of the mixer, V_{ref} is the magnitude of the reference signal, V_{res} is the magnitude of the signal after passing through the resonator, $d\theta/dC$ ($\approx 0.15^\circ/fF = 2.6 \text{ mrad}/fF$) [45] is the rate at which the phase of the resonator shifts with added capacitance at the resonance frequency and ΔC_{cell} is the capacitance change due to the presence of the cell (5-200 aF).

Figure 3-9 reveals the electromagnetic chamber containing the microscope, a panel for electrical connections, and all the RF electronic components labelled in Figure 3-8 apart from the RF source and lock-in amplifier, and power sources. Figure 3-10 shows a close-up view of the x-y-z translator, which is used to manoeuvre the transmission line resonator above the microfluidic chip, which contains four fluid ports and various electrode designs. The translator lowers the signal and ground probes extending from the resonator into contact with the electrode pads. At this point, it is important to mention that Dan Card was responsible for bringing our system into this semi-portable form by incorporating the system components into the chamber and building a power supply through which all internal components could be driven.

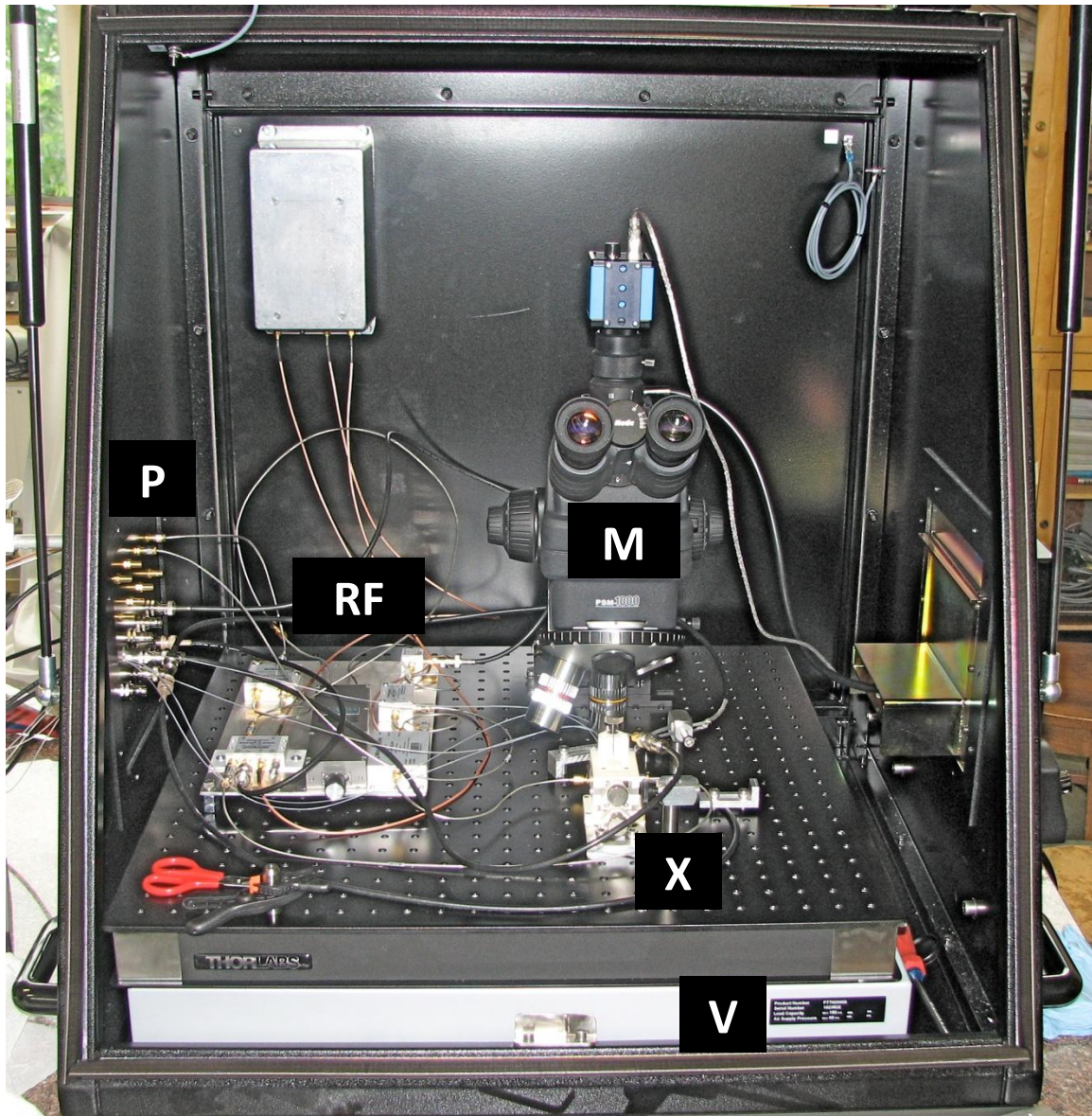


Figure 3-9: Electromagnetic chamber containing the microscope (M), a panel for electrical connections (P), and all the RF electronic components (RF) labelled in Figure 3-8 apart from the RF source and lock-in amplifier, and power sources. The resonator and microfluidic chip are manoeuvred under the microscope using an x-y-z translator (X). The microscope stage is mounted on an anti-vibration pad (V).

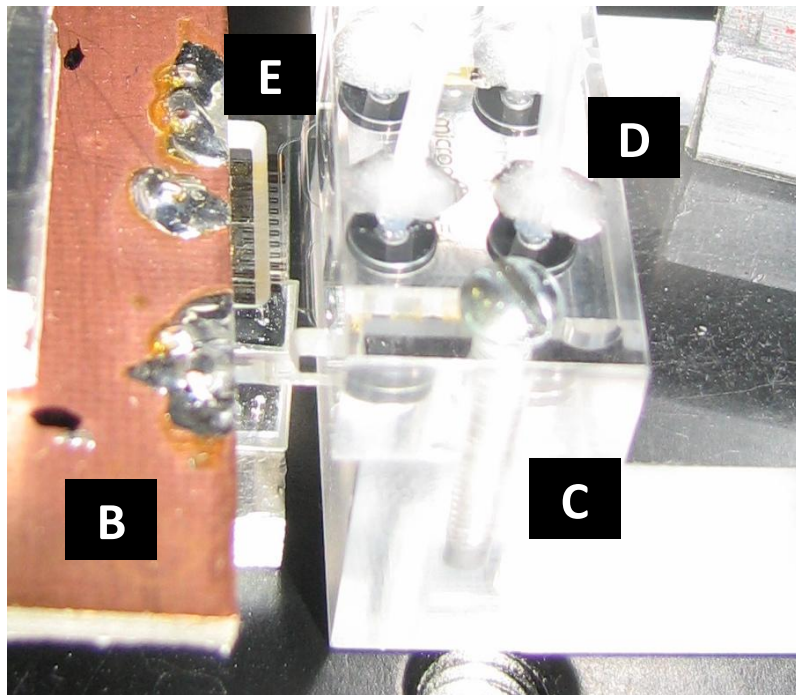
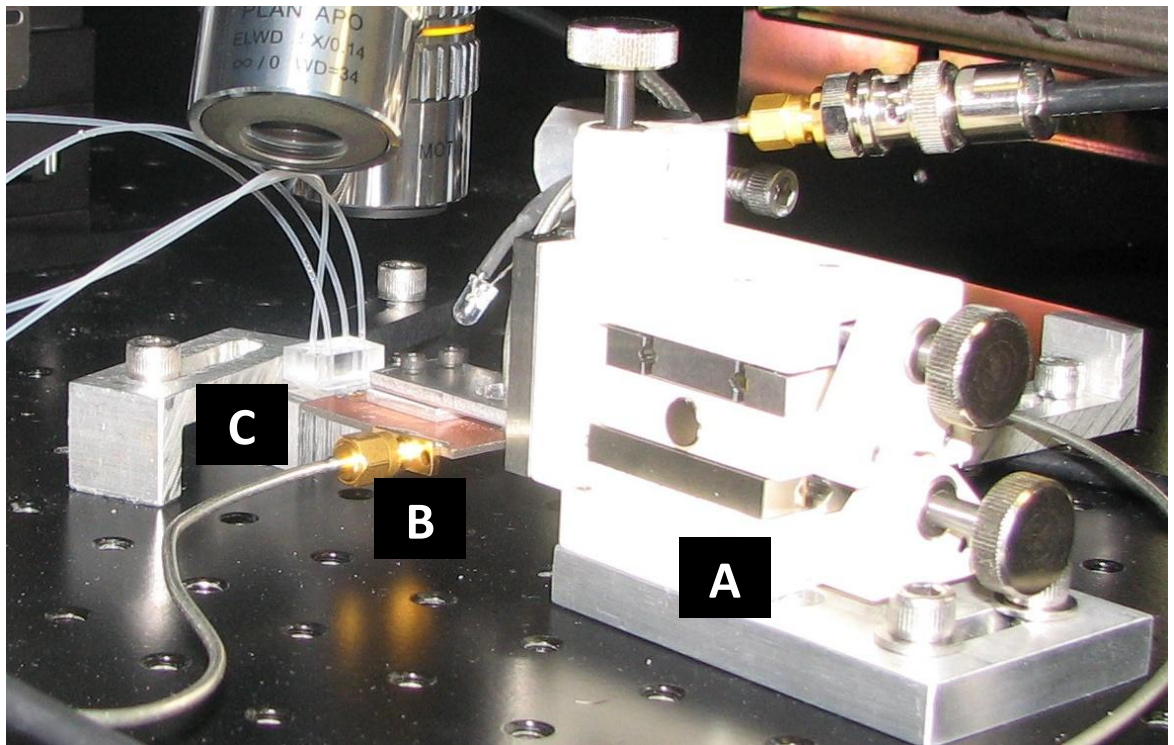


Figure 3-10: Close-up of x-y-z translator (A), which is used to manoeuvre the transmission line resonator (B) above the microfluidic chip (C), which contains four fluid ports (D) and various electrode designs (E). The translator lowers the signal and ground probes extending from the resonator into contact with the electrode pads.

3.2.1 Sensor calibration

The capacitance sensor is calibrated using $5.7 \pm 0.3 \mu\text{m}$ diameter polystyrene spheres diluted in deionized water. At low particle elevations, there is a large contrast between the large electric fields generated directly *above* the electrode edges and the relatively smaller fields occurring *between* the electrode edges. This electric field contrast emerges as signal peaks and valleys in the time-dependent capacitance signatures. The signal valleys above the electrode edges (Position A) are most sensitive to elevation (Figure 3-11), while the signal peaks occurring directly above the middle of the central electrode (Position B) are least sensitive to elevation. Indeed, the capacitance change at Position B drops monotonically with increasing elevation at a rate of approximately $40/11=3.6 \text{ aF}/\mu\text{m}$ (Figure 3-12). Therefore, at low particle elevations, the unique ratio between these signals (i.e., $\Delta C_A/\Delta C_B$) can be used to determine the particle's elevation (Figures 3-12 and 3-13).

The relationship between the capacitance ratio and particle elevation can be used as a calibration for the experimental trace. For example, the capacitance ratio of the experimental trace in Figure 3-14 is approximately $92/51=1.8$. By mapping this capacitance ratio to its corresponding particle elevation in Figure 3-13, we determine that this polystyrene sphere flows at an approximately $5 \mu\text{m}$ elevation. This allows us to scale the capacitance using point B in the experimental result as a reference point. The RMS noise is estimated by choosing a region without particles flowing over the electrodes and finding the RMS signal. With a 0.15 aF RMS noise (53 Hz bandwidth),

this corresponds to a minimum detectable particle displacement of 42 nm (0.15/3.6), see Figure 3-14).

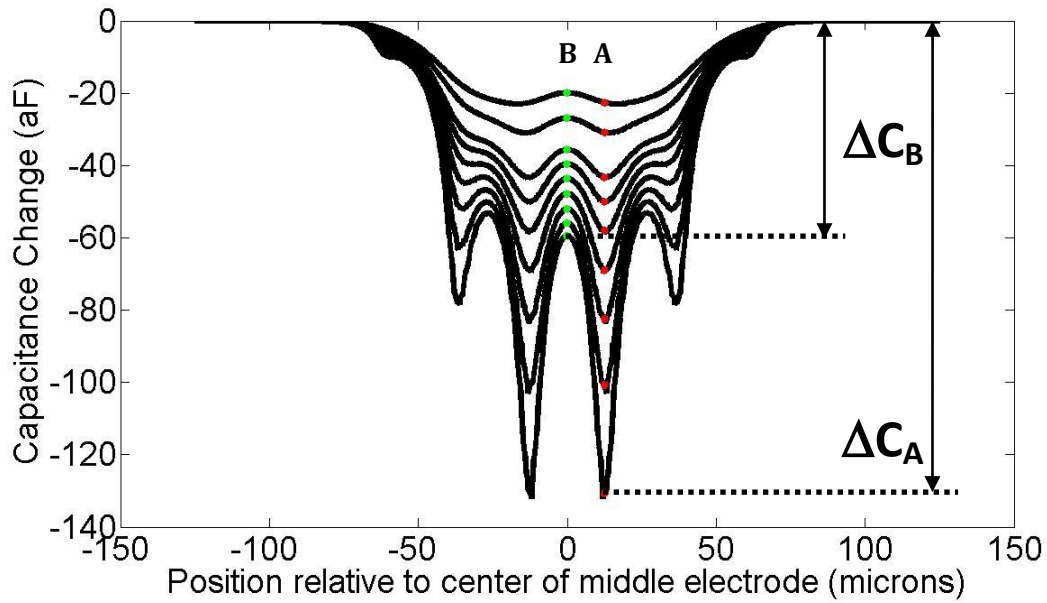


Figure 3-11: Simulated capacitance signatures from a 6 μm polystyrene sphere passing over the two-gap interdigitated electrodes at constant elevations. In order of decreasing capacitance change magnitude, the corresponding sphere elevations above the electrodes is $y=4, 5, 6, 7, 8, 9, 10, 12.5,$ and $15 \mu\text{m}$, respectively. The red dots indicate the capacitance changes occurring above the edge of the central electrode, ΔC_A , (Position A, $x=12.5 \mu\text{m}$) while the green dots indicate the capacitance changes occurring above the middle of the central electrode, ΔC_B (Position B, $x=0 \mu\text{m}$).

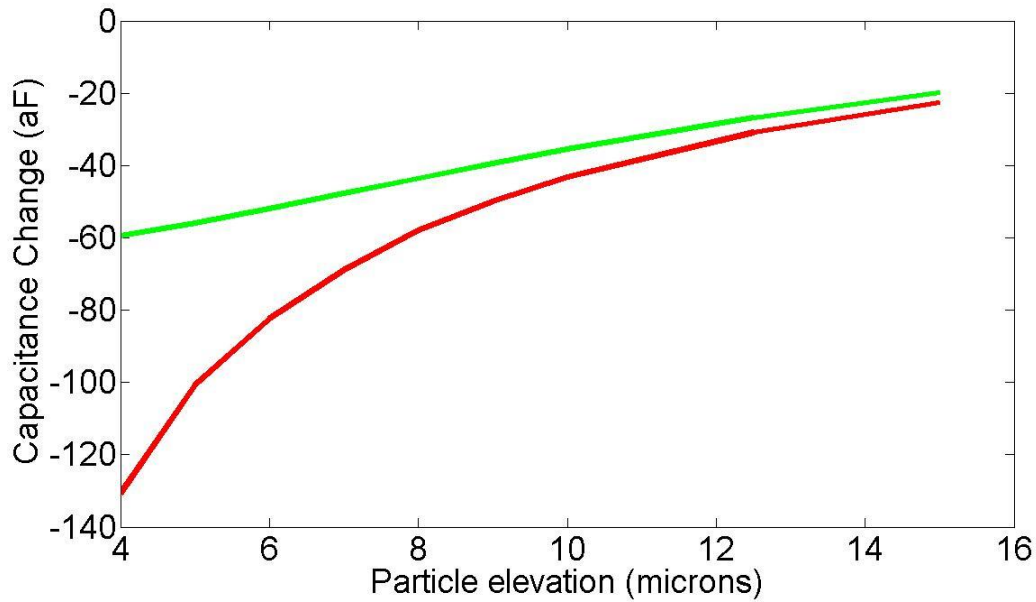


Figure 3-12: From Figure 3-11, we plot the simulated capacitance changes from the green and red dots vs. elevation. The red dots indicate position A and the green dots indicate position B. The capacitance varies least above the central electrode (position B), falling approximately $3.6 \text{ aF}/\mu\text{m}$ with increasing elevation.

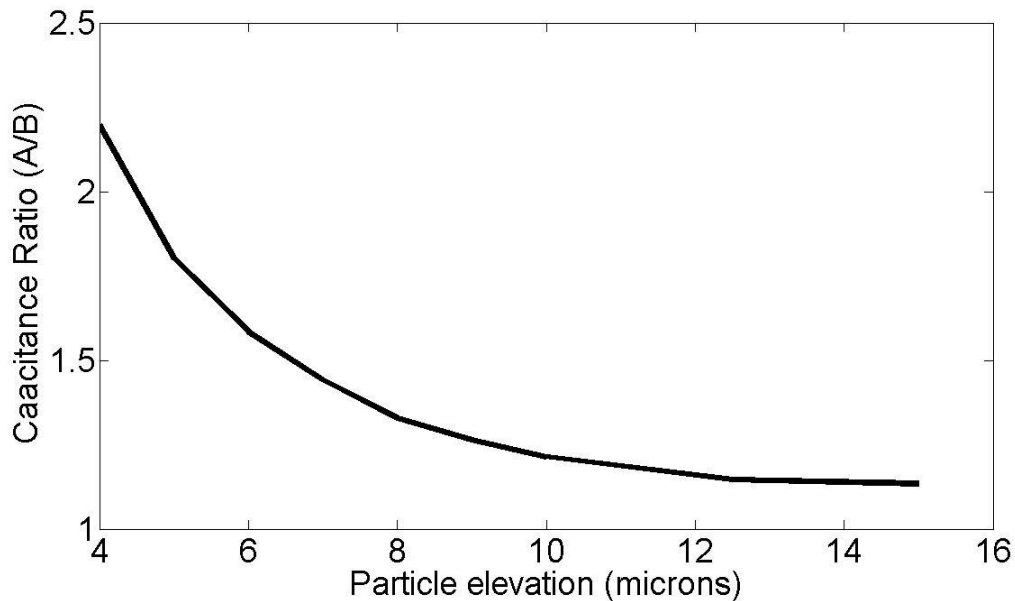


Figure 3-13: By taking the ratio of the simulated capacitance changes in Figure 3-12, the signal valleys and signal peaks corresponding to positions A and B, respectively, one can apply this figure to experimental traces (e.g., Figure 3-14) to determine the particle height above the electrodes.

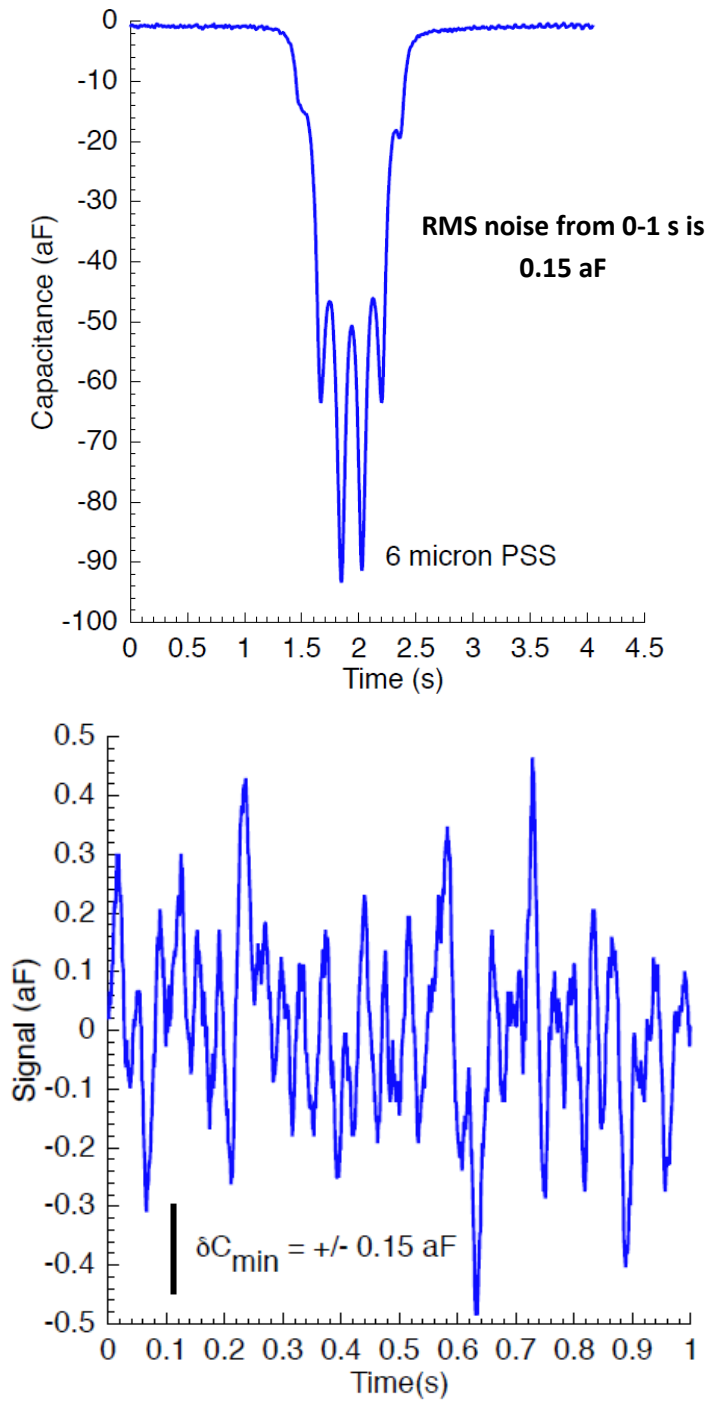


Figure 3-14: Experimental capacitance signature from a 6 μm polystyrene sphere (TOP) passing over the two-gap interdigitated electrodes as detected using the interferometric system. The capacitance ratio of the experimental trace is approximately $\Delta C_A/\Delta C_B=92/51=1.8$. According to Figure 3-13, we determine that this polystyrene sphere flows at an approximately 5 μm elevation. The RMS noise evaluated from 0-1 s is approx. $\pm 0.15 \text{ aF}$ (BOTTOM).

3.2.2 Operation in high conductivity media

The high operating frequency of the sensor allows this system to detect many different cell types - even in high conductivity cell buffers such as PBS, TRIS, α -MEM, and DMEM. Capacitance signatures from Chinese Hamster Ovary cells, activated T-lymphocytes, mouse fibroblasts, and breast cancer cells are shown in Figures 3-15 to 3-17. The minimum detectable capacitance change (noise) improved from 0.65 aF [65] to 0.15 aF [68], [69] after toggling the RF signal on the sensing path only, rather than directly at the source.

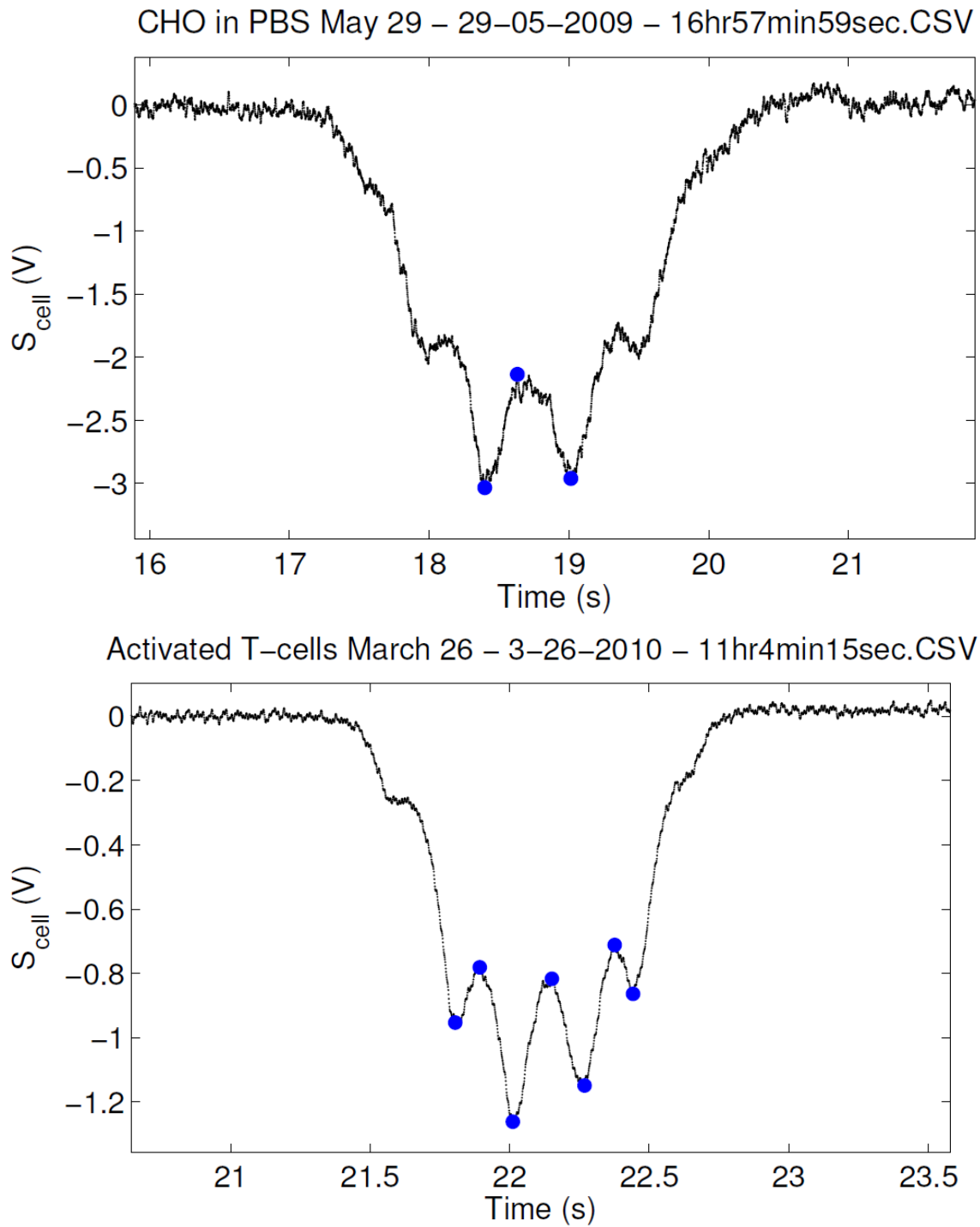


Figure 3-15: Examples of capacitance signatures from Chinese Hamster Ovary cells in PBS (TOP), and activated T-cells in RPMI-1640 (BOTTOM).

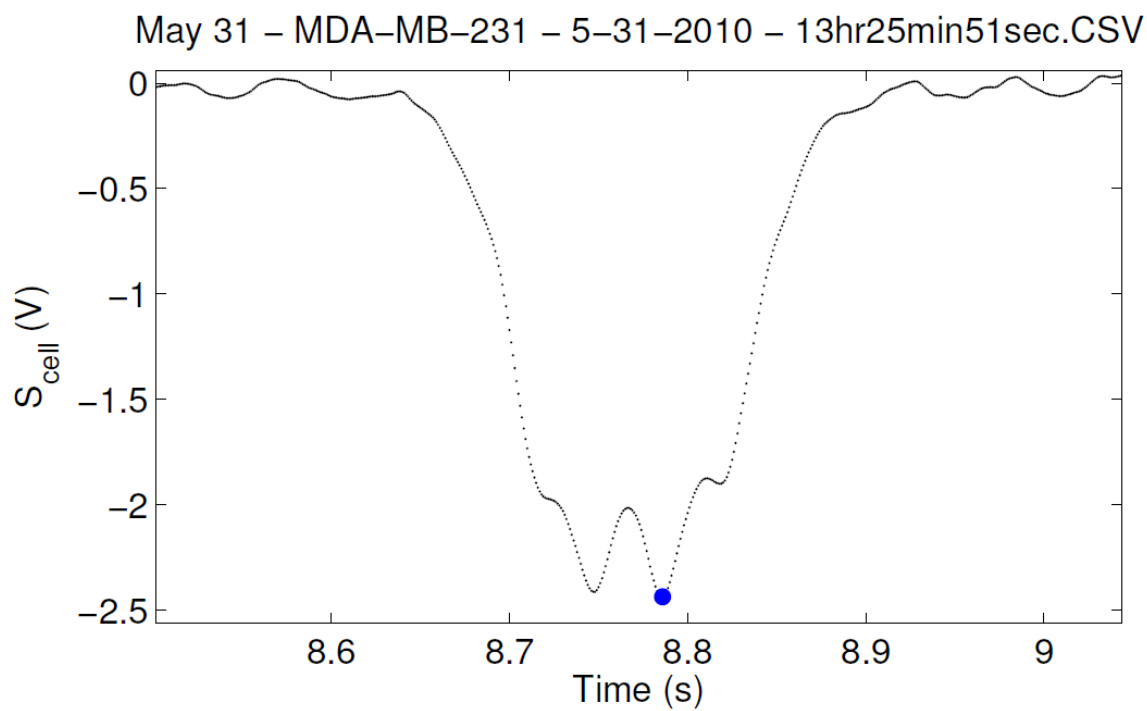
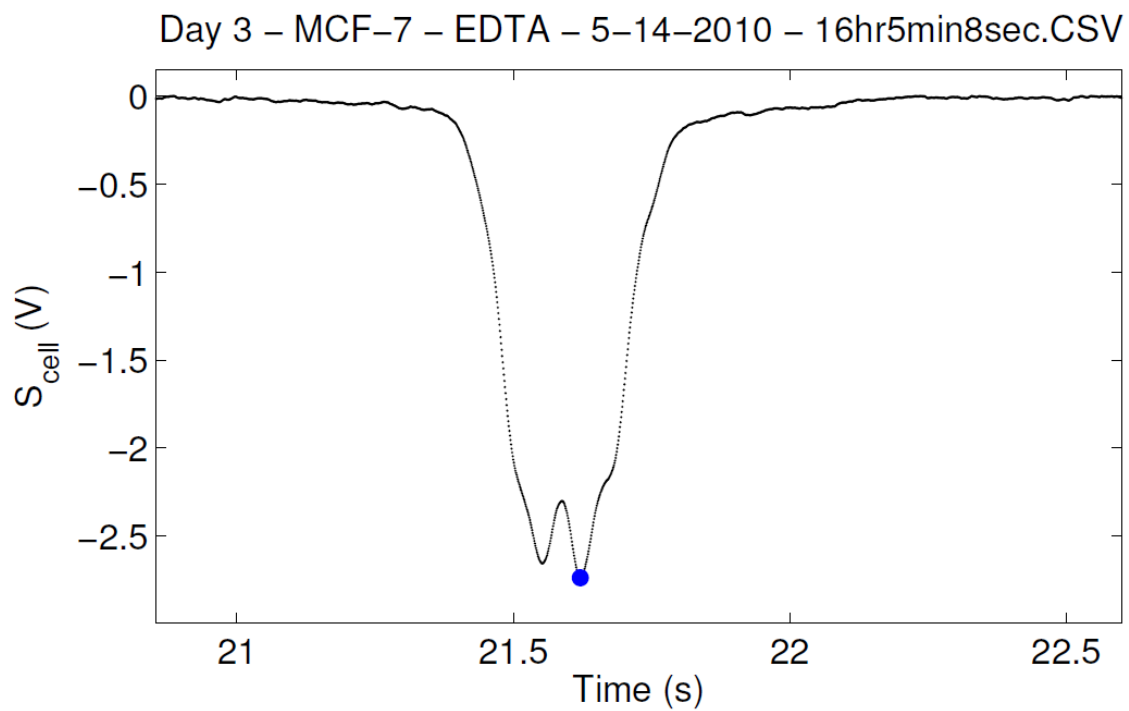


Figure 3-16: Examples of capacitance signatures from MCF-7 (TOP) and MDA-MB-231 cells (BOTTOM) in D-MEM.

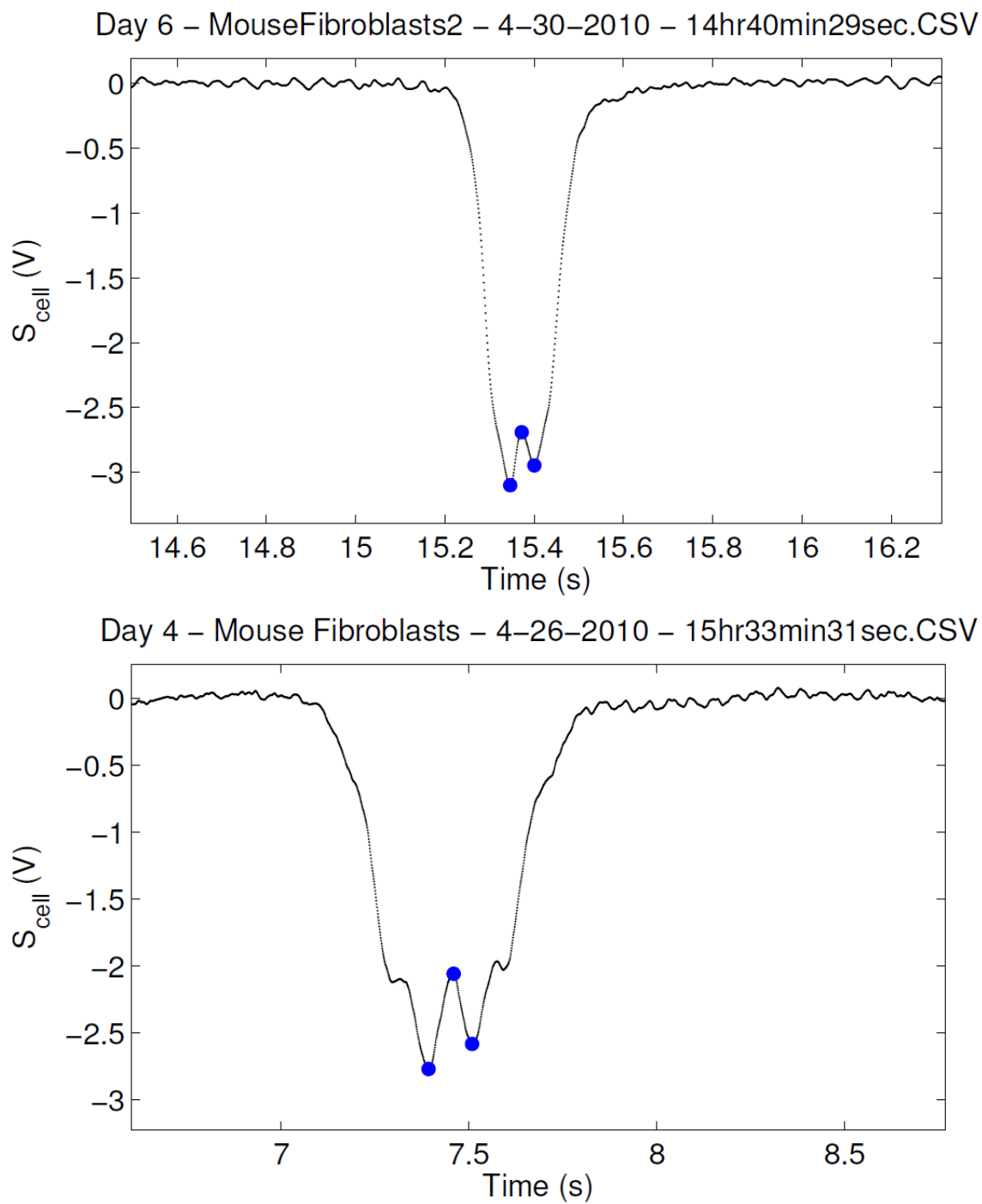


Figure 3-17: Examples of capacitance signatures from $10T\frac{1}{2}$ (TOP) and Ciras-3 (BOTTOM) mouse fibroblasts in α -MEM.

3.2.3 Fabrication of microfluidic channel and interdigitated electrodes

Microfluidic channel and interdigitated electrode designs were fabricated through CMC Microsystems using the Micronit process [70]. The microfluidic channel was etched to a 40 μm depth in a 1.1 mm thick Borofloat glass substrate, and the interdigitated electrodes were fabricated in a 0.7 mm thick Borofloat glass substrate. To align the electrodes with the glass surface, 400 nm trenches were etched (in the 0.7 mm substrate) and filled with a 20 nm Ta adhesion layer followed by a 380 nm Pt layer. Finally, the two glass surfaces containing the channel and electrodes were directly heat-bonded to form the final chip.

The channel and electrode geometries are shown in Figure 3-18. The interdigitated electrodes are 25 μm wide, separated by a 25 μm edge-to-edge spacing, and extend completely across the 120 μm channel width. The electrodes are wider (100 μm) outside the channel region to reduce electrical losses at GHz frequencies. To connect the electrodes with the interferometric system, copper wires extending from the transmission line resonator are placed on electrode contact pads located at the edge of the glass substrate. Once this is done, highly sensitive impedance sensing can detect the presence and time-dependent position of single flowing cells as they sequentially pass over the electrodes. Fluid connections are epoxied to powder-blasted access ports at the channel ends to achieve fluid flow.

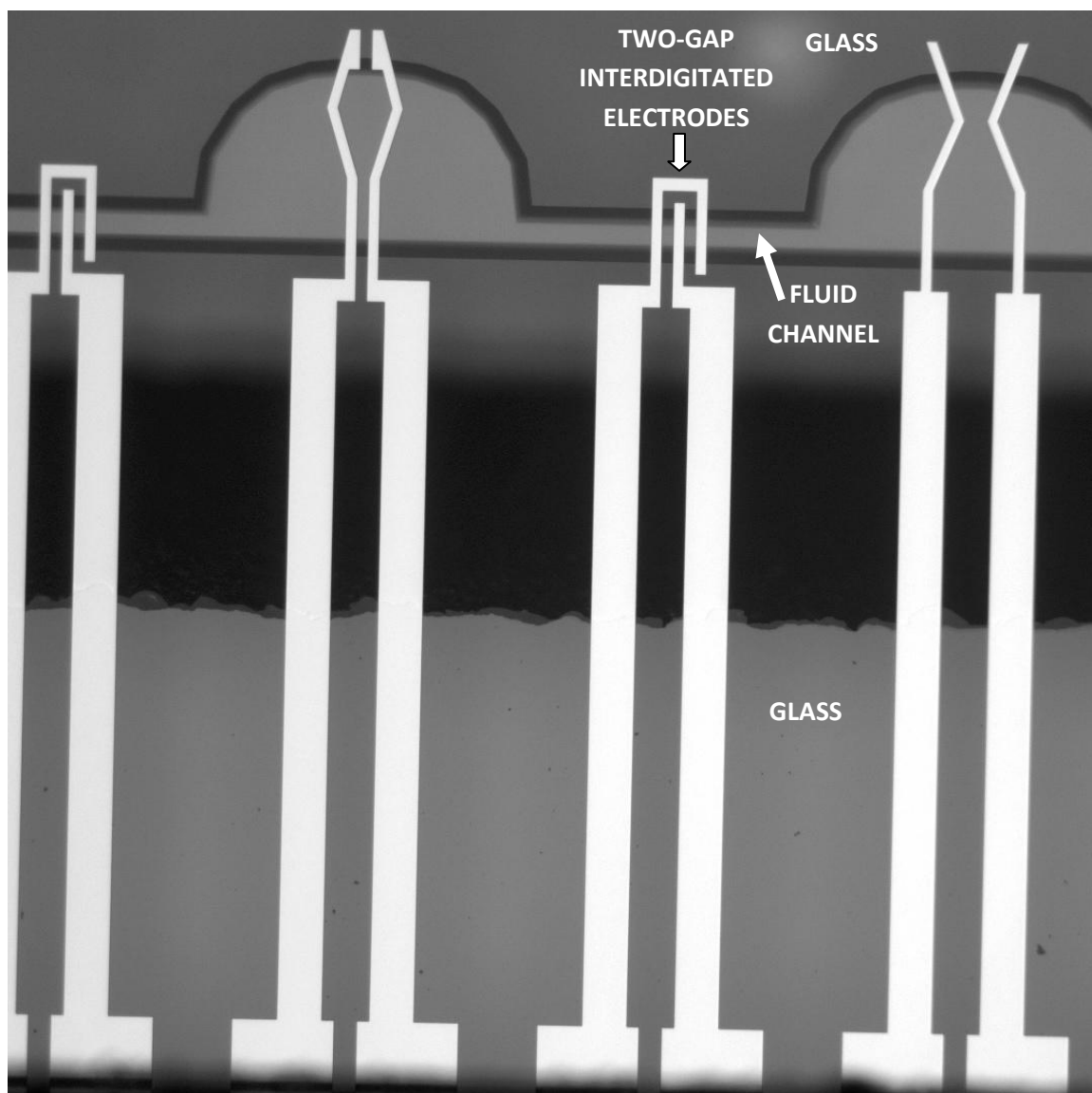


Figure 3-18: Various electrode designs fabricated across a microfluidic channel containing “cubbies”. The two-gap interdigitated electrodes are used in experiments in this thesis. Electrodes (white colour) are wider outside the channel to reduce the GHz frequency electrical losses.

3.2.4 Controlling the fluid flow

The microfluidic system design has undergone many versions. Initially, the fluid and cells were pumped through a two-port, 25 μm high microfluidic channel using syringes, initially pumping by hand, and subsequently by automatic syringe pumps capable of providing low flow rates. However, the cells gradually settled at the channel's entrance, where the large PEEK tubing met the much narrower microfluidic channel (Figure 3-1), eventually plugging the entrance and inhibiting further fluid flow. The flow channels were nearly impossible to unclog. Ultimately, the force generated from pumping fluid simply drove the trapped cells into more condensed clumps rather than propelling them through the channel. Therefore, it was necessary to provide more flow paths to sweep away debris to minimize the possibility of cells settling and then clogging in the channel.

We began using H-channel (four-port) designs, which work much better than one-way (two-port) channels. A differential flow is established in the intersection of an H-channel (Figure 3-19), which gives the experimenter freedom to choose the flow rates of the two input pumps. Unfortunately, the initial success of observing slow single cells was short-lived. It was soon discovered that fast pumping rates were required to drive cells into the "H" intersection because cells preferentially resided in the wider channels, making it difficult to achieve a steady stream of single cells. Since the cross section (25 μm height) of the intersection was comparable in size to the observed cells, it provided a large resistance to cells passing through. With this technique, one could only achieve flow situations where numerous cells passed the electrode array at once, making single

cell analysis impossible. Therefore, the next batch of H-channels were made larger (height = 40 μm) to accommodate the flow of many cell types, including white blood cells, Chinese Hamster Ovary cells, mouse fibroblasts, and human breast epithelial cells.

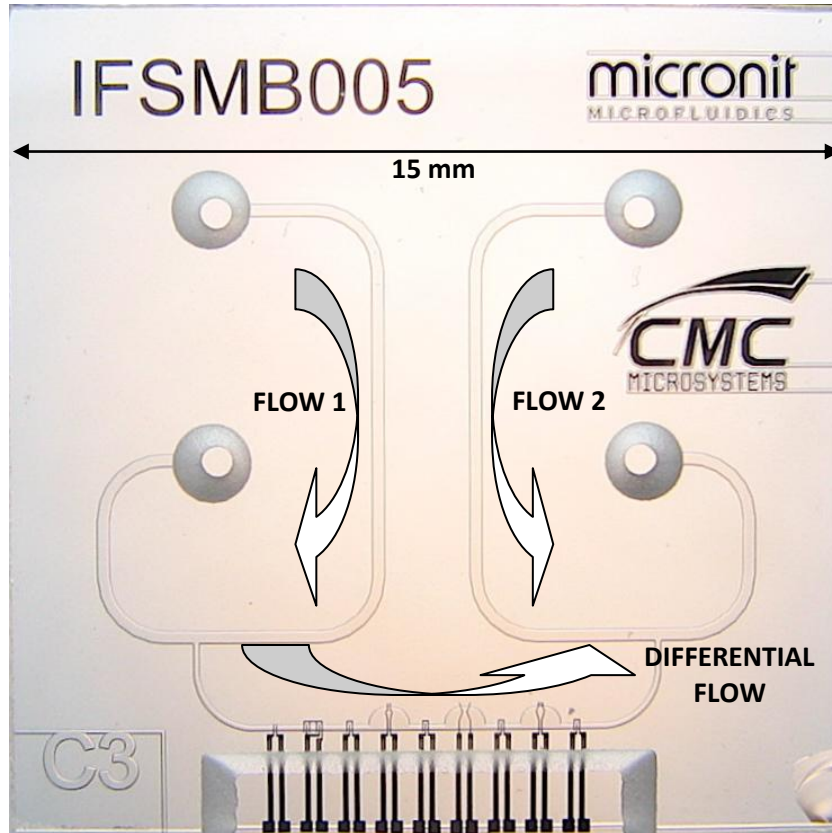


Figure 3-19: Micronit microfluidic chip in an H-channel design, used for delivering a differential flow through the intersection, which contains various electrode configurations. The 15 mm x 15 mm microfluidic chip was fabricated through CMC using the Micronit process [70]. The intersection and flow channel widths are 120 and 240 μm , respectively.

Pressurizing the channel had also promoted leaks, particularly in those areas where the connectors may not have been adequately epoxied to the PEEK tubing. The presence of leaks made the flow behaviour highly unpredictable. To overcome this, two solutions were used: 1) a gravity feed-thru technique, in which fluid flow depends on a small

difference in height between two fluid-filled, open-ended syringes and 2) a high precision pneumatic pressure controller for tuning the pressure across all four ports.

Although the gravity-based technique works reasonably well, it is susceptible to air pockets and requires careful, manual adjustment of the syringe height to achieve optimal flow, and additionally does not provide rapid control over the direction of fluid flow. Furthermore, as the syringes are often in close proximity to electrical connections and high frequency coaxial cables, the mere act of reaching for the syringes can momentarily shift the output signal.

Fortunately, precise and rapid control of the fluid (and cell) flow rate with minimal manual involvement is achieved using the **MicroFluidic Control System (MFCS-4C-70)** for four channels designed by Fluigent. The MFCS-4C is a high precision pneumatic pressure controller designed to handle fluid in microfluidics systems (Figure 3-20). A 500 mbar external pressure is used to control the fluid flow from four 2 ml vials that are connected to the four ports on the H-channel to establish a fully closed pressurized system. Using Fluigent's graphical user interface (Figure 3-21), the pressure in each vial is adjustable up to 70 mbar. The minimum pressure adjustment is 0.021 mbar.

To demonstrate precise and rapid control of fluid flow, polystyrene spheres are translated back and forth by clicking between two different pressure configurations. Data collected by my colleague, Dr. Marija Nikolic-Jaric, (Figure 3-22) shows that the spheres rapidly achieve their equilibrium velocities after rapid back and forth transitions (100 ms).

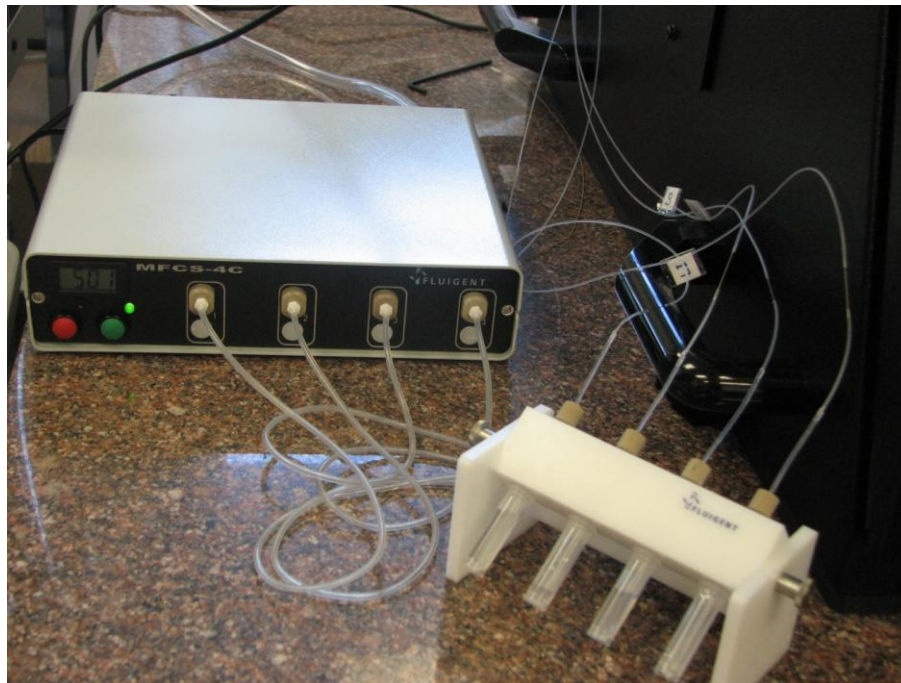


Figure 3-20: Photograph of the MFCS-4C Fluigent pumping system, which operates at a constant external pressure of 500 mbar that is used to control the fluid flow from four 2 ml Fluiwell vials. Each vial is connected to a port on the H-channel (Figure 3-19).

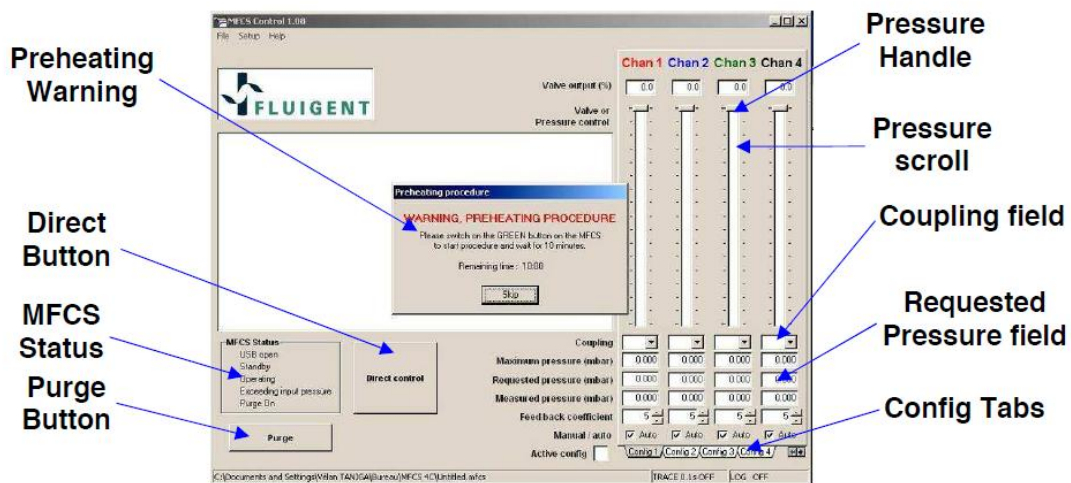


Figure 3-21: Graphical user interface provided by Fluigent for controlling the pressure in the microfluidic channel. The pressures in each of the 4 ports are controlled by entering a value directly, or using the scroll bar. Multiple configuration tabs allow the user to select specific pressure conditions for moving cells back and forth, or even stopping cells completely.

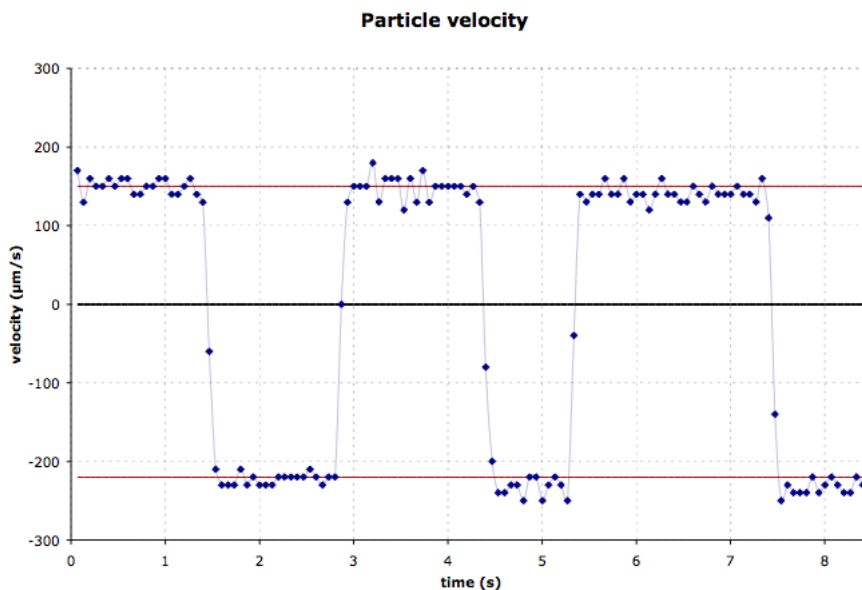


Figure 3-22: Velocities of 10 μm polystyrene spheres as they are translated left-to-right and then right-to-left across the electrodes by changing the pressure difference across the channel. This data was collected and shown here with permission from Dr. Marija Nikolic-Jaric [71].

3.2.5 Loading cells into the fluid channel

Once the electronics are prepared, approximately 2 ml of water and ethanol are purged sequentially, and exclusively at the full 500 mbar pressure from vial 1 to thoroughly clean the channel. Each purge lasts approximately 30 s, which is the time required to deliver cells to the microfluidic channel from the 2 ml vials. In addition, purging ensures that the channel is filled entirely with a single fluid phase, and is often used to systematically remove air bubbles, which may be present due to accidental delivery of air to the channel system or gas evolution from the fluid medium.

Cells are administered by pipetting small volumes (1 ml) into the four vials. The first vial usually contains cells in a buffer solution such as PBS (phosphate buffered saline),

while the remaining vials contain only the buffer solution. To establish a specific pressure differential across the channel, vials 1 and 2 are connected to ports 1 and 2 and each given a pressure $p_{1,2}$, while vials 3 and 4 are connected to ports 3 and 4 and each given a slightly different pressure $p_{3,4} = p_{1,2} - \Delta p$. Under this condition, the channel pressure, Δp_c , is [71] [72]:

$$\Delta p_c = \frac{R_c(R_1 + R_2)}{2R_1R_2 + R_c(R_1 + R_2)} \Delta p \quad (3-2)$$

where the hydraulic resistances leading into the wide channels are given by R_1 and R_2 , and that of the narrow channel is R_c . The average flow velocity in a narrow channel of cross-sectional area A_c , hydraulic resistance R_c , volumetric flow Q_c , and pressure differential Δp_c is

$$\langle v \rangle = Q_c / A_c = \Delta p_c / A_c R_c \quad (3-3)$$

Combining these equations, we have:

$$\langle v \rangle = \frac{R_c(R_1 + R_2)}{2R_1R_2 + R_c(R_1 + R_2)} \frac{\Delta p}{A_c R_c} \quad (3-4)$$

In Poiseuille flow, the flow velocity is parabolic according to Equation 2-19:

$$v = \frac{6\langle v \rangle}{H^2} h(H - h) \quad (3-5)$$

where H is the channel height and h is the vertical distance from a channel wall ($0 \leq h \leq H$). In Figure 3-23, the flow velocity for different particle elevations (h) is plotted vs. the pressure differential, Δp , using Equations 3-4 and 3-5.

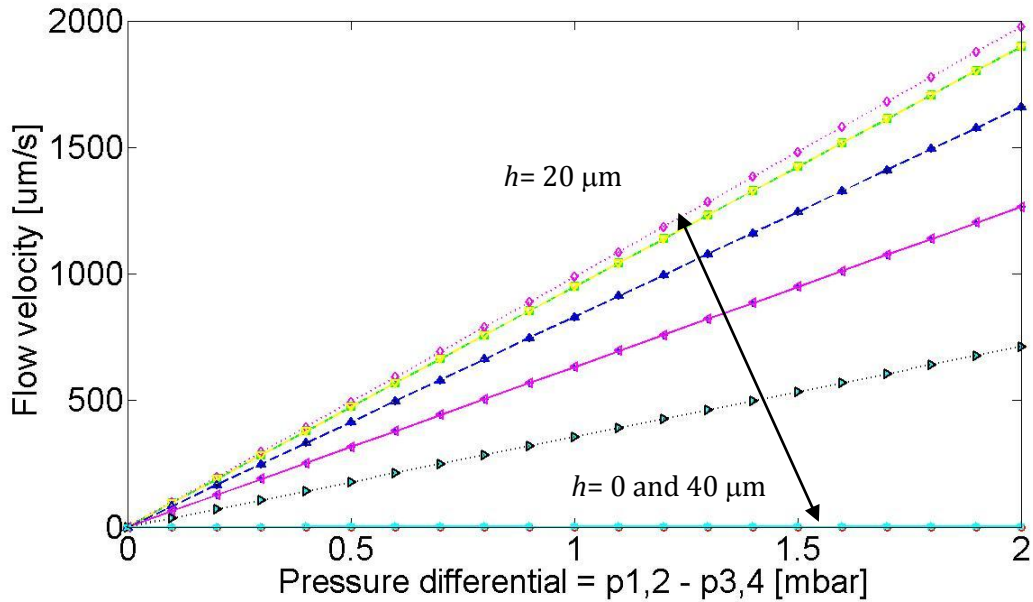


Figure 3-23: Flow velocity vs. pressure differential at different particle elevations. The elevation increases from 0 to 40 μm by 4 μm intervals. The channel height is 40 μm . To establish a flow of single cells that is visible in the microscope ($\sim 200\text{-}300 \mu\text{m/s}$), the pressure differential is typically set to 1-2 mbar. The hydraulic resistances are taken from [71], [72].

3.3 Chapter Summary

This chapter highlighted successful demonstrations of two versions of an electrical system, which simultaneously actuates and detects single polystyrene spheres as well as a variety of biological cells including yeast cells (*Saccharomyces cerevisiae*), Chinese hamster ovary cells, human breast epithelial cancer cells (MCF-7 and MDA-MB-231), human blood cells (T-lymphocytes, neutrophils, and red blood cells), and mouse fibroblasts (10T $\frac{1}{2}$, and the metastatic ras-transformed 10T $\frac{1}{2}$ cell line, Ciras-3). Whether these particles are un-actuated, DEP-actuated, or DEP-trapped in a fluid-flow, they are readily detected with enhanced capacitance sensitivity as they perturb high frequency fields, even in highly conductive cell buffers.

A microfluidic channel with a flattened semi-circular $40\ \mu\text{m} \times 120\ \mu\text{m}$ cross-section minimizes the interaction volume over the electrode region in order to maximize the capacitance sensitivity to a number of mammalian cell types and sizes. Two-gap interdigitated electrodes having $25\ \mu\text{m}$ widths and spacings generate effective DEP-actuation fields using moderate AC voltages ($< 10\ V_{pp}$). In addition, the time-dependent actuation and detection of flowing cells are monitored with minimal resistive losses as the electrodes extending outside the channel region toward the contact pad are wide ($100\ \mu\text{m}$), yet narrow enough to accommodate several such designs on the same chip ($15\ \text{mm} \times 15\ \text{mm}$).

In combination with an effective pneumatic pressure system for controlling fluid-flow, the H-shaped microfluidic channel accommodates the delivery of millions of cells, which flow predominantly into wide ($240\ \mu\text{m}$) side-channels while a much smaller fraction are monitored in a much narrower intersecting channel containing a slower, manageable differential flow (cell velocities below $1000\ \mu\text{m/s}$). This approach further minimizes channel clogging and facilitates channel cleaning. The improved capacitance resolution of the interferometric system is exploited in Chapter 4 to monitor the mechanical compression of cells that become maximally distant from the electrodes.

Chapter 4 – Dielectrophoretically-Induced Compression of Flowing Biological Cells into a Microfluidic Channel Wall

*"Do, or do not, there is no try."
- Yoda*

4.1 Introduction

Deformability cytometry is a new and rapidly developing research area based on continuously monitoring the mechanical response of single cells in microfluidic channels [7]. In Chapters 2 and 3, we successfully demonstrated that DEP-actuated cells can be simultaneously detected with capacitance detection using the same coplanar electrodes. Recall that low- (< 3 MHz) and high-frequency (1.6 GHz) electrical signals are coupled to the electrodes to actuate and detect cells, respectively.

In this chapter, strong low-frequency (< 3 MHz) DEP fields are used to force cells directly into contact with channel walls. In conductive cell buffers such as phosphate buffered saline (PBS), the low-frequency signal forces cells away from the electrodes toward the top surface (ceiling) of the channel. The cell-to-wall interaction is observed using high-frequency capacitive detection, which potentially forms the basis for a new rapid all-electrical approach to deformability cytometry. High-frequency signals provide the capacitance sensitivity required to dynamically detect the cell-to-wall interaction. In this way, we can electrically observe the induced cell trajectories to glean information about the electrical and physiological properties of the cell.

At sufficiently large DEP voltages ($> 6 V_{pp}$), suspended mammalian cells in a fluid flow are sequentially pressed into contact with microfluidic channel walls using repulsive dielectrophoretic forces (>30 pN) generated by coplanar interdigitated electrodes.

After being pressed into contact, the cell-to-wall interactions significantly alter the progress of the cell. Capacitive sensing can be used to monitor this movement and hence monitor the cell-to-wall interactions. Distinct electrical signatures are observed when cells are pressed into contact with the ceiling, as compared with those from pressed polystyrene spheres, which are far more rigid. In addition, different cell types (e.g., blood- vs. cancer cells) are found to exhibit distinctive cell-to-wall interactions.

Figure 4-1 illustrates the trajectory of a spherical particle that is subject to a strong low-frequency field. Spherical particles in a fluid flow obtain an equilibrium elevation, which is determined by a balance between gravity and a hydrodynamic lift force. When the particle encounters the strong low-frequency field, it experiences repulsive forces that direct the particle away from the electrodes.

Initially, as the rightward propagating particle approaches the leftmost electrode edge, the particle experiences a relatively weak but repulsive leftward force, which slightly decelerates the particle. After overcoming this relatively weak electrical barrier, the particle continues to experience repulsive forces that mostly direct the particle upward as it flows over the electrode region.

Strong low-frequency fields generated from interdigitated electrodes form a series of electrical barriers across the electrodes. The strongest barriers most significantly slow the horizontal progress of the particle. At particle elevations near the channel ceiling, these barriers exist along the edges of the *central electrode*. When the fluid flow velocity is sufficient to overcome these electrical barriers, the particle decelerates significantly above the central electrode, surpasses the barrier, and exits the electrode

region. Otherwise, the particle is simply trapped above the central electrode. Although surface-to-wall contact is initiated by strong vertical forces, the rigid PS spheres offer relatively little contact area from their smooth surfaces.

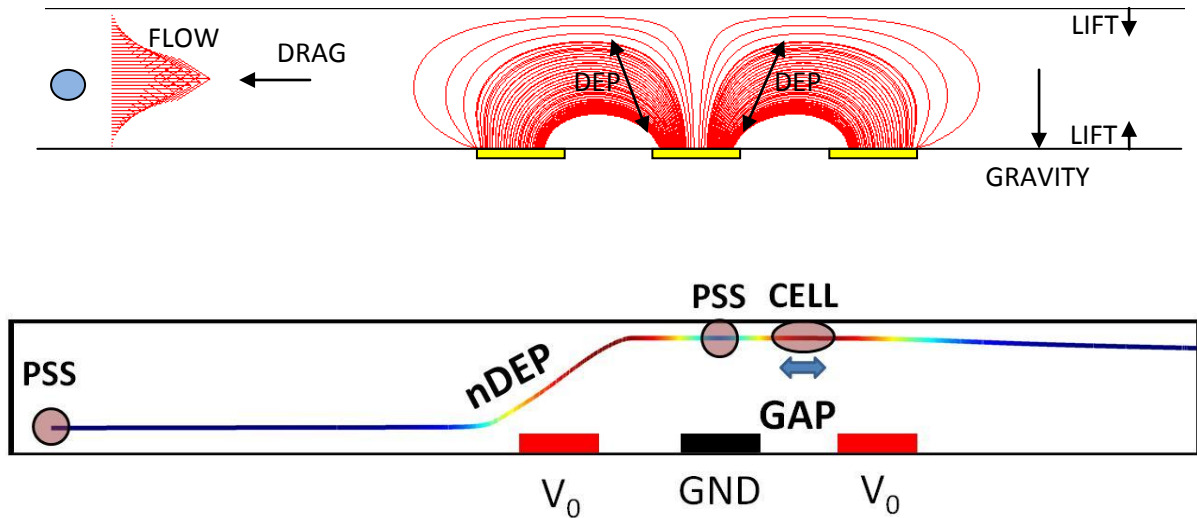


Figure 4-1: A laminar parabolic fluid flow drives the cell from left to right in a microfluidic channel. While passing over interdigitated electrodes, the cell is dielectrophoretically repelled from the electrodes toward the channel ceiling. When the fluid flow is stronger than the horizontal electrical barriers adjacent to the central electrode, the particle exits the electrode region. Otherwise, the particle is trapped above the central electrode. Biological cells experience a similar trajectory, but their softer mechanics potentially allow the cell-to-wall contact area to increase. In addition, this increases the probability of cell-to-wall adhesion, which may cause it to slowly translate along the channel ceiling due to the combination of fluid flow, DEP, and contact forces between the cell surface and channel ceiling. Deformable cells appear (from the top view) to stretch across the electrode gap.

Biological cells experience a similar trajectory, but their deformability allows the cell-to-wall contact area to increase compared with rigid spheres. This increases the probability of non-specific cell-to-glass adhesion [73], [74] through close-range van der Waals-London forces. In addition, the time for separation (de-adhesion) is

proportional to the area of contact. Cellular strain resulting in adhesive forces may assist cells in overcoming the electrical barriers exerted by strong low-frequency fields.

In general, cells slowly translate along the channel ceiling due to the combination of fluid flow, DEP, and contact forces between the cell surface and channel ceiling. Soft cells experience DEP-induced compression, and consequently appear (from the top view) to stretch across the electrode gap. This naturally occurs through Poisson's ratio assuming the cellular volume remains constant.

The capacitance changes induced by rigid polystyrene microspheres (PSS) are different from those of much softer, compressible cells (e.g., neutrophils & lymphocytes). Rigid spheres are trapped directly above the electrode surface, while the softer cells experience deformation as they dramatically slow above the electrode gap and subsequently release (Figure 4-1). Smaller capacitance changes are induced by "pressed cells" compared with those induced from free-flowing un-actuated cells because the pressed cells are simply further away from the electrodes. Subsequent compression of pressed cells may further reduce the induced capacitance changes.

Detecting the capacitance signatures of pressed cells provides a way of testing and utilizing our enhanced capacitance resolution. Furthermore, the surface morphology and mechanical properties can potentially provide insight into the physiological state of a cell. For example, separation of electroporated (§4.11.2) and non-electroporated cells using dielectrophoresis has raised the presumption that considerable changes in membrane permittivity and conductivity occur after electroporation [75].

4.2 Linking Cell Deformability to Physiological Functionality

The shape and deformability of a biological cell are essential aspects of its physiological functionality [76]. For instance, healthy red blood cells (RBCs) must deform readily in order to pass through smaller capillaries (2-3 μm) to transfer oxygen to vital organ systems. Increased RBC rigidity often indicates the presence of an undesirable pathological variation such as malaria, hereditary spherocytosis, or sickle cell disease [77]. On the other hand, larger deformability in breast cells may indicate enhanced metastatic potential (cancer) [7], [78]. Deformable cancer cells have greater motility, which enables them to access multiple areas of the body to establish multiple sites and enhance their destructive growth.

T-lymphocytes circulating in the bloodstream dramatically change their shape and rigidity when activated during an immune response [79], [80], [81]. Specifically, white blood cells (WBCs) reorder their cytoskeletal filaments to initiate and facilitate their deformation and transport through endothelial cells to navigate through chemical gradients generated between the WBCs and inflamed tissues. In the bloodstream, a rigid cytoarchitecture protects T-lymphocytes from repeated hydrodynamic and mechanical stress as they roll along the endothelial cell layer lining the interior vessel wall.

However, during an immune response, lymphocytes must rapidly convert from a semi-rigid to a highly deformable state and undergo extensive shape changes to penetrate the spaces between endothelial cells and enter inflamed tissue (i.e., chemokine-induced transendothelial migration). During transendothelial migration, lymphocytes become

highly polarized, a process driven by rapid reorganization of the three cytoskeletal filament systems: actin, microtubules, and intermediate filaments [82], [83].

The addition of a surfactant such as Pluronic F-68 can enhance the robustness of cell cultures to deformation [21], shear stresses, and offers a protective barrier and limited repair to cell membranes previously damaged by prolonged exposure (> 10 minutes) to trypsin [84]. Wong *et al.* investigated the influence of cytoskeletal actin on the viscoelastic properties of *Brassica oleracea* (cabbage) protoplasts by treating the protoplasts with actin-specific agents, latrunculin-A and jasplakinolide, which disrupt and stabilize the organization of actin filaments, respectively [85]. Protoplast electrodeformability increased significantly in latrunculin-A treated cells whereas jasplakinolide-treated cells showed little difference in deformability compared with that of control cells.

4.2.1 Structural cell polarization

Structural cell polarization refers to the process of creating a physical asymmetry in the cytoskeleton. Generally, actin and microtubules provide the structural basis for cell polarization because of their inherent structural polarity along the polymer lattices and intrinsic dynamics that allow them to respond rapidly to polarity cues [86]. The intermediate filaments, however, are nonpolar and are generally not involved in generating cell polarity. Along with transendothelial migration, cell polarization is critically important to other standard cell processes such as cell division and initiating the sporulation of starving cells [82].

Cytoskeletal motor proteins power unidirectional movement along actin filaments or microtubules by irreversibly moving from one tightly bound conformation to another using the energy of ATP hydrolysis. Myosins are motor proteins for actin. Some move along several consecutive steps before dissociating from the filament, making them suitable for transport over long distances. Others travel fewer steps, which makes them suitable for contractile movement through sliding of actin filaments.

Microtubule motors encompass kinesins and dynein, which move in opposite directions toward the plus and minus ends of the microtubule. Actin filaments have a key role in the initial symmetry breaking process and enable a rapid response to stimuli in cells of all sizes. Microtubules, however, build on and stabilize the initial asymmetry that is created by actin-based forces.

4.3 Biological Cells Are Nonlinear Viscoelastic Materials

Biological cells are nonlinear viscoelastic materials, which means that cells exhibit both viscous and elastic characteristics during their deformation. Elastic materials strain instantly when stretched and instantly return to their original state when the stress is removed. Viscous materials, like honey, resist shear flow and strain linearly with time when a stress is applied. Consequently, viscoelastic materials have both instantaneous and time-dependent responses to an applied stress.

The heterogeneity of biological cells makes it difficult to quantify viscoelastic mechanics. Indeed, the viscoelastic properties of biological cells vary widely across their components, which include the lipid/protein bilayer membrane, organelles, cytosol, and the three cytoskeletal filament systems – actin, microtubules, and

intermediate filaments [85]. In addition, unlike non-living things, cells are constantly adapting to physical and chemical variations in their environment to preserve their life, initiate their own demise, and perform physiological functions.

A number of models have been proposed for predicting the viscoelastic mechanics of various cell types [83]. To paint a simple picture of viscoelasticity, we will focus on the standard linear strain (SLS) model, in which the *compliance* of a cell follows the formula:

$$J(t) = \frac{1}{k_1} \left[1 - \left(\frac{k_2}{k_1 + k_2} \right) e^{-t/\tau_\sigma} \right] 1(t) \quad (4-1)$$

where the unit step function is $1(t)$, and relaxation time at constant stress is:

$$\tau_\sigma = \eta \frac{k_1 + k_2}{k_1 k_2}$$

The standard linear strain model is characterized by two elastic constants, k_1 and k_2 , and one viscous constant, η . The compliance (strain/stress), $J(t)$, is essentially the inverse Young's modulus (stress/strain). In response to a sudden stress, viscoelastic materials strain instantly by a certain amount. Upon continued application of this stress, the material strains progressively more easily, i.e., appears softer over time up to a limit. The instantaneous compliance is $J_0 = 1/(k_1 + k_2) = 1/E_0$, where E_0 is the initial elastic modulus, and the compliance at long application times is $J_\infty = 1/k_1 = 1/E_R$, where E_R is the relaxed elastic modulus. The rate of material relaxation is governed by a single time constant τ_σ [87]. The viscoelastic parameters of the SLS model for CHO cells and neutrophils are given in the table below.

Table 4-1: Viscoelastic parameters of the SLS model.

Cell type	k_1 (Pa)	k_2 (Pa)	η (Pa s)	τ_σ (s)	Reference
CHO	193 ± 130	1379 ± 930	2905 ± 1958	17.2 ± 11.6	[87]
Neutrophil	27.5 ± 12	73.7 ± 35	13.0 ± 5.4	0.65 ± 0.3	[88]

Dielectrophoretic pressing typically occurs over a few seconds (1-5 s), which is greater than the viscoelastic time constant of neutrophils, and shorter than the viscoelastic time constant of CHO cells. Consequently, we expect that CHO cells mainly behave according to their instantaneous modulus, and neutrophils would respond fully toward their relaxed modulus. The corresponding effective Young's moduli for CHO cells and neutrophils are therefore 1572 Pa and 27.5 Pa, respectively.

4.4 Methods for Mechanically Probing Cells & Subcellular Structures

Biomechanical assays currently used for probing subcellular regions include atomic force microscopy (AFM), magnetic twisting cytometry, and cytoindentation. Biophysical assays used for probing whole-cell deformation include optical tweezers, the microplate stretcher, the microfabricated post array detector, and micropipette aspiration (see [89], [90] and references therein).

Atomic force microscopy has been effective in examining the features of cellular surfaces, which themselves can be physiological markers. Iyer *et al.* recently demonstrated that healthy and cancerous epithelial cells can be identified based on the interaction between their "surface brush layers" (mainly microvilli, microridges, and

cellular cilia) and an AFM probe [91]. Other surface extensions such as blebs appear on Chinese Hamster Ovary (CHO) cells depending on their cell cycle phase [92].

As outlined in Table 4-1, the elastic moduli of various cell types can be evaluated using AFM. Since measurements are highly localized, they accurately capture the local stress-strain behaviour of subcellular components but likely overestimate the overall elastic response of the cell as obtained using whole cell techniques such as micropipette aspiration. Indeed, the table reveals significant variability in the Young's modulus for a given cell.

Table 4-2: Young's modulus of living cells using force microscopy. *b*=after destabilizing agent; *c*=resting; *d*=activated; *e*=apoptosis

Cell Type	Young's Modulus (kPa)	Reference	Probing Technique
MDA-MB-231	0.37-0.50	[93]	AFM
MCF-10A	0.72-1.11		
MCF-7 (living)	20-30	[94]	SFM
MCF-7 (fixed)	50-150		
HeLa (living)	100-200		
HeLa (fixed)	400-500		
MCF-7	0.3-0.5	[95]	AFM
MCF-10a	0.5-1.2		
Lymphocyte	1.24	[96]	AFM
Lymphocyte (b)	0.34		
Jurkat Cell	0.51		
Jurkat Cell (b)	0.23		
Lymphocyte (c)	11.2	[97]	AFM
Lymphocyte (d)	19.7		
Lymphocyte (e)	7.1		

Magnetic twisting cytometry probes the mechanical properties of an adherent cell by applying a torque to a magnetic bead that is tightly bound to the cell surface [98]. This tight bonding is achieved by coating the ferromagnetic bead with *ligands*, which are

signal triggering molecules that bind to compatible cell surface *receptors*. Receptors are defined as target protein molecules typically embedded in the plasma membrane of a cell, which receive chemical signals from neighbouring cells.

An external magnetic field applies a stress to the magnetic bead, which is tracked positionally using either video microscopy or with laser particle tracking. In addition to applying controlled mechanical stresses, this technique is used for examining ligand-receptor adhesion strengths, cytoskeletal rheology (for evaluating shear modulus, viscosity and motility), and the mechanical links between the cell surface receptor and the cytoskeleton. Although this technique probes local mechanics, uncertainties related to the nature of bead attachment to the cell make determining the true magnitude of the elastic and viscous moduli difficult [99].

Cyto-indentation uses a probe attached to a cantilever beam controlled by a piezoelectric actuator for load application, and the probe is smaller than the cell. The cytoindenter does not rely on video capture to determine probe position and deflection. Originally, detection was achieved using a photodiode system, but presently monitors the displacement of the cantilever via a laser reflected off the free end of a cantilever.

Micropipette aspiration is used for whole-cell deformation, and involves the application of negative pressure to aspirate the cell surface into a small glass tube while tracking the leading edge of its surface. Using small suction pressures (0.1-0.2 pN/ μm^2) and tracking the edges to an accuracy of $\pm 25 \text{ nm}$, both soft and rigid cells can be studied with this technique. Using continuum models, Hochmuth found that soft cells such as neutrophils and red blood cells behave as a liquid drop with a cortical (surface) tension

of 30 pN/ μm and a viscosity on the order of 100 Pa·s. On the other hand, chondrocytes and endothelial cells behave as solids with an elastic modulus of the order of 500 pN/ μm^2 (0.5 kPa) [100].

In a flow configuration, optical tweezers have been effective in determining that MCF-7 breast cancer cells stretch five times more than non-cancerous MCF-10A breast cells, depending on the metastatic potential [101], [7]. With this inspiration, several groups have recently developed technologies for “deformability cytometry”, where the mechanical deformation of a biological cell in microfluidic flow channels rapidly provides information about its physiological state [102], [103].

These groups have successfully used mechanical structures and/or competing fluid flows to monitor the deformation of malaria-infected RBCs and breast cancer cells (MCF-7). These approaches generally require sophisticated and expensive detection tools such as high-speed cameras and optical/fluorescent microscopes. Although they are unmatched for speed and spatial resolution, fluorescence microscopes are expensive, require fluorescent dyes for labelling and highly skilled users for handling and maintaining optical equipment, and are generally not conducive to portable lab-on-a-chip applications. Consequently, an electrical approach for cell detection known as impedance cytometry has been gaining considerable interest.

4.5 Impedance Cytometry for Single Cell Characterization

Recently, impedance cytometry has effectively identified cell populations based on their viability and phenotype [12], [104], [105], which are deduced from the induced electrical signals alone. This markerless approach potentially eliminates the need for

fluorescent or optical microscopes, which opens the door to affordable and portable lab-on-a-chip applications. Direct detection and manipulation of single biological cells [106], [107], [108] is advantageous because a single broad-sweeping measurement from a heterogeneous cell population masks the presence and properties of rare cells [6], [109] – for example, circulating tumour cells in the bloodstream [110].

Collecting an impedance measurement at a single frequency has been used for high throughput particle counting (5000 particles/s) [11], capacitance cytometry of cells [13], and recently, for coordinating the transfer of single cells to single droplets with high efficiency [111]. Single-frequency impedance measurements are generally appropriate when variations in impedance due to cell/particle size are insignificant. However, more degrees of freedom are required for cell diagnostics because the impedance signal induced by a single cell depends strongly on frequency (from 5 kHz – 200 MHz) [20] and contains information about its charged proteins (100 MHz), interfacial charge distributions (< 100 MHz), electrical properties (permittivity and conductivity), as well as electrode polarization (< 10 MHz) [42], [112], [113]. Consequently, two frequencies are often required to separate the electrical properties of the cell from those of its surroundings.

With the recent successes of impedance cytometry for single-cell characterization, researchers have begun combining well-established techniques such as micropipette aspiration with impedance measurements in microfluidic chips. For example, in a non-flow configuration, the impedance of breast cancer cells can be monitored during their aspiration through smaller mechanical capillaries [114]. Chen *et al.* extended this

approach to MC-3T3 osteoblasts and extracted effective Young's moduli based on the cell response at different aspiration pressures [115].

Techniques for whole and partial cell deformation often yield significantly different values for the elastic modulus of a cell. For example, whole-cell micropipette aspiration measurements of neutrophils predict a much lower elastic modulus (< 100 Pa) compared with atomic force microscopy, which probes individual subcellular components having elastic moduli that vary over several orders of magnitude. For example, the polymer-filled multi-lobed nucleus generally yields a large elastic modulus (100 kPa) compared with other subcellular features (< 10 kPa).

In addition to cell detection, actuation, and characterization, electrical signals can be used effectively for cell deformation. As a deformation technique, *electro-deformation* is more analogous to optical trapping and micropipette aspiration where the forces are applied over a substantial surface area to induce mostly whole-cell deformation, which may or may not involve deformation of subcellular structures (e.g., nucleus) depending on their fractional volume within the cell.

4.6 Dielectrophoresis for Cell Electro-deformation

According to a recent review by Ronald Pethig, the publishing trend suggests that the theory (5%) and technology (18%) of dielectrophoresis have matured sufficiently for efforts to be directed mainly toward the publication of applications (77%) [116]. Consequently, dielectrophoresis has been increasingly used as a tool for single-cell electro-deformation using simple electrode geometries [25], [117] [21], [85], [118], [52]. Typically, cells are trapped and stretched between electrode edges using positive

dielectrophoresis and imaged using optical microscopy. For this approach to be useful, great care is required to avoid potentially overheating and/or inducing irreversible electroporation in cells due to extremely large electric fields at the electrode edges.

For a given applied DEP voltage, stretching single cells between electrodes requires a small electrode spacing, which inherently generates large electric fields. Larger electrode spacings may be used if multiple cells are trapped and subsequently induced into contact via classic pearl-chain formations. In either case, acquiring measurements is a slow process because these systems are not made in a flow configuration. Furthermore, the detection of electro-deformation is typically done using optical microscopy in order to analyze the corresponding changes in cell dimensions, which again limits experiments to the laboratory.

Consequently, our aim is to develop an electrical approach to deformability cytometry where the capacitance signatures induced by the momentary deformation of single cells flowing in suspension provide a basis for rapid mechanical cell characterization.

4.7 An All-Electrical Approach to Deformability Cytometry

In this work, flow impedance and video microscopy are used to monitor the mechanical responses of single mammalian cells as they are dielectrophoretically compressed (nDEP) into a microfluidic channel wall. At high frequencies (1.5 GHz), the impedance change induced by single, flowing cells is mainly capacitive, which is induced simply by replacing one permittivity (cell buffer) with another (a cell) – i.e., electronic polarization. Consequently, the problem is greatly simplified as the capacitance change

is insensitive to charged proteins (100 MHz), interfacial charge distributions (< 100 MHz), and electrode polarization (< 10 MHz) [42], [112], [113].

In our microfluidic channel, suspended mammalian cells generate position-dependent capacitance signatures as they flow past an interdigitated coplanar electrode pair. Distinct capacitance signatures are observed when the cells are dielectrophoretically repelled into contact with a channel wall. We compare these signatures with those induced by rigid 10 μm polystyrene microspheres (PSS), which have an elastic modulus of approximately 1-2 GPa. Cells are much softer in comparison with elastic moduli ranging from 60-120 Pa (neutrophils, lymphocytes), to 1500 Pa (CHO cells) [87], [96].

Simulations of the equation of motion are used to estimate the experimental trajectories of both un-actuated and DEP-actuated cells as they pass over the electrodes. Since different cell types have different mechanical properties, their respective cell-to-wall interactions may form a basis for their differentiation. In addition, with electrical detection and manipulation, this system has great potential for use in portable lab-on-a-chip applications.

4.8 Recap of Interferometric System

The interferometric approach described in §3.2 is used to simultaneously manipulate and detect suspended mammalian cells in a flow configuration (see [119], [65], [45], for details). To briefly recap, a 1.5 GHz RF signal is split into two paths. The *reference* path is unperturbed, and the *sensing* path contains a transmission line resonator, which is coupled to coplanar interdigitated electrodes fabricated on the floor of a fluid-filled micro-channel. A cell flowing over the electrodes capacitively induces a phase change

in the *sensing* path, creating a net phase difference, $\Delta\theta$, between the two paths. The voltage signals in the reference and sensing paths (V_R and V_S) are recombined into a mixer and lock-in amplifier with an overall gain, G . At the resonant frequency, f_r , the phase varies linearly with capacitance. Therefore, a passing cell induces a capacitance change that is proportional to the final recombined signal, $S = GV_R V_S (d\theta/dC)|_{f_r} \Delta C_{cell}$. Corresponding video evidence confirms that signals arise from individual cell crossings.

4.9 Cell Preparation

Experiments on mammalian cells were conducted in Electrical Engineering and Physics laboratories at the University of Manitoba, as well as a lab at the Manitoba Institute of Cell Biology (Figure 4-2). In this multidisciplinary work, lab technicians from Dr. Michael Butler's Microbiology group, Dr. Francis Lin's Physics group, and Dr. Jim Davie's Biochemistry and Molecular Biology group at CancerCare Manitoba prepared the cells for the experiments. Cell preparation procedures are outlined in Appendix C.



Figure 4-2: Members of our group, along with our cell preparation expert, Cheryl Peltier, watch as the system is being prepared to manipulate flowing mouse fibroblasts on site at the Manitoba Institute of Cell Biology.

4.10 Data Acquisition & Analysis

The recombined signals, S , are collected sequentially (sampling rate = 1 kS/s) in real-time as 30 s data files that are subsequently analyzed using programs written in LabView [120] and MATLAB. To confirm that signals correspond to the passing of mammalian cells, corresponding videos are obtained at a 15 fps frame rate. Each data file is fitted with a polynomial baseline to account for temperature-induced fluctuations in the baseline capacitance signal. The polynomial baseline is subtracted from the raw

experimental traces to obtain the final capacitance signatures. For very small signals, a smoothing function is implemented. Some sample code and explanations are provided in Appendix D.

4.11 Capacitance Signatures from DEP-Actuated Cells

4.11.1 Polystyrene spheres as control particles

Polystyrene spheres (PSS) have a high Young's Modulus (~ 1 GPa), which renders them incompressible to the relatively small DEP forces (< 1 nN) used in the experiments. In addition, these microspheres are highly spherical with smooth surfaces, and exhibit a large dielectric contrast compared with water, making them ideal for use as control particles.

To electrically observe the particle trajectory, we initially used DEP voltages that forced PS spheres into different regions of the laminar fluid flow. Figures 4-3 and 4-4 illustrate typical experimental capacitance signatures induced by a flowing $10\ \mu\text{m}$ polystyrene sphere in water as the applied DEP voltage increases from 3 to $4\ V_{pp}$ ($f_{DEP} = 100\ \text{kHz}$).

At $3\ V_{pp}$, the capacitance signature is clearly asymmetric in amplitude. The PS sphere induces large capacitance changes upon entering the electrode region, and smaller capacitance changes while exiting the electrode region. In addition, the PS sphere clearly accelerates during this transition. Before entering the electrode region, the polystyrene sphere establishes an equilibrium flow height, which is determined by balancing the hydrodynamic lift and gravitational forces. This equilibrium height is below the vertical center of the channel where the fluid velocity is a maximum.

Therefore, particle acceleration may only occur when the particle is dielectrophoretically *repelled* upward into regions of faster fluid flow.

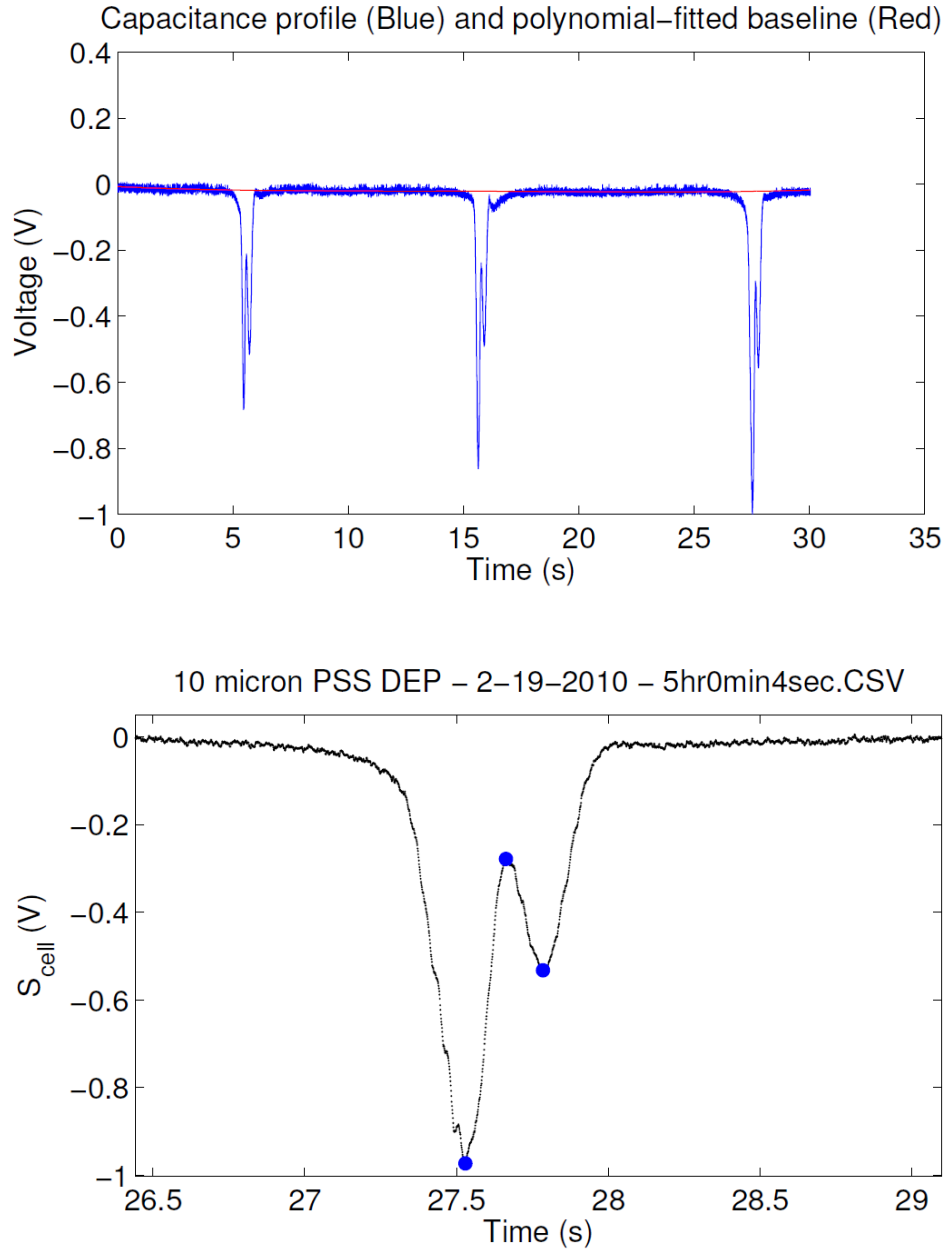


*Figure 4-3: Capacitance changes induced by a 10 μm polystyrene microsphere subjected to a 3 V_{pp} DEP voltage. At 100 kHz, the sphere is repelled from the electrode region. The capacitance-induced voltage shift is approx. -1 V. **Top:** Raw data with polynomial-fitted baseline. **Bottom:** Baseline-subtracted data.*

When the voltage increases to $4 V_{pp}$, the asymmetry is less pronounced, but the overall capacitance change has clearly decreased. The overall capacitance change is smaller due to stronger DEP forces repelling the PS sphere to higher elevations compared with those DEP forces from the $3 V_{pp}$ signal. In addition, the PS sphere enters the electrode region at slightly higher elevations due to the increased repulsive forces experienced before entering the electrode region. Consequently, the asymmetry in the $4 V_{pp}$ capacitance signature is less pronounced compared with the $3 V_{pp}$ signature.

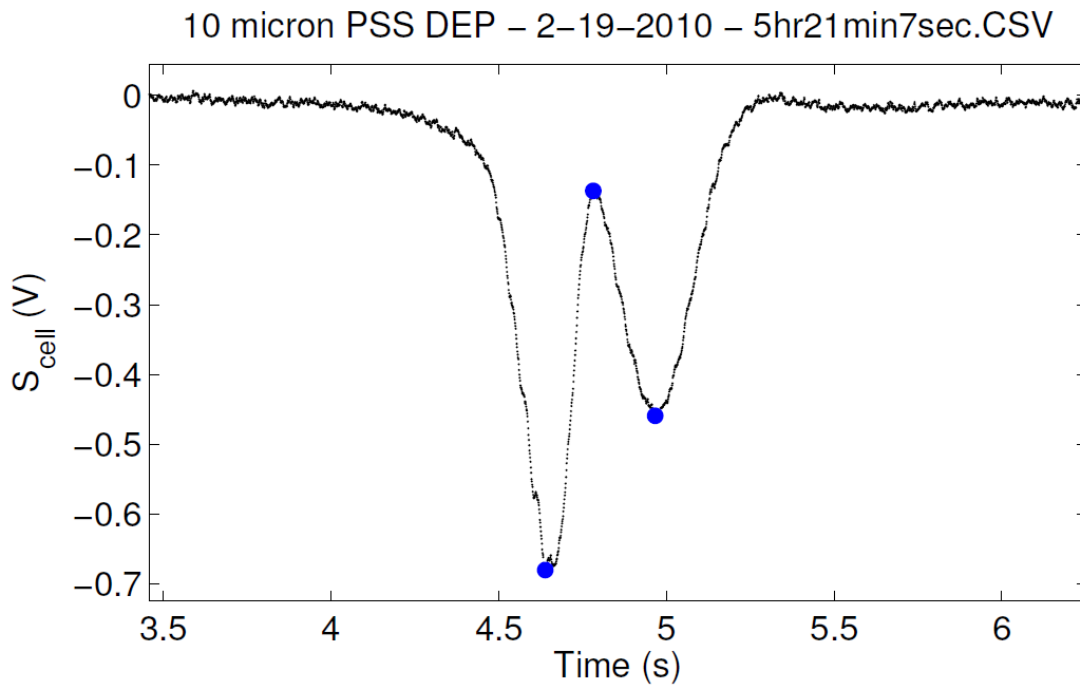


Figure 4-4: Capacitance changes induced by a $10 \mu\text{m}$ polystyrene microsphere subjected to a $4 V_{pp}$ DEP voltage. At 100 kHz , the sphere is repelled from the electrode region. The capacitance-induced voltage shift is approx. -0.7 V .

4.11.2 Clausius-Mossotti Factor of $10 \mu\text{m}$ polystyrene spheres

We may theoretically determine the direction of the DEP forces by calculating the Clausius-Mossotti factor (Equation 2-12), which requires the permittivities and

conductivities of the particle and the fluid environment. The relative permittivities of water and PSS are 78 and 2.5, respectively. Exposure to air increased the conductivity of deionized water from the ultrapure 5.5 $\mu\text{S}/\text{m}$ to a measured value of 1.8 mS/m (as measured by a conductivity meter). The conductivity of PSS is evaluated using:

$$\sigma_p = \sigma_{bulk} + 2K_s/r \quad (4-2)$$

where σ_{bulk} is the bulk conductivity of polystyrene, K_s is the surface conductance of the particle, and r is the radius of the particle.

In our case, when the particle radius is large (i.e., 10 μm) compared with the Debye length (< 680 nm, [121]), the electrical double layer consisting of the Stern and diffuse layers may be considered as a single infinitely thin sheet of charge with a net surface conductance, K_s . However, when the Debye length is a significant fraction of the radius of the particle, the total surface conductance, K_s , is the summation of the conductances of the Stern and diffuse layers. The maximum possible Debye length (generated in ultrapure water) is approximately 680 nm, which drops off rapidly with increasing bulk conductance. Since the bulk conductivity of polystyrene is small ($\sigma_{bulk} = 10^{-16} \text{ S}/\text{m}$), the overall conductivity is mainly dependent on the surface conductance, which has been recently measured to be 2.5-2.8 nS [122]. Therefore, a 10 μm diameter PSS has a conductivity of approximately 1 mS/m .

For 10 μm diameter PS spheres in deionized water, the Clausius-Mossotti factor (Equation 2-12) is approximately -0.18 at a frequency of 100 kHz (Figure 4-5), and

remains negative for all frequencies. Therefore, PS spheres are dielectrophoretically *repelled* over the full frequency range.

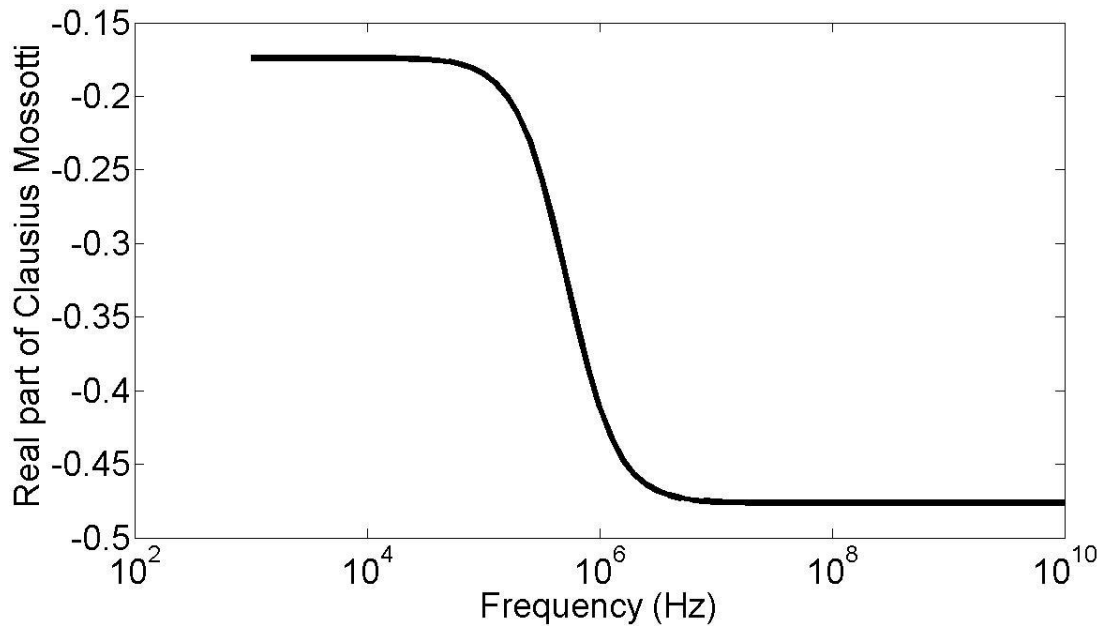


Figure 4-5: *Clausius-Mossotti factor for a 10 μm diameter (5 μm radius) polystyrene sphere (PSS) in deionized water (after prolonged exposure to air). The relative permittivity and conductivity of the PSS are 2.5 and 0.5 mS/m, respectively. After exposure to air, the deionized water permittivity remains at 78, and increases its conductivity to 1.8 mS/m.*

4.11.3 Large DEP potentials initiate unique capacitance signatures

When PS spheres are subject to even larger DEP signals (10 V_{pp} , 100 kHz), they are repelled to a maximum elevation above the electrodes and propagate essentially along the channel ceiling. Figure 4-6 illustrates a nice correlation between the simulated and experimental traces for a flowing rigid PS sphere subject to a 10 V_{pp} , 100 kHz repulsive DEP signal. The simulated trace was calculated using the average PS sphere velocity from the experimental trace, which was determined from actual video files obtained at

15 fps to be 288 $\mu\text{m/s}$. Again, recall that the output voltage, S , is proportional to the capacitance change.

The largest capacitance changes occur at A and C – the electrode gaps. The smallest capacitance change occurs directly over the central electrode, B. At 10 V_{pp} , the overall capacitance decrease is minimal, but a clear asymmetry in transit time is observed. Examination of the video reveals that the sphere repels very strongly toward the channel ceiling, and dramatically slows above the central electrode. The non-uniform fluid velocities experienced by the sphere in a parabolic fluid flow cause it to rotate and experience a net horizontal translation toward the electrode edge, after which it escapes the electrical trap.

The simulations assumed no contact between the wall and particle. Indeed, video evidence shows that PS spheres rotate after becoming trapped above the central electrode. In some instances, we observe that particles cease spinning after being trapped for some time. If the fluid velocity is not sufficient for the polystyrene sphere to overcome the dielectrophoretic forces, the sphere remains trapped above the central electrode.

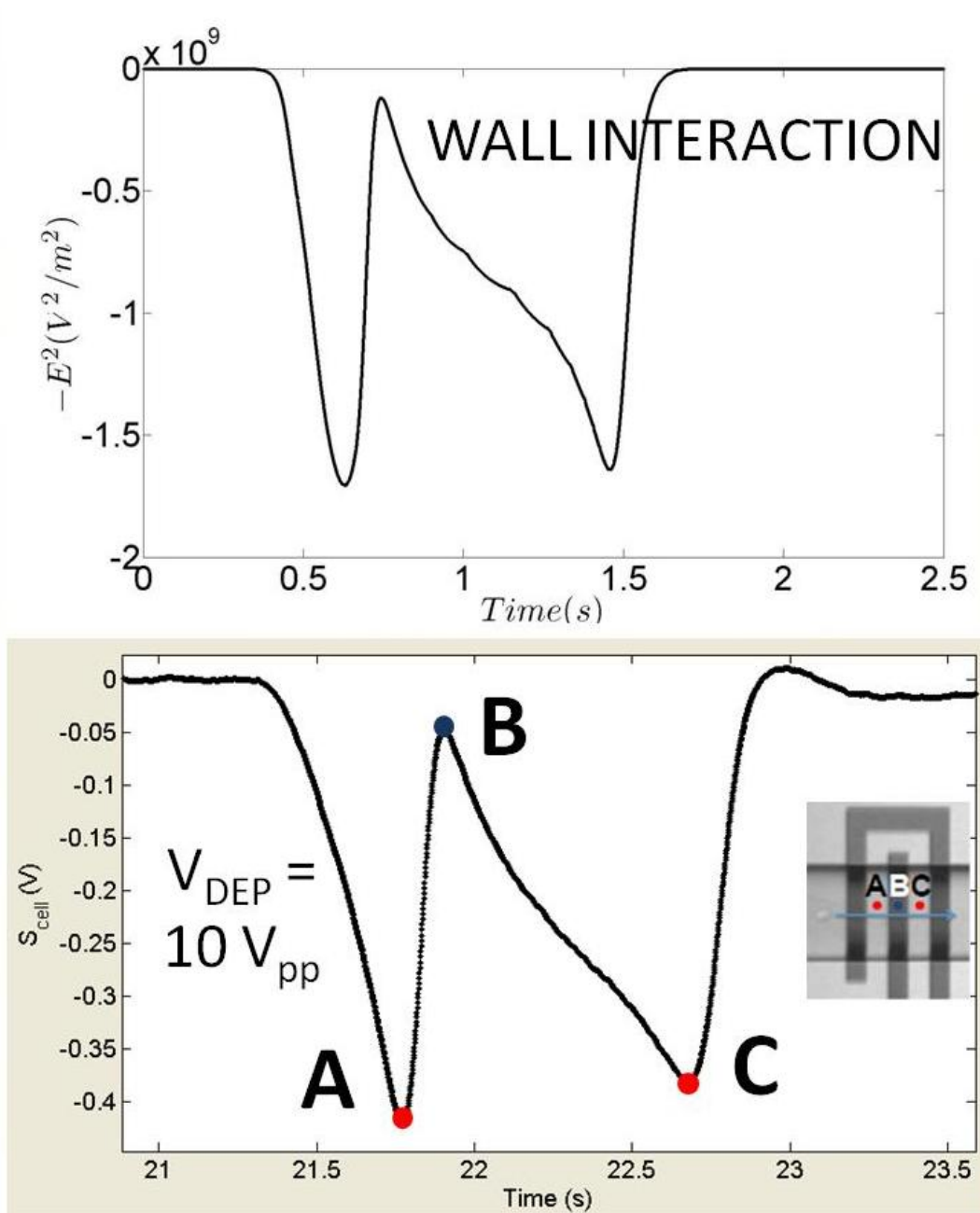


Figure 4-6: Comparison between simulated (Top) and experimental (Bottom) capacitance signatures for a flowing, rigid polystyrene bead subject to a 100 kHz, 10 V_{pp} repulsive DEP signal. The capacitance-induced voltage shift is approx. -0.4 V. As determined from actual video files obtained at 15 fps, the average bead velocity in both cases is 288 $\mu\text{m/s}$. The output voltage is proportional to the capacitance change. Two capacitance minima occur at A and C – the electrode gaps. The capacitance maximum occurs directly over the center electrode, B.

4.12 Dielectrophoretic Pressing of Blood Cells

Neutrophils, which are the most abundant leukocytes (white blood cells) in the circulatory system, have a low *initial elastic modulus* of approximately 60-100 Pa based on micropipette aspiration measurements [40], [88]. T-lymphocytes, which are also leukocytes, are found to be roughly twice as rigid [40]. The neutrophil also has a relatively large nucleus, which plays a significant role in the overall dielectric response at frequencies above 1 MHz. This is observed when comparing the Clausius-Mossotti factor using the single- and double-shell models, where the double-shell model additionally incorporates the dielectric parameters of the nucleoplasm and nuclear membrane (Figure 4-7).

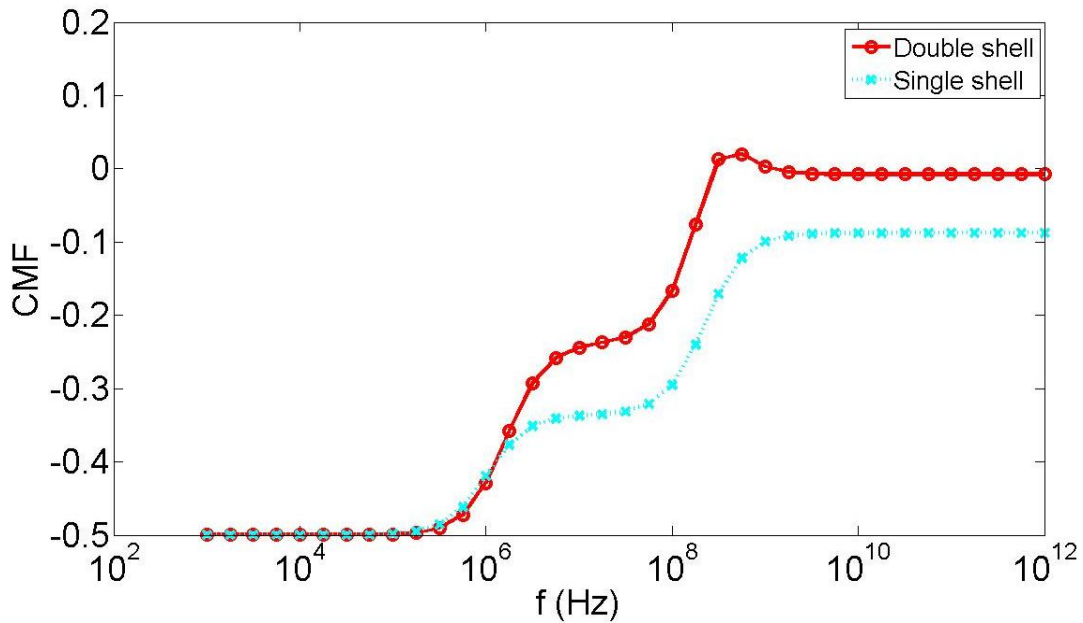


Figure 4-7: Calculated Clausius-Mossotti factor of neutrophils in RPMI-1640 medium using the single- and double shell models.

In this section, the simulated trajectories of rigid spheres having the dielectric properties of blood cells are compared with actual experimental traces to illuminate the impact of mechanical deformation. If deformation occurs, we expect the resulting induced capacitance signature to change compared with that from a rigid sphere.

4.12.1 Experimental neutrophil and red blood cell signatures

Typical experimental capacitance signatures from neutrophils and red blood cells in RPMI-1640 medium are shown in Figures 4-8 to 4-12. The applied DEP voltages are 0, 1, 2, 8, and 10 V_{pp} , respectively, and the DEP frequency is 450 kHz (CMF=-0.5) in all cases. Neutrophils induce the larger capacitance signatures due to their larger volume. As the DEP voltage increases, the capacitance signals decrease as both cell types are progressively more repelled from the electrodes.

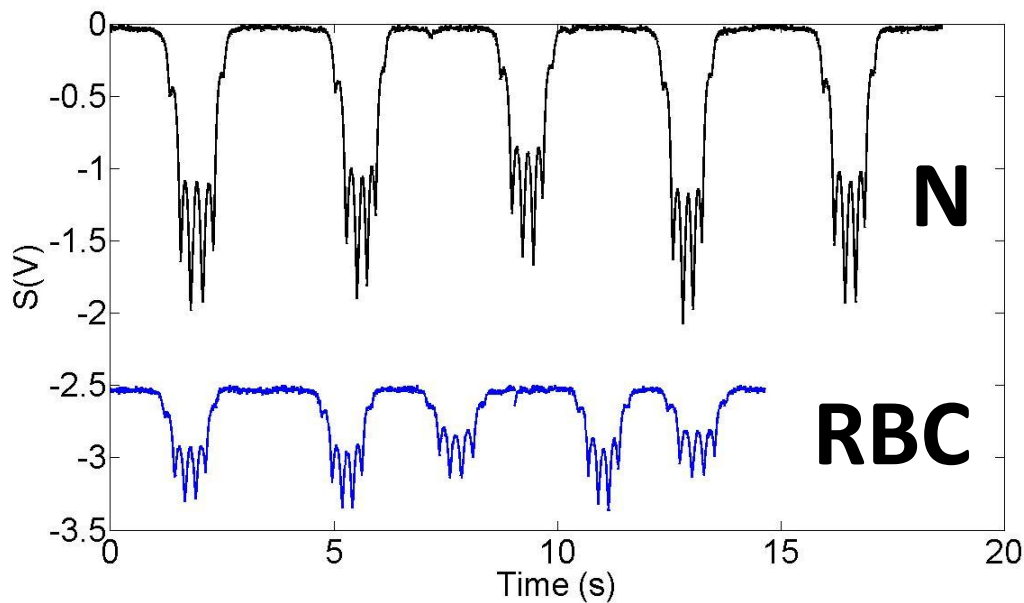


Figure 4-8: Capacitance signatures from un-actuated neutrophils (N) and red blood cells (RBCs).

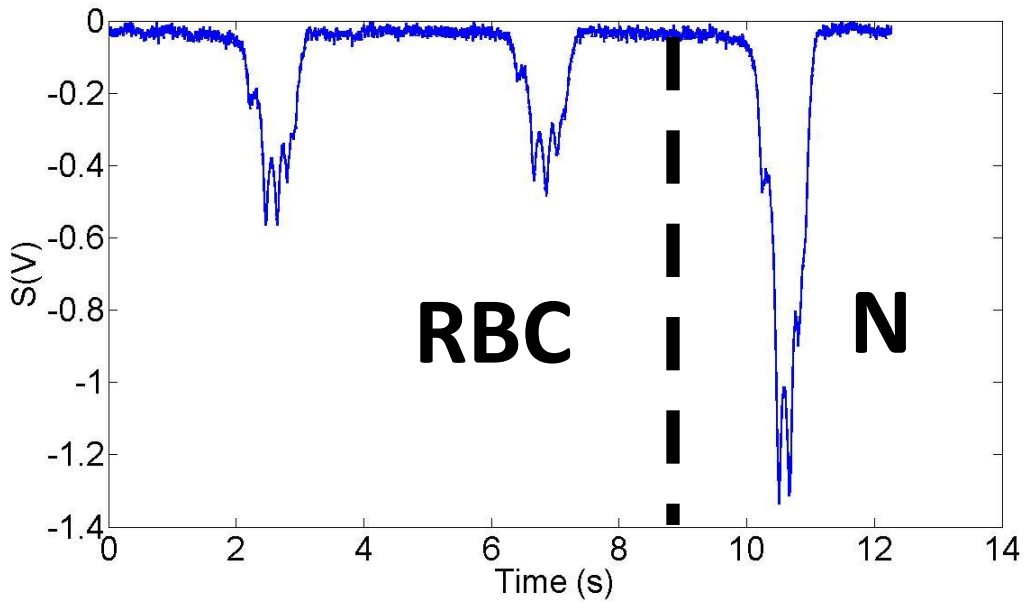


Figure 4-9: Capacitance signatures from two RBCs and one neutrophil subject to a 1 V_{pp} applied DEP voltage and 450 kHz frequency.

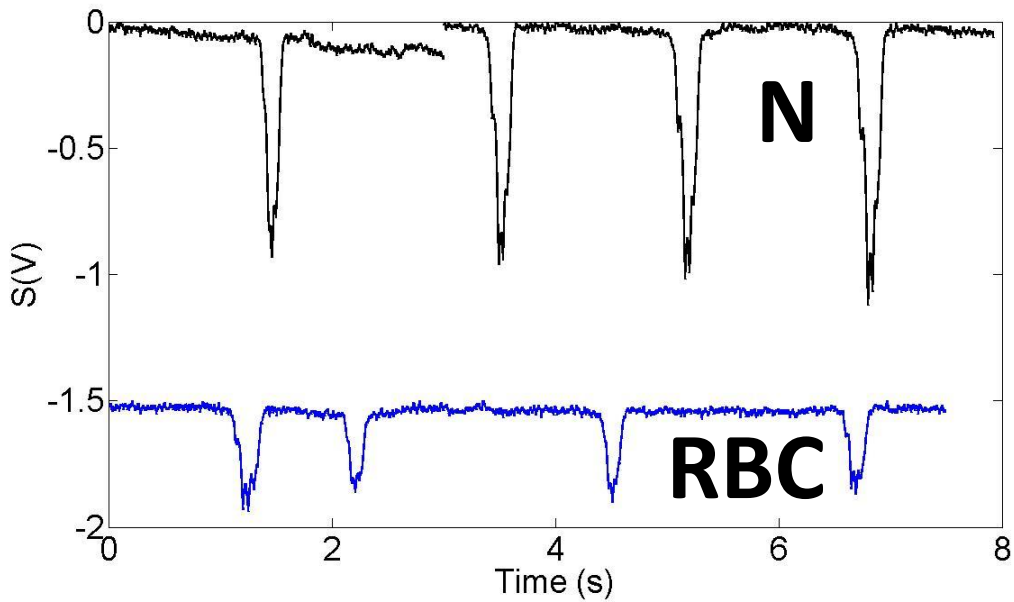


Figure 4-10: Capacitance signatures from four neutrophils and RBCs subject to a 2 V_{pp} applied DEP voltage and 450 kHz frequency.

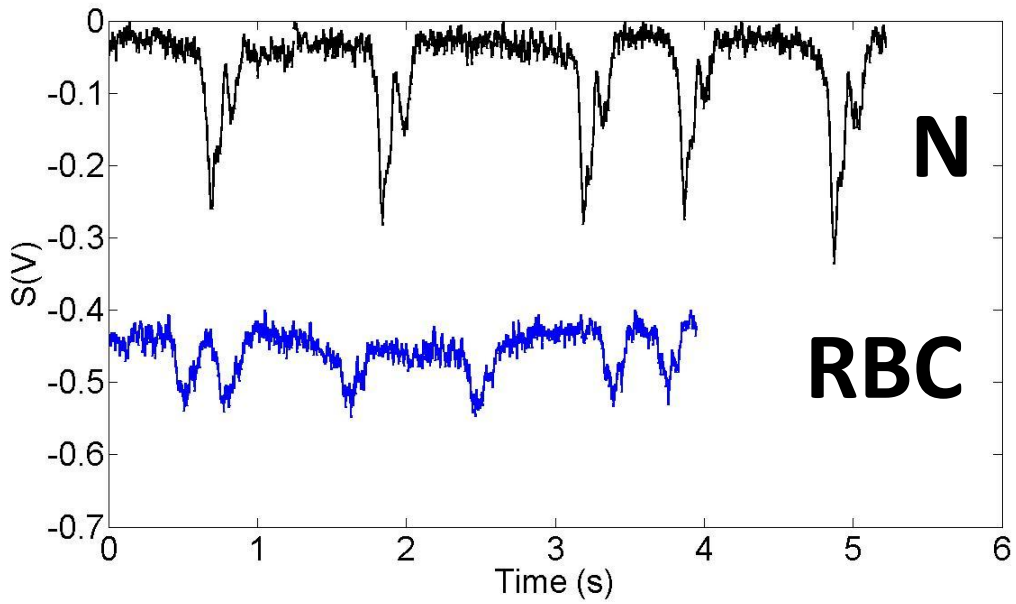


Figure 4-11: Capacitance signatures from five neutrophils and six RBCs subject to an 8 V_{pp} applied DEP voltage and 450 kHz frequency.

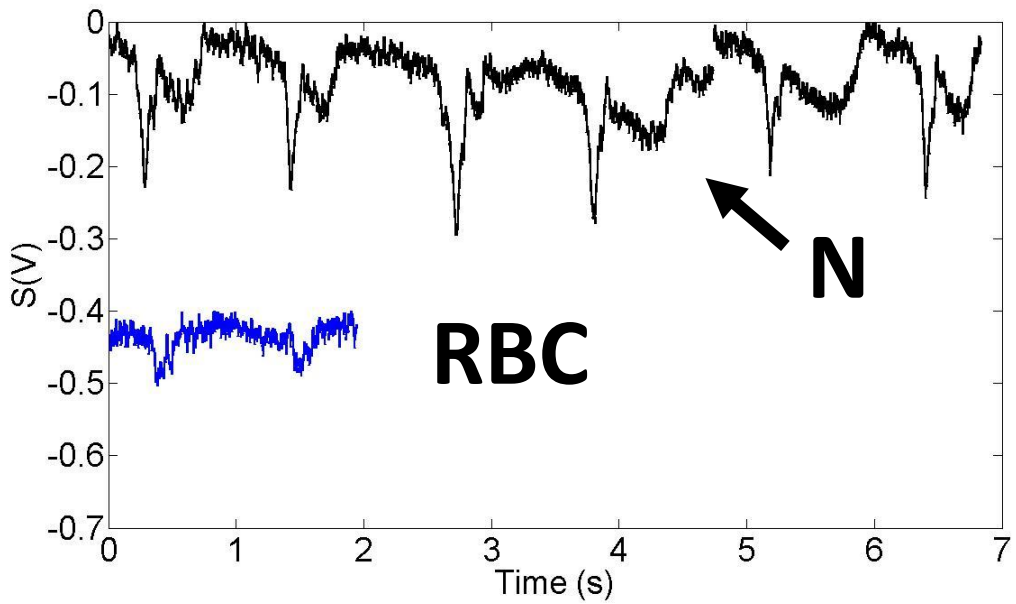


Figure 4-12: Capacitance signatures from six neutrophils and two RBCs subject to a 10 V_{pp} applied DEP voltage and 450 kHz frequency.

As expected, the cell velocity remains constant when no DEP signals are applied (Figure 4-8). Like the case for polystyrene spheres, the induced capacitance signature is large and contains a sequence of peaks and valleys. This indicates that free-flowing cells hover in close proximity to the electrode edges.

For moderate to high DEP signal strengths (1-8 V_{pp}), the repulsion accelerates blood cells through the electrode region. We know this because the time interval between successive peaks progressively decreases during the cell's transition across the electrodes. In addition, the capacitance amplitude progressively decreases. These features confirm that cells experience DEP repulsion from the electrodes into regions of faster fluid flow.

At 10 V_{pp} , small red blood cells have ascended to elevations where they are barely detectable. On the other hand, neutrophil signatures acquire a remarkable shape. After the cells rapidly ascend to the channel ceiling and flow over the central electrode (where the minimum capacitance change occurs), neutrophils experience a clear delay. Unlike PS spheres, which rapidly escape the electrode region after passing the leading edge of the central electrode, neutrophils appear to slowly extend into the second electrode gap. Consequently, the induced capacitance changes occurring after the cell passes the central electrode result from a slow transition across the electrode gap. This can also be observed in video recordings. This contrasts with PS spheres, whose subsequent capacitance changes arise from slowly overcoming the electrical barrier near the leading edge of the central electrode.

In addition, the induced capacitance changes of neutrophils before and after the central minimum have different amplitudes. We believe that subsequent compression of neutrophils may be a possible explanation as the capacitance signatures of rigid PS spheres are essentially symmetrical in amplitude.

For comparison, the capacitance signatures from T-lymphocytes in RPMI-1640 medium were also collected at 9 V_{pp} and 8.5 V_{pp} at 2 MHz frequency (Figures 4-13 and 4-14). In general, the signatures are more symmetric than those from neutrophils, which are of comparable size (neutrophils - 10 μm diameter, T-lymphocytes - 12 μm diameter) and half as rigid. However, T-lymphocytes produce both asymmetric and symmetric signatures (first and second signatures of Figure 4-13). By examining the video from cells that initiate asymmetric signatures, we notice that cells appear to stretch across the gap by a small amount. In Figure 4-15, the T-lymphocyte stretches from 10.8 to 12.3 μm . We can take measurements from video frames with reasonable confidence assuming that the cell flows in the same focal plane while transitioning across the electrode gap. Such cell stretching is likely induced by DEP-induced cell compression (through Poisson's ratio) combined with pressures exerted by fluid flow.

For neutrophils, T-lymphocytes, and mouse fibroblasts (rigid cells, signatures in Figure 4-16), we plot the symmetry of the induced capacitance change versus the entry/exit time ratio (Figure 4-17). To evaluate the symmetry of the capacitance magnitudes, we collect the minimum values in the capacitance signature before (*Min1*) and after (*Min2*) the capacitance null (position "C" in Figure 4-15) occurring above the central electrode. When their ratio equals 1, the amplitudes are equal. The entry and exit times are

evaluated by backstepping and forward stepping in time from position “C”, respectively, until the amplitude at position “C” is reached again. When the entry/exit ratio falls below 1, the cell is delayed. Otherwise, the time progress is unaltered or accelerated. When acceleration is observed, we conclude that no wall contact was made.

From Figure 4-17, we observe that for a given time delay, the exit amplitude decreases by 50-60% for neutrophils, 20-40% for T-lymphocytes, and remains mostly unchanged for mouse fibroblasts. Although the Young’s modulus for 10T½ mouse fibroblasts was not available, the main functionality of fibroblasts is to maintain the structural integrity of connective tissues, which requires the cells to be fairly rigid. From the supporting video, the outliers from the fibroblast data (notably showing apparent 40-50% amplitude variations for 2 cases) appear to arise due to large deviations from spherical symmetry, which can result in significant variations in the capacitance signal (approaching 20%) [123].

For T-lymphocytes, increasing the applied DEP voltage (and hence force) from 8.5 to 9 V_{pp} significantly prolonged the progress of cells across the electrode gap. Essentially, stronger DEP forces strengthen the electrical barrier as well as induce larger friction forces. The capacitance amplitude variations do not vary significantly for a 0.5 V_{pp} increase in applied voltage.

Finally, note that we collect data only from cells flowing exclusively within the central 40 μm of the channel width. Our *flattened semi-circular* cross section (described earlier in Chapter 2) has a flow velocity profile illustrated in the inset of Figure 4-18. At mid-height and mid-width, the velocity achieves a maximum rate, as expected for laminar

flow. Within the central 40 μm of the channel width, the flow velocity varies up to 8% across the width depending on particle elevation. This percentage rises significantly with increasing distance, beyond the central width, toward the side wall (Figure 4-18).

Furthermore, when cells flow along the side walls of the channel, subsequent DEP-actuation propels them not only upward but funnels them toward the channel center, which greatly influences the capacitance signature (Figure 4-19). Since we are mainly interested in cell movement along the channel depth and height, with electric fields parallel to the channel length, we discard signatures caused by cell movement along the channel width.

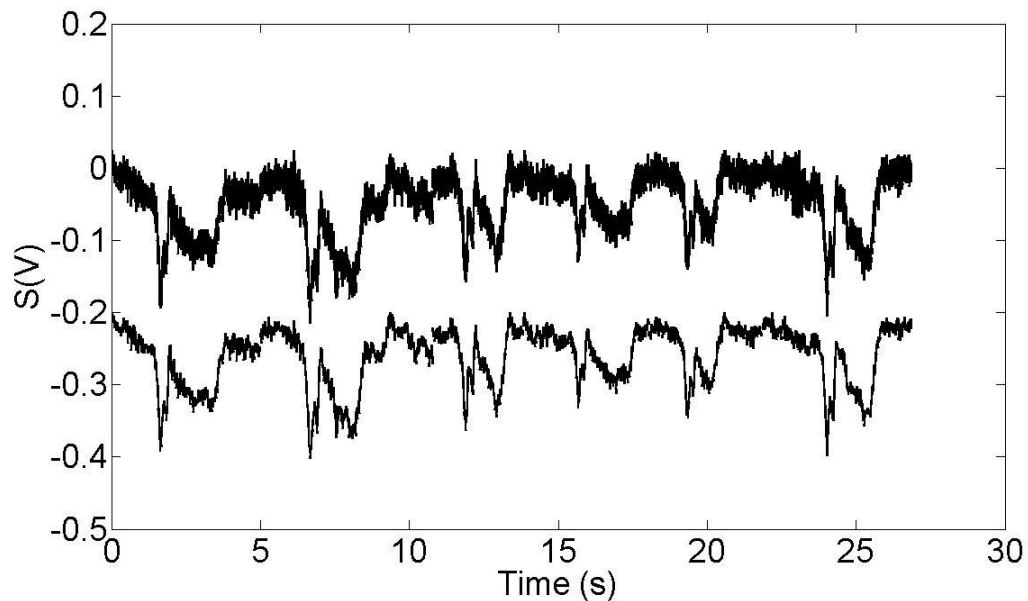


Figure 4-13: Capacitance signatures from 6 flowing T-lymphocytes experiencing strong nDEP forces from a 2 MHz, 9 V_{pp} DEP signal. The data are represented twice as the original raw data and smoothed (over 10 points) data. These data, which are quite typical, are chosen by literally taking the first 6 signatures generated by single cells flowing through the central third of the channel width. All data were taken within a 5-minute time interval wherein the fluid flow remained well controlled.

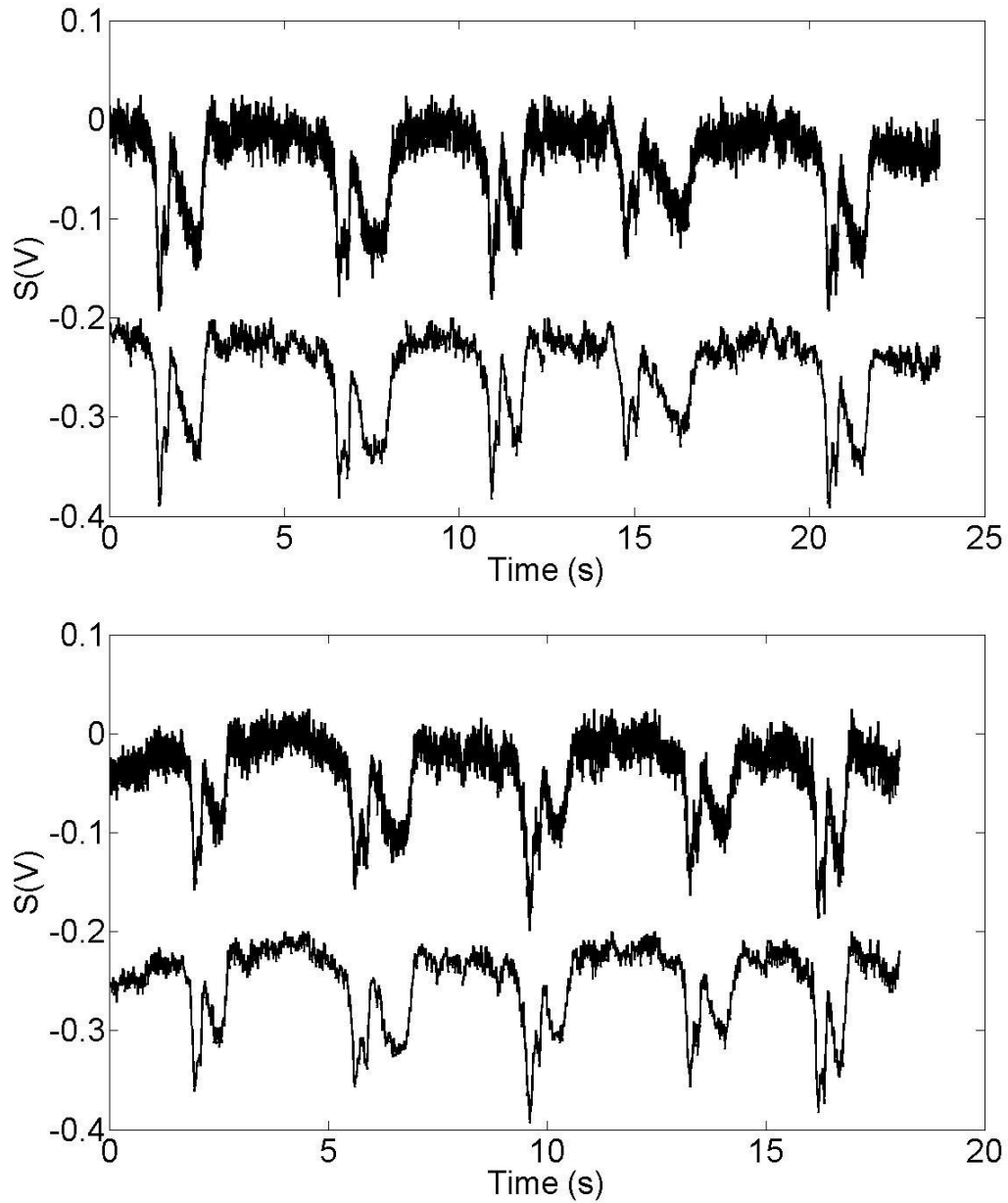


Figure 4-14: Capacitance signatures from 10 flowing T-lymphocytes experiencing strong nDEP forces from a 2 MHz, 8.5 V_{pp} DEP signal. The top graph shows the first 5 signatures and the bottom graph shows the remaining 5 signatures. In each graph, the data are represented twice as the original raw data and smoothed (over 10 points) data. These data, which are quite typical, are chosen by literally taking the first ten signatures generated by single cells flowing through the central third of the channel width. All data were taken within a 5-minute time interval wherein the fluid flow remained well controlled.

OBSERVATION OF T-LYMPHOCYTE STRETCHING

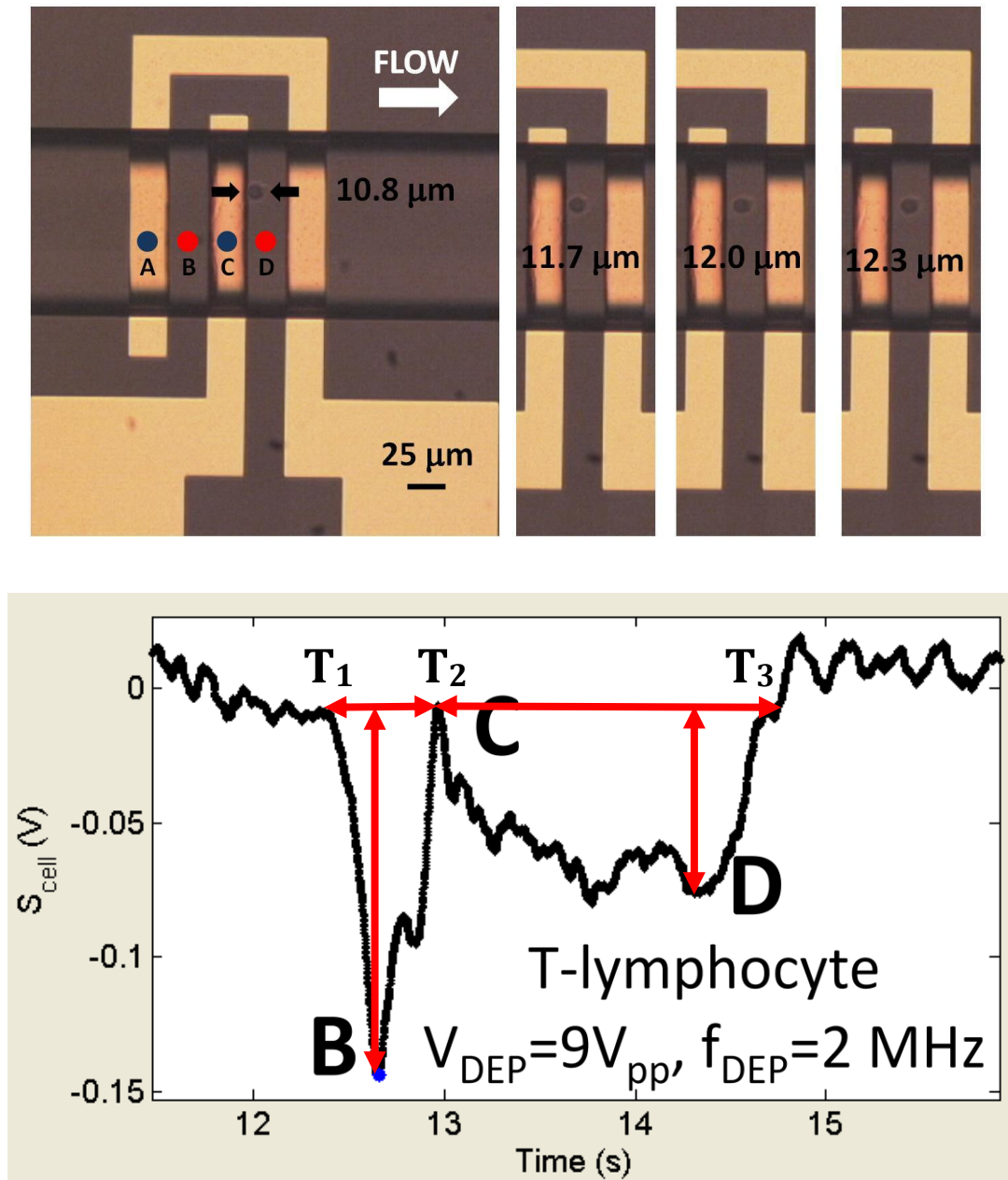


Figure 4-15: **Top:** Observation of T-lymphocyte stretching from 10.8 to 12.3 μm during its transition across the electrode gap. The applied DEP voltage is 9 V_{pp} at 2 MHz. **Bottom:** Capacitance signature corresponding to the entire transition of the cell across the electrodes. Smaller capacitance changes are observed as the cell traverses the second electrode gap (where the compression occurs). Note that this cell exhibits more deformability than what is typically observed in T-cells.

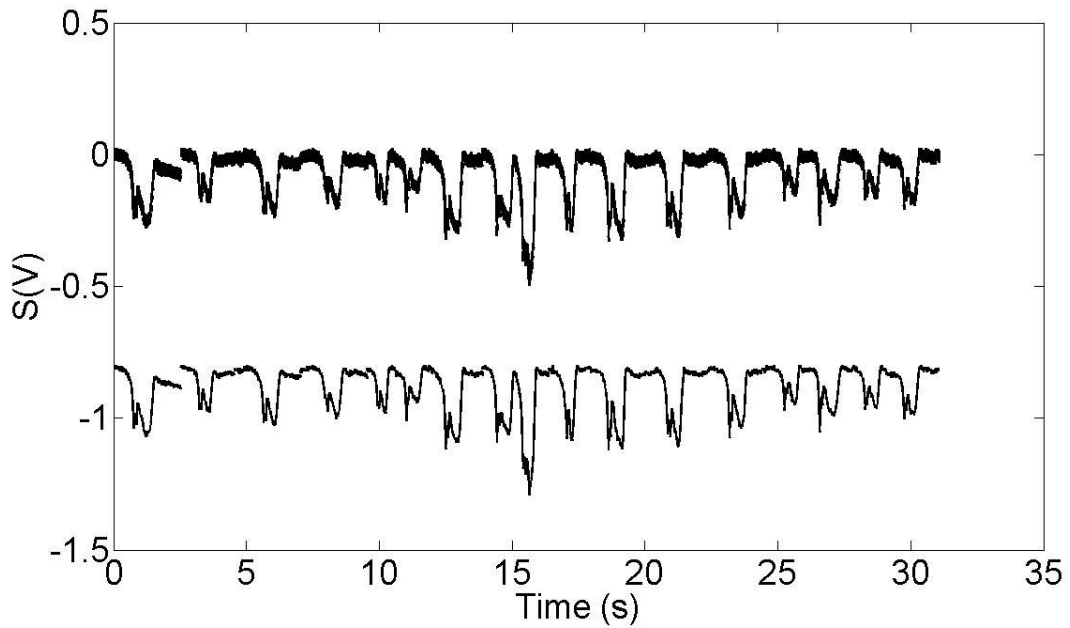


Figure 4-16: Capacitance signatures from $10T\frac{1}{2}$ mouse fibroblasts DEP-actuated with an $8 V_{pp}$, 1 MHz signal.

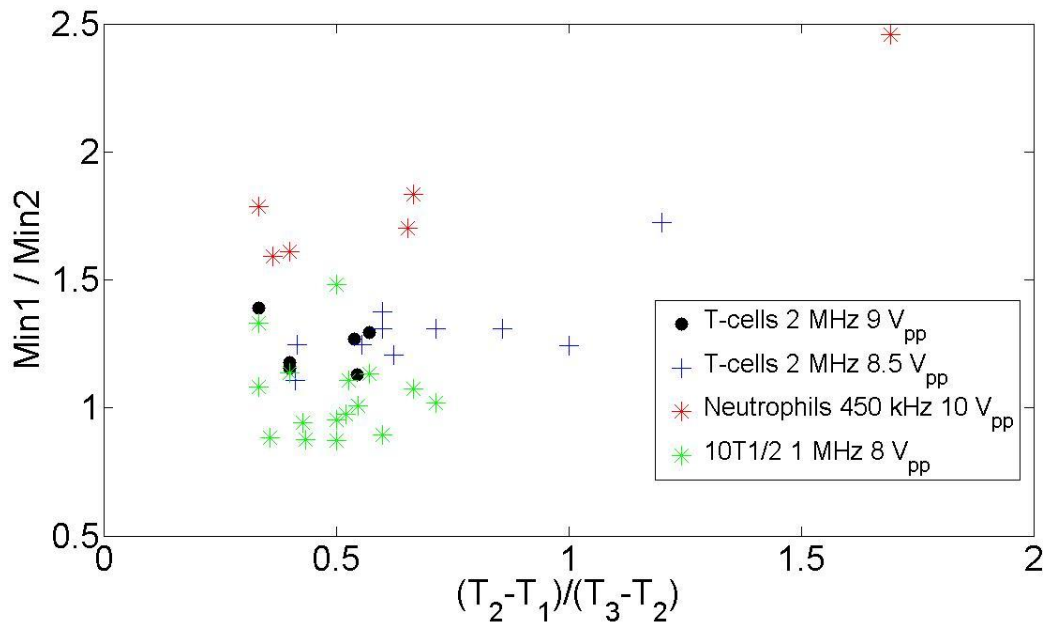


Figure 4-17: Symmetry of capacitance change versus the entry/exit time ratio of biological cells interacting with the channel wall. Note that the $10T\frac{1}{2}$ cells are approximately twice the diameter of the T-cells and neutrophils.

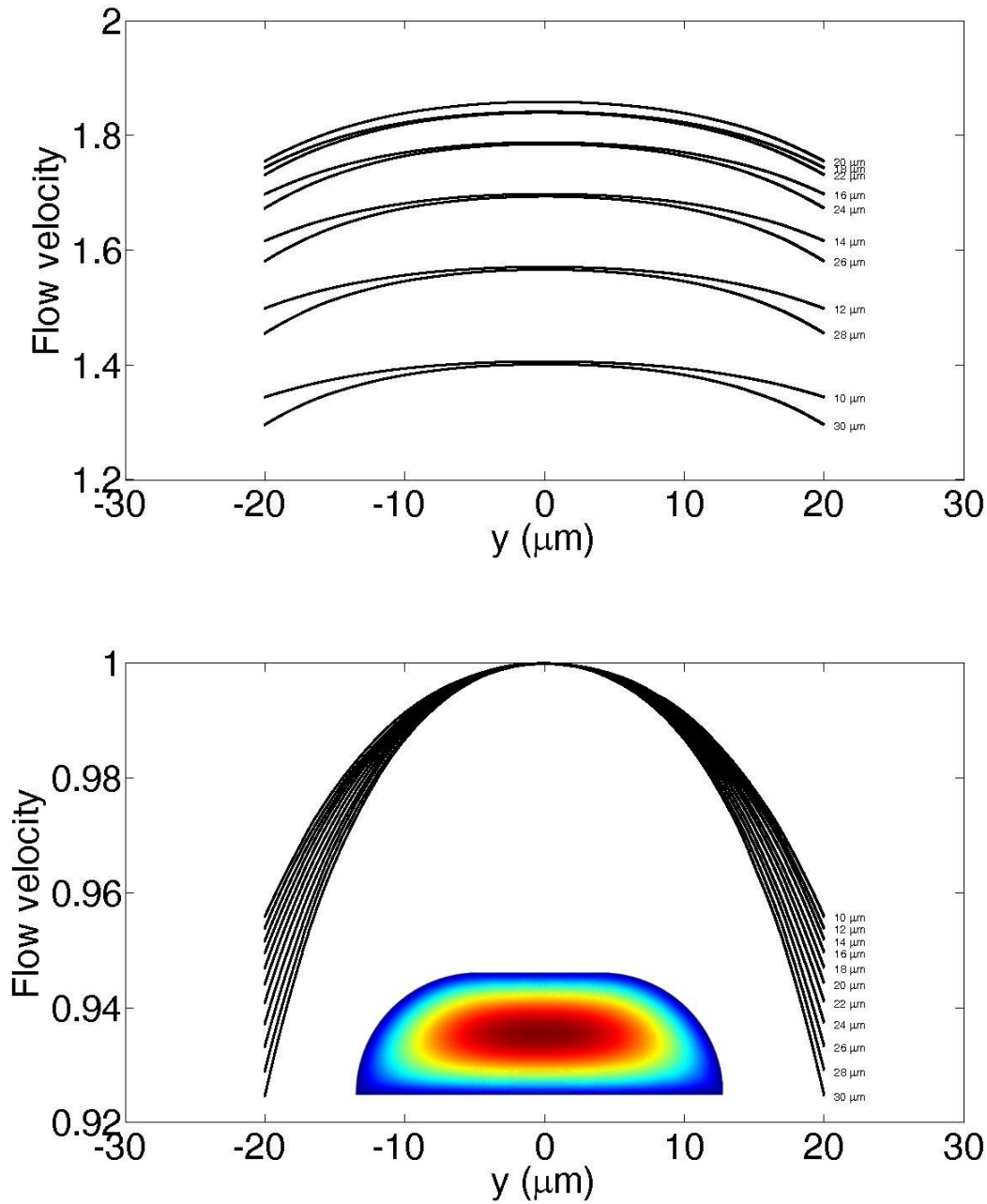
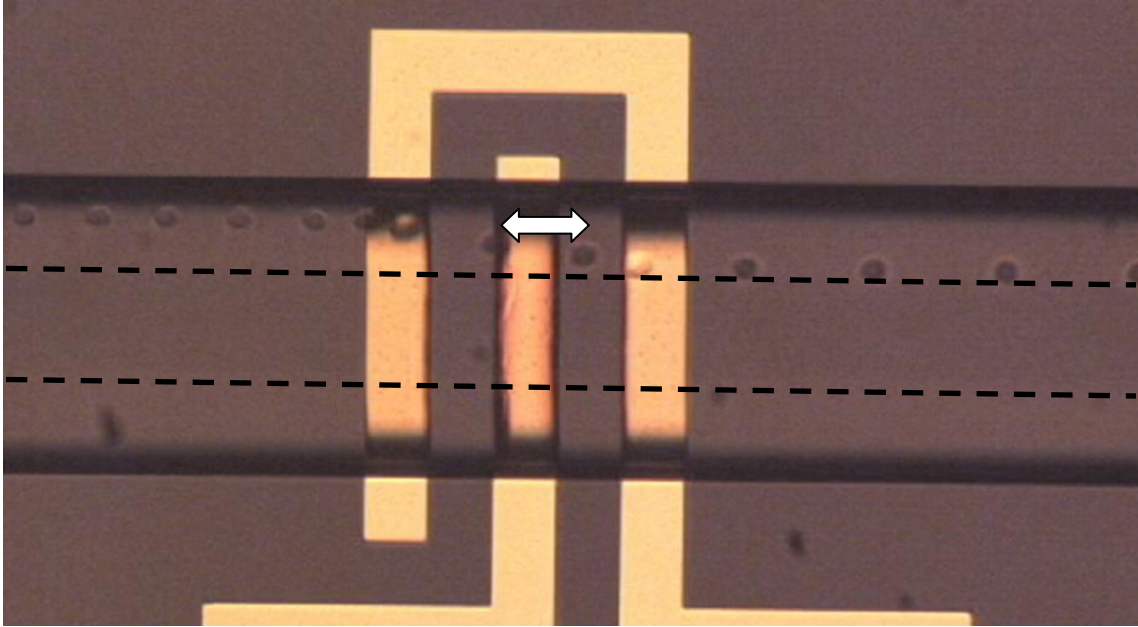


Figure 4-18: **TOP:** z-directed fluid velocity across the central 40 μm of channel width for varying elevations ($x=10, 12, 14 \dots 26, 28, 30 \mu\text{m}$). At mid-height (20 μm), the velocity achieves a global maximum at $y=0$, as expected. At all elevations, the velocities at $20+\Delta x$ and $20-\Delta x$ elevations are equal at $y=0$, but begin to deviate across the width due to the curvature of the cross section. **BOTTOM:** Largest deviations (nearly 8% of $y=0$ value) occur near the channel ceiling. Data are normalized to the maximum velocity (occurring at $y=0$) at the given elevation. Inset: Colour plot of velocity profile in channel cross section.



Activated T-cells March 26 – 3-26-2010 – 15hr22min0sec.CSV

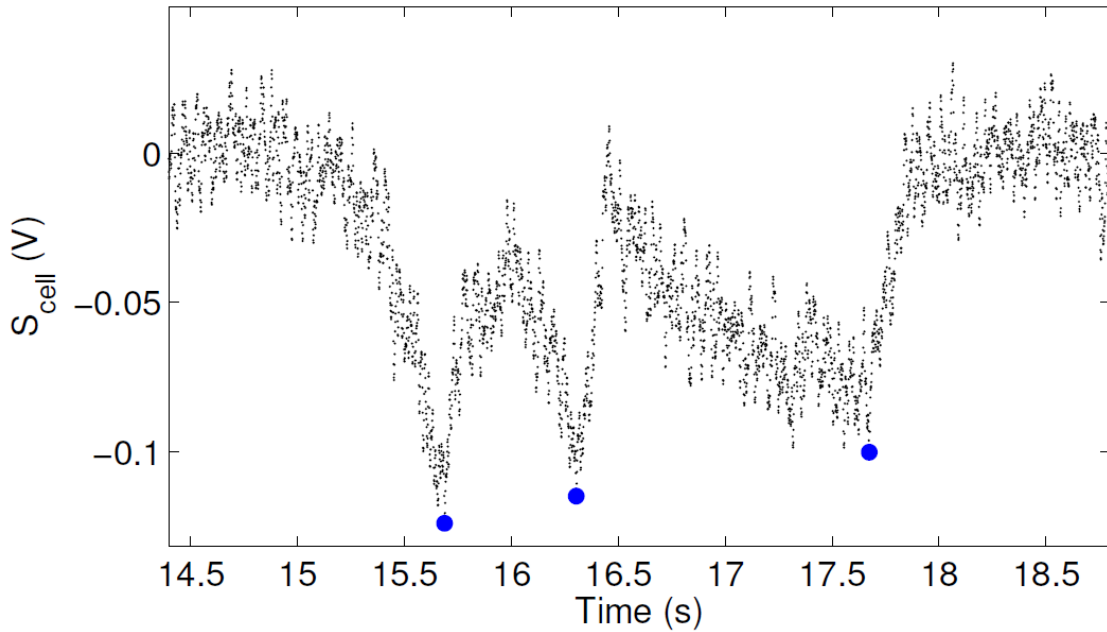


Figure 4-19: *TOP*: Time progression of a T-lymphocyte initially flowing near a channel side wall. The strong DEP force repels the cell, which then encounters the circular ceiling, which funnels the cell toward the channel center. The specific time interval shown by the arrow is 15 frames. All other cells are plotted every 5 frames (0.067 s per frame). Analyses consider cells flowing exclusively within the central third of the channel as indicated by dashed lines. *BOTTOM*: Corresponding capacitance signature.

4.12.2 Surveying the detection of structurally polarized T-lymphocytes

The capacitance signatures from *structurally polarized* T-lymphocytes activated using anti-CD3/CD28 antibodies (see Appendix C for preparation) reveal clear differences in the signal amplitudes of free-flowing and DEP-actuated cells. Free-flowing “de-activated” spherical T-cells generate clear peaks and valleys, which are “washed-out” in the case of free-flowing “activated” T-cells (Figure 4-20).

The orientations of activated T-cells also influence the capacitance signatures (Figure 4-21). For free-flowing activated T-cells of similar volume, subtle differences in their entrance orientation can lead to “Jeffery orbits” [124], which can diminish the overall capacitance signals [123]. In Figures 4-20 and 4-21, flowing particles are shown above the three electrode widths to reveal their shape and orientations at those positions.

Figures 4-22 and 4-23 reveal the influence of applying large DEP signals to actuate paired T-lymphocytes and single polarized T-lymphocytes, respectively. In both cases, the DEP signal realigns the long axis parallel to the applied field. After cell re-orientation and exit from the electrode region, they continue to rotate “end over end” due to large non-uniformities in fluid velocity near the channel ceiling. Therefore, in this work, only spherical cells were chosen for analysis to avoid the effects observed by polarized cells.

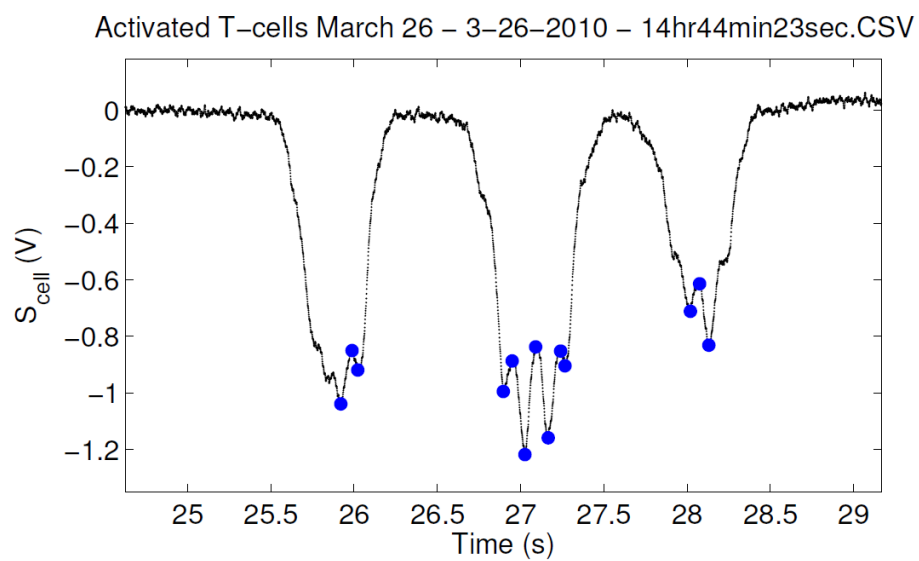
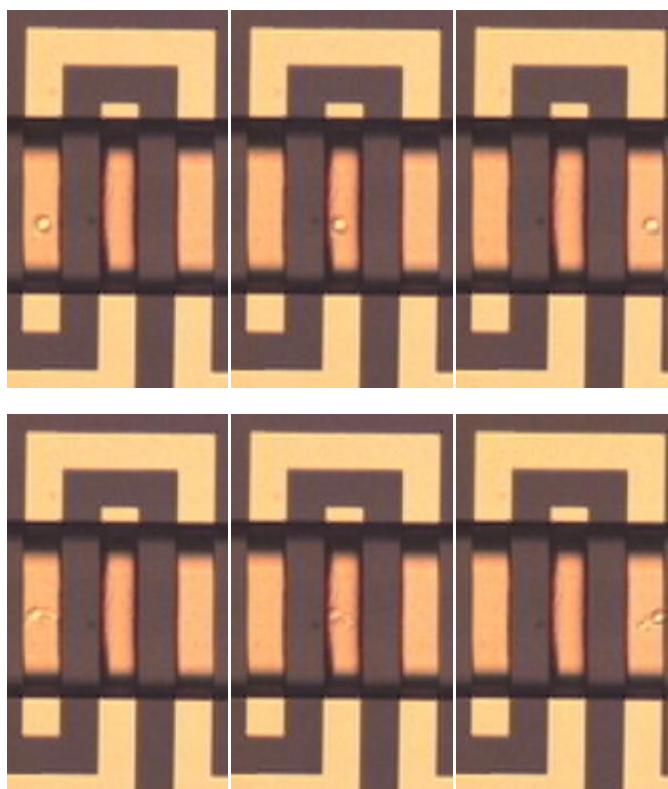


Figure 4-20: The capacitance peaks and troughs from rotating polarized T-cells (1st and 3rd signatures) are less defined in comparison with those generated by unpolarized or non-rotating polarized T-cells (2nd signature).

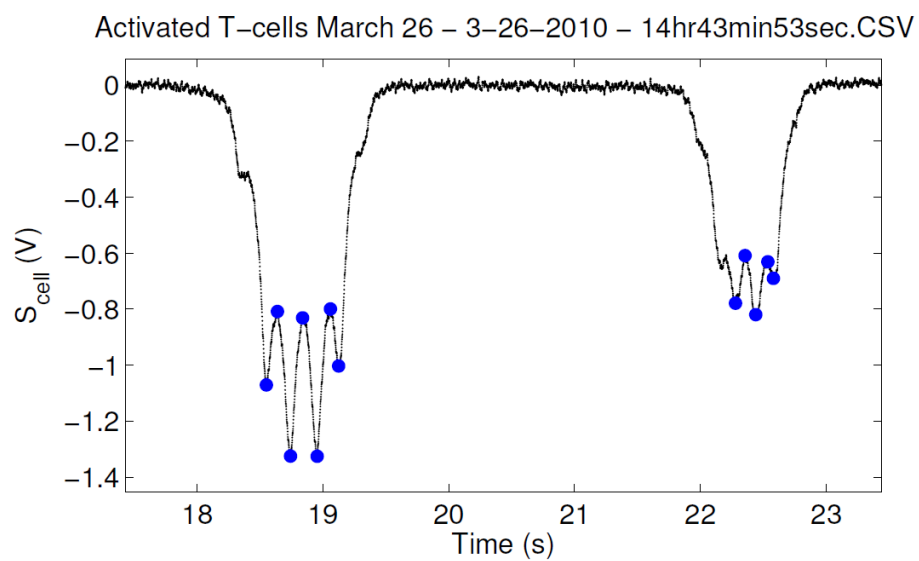
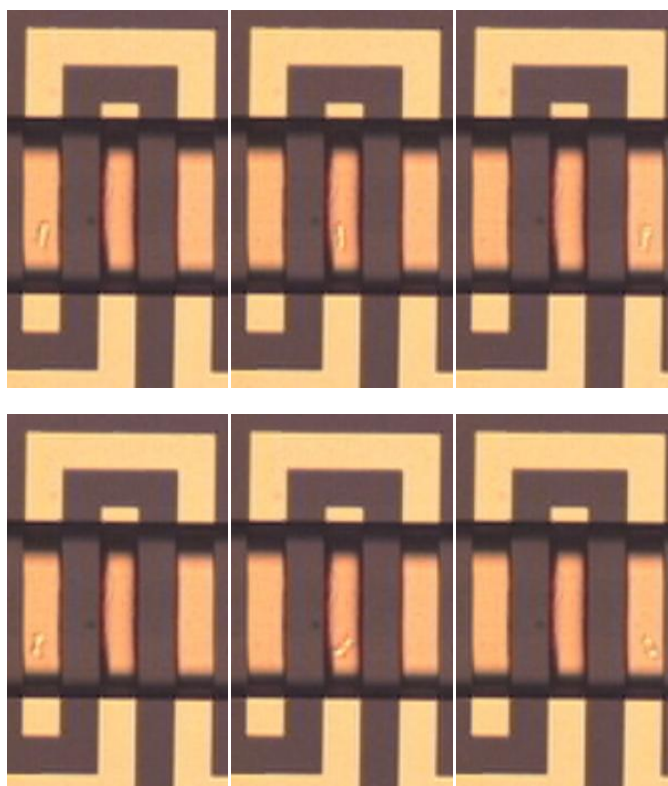


Figure 4-21: Free-flowing polarized T-cells that remain parallel with the electrodes during flow generate larger signals than polarized T-cells of similar volume that rotate with a larger “Jeffrey orbit”.

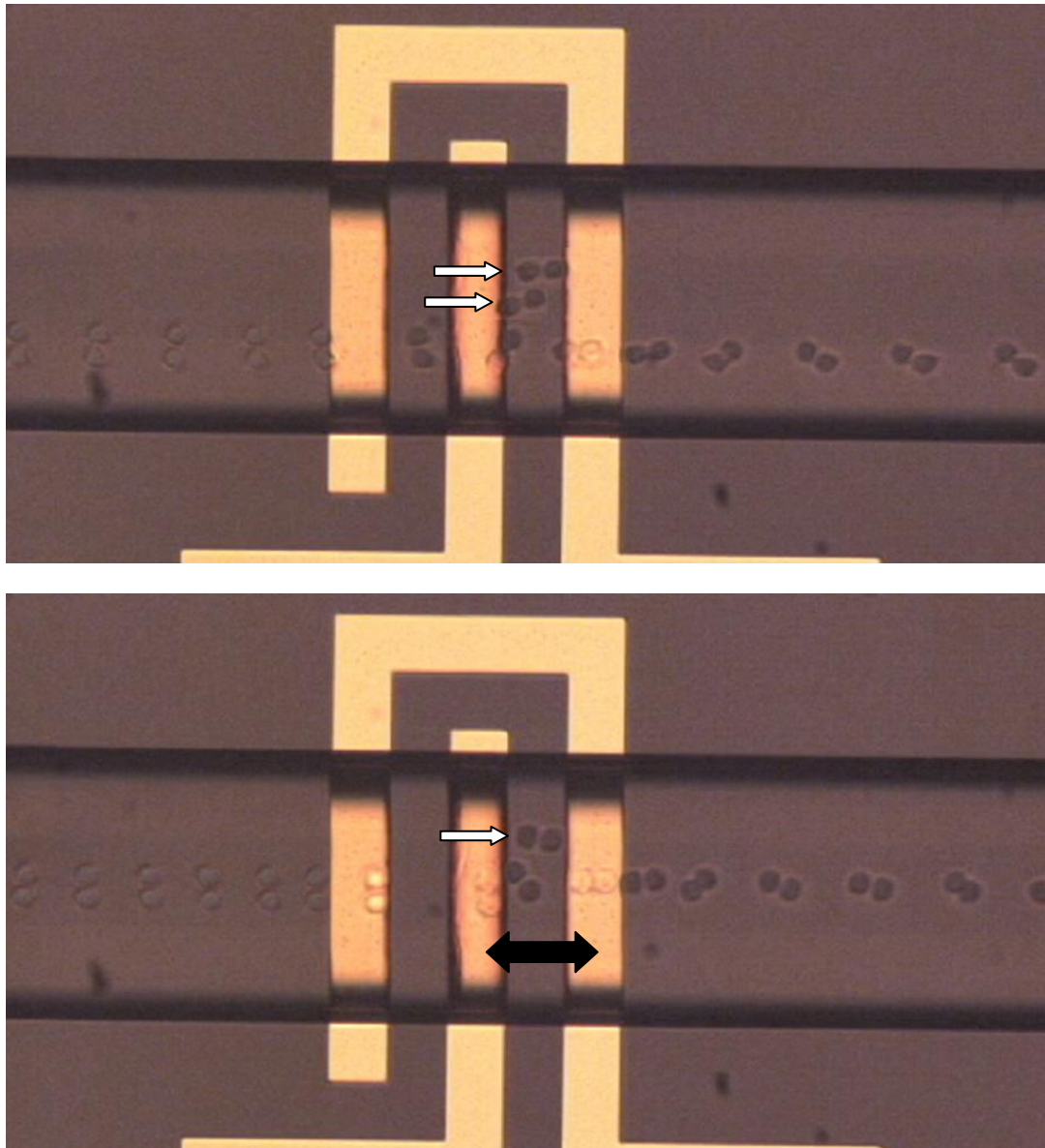
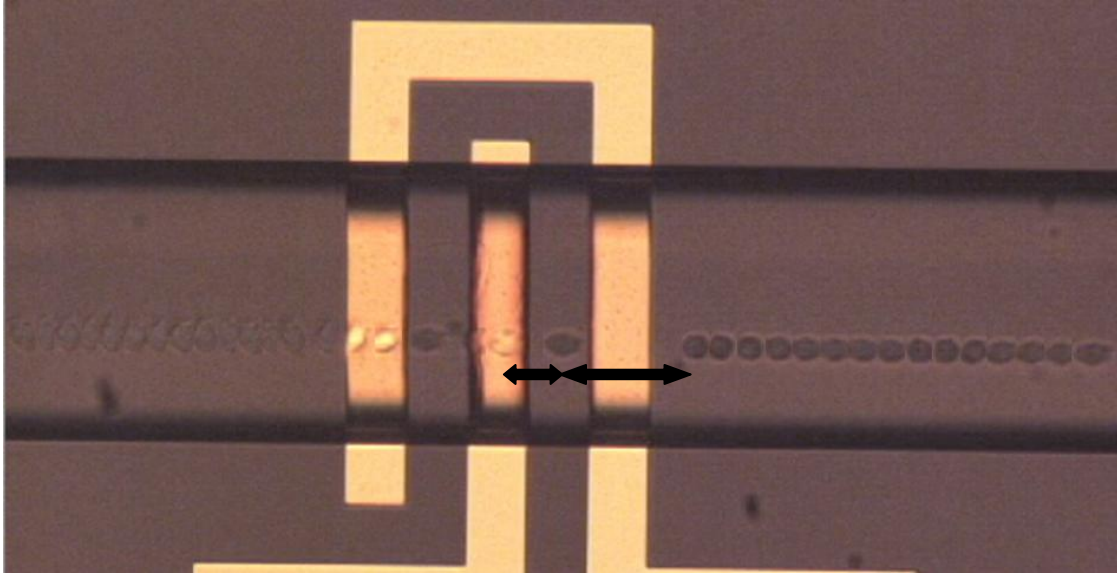


Figure 4-22: Time progression of paired T-lymphocytes experiencing strong negative DEP as they flow left to right over the electrodes. The cell-pair are plotted every 3 frames (0.067 s per frame). During nDEP, the cell-pair is reoriented parallel to the electric field direction. The cell-pair spends a significantly long time in the compression zone (second electrode gap). Consequently, for simplicity of viewing, the cells are artificially translated upward for some time steps (arrows). TOP: 8.5 V_{pp} , 2 MHz DEP signal. BOTTOM: 9 V_{pp} , 2 MHz DEP signal. The cells required 24 (12+6+6) frames to transition the compression zone (black arrow).



Activated T-cells March 26 – 3-26-2010 – 15hr25min31sec.CSV

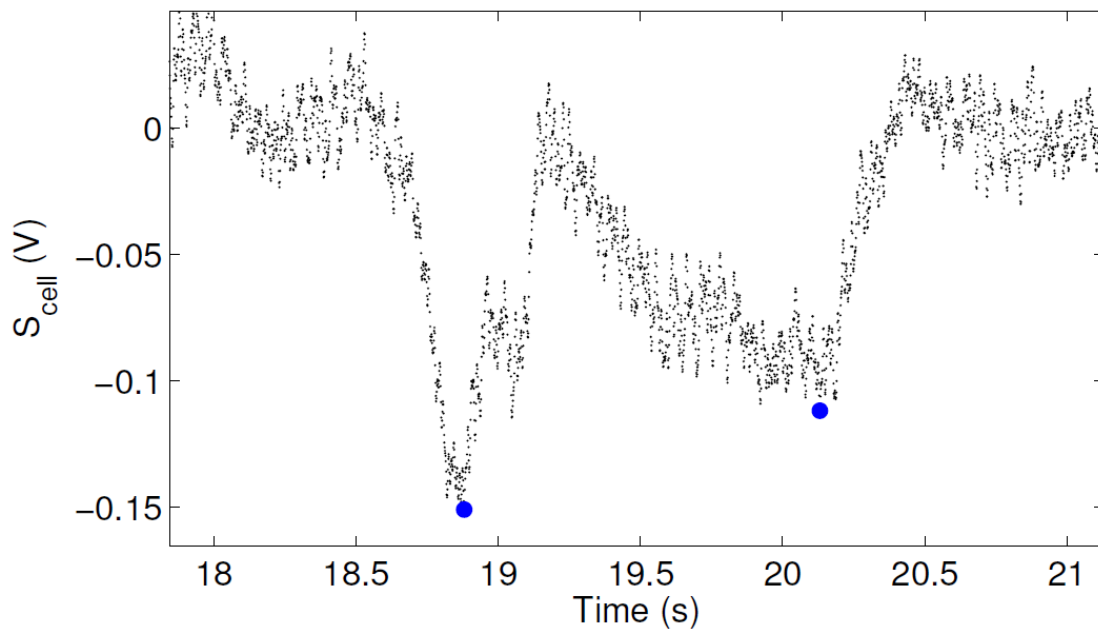


Figure 4-23: Time progression of a polarized T-lymphocyte experiencing strong negative DEP forces (9 V_{pp}, 2 MHz signal) as it flows left to right over the electrodes. The arrowed transition times are 11 frames each. For all other cases, the cell is plotted every frame (0.067 s per frame). Much like the paired lymphocytes, the cell reorients its long axis parallel to the electric field direction. After passing through the electrodes, the cell continues to flip end-over-end.

4.12.3 Simulated neutrophil signatures

Simulated cell trajectories were determined by solving the equation of motion using COMSOL Multiphysics, as outlined in §2.4.2. Electrothermal forces, as explained later in §4.13.3, may influence fluid flow and are therefore included in the calculation. The cell is assigned an initial velocity and position. The initial velocity is estimated from experimental traces while an equilibrium elevation is determined by equating the hydrodynamic lift- and gravitational forces. Particle positions are evaluated every 20 μs to ensure that solution convergence is achieved.

The average measured T-lymphocyte and neutrophil diameters are approximately 12 and 10 μm , respectively, and their density ranges are 1060-1080 kg/m^3 , and 1080-1090 kg/m^3 , respectively [125], [126], [127]. For the simulation of DEP-actuated neutrophils ($V_{\text{DEP}}=1, 2, 8$ and $10 V_{\text{pp}}$, frequency=450 kHz, and CMF=-0.5), the cell radius, cell viscosity, and average fluid velocities are $r = 5 \mu\text{m}$, $\rho = 1080 \text{ kg}/\text{m}^3$, and $\langle v \rangle = 333.33 \mu\text{m}/\text{s}$, respectively.

Figure 4-24 shows the vertical vs. horizontal neutrophil position. Note that the electrodes span the range, $-62.5 \mu\text{m} \leq x \leq 62.5 \mu\text{m}$. For high DEP voltages (8 and $10 V_{\text{pp}}$), the cell elevates rapidly upon encountering the first electrode edge. The repulsive DEP forces are adequate to initiate cell contact with the channel wall. The $1/(y-r)$ dependence of the lift force ensures that the maximum elevation occurs when the cell is exactly 1 radius away from the ceiling. At an elevation of $y=15 \mu\text{m}$, our point particle of radius 5 μm is touching the channel ceiling ($y=20 \mu\text{m}$). Larger DEP forces prolong the transition time across the electrodes.

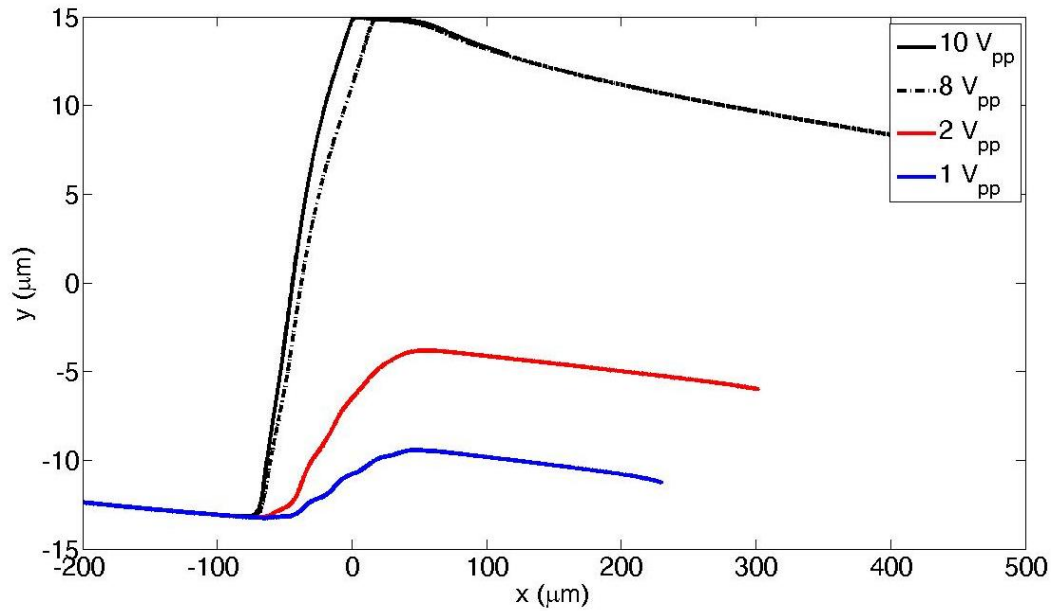


Figure 4-24: Neutrophil cell elevation vs. horizontal channel position. Note that the electrodes span the range, $-62.5 \mu\text{m} \leq x \leq 62.5 \mu\text{m}$.

At lower applied voltages (1 and $2 V_{pp}$), the cell begins to elevate within the electrode region toward moderate elevations where the fluid flows are faster. Consequently, cells accelerate through the electrode region. In all cases, after exiting the electrode region, the gravitational force takes over and the elevation decreases steadily.

To understand the time dependence, the horizontal and vertical positions are plotted versus time in Figure 4-25. For the larger voltages, the cell experiences an obvious deceleration upon encountering the electrode edge. Afterward, the cell is rapidly repelled upward into contact with the ceiling after which the fluid flow competes with the dielectrophoretic barrier. Again, larger DEP voltages prolong the journey. At lower voltages, the cell accelerates more rapidly through the electrode region when repelled

into faster fluid flows. Since the cell is repelled into elevations nearer the mid-channel height at $2 V_{pp}$ (compared with $1 V_{pp}$), the cell accelerates more rapidly at $2 V_{pp}$.

To understand what forces are required to repel cells into contact with the ceiling, we plot the DEP vertical force vs. time in Figure 4-26. Neutrophils appear to barely make contact at $8 V_{pp}$, in which the maximum DEP vertical force is about 18 pN. The largest DEP forces experienced by cells occur at their lowest elevations. As they are repelled, they feel progressively less repulsion. Upon contact, the DEP force plateaus at approximately 7 pN at $10 V_{pp}$. At the lower voltages, the rippling in the force plot occurs because cells are low enough to experience the local electric fields from the electrode edges. Finally, we can plot the capacitance change versus time to gain a point of comparison for the experimental Figures 4-9 to 4-12.

The simulated and experimental signatures compare favourably. Indeed, at $10 V_{pp}$, they both capture the prolonged transition time. The relative magnitudes of the signals are quite close. The maximum capacitance signals induced by cells at 8 and $10 V_{pp}$ are nearly equal in the simulated and experimental traces, with $10 V_{pp}$ forcing longer transit times. Cells experiencing $2 V_{pp}$ signals induce smaller capacitance changes, and flow through the electrode region faster than cells repelled by $1 V_{pp}$ signals.

The main observable difference lies in how the $10 V_{pp}$ signatures vary locally after the capacitance null (e.g., position C in Figure 4-15). The experimental traces of actuated neutrophils often exhibit a capacitance plateau following the capacitance null. According to video evidence, the corresponding cells appear to make intimate contact with the channel ceiling and slowly progress and deform across the electrode gap.

When the deformation is less obvious, the signatures generally coincide with the patterns of the simulated trace, where the induced capacitance changes following the capacitance null exhibit a clear slope.

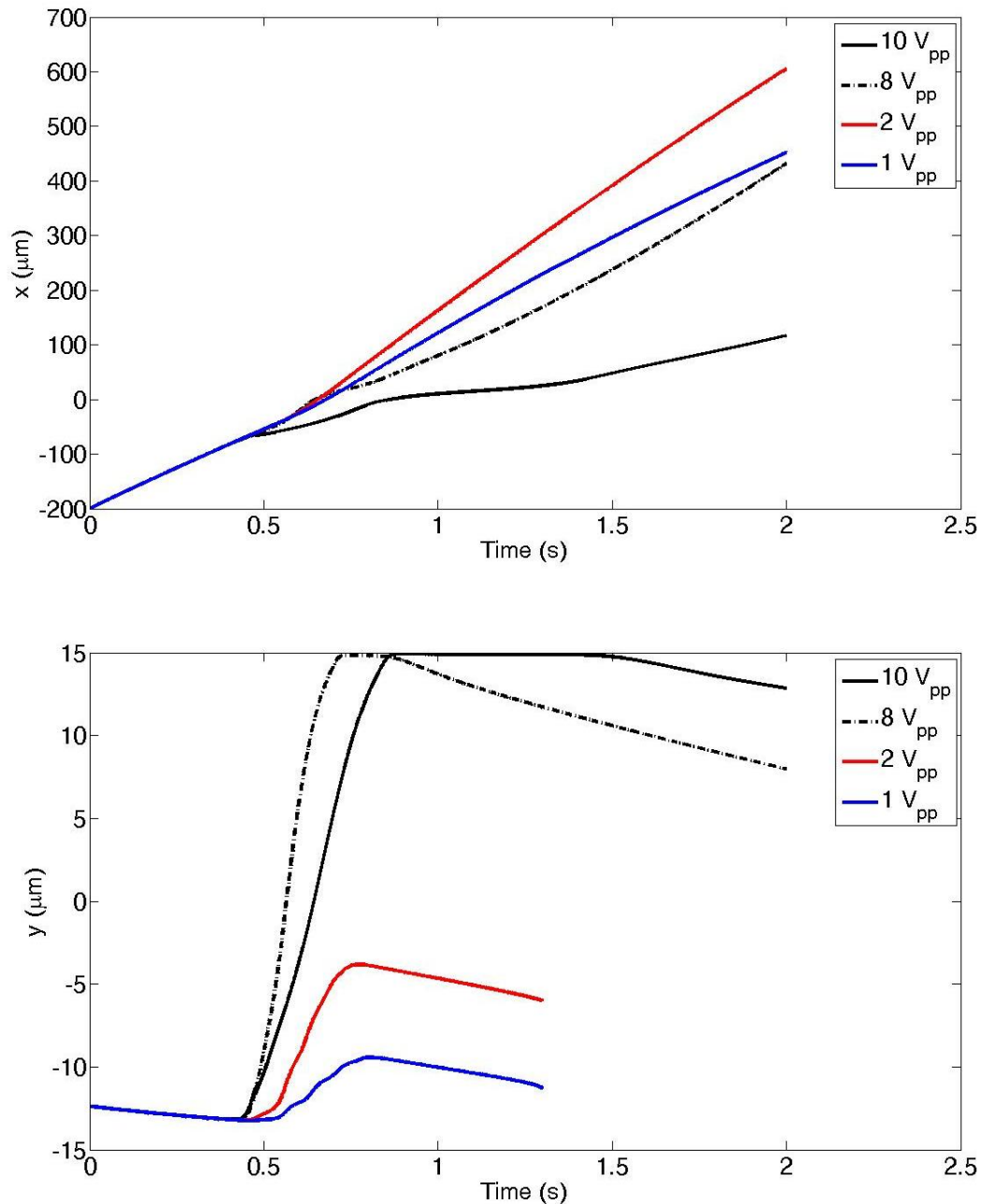


Figure 4-25: Neutrophil cell position vs. time ($V_{DEP} = 1, 2, 8, 10 V_{pp}$) Top: Position along channel. Bottom: Cell elevation.

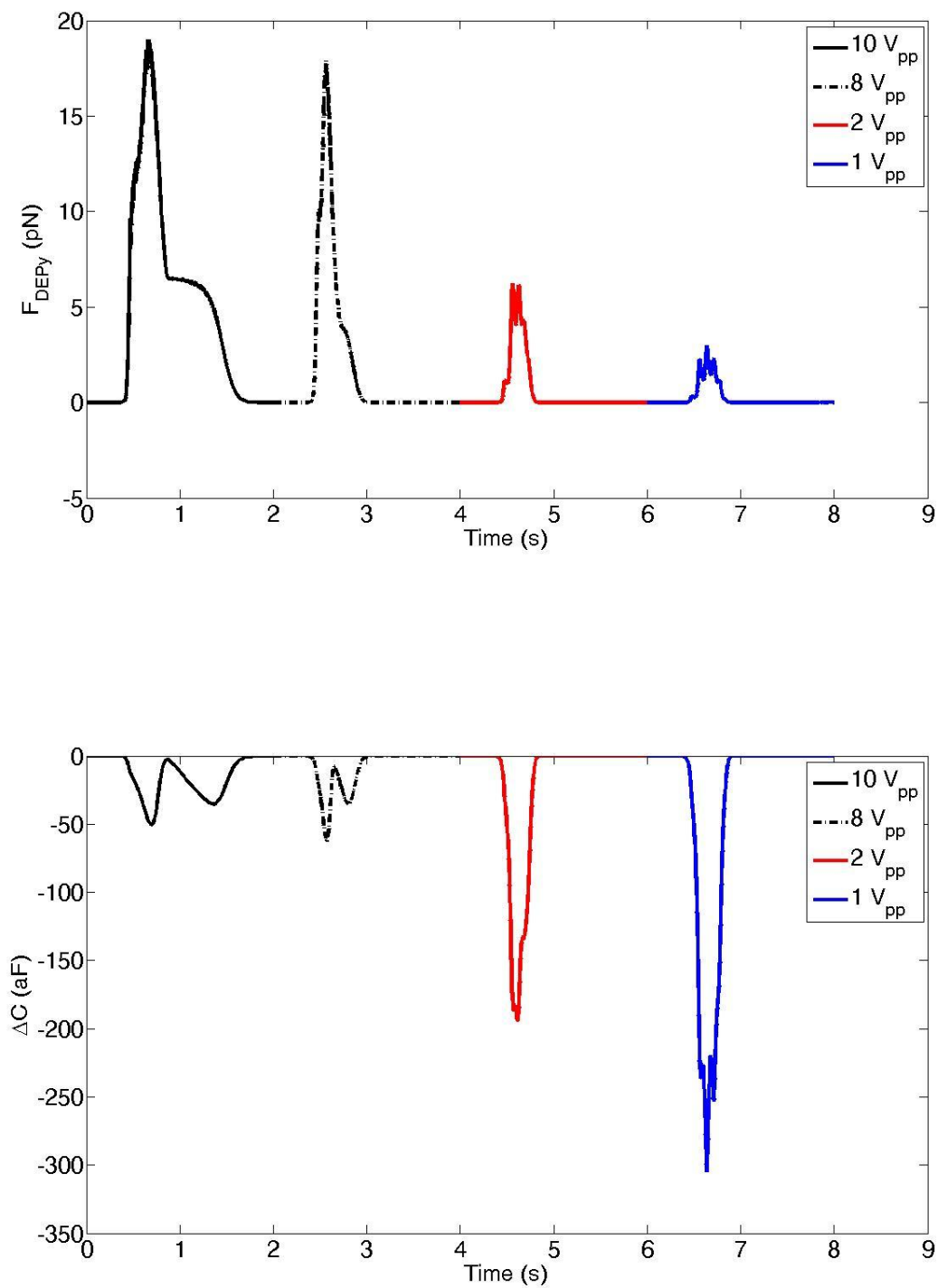


Figure 4-26: Vertical DEP forces (top) and induced capacitance changes (bottom) of DEP actuated neutrophils. The DEP voltages are 1, 2, 8, and 10 V_{pp}.

4.13 Influence of Electroporation and Electrokinetic Mechanisms on the Flow of Biological Cells Across Interdigitated Electrodes in Microfluidic Channels

When biological cells interact with electric fields in microfluidic systems, they potentially experience a number of electrokinetic mechanisms, many of which are highlighted in excellent reviews [128], [129], [130], [131], [132]. We will first cover dielectrophoresis and electroporation, which are two electrical mechanisms that act directly on cells. Afterward, we will discuss electro-thermal and electro-osmotic flows, which are electrically-induced fluid flows that may indirectly cause particle motion.

4.13.1 Dielectrophoresis

Dielectrophoresis is the dominant mechanism for electrical actuation of biological cells at MHz frequencies in high-conductivity media. Strong non-uniform electric fields repel biological cells into contact with the ceiling and exert a distribution of DEP forces as each cell translates across the electrodes.

At various elevations, the horizontal and vertical DEP forces are calculated across the electrode region in Figure 4-27. The dielectric parameters of a CHO cell are used in the calculation ($r=7.5 \mu\text{m}$, and $\text{CMF}=-0.4$ at 1 MHz). Positive vertical DEP forces indicate that the particle is directed exclusively upward, and away from the electrodes. Although the vertical forces are stronger, the horizontal forces additionally exert inward directed forces that facilitate particle containment above the central electrode.

This is clear when we consider for a moment the central region (approximately $-37.5 \mu\text{m} \leq x \leq 37.5 \mu\text{m}$), which covers the central electrode and the electrode gaps. For all elevations, negative (leftward directed) horizontal DEP forces are experienced at positive values of x (horizontal locations to right of center), and vice versa. Outside this central region, the horizontal forces change sign, and resist the flow of incoming cells.

Strong electric fields can cause the deformation of soft cells. This deformation, Δy , may be calculated using a Hertz model [133] for small deformations of elastic objects:

$$F(\Delta y) = -\frac{2E\sqrt{R}}{3(1-\delta^2)} \cdot \Delta y^{3/2} \quad (4-3)$$

where E is Young's modulus, R is the cell radius, and δ is the Poisson ratio. Assuming $E = 1572 \text{ Pa}$, $\delta = 0.5$, and $R = 7.5 \mu\text{m}$, the horizontal and vertical deformations occurring across the electrode gap are calculated in Figure 4-28 at elevations above mid-height. As expected, the largest deformations are vertical, which correspond to the larger vertical DEP forces. CHO cells ($R = 7.5 \mu\text{m}$) subject to an $8 V_{\text{pp}}$, 1 MHz DEP signal will experience a maximum theoretical vertical deformation of only $\sim 60 \text{ nm}$. However, neutrophils ($R = 5.0 \mu\text{m}$, $E = 27.5 \text{ Pa}$), which are subject to slightly elevated DEP signal strengths ($10 V_{\text{pp}}$, 450 kHz) can deform up to 500 nm (Figure 4-29), and larger cells deform to greater extents (if $R = 6.0 \mu\text{m}$, $\Delta y = 750 \text{ nm}$). Such deformations are comparable to those observed through video microscopy (Figure 4-15). Although Equation 4-3 assumes instantaneous deformation, recall that the choice of Young's modulus for each cell type was made based on the time scale over which the cell was deformed (§4.3). That is, the time scale of deformation depends on the Young's modulus, which strongly depends on frequency in viscoelastic materials such as cells.

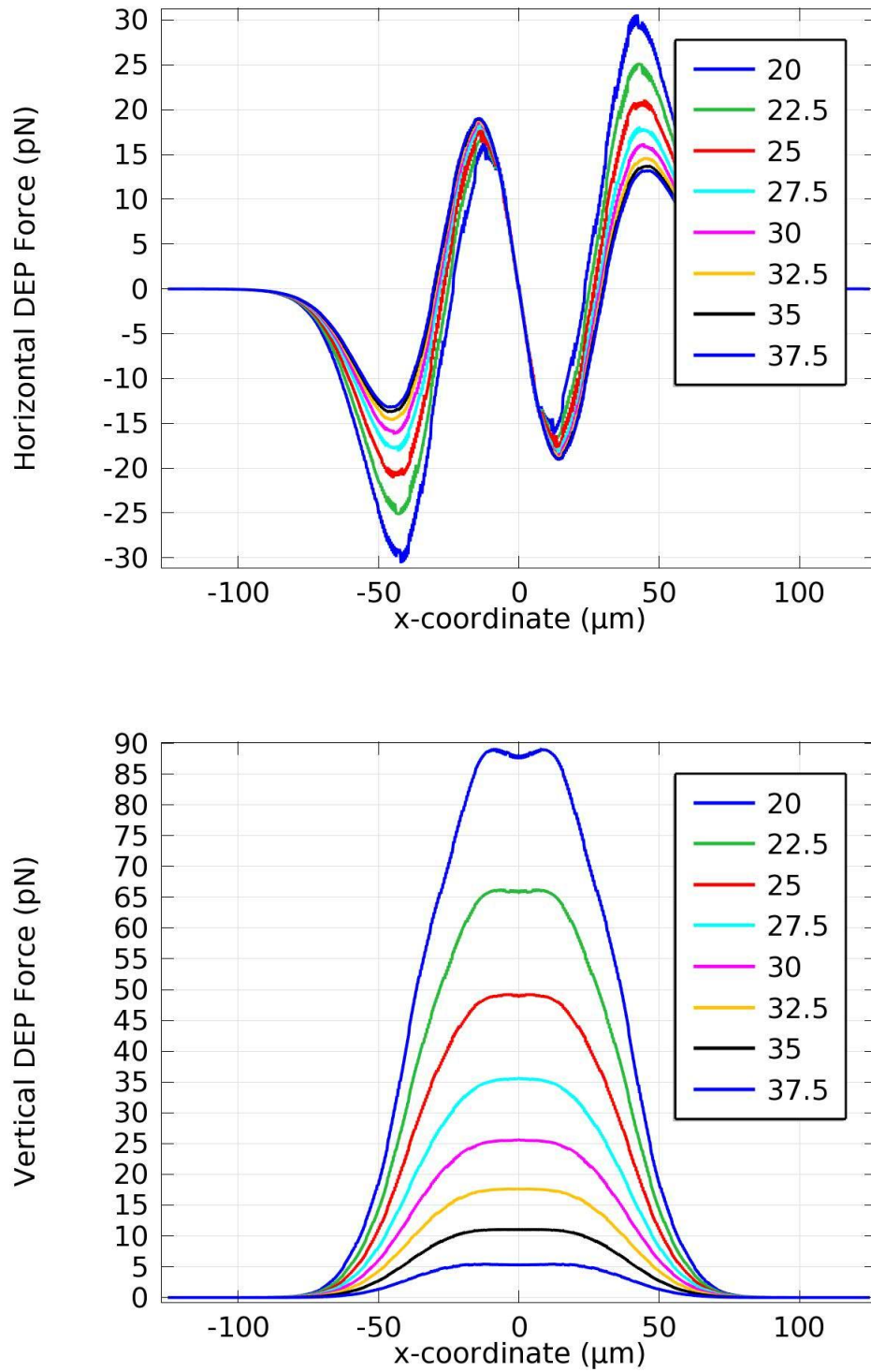


Figure 4-27: Simulated tangential (E_x) and normal (E_y) DEP forces on a 15- μm -diameter CHO cell at various elevations (20 to 37.5 μm - i.e., from mid-channel to 2.5 μm from the ceiling) above the electrode region ($-62.5 \mu\text{m} < x < 62.5 \mu\text{m}$). The applied voltage was 8 V_{pp} at 1 MHz frequency.

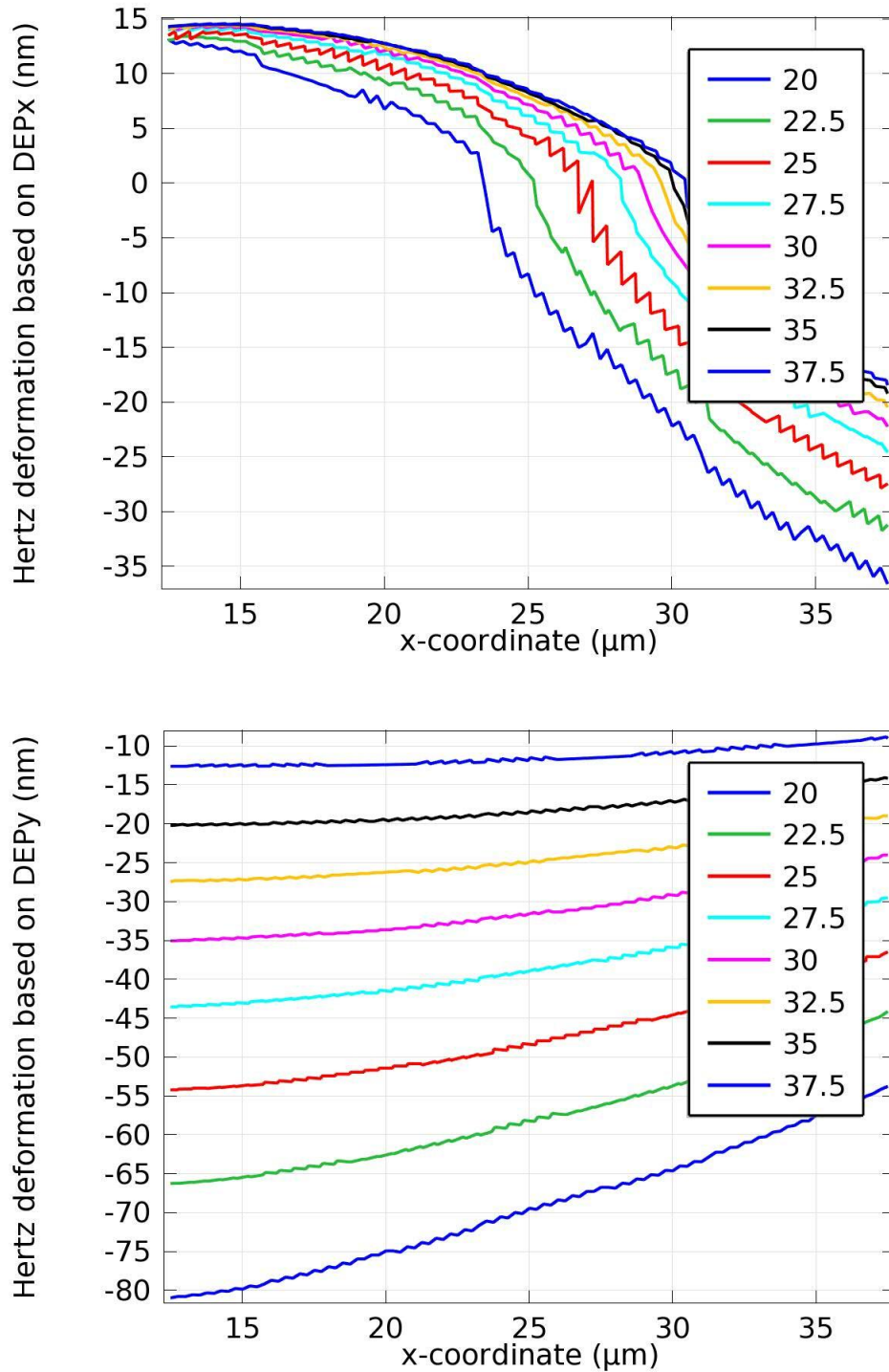


Figure 4-28: Simulated Hertz deformation from horizontal ($F_{DEP,x}$) and vertical ($F_{DEP,y}$) DEP forces on CHO cells at various elevations (increasing from 20 to 37.5 μm - i.e., from mid-channel to 2.5 μm from the ceiling) above the electrode gap ($12.5 \mu\text{m} < x < 37.5 \mu\text{m}$). The applied voltage was 8 V_{pp} at 1 MHz frequency. The Young's modulus is 1572 Pa.

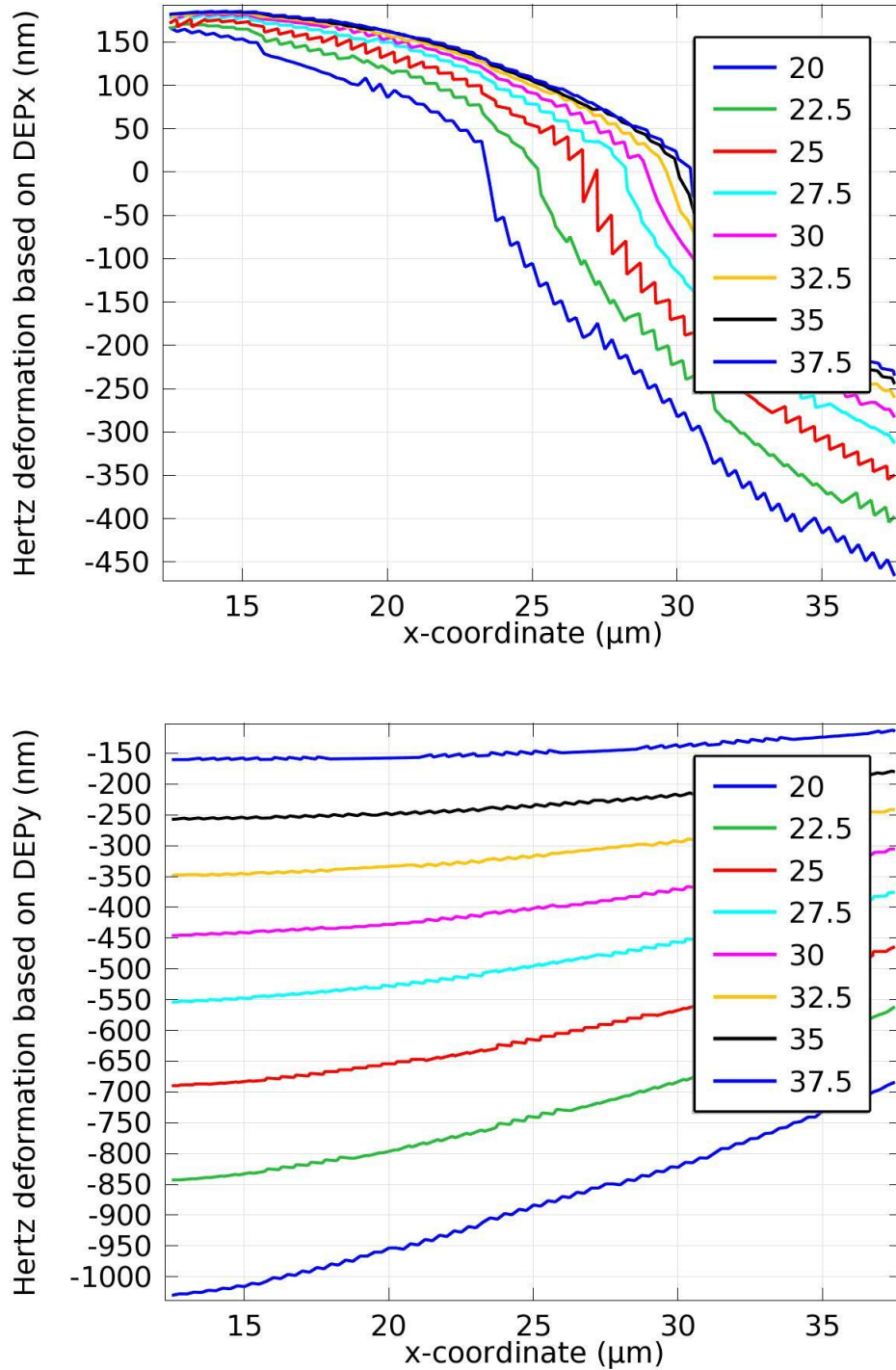


Figure 4-29: Simulated Hertz deformation from horizontal ($F_{DEP,x}$) and vertical ($F_{DEP,y}$) DEP forces on neutrophils at various elevations (increasing from 20 to 37.5 μm - i.e., from mid-channel to 2.5 μm from the ceiling) above the electrode gap ($12.5 \mu\text{m} < x < 37.5 \mu\text{m}$). The applied voltage was 10 V_{pp} at 450 kHz frequency. The Young's modulus is 27.5 Pa.

4.13.2 Electroporation

External electric fields can induce nanometer sized pores in cell membranes when the resulting potential drop across the cell membrane exceeds a critical threshold. This process, called electroporation [134], [135], [18], [136] [137], can lead to uncontrollable ion exchange and eventual cell expansion, which momentarily and/or permanently alter the dielectric properties of the cell.

A first-order process with the following time constant, τ_m , is appropriate for describing the frequency dependence of the transmembrane voltage for frequencies below 10 MHz [138], [139]:

$$\tau_m = \frac{RC_m}{\frac{2\sigma_c\sigma_e}{\sigma_c + 2\sigma_e} + \frac{R}{d}\sigma_m} \quad (4-4)$$

where R is radius, d is membrane thickness, $C_m = \varepsilon_m/d$ is the specific membrane capacitance [F/m²], and the conductivities of the cytoplasm, membrane and external medium are σ_c , σ_m , and σ_e respectively. The corresponding transmembrane voltage is given by [140]:

$$U_{TM} = 1.5 \frac{E_e R \cos\theta}{1 + j\omega\tau_m} \quad (4-5)$$

where E_e is external field magnitude, and θ is the incident angle between the field vector and the cell surface. Maximum interaction occurs when $\theta = 0$, leaving us with:

$$U_{TM} = 1.5 \frac{E_e R}{1 + j\omega\tau_m} \quad (4-6)$$

Wang and Lu subjected CHO cells to enhanced electric fields by delivering them into a channel of reduced size [141]. They found that a 400 V/cm (40 kV/m) continuous DC field was the starting threshold for electroporation of CHO cells. Taking the dimensions, conductivities, and specific membrane capacitance values for CHO cells from Table 2-1, and considering a 40 kV/m external field magnitude, we can plot the transmembrane voltage dependence on frequency (Figure 4-30). The transmembrane voltages required for electroporation are typically between 0.7-1.5 V [142]. Indeed, the low frequency limit is close to 0.7 V.

To determine whether electroporation occurs during experiments, we simply use Equation 4-5 to calculate the transmembrane voltages from the corresponding electric fields in the channel. According to Figure 4-31, an 8 V_{pp} applied AC voltage (1 MHz) generates transmembrane voltages less than 0.15 V for all positions above the mid-height of the channel. Consequently, CHO cells do not likely experience electroporation when an 8 V_{pp}, 1 MHz signal is applied.

Elham Salimi recently developed a non-linear dispersive formulation to model the electric field interaction with biological cells [142], [143]. According to her model, an applied electric field of 100 kV/m amplitude and 1 MHz frequency generate a 0.4 V transmembrane voltage using typical mammalian cell dimensions and electrical parameters. Consequently, at 1 MHz, there is room for increasing the DEP signal amplitude to initiate further cell compression while avoiding electroporation.

We conclude this section with a brief demonstration that strong electric fields at lower frequencies can induce the electroporative expansion of CHO cells. In a minimal fluid

flow ($<50 \mu\text{m/s}$), we used large DEP signals to propel a pair of attached CHO cells toward the channel ceiling, which was aligned to the focal plane of the microscope (Figure 4-32). After some time, the cells began to expand until they finally appeared to fill with external medium as the process became irreversible. Consequently, the cells felt progressively less DEP force and simply released from the electrical trap after 65 s.

Coplanar electrodes generate non-uniform fields in electrolytes and create electrical double layers at the electrode-fluid interface, giving rise to two mechanisms of electrically-induced fluid flow. The first involves the linear dependence of the permittivity and conductivity of the fluid with temperature. Non-uniform fields induce non-uniform Joule heating of an electrolyte solution through its bulk conductivity ($Q_{AC} = \sigma E_{RMS}^2$). Consequently, spatial variations of the permittivity and conductivity (temperature) lead to *electrothermal* fluid forces.

The second mechanism, called *electro-osmotic flow*, concerns non-uniform fields that are generated across the Stern-diffuse Debye double layer. The resulting fluid flow may subsequently induce electrophoretic particle flow. The impact of electrothermal and electro-osmotic flows on our measurements is discussed in the following two subsections.

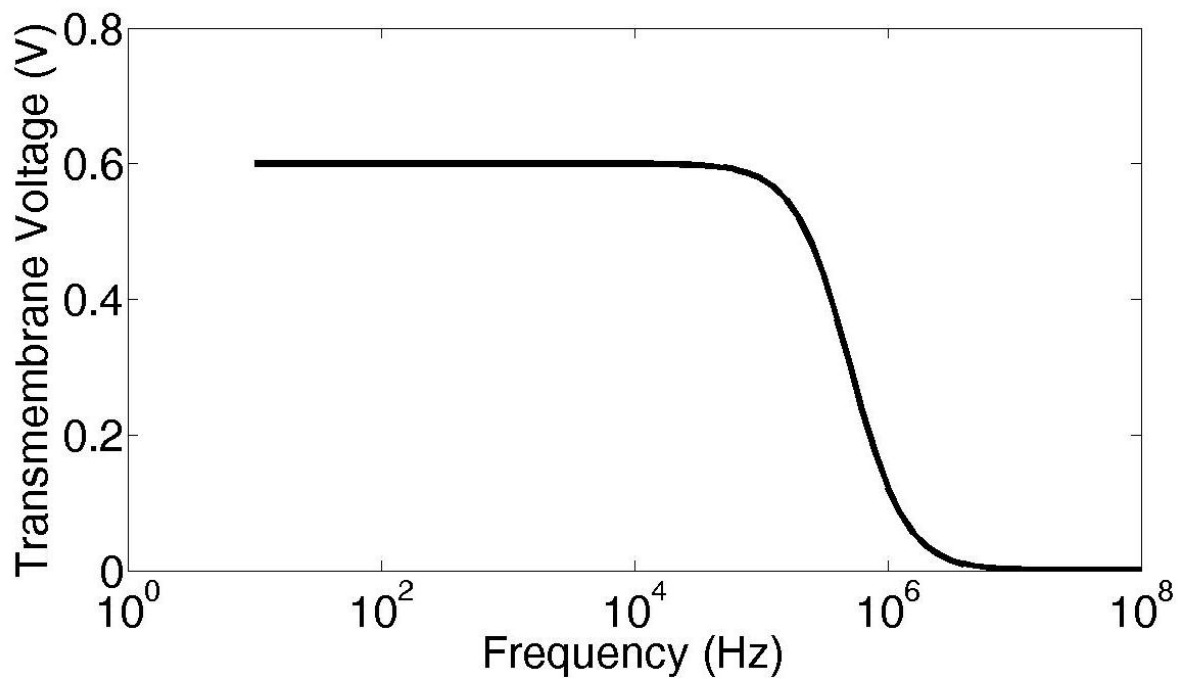


Figure 4-30: Simulated frequency dependence of the transmembrane voltage across a CHO cell immersed in PBS. The applied external field is 40 kV/m. The transmembrane voltage is approximately 0.6 V at frequencies below 100 kHz, and drops dramatically at higher frequencies. A higher order treatment of the process is required to predict the transmembrane voltages at higher frequencies (> 10 MHz).

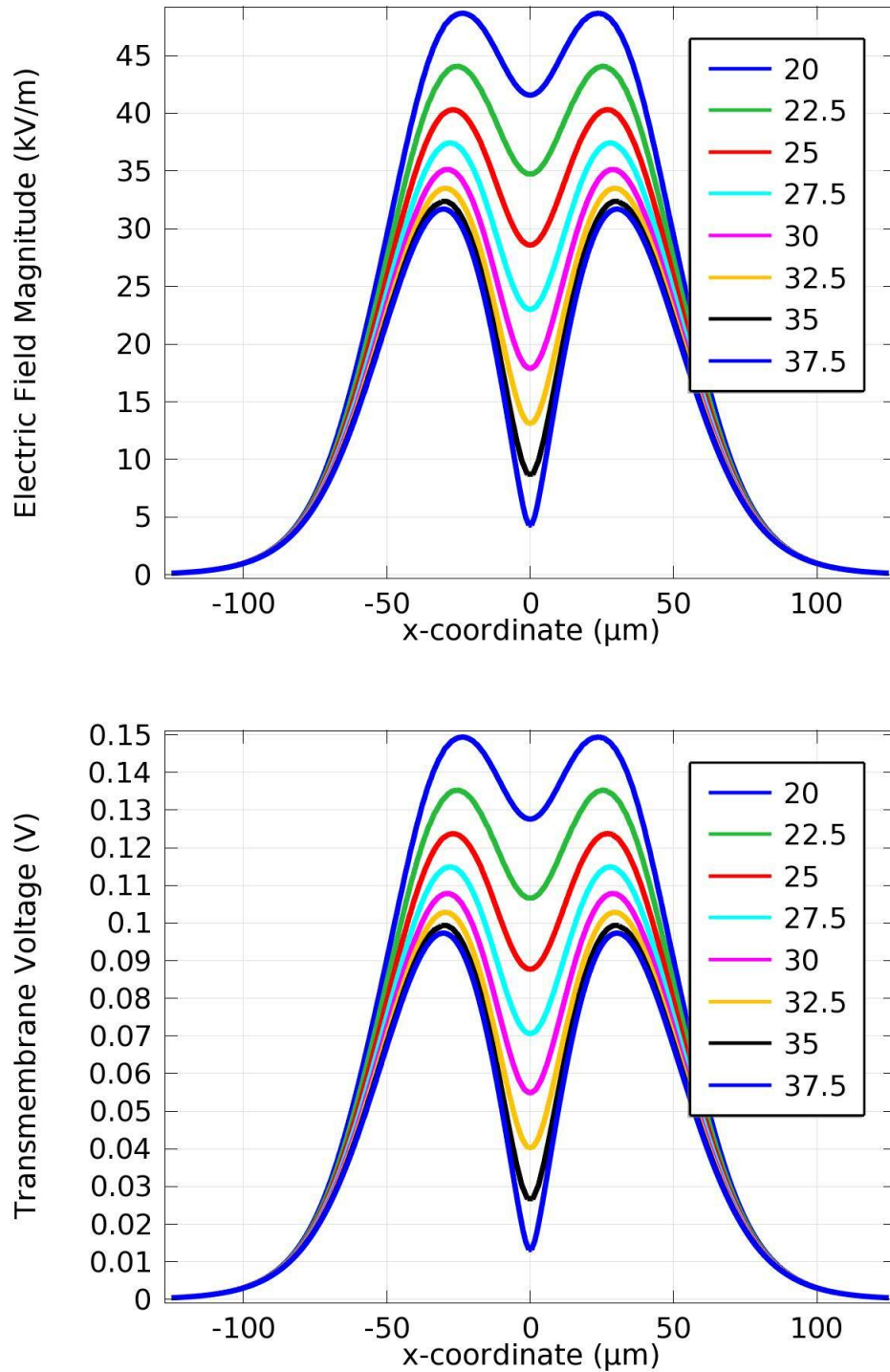


Figure 4-31: Simulated electric field amplitude and transmembrane voltage across a CHO cell membrane at elevations ranging from mid-channel height to just 2.5 μm from the channel ceiling (20-37.5 μm). In PBS, a 40 kV/m electric field amplitude generates a 0.13 V transmembrane voltage at 1 MHz, which falls short of electroporation.

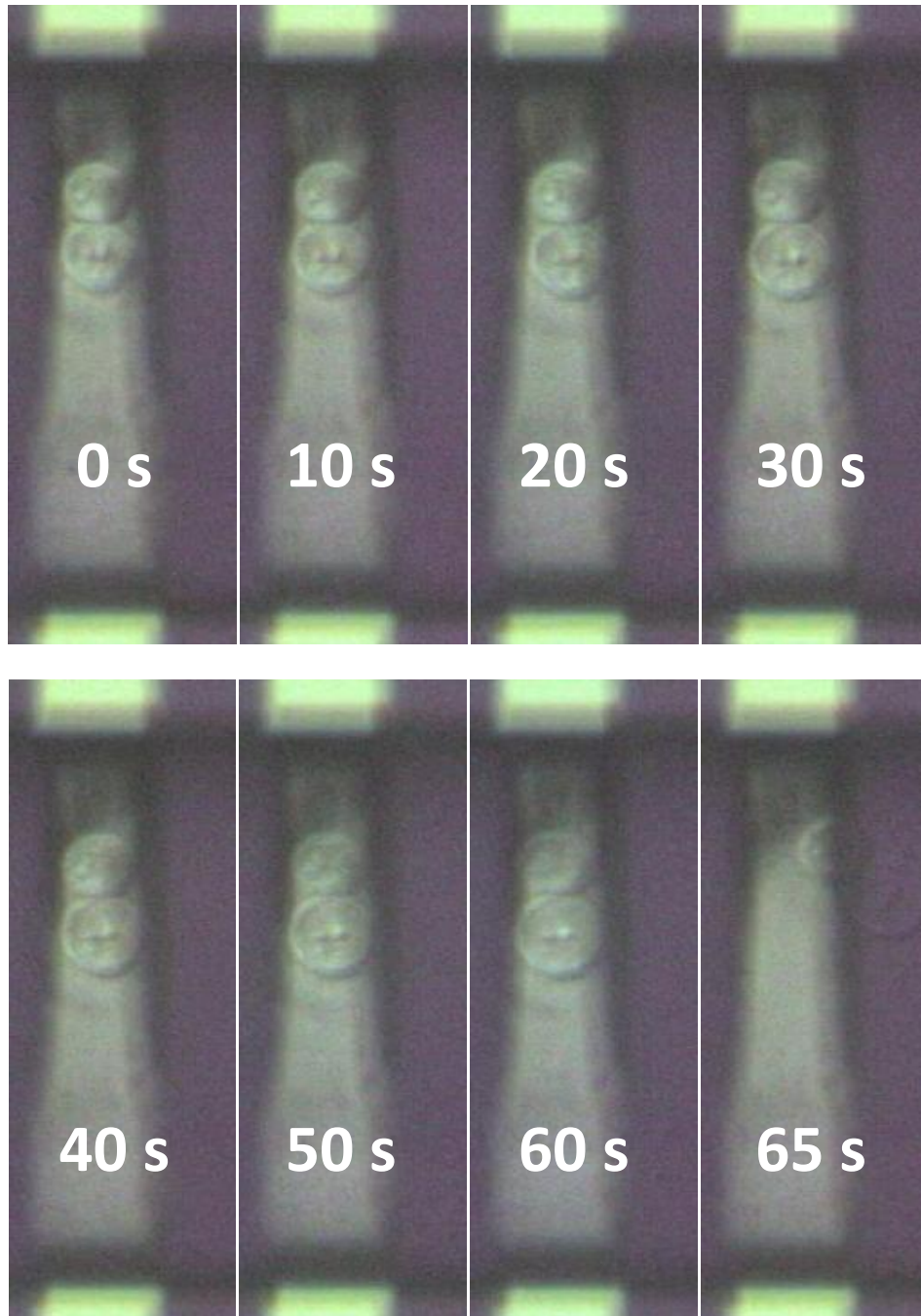


Figure 4-32: Connected CHO cells are subject to a $9 V_{pp}$, 20 kHz DEP signal as they are placed above the central electrode. Over time, the cells, which are strongly repelled toward the ceiling (in focal plane of microscope), expand and eventually become released, presumably due to electroporation.

4.13.3 AC electrothermal flow

Coplanar electrodes generate non-uniform electric fields, which generate temperature gradients through non-uniform heating of the channel. These temperature gradients further induce conductivity and permittivity gradients. The interaction between the electric field and these gradients generates an electrical force on the bulk fluid, which is called the *electrothermal force* [129], [144], [145], [146], [147], [148]. The time-averaged electrothermal body force [N/m³] is given by:

$$\langle f_E \rangle = -\frac{1}{2} \left[\left(\frac{\nabla \sigma}{\sigma} - \frac{\nabla \varepsilon}{\varepsilon} \right) \cdot \vec{E}_0 \frac{\varepsilon \vec{E}_0}{1 + (\omega\tau)^2} + \frac{1}{2} |E_0|^2 \nabla \varepsilon \right] \quad (4-7)$$

The first and second terms in this expression represent the Coulomb and dielectric forces, respectively. The conductivity and permittivity gradients can be rewritten as:

$$\frac{\nabla \varepsilon}{\varepsilon} = \left\{ \frac{1}{\varepsilon} \frac{\partial \varepsilon}{\partial T} \right\} \nabla T = \alpha \nabla T \quad (4-8)$$

$$\frac{\nabla \sigma}{\sigma} = \left\{ \frac{1}{\sigma} \frac{\partial \sigma}{\partial T} \right\} \nabla T = \beta \nabla T. \quad (4-9)$$

Note that the permittivity is absolute permittivity ($\varepsilon = \varepsilon_r \varepsilon_0$ [F/m]), $\tau = \varepsilon/\sigma$, and ∇T represents the spatial derivative of temperature [K/m]. For aqueous saline solutions, α and β are estimated to be -0.4 %/K and 2 %/K, respectively. Figure 4-33 considers the measured temperature dependence of conductivity and relative permittivity of a 5000 ppm NaCl solution (Note that [NaCl]_{PBS}=8000 ppm) [149]. Taking a best-fit line to each plot, we find that $\partial \varepsilon / \partial T = -0.33$ and $\partial \sigma / \partial T = 0.02$, which indeed give $\alpha = -0.4$ %/K and $\beta = 2$ %/K at room temperature.

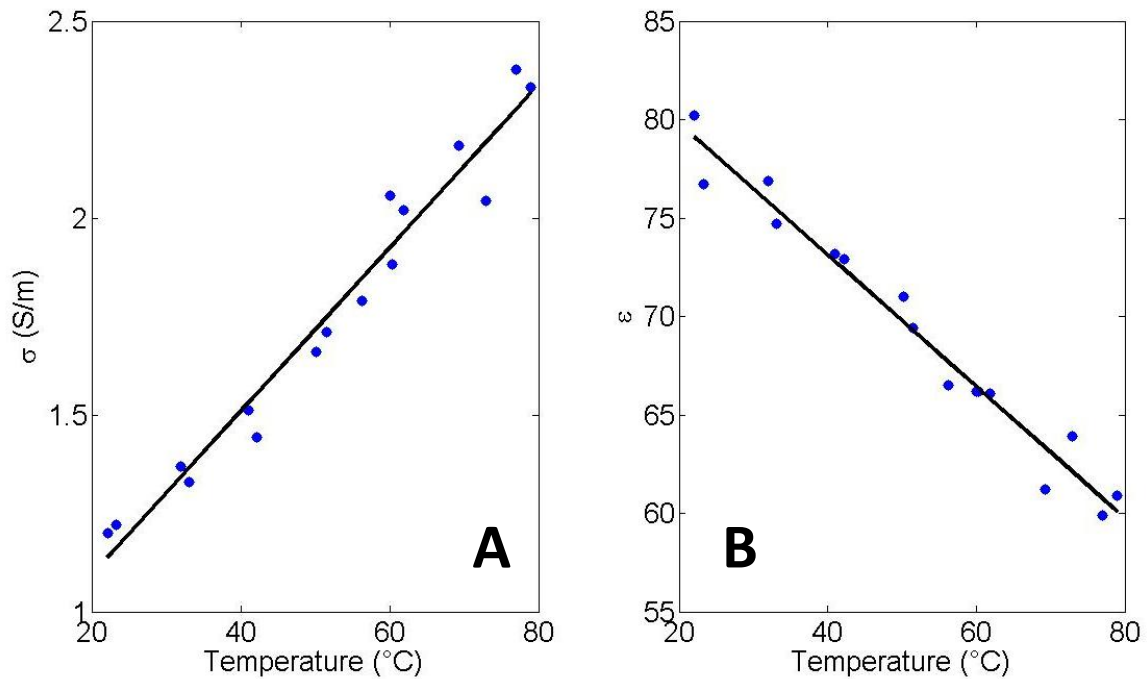


Figure 4-33: A) Conductivity and B) relative permittivity of a 5000 ppm saline solution versus temperature. Dots are measured values from [149], which are fitted here using best-fit lines.

To simulate electrothermal flow in COMSOL Multiphysics, we couple three equations governing the AC quasi-electrostatics, general heat transfer, and the incompressible Navier-Stokes fluid flow. These equations are coupled through the heat flux, Q , and temperature variables. Through the fluid conductivity, σ , the electric field generated by coplanar electrodes generates heat ($Q_{AC} = \sigma E_{RMS}^2$), which locally and non-uniformly increases the temperature in the channel. The general heat transfer module captures these temperature increases, which are incorporated into an electrothermal body force expression, which is included as an external force in the incompressible Navier-Stokes equation.

The simulation geometry is shown in Figure 4-34. The 1.1 mm and 0.7 mm dimensions represent the actual dimensions of the experimental chip. Again, the channel height is 40 μm and the electrode widths and spacings are 25 μm each. As usual, we begin by solving the Laplace equation given by $\nabla \cdot (\sigma + j\omega\epsilon)\nabla V = 0$, which solves for the electric fields ($E = -\nabla V$) in the channel. Our central electrode is given a 4 V potential (8 V_{pp} , 1 MHz), and the neighbouring electrodes are ground. The outer boundaries are electrically insulated ($\mathbf{n} \cdot \mathbf{J} = 0$) and the remaining inner boundaries are given a continuous boundary condition ($\mathbf{n} \cdot (\mathbf{J}_1 - \mathbf{J}_2) = 0$). The borosilicate glass layers surrounding the channel are given a permittivity of 4.8 and have negligible conductivity. For maximum effect, we fill the channel with phosphate buffered saline (PBS), which has an estimated permittivity of 78 and the highest conductivity of all tested buffers (1.6 S/m).

In conductive cell buffers, Joule heating can lead to significant heating of cells, which can lead to denaturation of their proteins. To determine the corresponding temperature increases, we solve the following equation, $\rho C_p \mathbf{u} \cdot \nabla T = \nabla \cdot (k \nabla T) + Q$, where the left and right side of the expression represent convective and conductive heat transfer terms. The fluid velocity, density, heat capacity at constant pressure, and thermal conductivity are \mathbf{u} , ρ , C_p , and k , respectively. The heat flux, Q , as described earlier, couples the electric field and heat transfer simulations. For water, ρ , C_p , and k are 1000 kg/m^3 , 4189 $\text{J}/\text{kg} \cdot \text{K}$, and 0.6 $\text{W}/\text{m} \cdot \text{K}$. For borosilicate glass, they are 2230 kg/m^3 , 754 $\text{J}/\text{kg} \cdot \text{K}$, and 1.13 $\text{W}/\text{m} \cdot \text{K}$. Other than the rightmost boundary of the fluid channel, which is given a convective flux output boundary condition (no viscous stress),

all outer boundaries are given a temperature of 293.15 K. The inner boundaries between two adjacent domains, u and d , are given a continuity boundary condition ($-\mathbf{n}_u \cdot (-k_u \nabla T_u) - \mathbf{n}_d \cdot (-k_d \nabla T_d) = 0$).

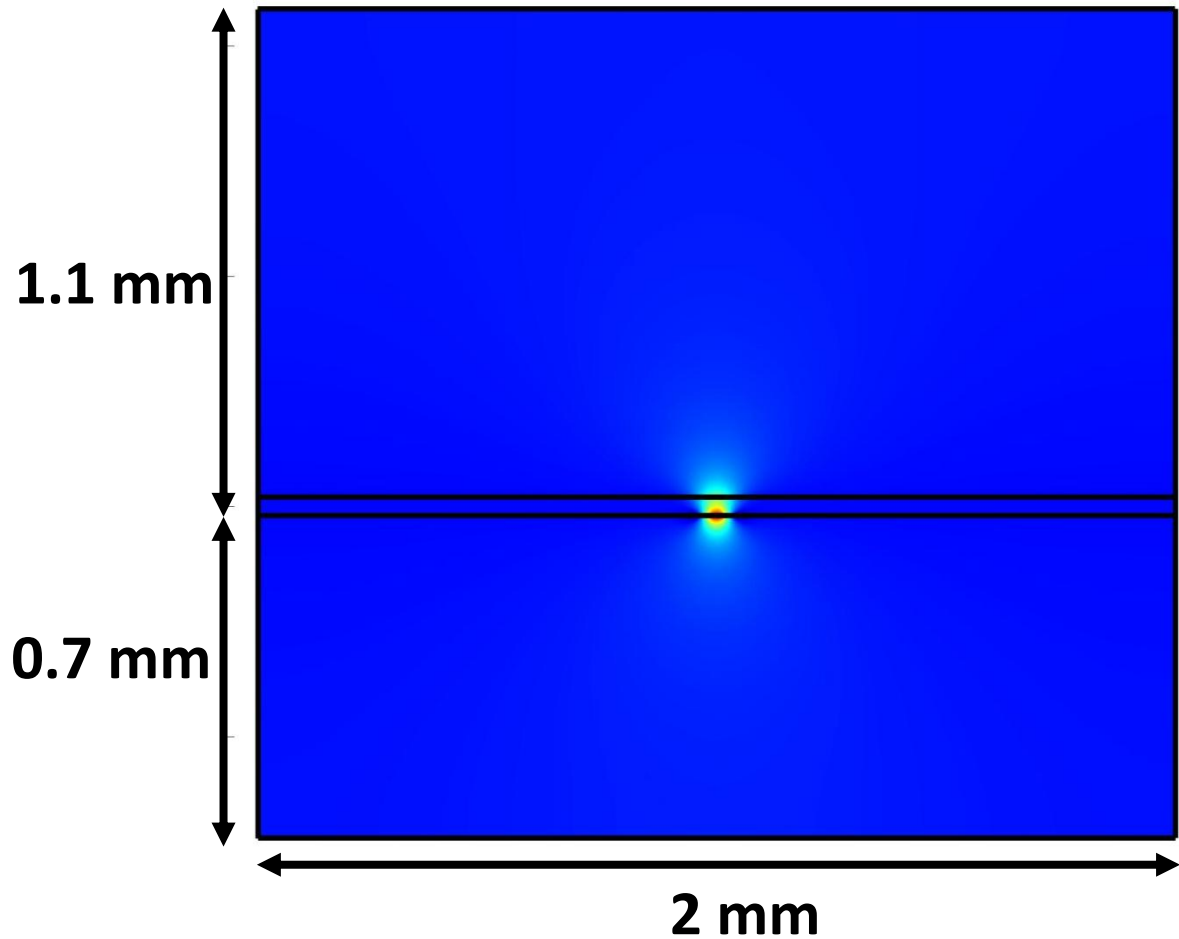


Figure 4-34: Simulated geometry with three domains: 1.1 mm upper borosilicate layer, which contains a 40 μm fluid channel, and a 0.7 mm borosilicate layer.

Finally, we solve the incompressible Navier-Stokes equation for a Newtonian fluid:

$$\rho(\mathbf{u} \cdot \nabla)\mathbf{u} = \eta \nabla^2 \mathbf{u} + \langle f_E \rangle \quad (4-10)$$

The left term represents convective acceleration, and the right terms represent viscosity and the electrothermal body force (described above), which couples the temperature variations to fluid flow. This expression is valid when the Reynolds number ($Re = \rho ul/\eta$) is very small. The fluid density and viscosity are assumed to be 10^3 kg/m^3 and $10^{-3} \text{ Pa}\cdot\text{s}$, respectively. With water flowing at approximately $300 \text{ }\mu\text{m/s}$ in a channel where the characteristic length, l , is $40 \text{ }\mu\text{m}$, $Re = 1.2 \times 10^{-2} \ll 1$. In an incompressible fluid, the mass-conservation equation, $\nabla \cdot \vec{u} = 0$, is also solved.

All boundaries are given a no-slip condition ($\vec{u} = 0$), except for the inlet and outlet channel boundaries. The leftmost inlet boundary has laminar inflow of a specified average velocity and entrance length. The outlet boundary is made free of viscous stress (zero pressure). The mesh concentration is finest within the channel and moderate in the borosilicate with maximum element sizes of 0.5 and $35 \text{ }\mu\text{m}$, respectively.

In the absence of a pressurized fluid flow, the electrothermal forces generate spiral fluid flow patterns above the coplanar electrodes (Figure 4-35). Conversely, the presence of a parabolic laminar fluid flow (average velocity is $333.33 \text{ }\mu\text{m/s}$) overwhelms the flow patterns generated by electrothermal forces, which contribute only to slightly perturb the flow over the full range of channel elevations (Figure 4-36).

Horizontal fluid velocities at fixed elevations (2.5 to $37.5 \text{ }\mu\text{m}$) above the electrodes are shown in Figure 4-36. At mid-channel elevation ($20 \text{ }\mu\text{m}$), the fluid velocity matches the input maximum velocity of $500 \text{ }\mu\text{m/s}$. At other elevations, the velocity falls off according to the parabolic formula for laminar flow (e.g., the velocities at 10 and $30 \text{ }\mu\text{m}$

elevations are equal). As the electrode region is traversed, the fluid accelerates and then decelerates (or vice versa) according to the spiral profile in Figure 4-35, which generates velocity differentials approaching an absolute maximum of 25 $\mu\text{m/s}$. This velocity generates small 3.5 pN drag forces on a sphere of 7.5 μm radius flowing in PBS. In conclusion, electrothermal flow does cause perturbations in particle flow, but does not contribute significantly to the signatures observed.

Electric fields locally generate heat through the relatively high conductivity of saline solutions. In the presence of a laminar fluid flow, this heat may be convectively transferred depending on the fluid velocity, density, and heat capacity. The overall temperature rises for an 8 V_{pp} , 1 MHz signal are shown in Figure 4-37. Convective heat transfer is slow compared with heat diffusion for typical fluid flows ($\langle u \rangle = 333.33 \mu\text{m/s}$). Therefore, the generated temperature profiles are symmetric about the electrodes, yielding an 8.5 K maximum temperature increment. Since this value decays very slowly away from the electrodes, cell heating is fairly significant. However, since our experiments were conducted at room temperature ($\sim 23 \text{ }^\circ\text{C}$), an 8.5 K temperature increase temporarily warms cells to temperatures nearer the optimal value ($37 \text{ }^\circ\text{C}$). The temperature increases are comparable to those found by Williams *et al.* [150] for a similar geometry.

However, when the fluid flow increases to a rate given by our purge function (0.102 m/s), the fluid flow does reduce the maximum temperature increment to approximately 1.8 K, which decays rapidly away from the electrodes. In purge mode, the channel pressure is $\Delta p_c = 0.25 p_{purge}$, where the total purge pressure is $p_{purge} = 500 \text{ mbar}$

(50 kPa). Based on §3.2.5, the corresponding average fluid velocity in the channel while purging is therefore $\langle v \rangle = \Delta p_c / AR = 0.102 \text{ m/s}$. We mention this because significant signal swings occur during channel purging. Much larger signal swings occur when purging conductive cell buffers compared to purging water or solutions of much weaker salinity.

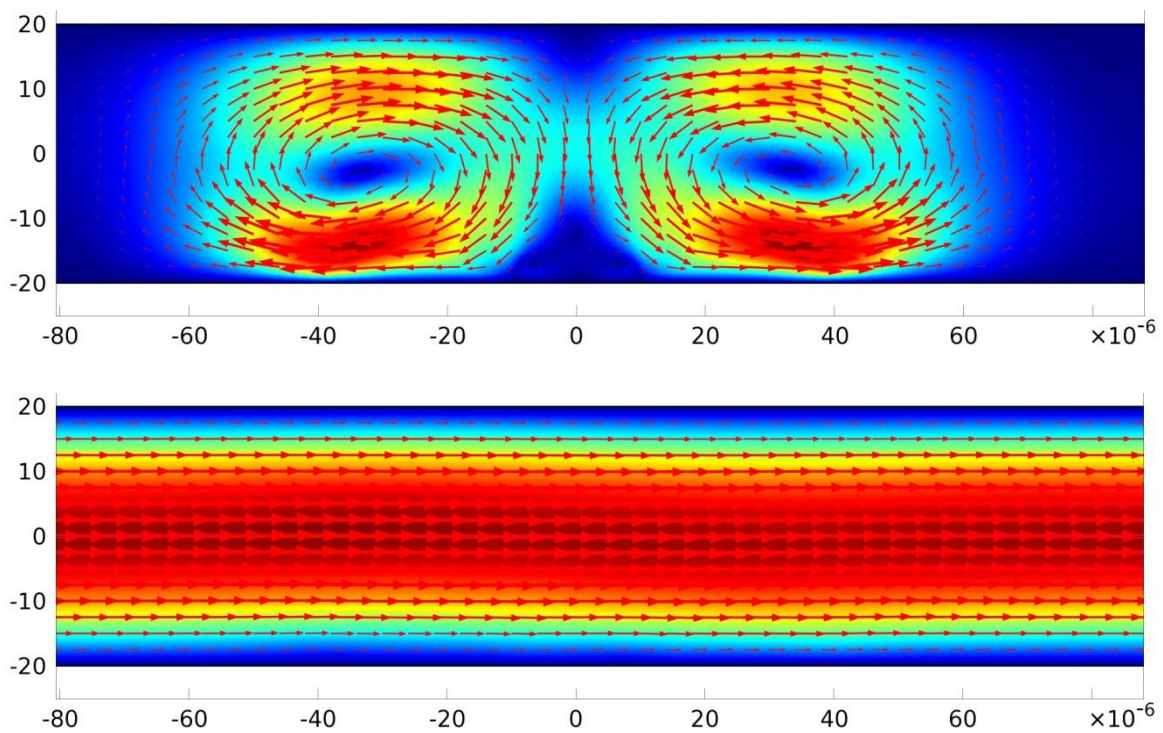


Figure 4-35: Influence of electrothermally-induced flow on the overall fluid flow. TOP: Electrothermal flow spirals are induced by an $8 V_{pp}$, 1 MHz signal when there is no pressurized fluid flow. BOTTOM: A typical parabolic laminar fluid flow (average velocity = $333.33 \mu\text{m/s}$) dominates the flow profile. However, the electrothermal contribution does appear as a perturbation as shown in the next figure.

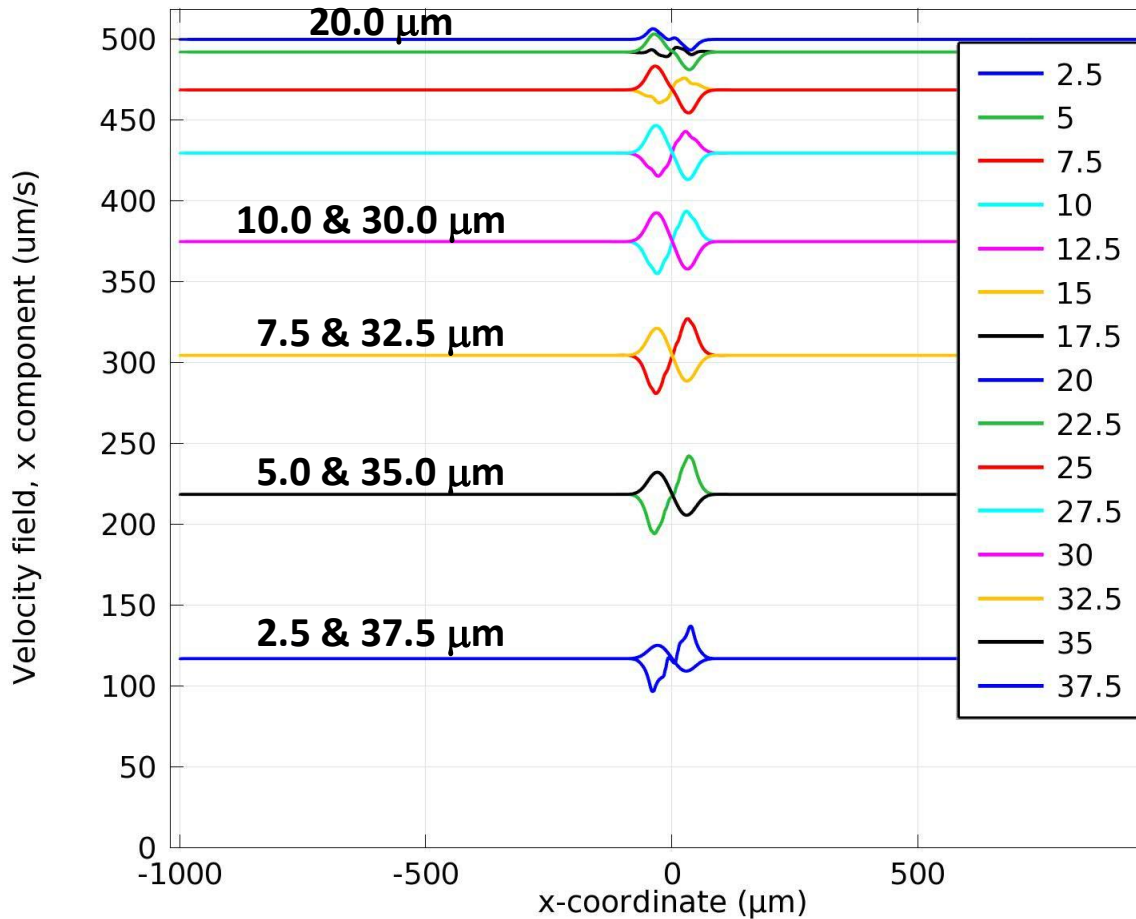


Figure 4-36: Horizontal fluid velocities at fixed elevations (2.5 to 37.5 μm) above the electrodes. At the mid-channel elevation (20 μm), the fluid velocity matches the input maximum velocity of 500 $\mu\text{m/s}$. At other elevations, the velocity falls off according to the parabolic formula for laminar flow (e.g., the velocities at 10 and 30 μm elevations are equal). As the electrode region is traversed, the fluid accelerates and then decelerates (or vice versa) according to the spiral profile in Figure 4-35, which generates velocity differentials approaching an absolute maximum of 25 $\mu\text{m/s}$, which, in PBS, generates small 3.5 pN drag forces on a sphere of 7.5 μm radius.

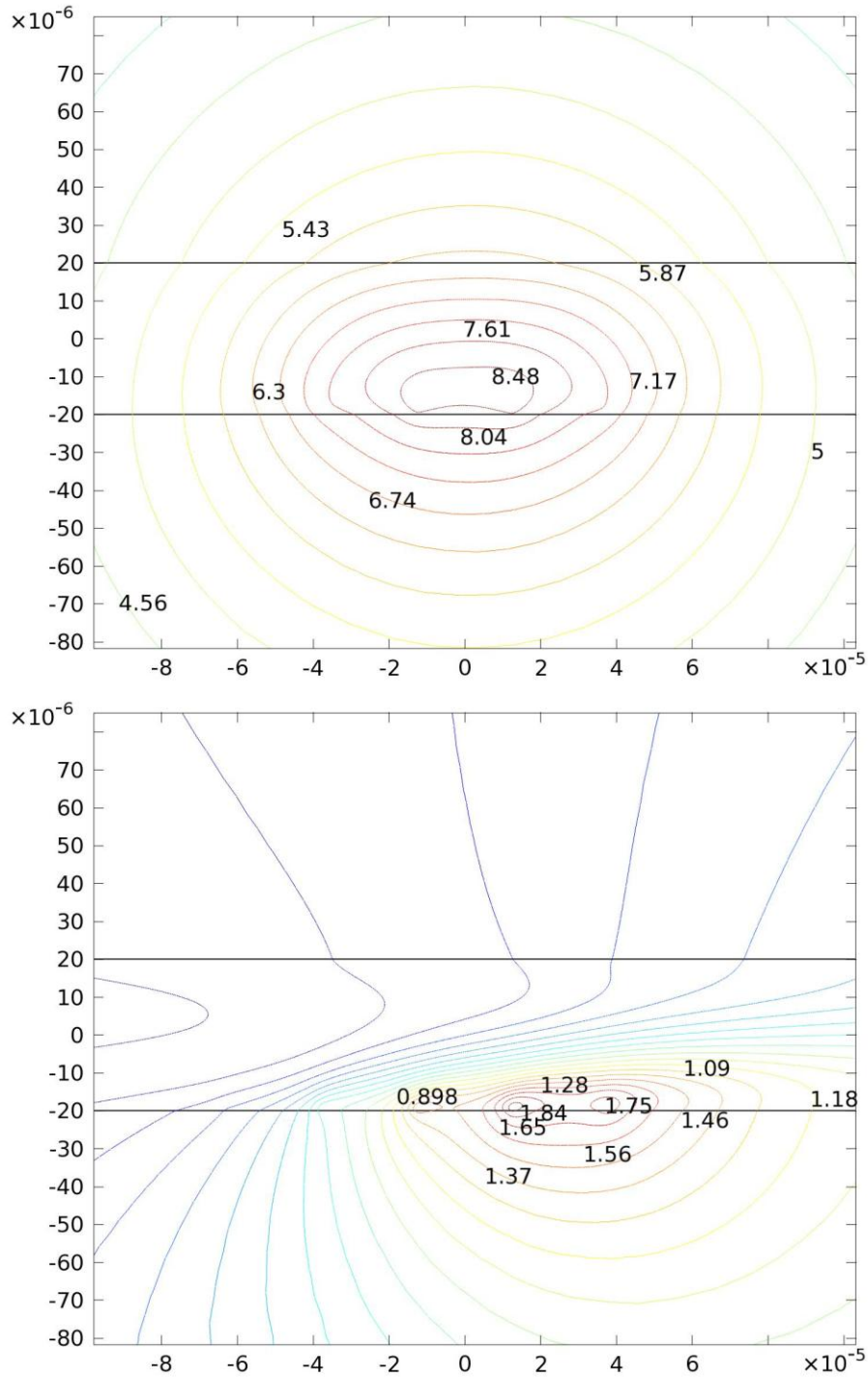


Figure 4-37: Joule heating – temperature rise vs. flow rate. TOP: Typical fluid velocities ($\langle \mathbf{u} \rangle = 333.33 \mu\text{m/s}$) do not transfer the heat efficiently. BOTTOM: When we purge the fluid ($\langle \mathbf{u} \rangle = 102 \text{ mm/s}$), the temperature rises in the channel significantly decrease. For an 8 V_{pp} , 1 MHz signal, the maximum temperature rises are approximately 8.5 K and 1.8 K, respectively.

4.13.4 AC electro-osmotic flow

AC electro-osmotic flow arises from the movement of ions in the electric double layer at the electrode/electrolyte interface, producing microflows because of fluid viscosity. Electro-osmotic flow generally dominates at lower frequencies because most of the applied voltage drops across the double layer, but becomes negligible above the characteristic frequency for double layer charging, $f = (\sigma/2\pi\epsilon)(L_d/l)$ [151], which is significantly lower than the relaxation frequency of the bulk fluid, $f = (\sigma/2\pi\epsilon)$.

For an estimated characteristic length (l) of 25 μm (electrode spacing), and a 1 \times PBS solution of 1.6 S/m conductivity, 78 relative permittivity and 0.7 nm Debye length (L_d) [152], the double layer charging frequency is about 10.3 kHz. Therefore, for our typical operating DEP frequencies (100 kHz – 2 MHz), electro-osmotic flow is negligible. High conductivity fluids compress the thickness of the double layer, which makes electro-osmosis ineffective. For the same applied voltage, more conductive fluids have a lower peak velocity at the characteristic frequency. Studer *et al.* have shown that AC electro-osmotic flow is not observable in fluids with conductivity above 140 mS/m [153]. Therefore, AC electro-osmotic flow is not expected to significantly contribute to the motion of cells in this work.

4.13.5 Brief summary of mechanisms

A number of force mechanisms were investigated to determine their possible influence on the DEP-induced pressing of cells into the channel ceiling. At typical operating voltages (8-10 V_{pp}) and MHz frequencies:

- 1) Dielectrophoresis is the dominant electrokinetic mechanism for cell actuation.
- 2) The minimum threshold for electroporation may be reached when low frequencies are used (<100 kHz) but electroporation is unlikely to occur at the higher frequencies (1 MHz) and fields (40 kV/m) used in this work.
- 3) AC electrothermal flow does produce peak fluid velocities approaching 25 $\mu\text{m/s}$ near the electrodes, which may slightly perturb the trajectory of cells, whose flow velocities are typically $\sim 300 \mu\text{m/s}$.
- 4) AC electro-osmotic flow does not significantly contribute to motion in high-conductivity buffers as the Debye length is heavily suppressed.

4.14 Chapter Summary

Strong low-frequency DEP forces were used to actuate single mammalian cells flowing in suspension toward the ceiling of a microfluidic channel. Simultaneously, the corresponding cell-to-wall interactions were capacitively detected using high-frequency (1.6 GHz) electric fields for detection. The strong DEP forces effectively generate an electronic capillary that flowing particles traverse using many possible mechanisms.

The strongest vertical DEP forces (<90 pN) occur above the central electrode while moderate inward-directed horizontal DEP forces (<20 pN) exist along the electrode edges for particle containment. This combination dramatically slows the flow of particles and cells. Due to their smooth surface and inability to deform ($E = 1 \text{ GPa}$), polystyrene spheres offer little contact area for interaction with the channel ceiling. Consequently, little to no contact occurs and the spheres rotate during their sudden deceleration over the central electrode. This sphere rotation likely occurs due to non-

uniform fluid velocities across its surface. If the fluid flow is sufficient for the particle to overcome the containment forces, the PSS escapes the electrode region. Otherwise, it continues to spin while remaining trapped within the central electrode width.

Conversely, mammalian cells are deformable and contain an assortment of embedded proteins in their plasma membranes, making them relatively rough on the nm scale. In addition, we expect that the fabricated glass surfaces are rough on the nm scale. Consequently, the compression of mammalian cells gives them an ability to offer more surface area to increase the probability of non-specific cell-to-wall adhesion, possibly through close-range van der Waals-London forces. Since the rate of de-adhesion is inversely proportional to the contact area, such forces may additionally slow the release of soft cells from the channel ceiling compared with more rigid particles and cells.

For strong low-frequency DEP signals, neutrophils and T-lymphocytes were observed to experience compression while PS spheres and rigid cells such as 10T½ mouse fibroblasts did not experience compression. These events were captured in the respective capacitance signatures. Rigid spheres spend an extended time overcoming the local electrical barrier at the electrode edge, while biological cells spend their extended time stretching across the electrode gap under the influence of DEP-induced vertical compression.

Chapter 5 – Research Highlights & Future Directions

*“History will be kind to me for I intend to write it.”
-Winston Churchill*

Simultaneous dielectrophoretic actuation and capacitive detection of biological cells has been achieved in two systems. In the first system, which uses frequency modulation, polystyrene spheres and yeast cells (*Saccharomyces cerevisiae*) were successfully detected using a single pair of gold electrodes. The resulting capacitance changes agreed favourably with finite element simulations (~ 10 aF for $6\ \mu\text{m}$ yeast cells and ~ 100 aF for $10\ \mu\text{m}$ polystyrene spheres). To show that dielectrophoretic actuation was possible, a $3\ V_{pp}$, 1 MHz signal was coupled to the cavity resonator using an RC circuit. Since viable yeast experiences positive dielectrophoresis at 1 MHz, yeast cells were trapped on the electrode edges.

The low frequency (1 MHz) signal was switched on and off every 5 s to demonstrate successful dielectrophoretic trapping of yeast cells. When yeast cells passed over the electrodes during the on-cycle, the resulting large capacitance changes indicated that those yeast cells were trapped in succession (Figure 3-7) whereas during the off-cycle, much smaller capacitance changes resulted from the detection of free-flowing untrapped yeast cells.

Later, an interferometer-based approach was developed to exploit the high sensitivity between phase and capacitance change. Indeed, the minimum detectable RMS capacitance change improved from ± 2 aF to ± 0.15 aF. At this noise level, a variety of cell types were readily detected with high signal-to-noise ratios. Interdigitated

electrodes were designed to monitor the time-dependence of dielectrophoretically-actuated cells. The resulting trajectories are adequately predicted by solving the equation of motion, which includes dielectrophoretic, gravitational, electrothermal, drag, and hydrodynamic lift forces. This should provide a theoretical framework that future researchers can build from and optimize future implementations.

When biological cells are dielectrophoretically-pressed into the channel ceiling, they may compress depending on their rigidity. Limited compression was observed in neutrophils and T-lymphocytes but was not observed in more rigid cells such as fibroblasts. Under the influence of strong repulsive DEP actuation, rigid particles induced capacitance signatures with symmetric amplitudes, whereas deformable cells generated asymmetric amplitudes.

A number of force mechanisms were investigated to determine their possible influence on the DEP-induced pressing of cells into the channel ceiling. At typical operating voltages (8-10 V_{pp}), the minimum threshold for electroporation may be reached when low frequencies are used (<100 kHz) but electroporation is unlikely to occur at higher frequencies (1 MHz). AC electro-osmotic flow does not significantly contribute to motion in high-conductivity buffers as the Debye length is heavily suppressed. However, AC electrothermal flow does produce peak fluid velocities approaching 25 $\mu\text{m/s}$ near the electrodes, which may perturb the trajectory of flowing cells (typically 300 $\mu\text{m/s}$).

Ultimately, this work presents an all-electrical approach to deformability cytometry, in which the mechanical responses of single DEP-actuated cells are rapidly detected (< 5

s) in a flow configuration. Capacitance responses at GHz frequencies avoid a number of conflicting polarization mechanisms to sense the permittivity changes due to single cells.

5.1 Future Work

The interferometric system has been used in several investigations by members of our microfluidics group, which is headed by Professors Douglas Thomson, Greg Bridges, and Mark Freeman. Other than the work presented in this thesis, we have investigated the DEP response of yeast cells [119], [120], [154], fully modelled the RF response of the interferometric system [45], determined the errors of impedance-based detection of ellipsoidal cells [155], [123], and, using a single loop electrode, inductively sensed single magnetic beads in a flow configuration [156], [157], which can be potentially attached to single cells in subsequent experiments. In addition, we have recently shown that the cell-to-wall interactions of DEP-pressed breast cancer cells can vary depending on metastatic potential [158].

This author believes there is great potential for this system in characterizing biological cells. Our group is currently investigating the DEP response of single cells in low conductivity media (sucrose-based buffers) to determine the Clausius-Mossotti response of various cell types based on the corresponding capacitance signatures. This may be an effective approach for determining the CMF of arbitrary cell types.

Elham Salimi has developed a nice theoretical framework for the electroporation of cells [142], [143]. Since electroporation influences the mechanical properties of cells,

which typically deform according to a power law time-dependence, the transient mechanical response of biological cells to an electroporative stimulus could be explored by applying electrical pulses of varying length. Since the electroporation threshold is not reached at MHz frequencies for typical applied voltages (8-10 V_{pp}), we could increase the applied voltage in subsequent experiments to accentuate the compression of soft cells, particularly as they typically experience large compressions *in vivo*.

Appendix A – Derivation of DEP Equation for Spherical Particles

Let's begin with the Laplace equation in spherical coordinates containing no azimuthal dependence ($\partial/\partial\varphi = 0$):

$$\frac{1}{r^2} \frac{\partial}{\partial r} \left(r^2 \frac{\partial V}{\partial r} \right) + \frac{1}{r^2 \sin\theta} \frac{\partial}{\partial \theta} \left(\sin\theta \frac{\partial V}{\partial \theta} \right) = 0$$

Assuming a solution of the form, $V = \Gamma(r)\Theta(\theta)$, we have:

$$\frac{1}{r^2} \frac{\partial}{\partial r} \left(r^2 \frac{\partial [\Gamma(r)\Theta(\theta)]}{\partial r} \right) + \frac{1}{r^2 \sin\theta} \frac{\partial}{\partial \theta} \left(\sin\theta \frac{\partial [\Gamma(r)\Theta(\theta)]}{\partial \theta} \right) = 0$$

$$\frac{\Theta(\theta)}{r^2} \frac{\partial}{\partial r} \left(r^2 \frac{\partial [\Gamma(r)]}{\partial r} \right) + \frac{\Gamma(r)}{r^2 \sin\theta} \frac{\partial}{\partial \theta} \left(\sin\theta \frac{\partial [\Theta(\theta)]}{\partial \theta} \right) = 0$$

$$\frac{\Theta(\theta)}{r^2} \left(r^2 \frac{\partial^2 [\Gamma(r)]}{\partial r^2} + 2r \frac{\partial [\Gamma(r)]}{\partial r} \right) + \frac{\Gamma(r)}{r^2 \sin\theta} \left(\sin\theta \frac{\partial^2 [\Theta(\theta)]}{\partial \theta^2} + \cos\theta \frac{\partial [\Theta(\theta)]}{\partial \theta} \right) = 0$$

After separating terms in r and θ , we have:

$$\frac{1}{\Gamma(r)} \left(r^2 \frac{\partial^2 [\Gamma(r)]}{\partial r^2} + 2r \frac{\partial [\Gamma(r)]}{\partial r} \right) + \frac{1}{\Theta(\theta) \sin\theta} \left(\sin\theta \frac{\partial^2 [\Theta(\theta)]}{\partial \theta^2} + \cos\theta \frac{\partial [\Theta(\theta)]}{\partial \theta} \right) = 0$$

Since the two terms are independent of each other, we can equate the radial and polar angle terms to constants k^2 and $-k^2$, respectively [159], [160].

The first term is the radial solution:

$$\frac{1}{\Gamma(r)} \left(r^2 \frac{\partial^2 [\Gamma(r)]}{\partial r^2} + 2r \frac{\partial [\Gamma(r)]}{\partial r} \right) = k^2$$

$$r^2 \frac{\partial^2 [\Gamma(r)]}{\partial r^2} + 2r \frac{\partial [\Gamma(r)]}{\partial r} - k^2 \Gamma(r) = 0$$

This is a Cauchy-Euler differential equation

$$x^2 \frac{\partial^2 y}{\partial x^2} + 2x \frac{\partial y}{\partial x} - k^2 y = 0$$

Solving the Cauchy-Euler equation requires the following transformations:

$$x = e^t \xrightarrow{\text{yields}} x \frac{\partial y}{\partial x} = \frac{\partial y}{\partial t}, \quad x^2 \frac{\partial^2 y}{\partial x^2} = \frac{\partial^2 y}{\partial t^2} - \frac{\partial y}{\partial t}$$

Substitution gives:

$$\begin{aligned} \frac{\partial^2 y}{\partial t^2} - \frac{\partial y}{\partial t} + 2 \frac{\partial y}{\partial t} - k^2 y &= 0 \\ \frac{\partial^2 y}{\partial t^2} + \frac{\partial y}{\partial t} - k^2 y &= 0 \end{aligned}$$

The corresponding auxiliary equation is $a^2 + a - k^2 = 0$ with two roots:

$$a = \frac{-1 \pm \sqrt{1 + 4k^2}}{2}$$

The general solution has the form:

$$y(t) = c_1 e^{a_1 t} + c_2 e^{a_2 t}$$

$$y(t) = c_1 (e^t)^{a_1} + c_2 (e^t)^{a_2}$$

$$y(x) = c_1 (x)^{a_1} + c_2 (x)^{a_2}$$

$$a_1 = \frac{-1 + \sqrt{1 + 4k^2}}{2} = n$$

$$a_2 = \frac{-1 - \sqrt{1 + 4k^2}}{2} = -(n + 1)$$

$$y(x) = c_1 x^n + c_2 x^{-(n+1)}$$

And finally, the radial solution is given by:

$$\Gamma(r) = A_n r^n + B_n r^{-(n+1)}$$

where $n(n + 1) = k^2$, and A_n, B_n are arbitrary constants.

Now, the polar angle treatment (second term):

$$\begin{aligned} \frac{1}{\Theta(\theta)\sin\theta} \left(\sin\theta \frac{\partial^2[\Theta(\theta)]}{\partial\theta^2} + \cos\theta \frac{\partial[\Theta(\theta)]}{\partial\theta} \right) &= -k^2 \\ \sin\theta \frac{\partial^2[\Theta(\theta)]}{\partial\theta^2} + \cos\theta \frac{\partial[\Theta(\theta)]}{\partial\theta} + k^2\Theta(\theta)\sin\theta &= 0 \\ \frac{\partial^2[\Theta(\theta)]}{\partial\theta^2} + \frac{\cos\theta}{\sin\theta} \frac{\partial[\Theta(\theta)]}{\partial\theta} + n(n + 1)\Theta(\theta) &= 0 \end{aligned}$$

Let's show that this expression has the form of the associated ($m=0$) Legendre's equation [161]:

$$\begin{aligned} (1 - x^2) \frac{\partial^2 y}{\partial x^2} - 2x \frac{\partial y}{\partial x} + n(n + 1)y &= 0 \\ \frac{\partial}{\partial x} \left[(1 - x^2) \frac{\partial y}{\partial x} \right] + n(n + 1)y &= 0 \end{aligned}$$

Assigning $x = \cos\theta$ gives the following:

$$\begin{aligned} \partial x &= \partial[\cos\theta] = -\sin\theta \partial\theta \\ 1 - x^2 &= 1 - \cos^2\theta = \sin^2\theta \end{aligned}$$

Substituting these expressions into the Legendre equation gives:

$$\begin{aligned} \frac{\partial}{-\sin\theta \partial\theta} \left[\sin^2\theta \frac{\partial y}{-\sin\theta \partial\theta} \right] + n(n + 1)y &= 0 \\ \frac{1}{\sin\theta} \frac{\partial}{\partial\theta} \left[\sin\theta \frac{\partial y}{\partial\theta} \right] + n(n + 1)y &= 0 \\ \frac{1}{\sin\theta} \left\{ \sin\theta \frac{\partial^2 y}{\partial\theta^2} + \cos\theta \frac{\partial y}{\partial\theta} \right\} + n(n + 1)y &= 0 \\ \frac{\partial^2 y}{\partial\theta^2} + \frac{\cos\theta}{\sin\theta} \frac{\partial y}{\partial\theta} + n(n + 1)y &= 0 \end{aligned}$$

This expression is identical to the polar angle term above, where $y = \Theta(\theta)$. For

$\theta \in [0, \pi]$, the solutions to Legendre's equation are Legendre functions, $P_n(\cos\theta)$. Legendre functions for integer values of n are polynomials in $\cos\theta$ (recall the transformation, $x = \cos\theta$). Table A.1 lists the first four Legendre polynomials.

Table A.1: Legendre Polynomials

N	$P_n(\cos\theta)$
0	1
1	$\cos\theta$
2	$\frac{1}{2}(3\cos^2\theta - 1)$
3	$\frac{1}{2}(5\cos^3\theta - 3\cos\theta)$

Therefore the potential can be expressed as:

$$V(r, \theta) = \Gamma(r)\Theta(\theta) = [A_n r^n + B_n r^{-(n+1)}]P_n(\cos\theta)$$

Since the dipole contribution to the electric potential arises when $n=1$,

$$V(r, \theta)|_{DIPOLE} = [Ar + B/r^2]\cos\theta$$

For a uniform dielectric sphere in a dielectric medium

$$V_1(r, \theta) = [-E_0 r + B/r^2]\cos\theta \quad r > R$$

$$V_2(r, \theta) = [-Cr + D/r^2]\cos\theta \quad r < R$$

Since the field does not decay inside the sphere, $D=0$.

At the sphere's radius, $r = R$, two boundary conditions are satisfied:

$$V_1 = V_2 \quad (A-1)$$

$$\epsilon_1 \left(-\frac{\partial V_1}{\partial r} \right) = \epsilon_2 \left(-\frac{\partial V_2}{\partial r} \right) \quad (A-2)$$

The first boundary condition (A-1) leads to the relation:

$$-E_0 R \cos\theta + B \cos\theta / R^2 = -C R \cos\theta$$

$$C = E_0 - B/R^3 \quad (A-3)$$

The second boundary condition (A-2) gives:

$$-\frac{\partial V_1}{\partial r} = E_0 \cos\theta + 2B \cos\theta / R^3$$

$$-\frac{\partial V_2}{\partial r} = C \cos\theta$$

$$\epsilon_1 (E_0 \cos\theta + 2B \cos\theta / R^3) = \epsilon_2 (C \cos\theta)$$

Cancelling the cosine terms and substituting (A-3) for C, we get:

$$B = \frac{\varepsilon_2 - \varepsilon_1}{\varepsilon_2 + 2\varepsilon_1} E_0 R^3$$

And therefore,

$$C = E_0 - B/R^3 = E_0 - \frac{\varepsilon_2 - \varepsilon_1}{\varepsilon_2 + 2\varepsilon_1} E_0$$

$$C = \frac{3\varepsilon_1}{\varepsilon_2 + 2\varepsilon_1} E_0$$

Potential due to induced dipole [44]:

$$V_{induced} = \frac{\rho_{eff} \cos\theta}{4\pi\varepsilon_1 r^2}$$

Equate to the induced dipole term in V_1 :

$$\frac{\rho_{eff} \cos\theta}{4\pi\varepsilon_1 r^2} = \frac{B \cos\theta}{r^2}$$

$$\rho_{eff} = 4\pi\varepsilon_1 B$$

$$\rho_{eff} = 4\pi\varepsilon_1 \left(\frac{\varepsilon_2 - \varepsilon_1}{\varepsilon_2 + 2\varepsilon_1} \right) E_0 R^3$$

Force on a small dipole [44]:

$$\vec{F} = q\vec{E}(\vec{r} + \vec{d}) - q\vec{E}(\vec{r})$$

If \vec{d} is small compared with the field's non-uniformity, the first term can be Taylor series expanded:

$$\vec{E}(\vec{r} + \vec{d}) = \vec{E}(\vec{r}) + \vec{d} \cdot \nabla \vec{E}(\vec{r}) + \dots$$

$$\vec{F} = q\vec{E}(\vec{r}) + q\vec{d} \cdot \nabla \vec{E}(\vec{r}) - q\vec{E}(\vec{r}) + \dots$$

$$\vec{F} = q\vec{d} \cdot \nabla \vec{E}(\vec{r}) = \rho_{eff} \cdot \nabla \vec{E}(\vec{r}) = 4\pi\varepsilon_1 \left(\frac{\varepsilon_2 - \varepsilon_1}{\varepsilon_2 + 2\varepsilon_1} \right) \vec{E}_0 R^3 \cdot \nabla \vec{E}(\vec{r})$$

For quasi-electrostatic electric fields,

$$\vec{E}_0 \cdot \nabla \vec{E}(\vec{r}) = 1/2 \nabla \vec{E}_0^2$$

Therefore, the time-averaged dielectrophoretic force for a uniform sphere is:

$$\langle \vec{F}_{DEP} \rangle = 2\pi R^3 \varepsilon_1 \left(\frac{\varepsilon_2 - \varepsilon_1}{\varepsilon_2 + 2\varepsilon_1} \right) \nabla \vec{E}_{RMS}^2$$

Appendix B – Clausius-Mossotti Factor for a Uniform Sphere is a Debye Function

The following derivation shows that the Clausius-Mossotti factor for a uniform dielectric sphere is a Debye function characterized by a single relaxation time.

$$K(\omega) = \frac{\varepsilon_2^* - \varepsilon_1^*}{\varepsilon_2^* + 2\varepsilon_1^*}$$

$$K(\omega) = \frac{(\varepsilon_2 - j\sigma_2/\omega) - (\varepsilon_1 - j\sigma_1/\omega)}{(\varepsilon_2 - j\sigma_2/\omega) + 2(\varepsilon_1 - j\sigma_1/\omega)}$$

$$K(\omega) = \frac{(\varepsilon_2 - \varepsilon_1) - j(\sigma_2 - \sigma_1)/\omega}{(\varepsilon_2 + 2\varepsilon_1) - j(\sigma_2 + 2\sigma_1)/\omega}$$

Multiply top and bottom by $j\omega$:

$$K(\omega) = \frac{j\omega(\varepsilon_2 - \varepsilon_1) + (\sigma_2 - \sigma_1)}{j\omega(\varepsilon_2 + 2\varepsilon_1) + (\sigma_2 + 2\sigma_1)}$$

Rearranging gives:

$$K(\omega) = \frac{\sigma_2^* - \sigma_1^*}{\sigma_2^* + 2\sigma_1^*}$$

Rearranging also gives:

$$K(\omega) = \frac{\sigma_2 - \sigma_1}{\sigma_2 + 2\sigma_1} \cdot \frac{1 + j\omega\tau_0}{1 + j\omega\tau_{MW}}$$

Where $\tau_0 = \frac{\varepsilon_2 - \varepsilon_1}{\sigma_2 - \sigma_1}$; $\tau_{MW} = \frac{\varepsilon_2 + 2\varepsilon_1}{\sigma_2 + 2\sigma_1}$; implies that $\tau_0 = \tau_{MW} \frac{\varepsilon_2 - \varepsilon_1}{\varepsilon_2 + 2\varepsilon_1} \frac{\sigma_2 + 2\sigma_1}{\sigma_2 - \sigma_1}$,

Now, we verify that the Clausius-Mossotti factor has a single relaxation term, τ_{MW} :

$$K(\omega) = \frac{\sigma_2 - \sigma_1}{\sigma_2 + 2\sigma_1} \cdot \frac{1}{1 + j\omega\tau_{MW}} + \frac{\sigma_2 - \sigma_1}{\sigma_2 + 2\sigma_1} \cdot \frac{j\omega\tau_0}{1 + j\omega\tau_{MW}}$$

$$K(\omega) = \frac{\sigma_2 - \sigma_1}{\sigma_2 + 2\sigma_1} \cdot \frac{1}{1 + j\omega\tau_{MW}} + \frac{\sigma_2 - \sigma_1}{\sigma_2 + 2\sigma_1} \cdot \frac{j\omega\tau_{MW}}{1 + j\omega\tau_{MW}} \frac{\varepsilon_2 - \varepsilon_1}{\varepsilon_2 + 2\varepsilon_1} \frac{\sigma_2 + 2\sigma_1}{\sigma_2 - \sigma_1}$$

$$K(\omega) = \frac{\sigma_2 - \sigma_1}{\sigma_2 + 2\sigma_1} \cdot \frac{1}{1 + j\omega\tau_{MW}} + \frac{j\omega\tau_{MW}}{1 + j\omega\tau_{MW}} \cdot \frac{\varepsilon_2 - \varepsilon_1}{\varepsilon_2 + 2\varepsilon_1}$$

Add and subtract $\frac{\varepsilon_2 - \varepsilon_1}{\varepsilon_2 + 2\varepsilon_1} \frac{1}{1 + j\omega\tau_{MW}}$ to the second term to get:

$$K(\omega) = \frac{\sigma_2 - \sigma_1}{\sigma_2 + 2\sigma_1} \cdot \frac{1}{1 + j\omega\tau_{MW}} + \frac{1}{1 + j\omega\tau_{MW}} \cdot \left(\frac{\varepsilon_2 - \varepsilon_1}{\varepsilon_2 + 2\varepsilon_1} (1 + j\omega\tau_{MW}) - \frac{\varepsilon_2 - \varepsilon_1}{\varepsilon_2 + 2\varepsilon_1} \right)$$

$$K(\omega) = \frac{1}{1 + j\omega\tau_{MW}} \left\{ \frac{\sigma_2 - \sigma_1}{\sigma_2 + 2\sigma_1} - \frac{\varepsilon_2 - \varepsilon_1}{\varepsilon_2 + 2\varepsilon_1} \right\} + \frac{\varepsilon_2 - \varepsilon_1}{\varepsilon_2 + 2\varepsilon_1}$$

Finally, we have

$$K(\omega) = U_h + \frac{\Delta U}{1 + j\omega\tau_{MW}}$$

Taking the real and imaginary parts, we have [47]:

$$K(\omega) = U_h + \frac{\Delta U}{1 + j\omega\tau_{MW}} \frac{1 - j\omega\tau_{MW}}{1 - j\omega\tau_{MW}}$$

$$K(\omega) = U_h + \frac{\Delta U}{1 + \omega^2\tau_{MW}^2} - \frac{j\Delta U\omega\tau_{MW}}{1 + \omega^2\tau_{MW}^2}$$

$$\text{Re}\{K(\omega)\} = U_h + \frac{\Delta U}{1 + \omega^2\tau_{MW}^2}$$

$$\text{Im}\{K(\omega)\} = \frac{-\Delta U\omega\tau_{MW}}{1 + \omega^2\tau_{MW}^2}$$

Appendix C – Preparation of Blood Cells, Breast Cancer Cells, and Fibroblasts

C.1 Chinese Hamster Ovary- and Human Blood Cell Preparations

Chinese Hamster Ovary cells transfected with the gene for human Inteferon-beta were provided by Cangene Corporation, and prepared according to procedures in Chapter 2 of Kevin Sunley's thesis [162]. Human peripheral blood mononuclear cells (PBMC) were isolated from whole blood from healthy blood donors in collaboration with the Victoria General Hospital at Winnipeg, using a standard gradient centrifugation method. T-lymphocytes are selectively activated by incubating the PBMCs in supplemented culture medium (RPMI-1640 medium with 25 mM HEPES buffer, 2% Bovine Serum Albumin, 1% penicillin-streptomycin with L-Glutamine) with anti-CD3/CD28 antibodies in a 37°C incubator with 8% CO₂ injection for 2 days. After the activation, cells in the solution were transferred to a new flask and cultured in the presence of Interleukin-2 (IL-2) for at least 3 days before experiments [79], [81], [163].

C.2 Preparation of 10T1/2 and Ciras-3 Mouse Fibroblasts

Cells used were 10T $\frac{1}{2}$ and Ciras-3 mouse fibroblasts. 10T $\frac{1}{2}$ is the normal, parental cell line [164]. Ciras-3 are ras-transformed 10T $\frac{1}{2}$ cells with a high metastatic potential [165], [166], [167]. They were both grown in a humidified incubator set at 37°C and 5% CO₂. Media used was Alpha Minimum Essential Media (GIBCO/Invitrogen, Carlsbad, CA) and supplemented with 10% fetal bovine serum (FBS) (GIBCO/Invitrogen, Carlsbad, CA) and antibiotic-antimycotic solution diluted from the 100x stock to 1x

final, i.e., 5 ml in 500 ml media (10,000 units of penicillin (base), 10,000 µg of streptomycin (base), and 25 µg of amphotericin B/ml utilizing penicillin G (sodium salt) GIBCO/Invitrogen, Carlsbad, CA). Cells were grown on 100 mm plastic plates (Sarstedt, Nümbrecht, Germany) until roughly 70% confluency.

On day of analysis, cells were washed once with 5 ml of 1x sterile phosphate buffer saline (PBS). The PBS was aspirated and cells were dissociated from the plates using 1 mL TrypLE™ Express (GIBCO/Invitrogen, Carlsbad, CA). This plate was placed back into the incubator for 1-3 minutes to help facilitate lifting of the cells from the plate. Following incubation, plates were tapped gently to dissociate cells from the substratum, and dissociated cells were resuspended in 3 ml of complete media and centrifuged at 2000 rpm for 4 minutes using an accuSpin 1R centrifuge (swing-bucket rotor) (Fisher Scientific, Ottawa, ON) at 4°C. Following centrifugation, the supernatant was aspirated and the resulting cell pellet was resuspended in 5 ml of PBS.

C.3 Preparation of MCF-7 and MDA-MB-231 Breast Cancer Cells

The human breast cancer cell lines MCF-7 (estrogen receptor (ER) positive) and MDA-MB-231 (ER negative) are used in this study as model systems of non-malignant or malignant breast cancer cells, respectively. Both cell lines are cultured in DMEM (GIBCO/Invitrogen, Carlsbad, CA) medium, supplemented with 10% fetal bovine serum (FBS) (Invitrogen, Carlsbad, CA), 2 mM glutamine (GIBCO/Invitrogen, Carlsbad, CA), 3 mL/500mL media of antibiotic-antimycotic (10,000 units of penicillin (base), 10,000 µg of streptomycin (base), and 25 µg of amphotericin B/ml utilizing penicillin G (sodium salt)) (GIBCO/Invitrogen, Carlsbad, CA), and 0.3% glucose. Cells are grown on 100 mm

plastic plates (Sarstedt, Nümbrecht, Germany) and maintained in a 37°C humidified incubator with 5% CO₂.

On day of analysis, cells are washed once with 5 ml of 1x sterile phosphate buffer saline (PBS). The PBS is aspirated and cells are dissociated from the plates using 1 ml TrypLE™ Express (GIBCO/Invitrogen, Carlsbad, CA). The TrypLE containing plate is placed in a 37°C humidified incubator for 2-4 minutes depending on confluence. Following incubation, plates were tapped gently to dissociate cells from the substratum, and dissociated cells were resuspended in 5 ml of 10% FBS and centrifuged at 2000 rpm for 4 minutes using an accuSpin 1R centrifuge (swing-bucket rotor) (Fisher Scientific, Ottawa, ON) at 4°C. Following centrifugation, the supernatant was aspirated and the resulting cell pellet was resuspended in 5 ml of fresh DMEM supplemented as listed above, without 10% FBS.

Serum-free conditions facilitate the maintenance of a single cell suspension by eliminating serum elements that may facilitate cell-cell adhesion. MCF-7 cells have a more epithelial phenotype than MDA-MB-231 cells in that they exhibit more cell-cell contacts, and therefore require further separation using chemical and mechanical means. To further dissociate MCF-7 cells, cells are resuspended in serum-free DMEM with 5 mM EDTA (Fisher Scientific, Ottawa, ON) and passed through a 22 gauge syringe (BD, Franklin Lakes, NJ) 5 times, to achieve single cell suspensions. EDTA is a calcium/magnesium chelating agent that interferes with cell adhesion proteins by taking up calcium and magnesium ions required by these proteins to achieve their functional state.

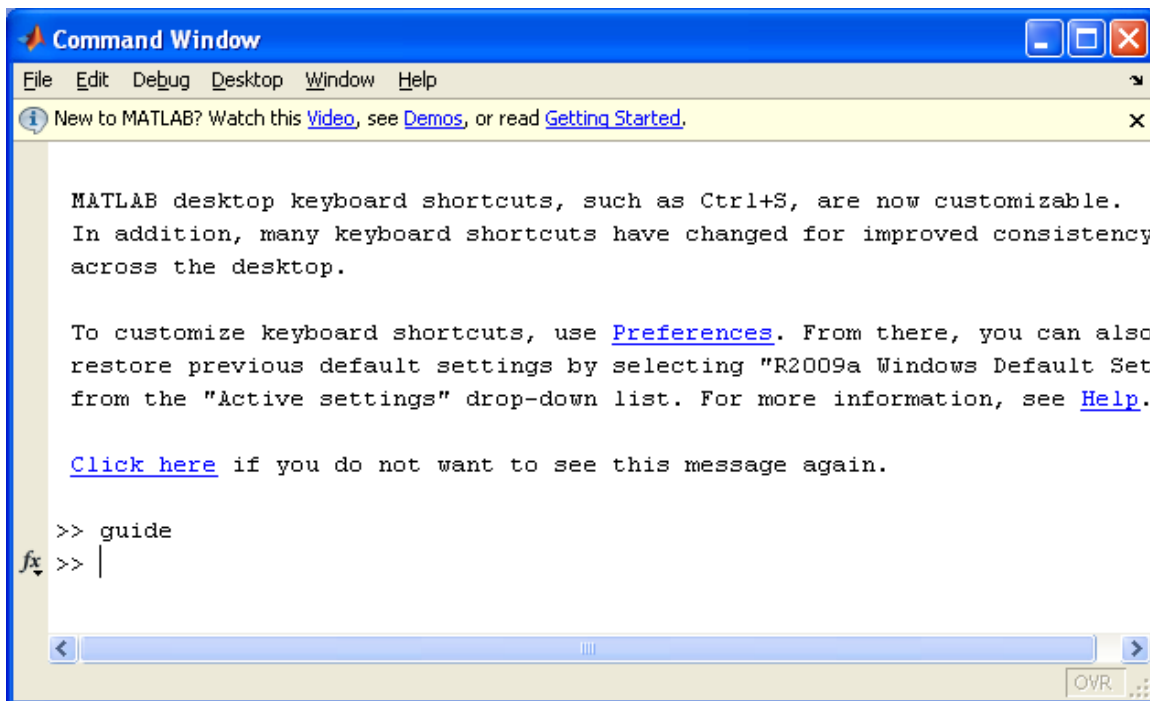
C.4 Trypan Blue Staining

Trypan Blue is used to stain cells to verify their viability. This is done by diluting cells in the buffer solution to a concentration of approximately 10^5 cells/ml. Approximately 0.1 ml of 0.4 % Trypan Blue stain is mixed thoroughly with 0.5 ml of cell suspension, and allowed to stand 5 minutes at room temperature (15-30°C is appropriate) [168].

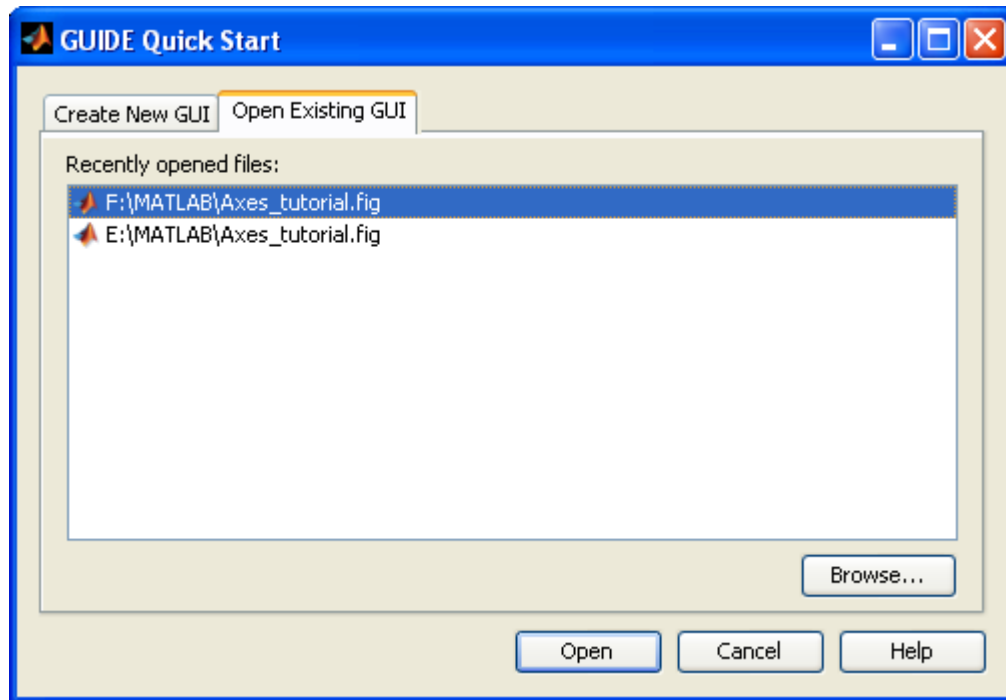
Appendix D – MATLAB Graphical User Interface

A graphical user interface (GUI) is compiled by this author in MATLAB to analyze the capacitance signatures from flowing biological cells. During each experiment, 30 s data files are acquired continuously using a LABVIEW program originally written by Sean Romanuik [119], [120], [154], and recently, in MATLAB, by Tim Cabel [169]. These data files are observed quickly in this MATLAB GUI using a scroll bar. The file name and number are displayed along with the number of detected events (maxima or minima). The “save axes” buttons are used for saving plots to a journal-ready pdf file.

To run this file, the user simply opens MATLAB and types “guide” in the command prompt.



Then, the existing GUI file is opened, which has a .fig extension.



When the .fig file is opened, the user clicks the green arrow to run the GUI shown in Figure D-1. The leftward plot in Figure D-1 contains the raw experimental data along with a calculated polynomial-fitted baseline. The rightward plot contains the raw experimental data subtracted from the polynomial-fitted baseline.

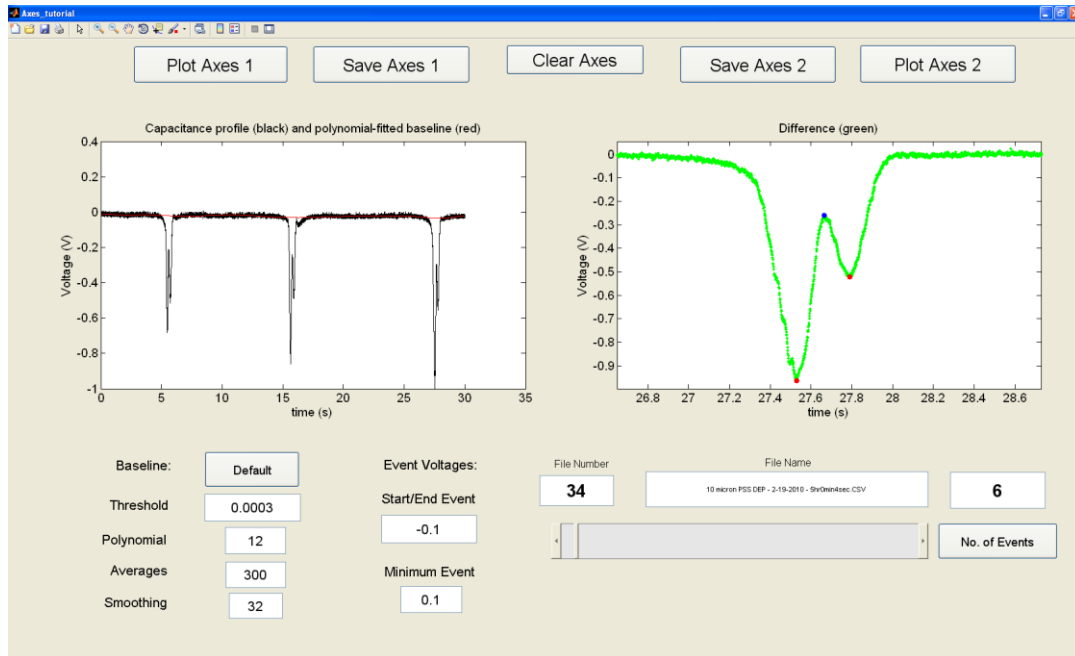
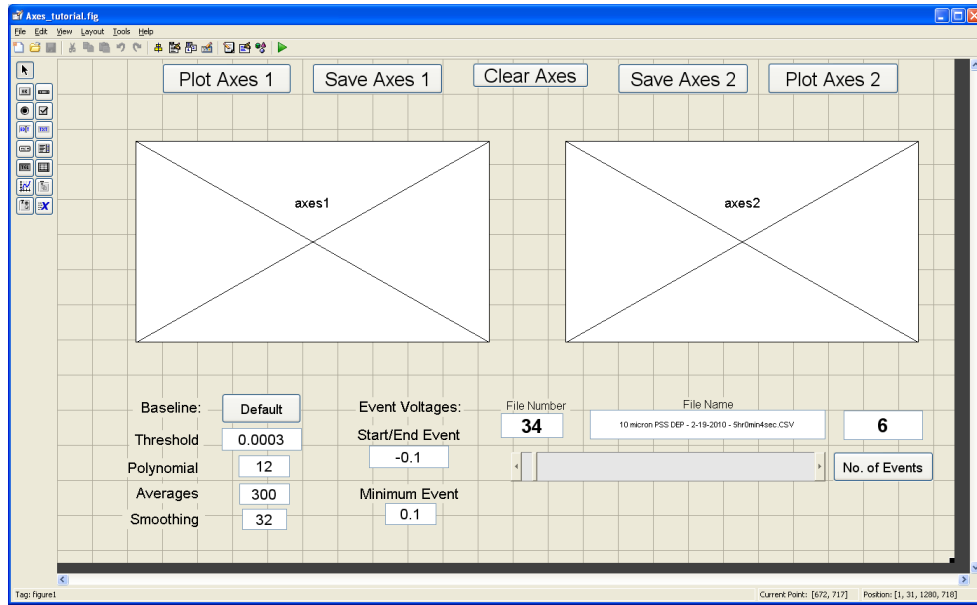


Figure D-1: *MATLAB graphical user interface for analyzing the capacitance signatures from biological cells. Zoom buttons in the menu bar allow users to zoom on specific events. The threshold, polynomial, averages, and smoothing values handle how the baseline is determined. The **Start/End Event** value indicates when the event begins/ends. If a peak neighbours a valley (and vice versa), and their voltage difference is at least a value, **Minimum Event**, the peak/valley is displayed in axes2. Once satisfied with the visual, the user can save the plots individually as journal-ready pdf files.*

D.1 MATLAB Code for Plotting Data

```
axes(handles.axes1)
listOFcsvs = dir('*.CSV');
[tmp ind]=sort([listOFcsvs.datenum]);
listOFcsvs2=listOFcsvs(ind);
listOFcsvs2.date;
```

*Current axes is "axes1"
Find all .CSV files in directory
Sort CSV files by date*

```
numberOfcsvs = numel(listOFcsvs2);
guidata(gcbo);
```

To know the number of CSV files

```
k = get(handles.slider1,'Value');
```

Collect the "Index" of the kth CSV file from GUI

```
information = listOFcsvs2(k);
csvName = information.name;
```

Process the file; store its name in csvName

```
[labels,Vo,V2V3] = readColData(csvName,3,10);
```

Read labels & x-y data from the CSV file; exclude headers

```
y=Vo(:,1);
x=[1:length(y)].';
x1=x./1000;
```

*y-data are voltages in the first column of .CSV file
x-data represents time in ms
Convert x-data to s*

```
avgValue = get(handles.avg_editText,'Value');
b=ones(1,avgValue)/avgValue;
a=1;
filteredData=filter(b,a,y);
```

*Gather averaging filter from GUI
Perform averaging filter on y-data*

```
difference=(y-filteredData);
```

Difference between raw and filtered data

If the difference between the raw and filtered data is smaller than a threshold, use that particular selected raw data to fit the baseline polynomial. Consequently, cell crossing events, which are larger than the threshold, are excluded from the baseline calculation.

```
thresholdValue = get(handles.threshold_editText,'Value');
xnew=find(abs(difference)<thresholdValue);
ynew=y(xnew);
```

Now, let's plot the baseline. Take these points (xnew,ynew), fit an nth order polynomial to them, and interpolate the fitted polynomial to the remaining elements in (x). The polynomial order is user assigned.

```
polyValue = get(handles.poly_editText,'Value');
```

```

p = polyfit(xnew,ynew,polyValue);
f = polyval(p,xnew);
f1= interp1q(xnew,f,x);
plot(x1,y,'b-',x1,f1,'r-','MarkerSize',3);
xlabel('Time (s)');           % add axis labels and plot title
ylabel('Voltage (V)');
title('Capacitance profile (Blue) and polynomial-fitted baseline (Red)');

```

```

guidata(hObject, handles); %updates the handles
% hObject handle to plotAxes1_pushbutton (see GCBO)
% eventdata reserved - to be defined in a future version of MATLAB
% handles structure with handles and user data (see GUIDATA)

```

For the righthand panel, axes2, additional commands are used to smooth the data for especially weaker signals; for example, those generated from strongly repelled cells. Axes2 displays the difference between the raw data and the polynomial-fitted baseline.

```

smoothValue = get(handles.smoothing_editText,'Value');
y1=smooth(y-f1,smoothValue);
plot(x1,y1,'k.','MarkerSize',3);

```

```

xlabel('Time (s)');
ylabel('S_{cell} (V)');

```

Add axes labels and plot the CSV filename as the title in Axes2. When the plot is later saved as a pdf, having a labelled title helps the user to recall when cell events occurred.

```

title_filename=get(handles.filename_editText,'String');
title(title_filename);

```

To find the maxima and minima in the capacitance data, a MATLAB function called “peakdet.m” developed previously by Eli Billauer was used. This function is freely available to the public and described thoroughly at <http://billauer.co.il/peakdet.html>.

The command [maxtab, mintab] = peakdet(y,b) finds all maxima and minima in a data set y with the requirement that a maximum or a minimum is identified only when it differs from its neighbouring environment by a threshold amplitude, b.

Based on the particular noise within a given data set, the user assigns a value to this threshold in the GUI directly. The following commands determine the corresponding peaks and valleys.

```

peakdet_Value = get(handles.EventMin_editText,'Value');

```

```
[maxtab, mintab] = peakdet(y1, peakdet_Value)
```

Now, let's figure out when events (cell crossings) begin and end. We first collect an "event width threshold" voltage, which is assigned by the GUI user. This value is usually chosen just below the noise floor. For example, if the baseline with noise is 0.0 +/- 0.2 V, then -0.3 V would be a suitable choice assuming that it's consistently used in subsequent analyses.

```
EventWidth_threshold = get(handles.EventWidth_editText, 'Value');
```

If no event peaks are found, set the number of events displayed in the GUI to ZERO. Otherwise, collect the number of peaks and valleys, as well as their corresponding times and amplitudes. Next, determine if your peaks-to-valley distances are larger than the "event width threshold". If they are, collect them. If they aren't, discard them.

```
if (size(mintab)==[0,0] | size(maxtab)==[0,0]), set(handles.events_editText, 'String', '0');  
else
```

```
    numberOFmaxs = numel(maxtab(:,1));  
    numberOFmins = numel(mintab(:,1));
```

```
times=[maxtab(:,1) ; mintab(:,1)];
```

```
amps=[maxtab(:,2) ; mintab(:,2)];
```

```
u=0;
```

```
for k=1:length(times)
```

```
    if amps(k)>EventWidth_threshold
```

```
        u=u+1;
```

```
        C(u)=k;
```

```
    end
```

```
end
```

```
times(C)= [];
```

```
amps(C)= [];
```

Collect the times and amplitudes of events larger than the "event threshold voltage", and sort them by their time of occurrence.

```
data=[times , amps];
```

```
H2=sortrows(data,1);
```

```
hold on;
```

If no events were found that have amplitudes larger than the "event threshold voltage", display "0" in the GUI, otherwise display the number of events found in the GUI, and plot the events as blue dots in axes2.

```

if length(times)==0, set(handles.events_editText,'String','0');
else
set(handles.events_editText,'String', num2str(length(times)));

```

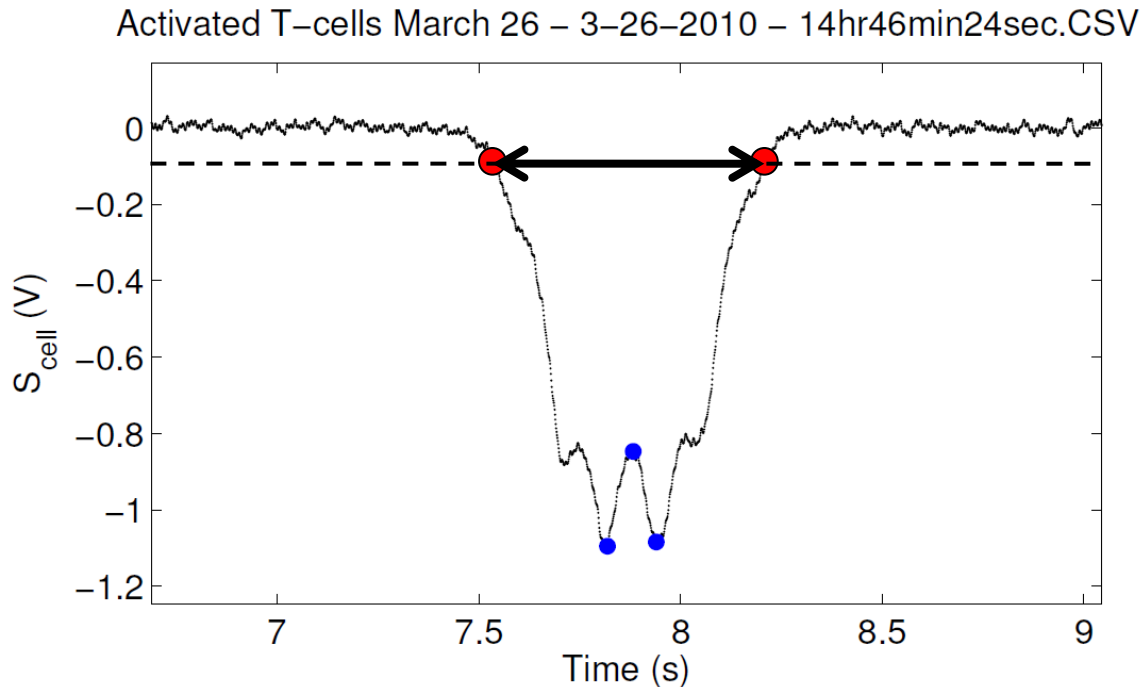
```

%Plot events
plot(times/1000, amps, 'b.','MarkerSize',20);

```

For a given DEP condition, the asymmetry of the capacitance signature can provide insight into whether it experienced positive or negative DEP, and how much it translated.

Each event is considered to endure from the time a cell enters the electrode region to the time it exits. The signal level at the entrance and exit times is the “event width threshold”, which is a value chosen by the user that is usually a value slightly below the noise. In the example below, it is -0.1 V. The event width or duration is determined by stepping forward and backward in time from the calculated events until the threshold is reached on either side. The degree of asymmetry can be determined by comparing the summed signal amplitudes on either side of the event’s midpoint.



Bibliography

- [1] Bill and Melinda Gates Foundation. (2009, September) Create Low-Cost Diagnostics for Priority Global Health Conditions. [Online].
http://www.grandchallenges.org/GCGHDocs/Topic_Template-LowCostDiagnostics_R4.pdf
- [2] J. den Toonder, "Circulating tumor cells: the Grand Challenge," *Lab Chip*, vol. 11, pp. 375-377, 2011.
- [3] (2008, January) Life expectancy hits 80.4 years: Statistics Canada. [Online].
<http://www.cbc.ca/canada/story/2008/01/14/death-stats.html>
- [4] J.D. Newman and A.P.F. Turner, "Home blood glucose biosensors: a commercial perspective," *Biosensors and Bioelectronics*, vol. 20, no. 12, pp. 2435-2453, June 2005.
- [5] Y. Mendelson, "Pulse oximetry: theory and applications for noninvasive monitoring," *Clinical Chemistry*, vol. 38, no. 9, pp. 1601-1607, 1992.
- [6] D. Di Carlo and L.P. Lee, "Dynamic single-cell analysis for quantitative biology," *Anal. Chem.*, vol. 78, no. 23, pp. 7918-7925, 2006.
- [7] B. Lincoln et al., "Deformability-based flow cytometry," *Cytometry Part A*, vol. 59A, pp. 203-209, 2004.
- [8] M.P. Hughes, *Nanoelectromechanics in engineering and biology*. Boca Raton, Florida, USA: CRC Press, 2003.
- [9] J.A. Geen, S.J. Sherman, J.F. Chang, and S.R. Lewis, "Single-chip surface micromachined integrated gyroscope with 50°/h Allan deviation," *IEEE J. Solid State Circ.*, vol. 37, pp. 1860-1866, 2002.
- [10] W.H. Coulter, "Means for counting particles suspended in a fluid," 2,656,508, 1953.
- [11] D.K. Wood, M.V. Requa, and A.N. Cleland, "Microfabricated high-throughput electronic particle detector," *Rev. Sci. Inst.*, vol. 78, 104301, 2007.
- [12] S. Gawad, L. Schild, and P. Renaud, "Micromachined impedance spectroscopy flow cytometer for cell analysis and particle sizing," *Lab Chip*, vol. 1, pp. 76-82, 2001.
- [13] L.L. Sohn et al., "Capacitance cytometry: measuring cells one by one," *Proc. Natl. Acad. Sci. USA*, vol. 97, pp. 10687-10690, 2000.
- [14] A. Romani, R. Guerrieri, M. Tartagni, N. Manaresi, and G. Medoro, "Beyond the microscope: Embedded detectors for cell biology applications," *Proc. IEEE Intl. Symp. Circ. & Systems*, vol. 3, pp. 2911-2914, 2005.
- [15] S. Sengupta, D.A. Battigelli, and H.-C. Chang, "A micro-scale multi-frequency reactance measurement technique to detect bacterial growth at low bio-particle concentrations," *Lab Chip*, vol. 6, pp. 682-692, 2006.
- [16] J. Yang et al., "Dielectric properties of human leukocyte subpopulations determined by electrorotation as a cell separation criterion," *Biophys. J.*, vol. 76, pp. 3307-3314, 1999.
- [17] G. DeGasperis, X.-B. Wang, J. Yang, F.F. Becker, and P.R.C. Gascoyne, "Automated electrorotation: dielectric characterization of living cells by real time motion estimation," *Meas. Sci. Technol.*, vol. 9, pp. 518-529, 1998.
- [18] S.B. Dev, D.P. Rabussay, G. Widera, and G.A. Hofmann, "Medical applications of

- electroporation," *IEEE Trans. Plasma. Sci. - Invited Paper*, vol. 28, pp. 206-223, 2000.
- [19] K.H. Schoenbach, R. Nuccitelli, and S.J. Beebe, "Zap: Extreme voltage could be a surprisingly delicate tool in the fight against cancer," *IEEE Spectrum*, vol. 43, pp. 20-26, 2006.
- [20] P.R.C. Gascoyne and J.V. Vykoukal, "Dielectrophoresis-based sample handling in general-purpose programmable diagnostic instruments," *Proc. IEEE - Invited Paper*, vol. 92, pp. 22-42, 2004.
- [21] U. Zimmermann et al., "Electromanipulation of mammalian cells: fundamentals and application," *IEEE Trans. Plasma Sci.*, vol. 28, pp. 72-82, 2000.
- [22] X.-B. Wang, Y. Huang, R. Holzel, J.P.H. Burt, and R. Pethig, "Theoretical and experimental investigations of the interdependence of the dielectric, dielectrophoretic, and electrorotational behaviour of colloidal particles," *J. Phys. D: Appl. Phys.*, vol. 26, pp. 312-322, 1993.
- [23] N. Lewpiriyawong, C. Yang, and Y.-C. Lam, "Dielectrophoretic manipulation of particles in a modified microfluidic H filter with multi-insulating blocks," *Biomicrofluidics*, vol. 2, 034105, 2008.
- [24] G.O.F. Parikesit et al., "Size-dependent trajectories of DNA macromolecules due to insulative dielectrophoresis in submicrometer-deep fluidic channels," *Biomicrofluidics*, vol. 2, p. 024103, 2008.
- [25] T.L. Mahaworasilpa, "Cell electro-dynamics: the mechanics of living cells in intense alternating electric fields," Faculty of Science, The University of South Wales, Australia, Ph.D. Dissertation 1992.
- [26] T. Tran, D.R. Oliver, D.J. Thomson, and G.E. Bridges, "Zeptofarad (10^{-21} F) resolution capacitance sensor for scanning capacitance microscopy," *Rev. Sci. Instrum.*, vol. 72, pp. 2618-2623, 2001.
- [27] K.C. Kao, *Dielectric phenomena in solids: with emphasis on physical concepts of electronic processes*. Boston, United States of America: Elsevier Academic Press, 2004.
- [28] P. Debye, "Zur Theorie der anomalen Dispersion im Gebiete der langwelligen elektrischen Strahlung (in German)," *Verhandlungen der deutschen physikalischen Gesellschaft*, vol. 15, pp. 777-793, August 1913.
- [29] P. Debye, "The theory of anomalous dispersion in the region of long-wave electromagnetic radiation," in *The Collected Papers of Peter J.W. Debye*, P.J.W. Debye, Ed. New York: Wiley Interscience, 1954, pp. 158-172.
- [30] R. Buchner, J. Barthel, and J. Stauber, "The dielectric relaxation of water between 0 °C and 35 °C," *Chem. Phys. Lett.*, vol. 306, pp. 57-63, 1999.
- [31] R. Pethig and D.B. Kell, "The passive electrical properties of biological systems: their significance in physiology, biophysics and biotechnology," *Phys. Med. Biol.*, vol. 32, no. 8, pp. 933-970, 1987.
- [32] C. Starr and B. McMillan, *Human biology*, 8th ed. Belmont, CA, United States: Brooks/Cole, Cengage Learning, 2010.
- [33] K. Nörtemann, J. Hilland, and U. Kaatze, "Dielectric properties of aqueous NaCl solutions at microwave frequencies," *J. Phys. Chem. A.*, vol. 101, pp. 6864-6869, 1997.

- [34] W.M. van Beek, University of Leiden, Ph.D. Thesis 1975.
- [35] R. Somaraju and J. Trumpf, "Frequency, temperature and salinity variations of the permittivity of sea water," *IEEE Transactions on Antennas and Propagation*, vol. 54, no. 11, pp. 3441-3448, November 2006.
- [36] S. Seo, "High frequency MIS-based III-nitride transistor and integrated bio-sensor technology," Electrical Engineering, University of Michigan, Ph.D. Thesis 2009.
- [37] R. Hölzel, Freie Universität Berlin, Ph.D. Thesis 1990.
- [38] Y. Huang, R. Hölzel, R. Pethig, and X.-B. Wang, "Differences in the AC electrodynamics of viable and non-viable yeast cells determined through combined dielectrophoresis and electrorotation studies," *Phys. Med. Biol.*, vol. 37, no. 7, pp. 1499-1517, 1992.
- [39] C. Waymouth, "Osmolality of mammalian blood and of media for culture of mammalian cells," *In Vitro Cellular & Developmental Biology - Plant*, vol. 6, no. 2, pp. 109-127, 1970.
- [40] S. Chien et al., "Rheology of Leukocytes," *Annals of the New York Academy of Sciences*, vol. 516, no. 1, pp. 333-347, 1987.
- [41] P.R.C. Gascoyne, X.-B. Wang, Y. Huang, and F.F. Becker, "Dielectrophoretic Separation of Cancer Cells from Blood," *IEEE Transactions on Industry Applications*, vol. 33, no. 3, pp. 670-678, 1997.
- [42] K.R. Foster and H.P. Schwan, "Dielectric properties of tissues and biological materials: a critical review," *CRC Crit. Rev. Biomed. Eng.*, vol. 17, pp. 25-104, 1989.
- [43] H.G.L. Coster, "The physics of cell membranes," *J. Biol. Phys.*, vol. 29, pp. 363-399, 2003.
- [44] T.B. Jones, *Electromechanics of particles*. New York: Cambridge University Press, 1995.
- [45] M. Nikolic-Jaric et al., "Microwave frequency sensor for detection of biological cells in microfluidic channels," *Biomicrofluidics*, vol. 3, no. 3, p. 034103, 2009.
- [46] H.A. Pohl, *Dielectrophoresis*. Cambridge (UK): Cambridge University Press, 1978.
- [47] K. Asami, "Characterization of heterogeneous systems by dielectric spectroscopy," *Progress in Polymer Science*, vol. 27, pp. 1617-1659, 2002.
- [48] F.F. Becker et al., "Separation of human breast cancer cells from blood by differential dielectric affinity," *Proc. Natl. Acad. Sci. USA*, vol. 92, pp. 860-864, 1995.
- [49] H. Morgan, M.P. Hughes, and N.G. Green, "Separation of submicron bioparticles by dielectrophoresis," *Biophysical Journal*, vol. 77, pp. 516-525, July 1999.
- [50] P.R.C. Gasocyne and J. Vykoukal, "Particle separation by dielectrophoresis," *Electrophoresis*, vol. 23, no. 13, pp. 1973-1983, July 2002.
- [51] Y. Huang, X.-B. Wang, R. Hölzel, F.F. Becker, and P.R.C. Gascoyne, "Electrorotational studies of the cytoplasmic dielectric properties of Friend murine erythroleukaemia cells," *Phys. Med. Biol.*, vol. 40, pp. 1789-1806, 1995.
- [52] J. Chen et al., "Electrodeformation for single cell mechanical characterization," *Journal of Micromechanics and Microengineering*, vol. 21, 054012, 2011.
- [53] X.-B. Wang, Y. Huang, X. Wang, F.F. Becker, and P.R.C. Gascoyne, "Dielectrophoretic

- manipulation of cells with spiral electrodes," *Biophysical Journal*, vol. 72, pp. 1887-1899, April 1997.
- [54] H.M. Coley, F.H. Labeed, H. Thomas, and M.P. Hughes, "Biophysical characterization of MDR breast cancer cell lines reveals the cytoplasm is critical in determining drug sensitivity," *Biochimica et Biophysica Acta*, vol. 1770, pp. 601-608, 2007.
- [55] J. An, J. Lee, S.H. Lee, J. Park, and B. Kim, "Separation of malignant human breast cancer epithelial cells from healthy epithelial cells using an advanced dielectrophoresis-activated cell sorter (DACS)," *Anal. Bioanal. Chem.*, vol. 394, pp. 801-809, 2009.
- [56] M. Schmeer, T. Seipp, U. Pliquett, S. Kakorin, and E. Neumann, "Mechanism for the conductivity changes caused by membrane electroporation of CHO cell-pellets," *Phys. Chem. Chem. Phys.*, vol. 6, pp. 5564-5574, 2004.
- [57] H. Saito, Y. Suzuki, and M. Taki, "Measurement of complex permittivity for biological cells at 1.7-2.6 GHz by waveguide penetration method," in *URSI General Assembly, Paper K01p2*, 2008.
- [58] A.W. Griffith and J.M. Cooper, "Single-cell measurements of human neutrophil activation using electrorotation," *Analytical Chemistry*, vol. 70, no. 13, pp. 2607-2612, July 1, 1998.
- [59] Y. Huang, X.-B. Wang, P.R.C. Gascoyne, and F.F. Becker, "Membrane dielectric responses of human T-lymphocytes following mitogenic stimulation," *Biochimica et Biophysica Acta*, vol. 1417, pp. 51-62, 1999.
- [60] P.S. Williams, T. Koch, and J.C. Giddings, "Characterization of near-wall hydrodynamic lift forces using sedimentation field-flow fractionation," *Chem. Eng. Comm.*, vol. 111, pp. 121-147, 1992.
- [61] P.S. Williams, M.H. Moon, Y. Xu, and J.C. Giddings, "Effect of viscosity on retention time and hydrodynamic lift forces in sedimentation/steric field flow fractionation," *Chemical Engineering Science*, vol. 51, no. 19, pp. 4477-4488, 1996.
- [62] Y. Huang, X.-B. Wang, F.F. Becker, and P.R.C. Gascoyne, "Introducing dielectrophoresis as a new force field for field-flow fractionation," *Biophysical Journal*, vol. 73, pp. 1118-1129, August 1997.
- [63] D. Brown. (2011) Tracker Video Analysis and Modeling Tool for Physics Education. [Online]. <http://www.cabrillo.edu/~dbrown/tracker/>
- [64] G.A. Ferrier et al., "Microfluidic electromanipulation with capacitive detection for the mechanical analysis of cells," *Biomicrofluidics*, vol. 2, no. 4, 044102, 2008.
- [65] G.A. Ferrier, S.F. Romanuik, D.J. Thomson, G.E. Bridges, and M.R. Freeman, "A microwave interferometric system for simultaneous actuation and detection of single biological cells," *Lab on a Chip*, vol. 9, pp. 3406-3412, 2009.
- [66] J.K. Clemens, "Capacitive pickup and the buried subcarrier encoding system for the RCA VideoDisc," *RCA Review*, vol. 39, pp. 33-59, 1978.
- [67] T.D. Tran, "Development of a zeptofarad resolution capacitance sensor for scanning capacitance microscopy," Electrical and Computer Engineering, University of Manitoba, Canada, M.Sc. Thesis 2001.
- [68] G.A. Ferrier, S.F. Romanuik, D.J. Thomson, G.E. Bridges, and M.R. Freeman, "Rapid

- classification of biological cells based on dielectrophoretic actuation with simultaneous capacitive detection," in *Proc. MicroTAS*, Jeju, South Korea, 2009.
- [69] G.A. Ferrier et al., "Dielectrophoretic pressing of biological cells into contact with surfaces: a mechanism for biophysical flow cytometry," in *Proc. MicroTAS*, Groningen, Netherlands, 2010.
- [70] (2007) Sensorit glass-based microfluidic technology with metallization - design rules and process steps. [Online]. <http://www.micronit.com>
- [71] M. Nikolic-Jaric, "Cell detection and manipulation," CMC Application Note 2010.
- [72] M. Nikolic-Jaric, "Automated low pressure microfluidic pumping system," CMC Application Note 2010.
- [73] A.S.G. Curtis, "The mechanism of adhesion of cells to glass. A study by interference reflection microscopy," *The Journal of Cell Biology*, vol. 20, no. 2, pp. 199-215, February 1964.
- [74] Z. Xia, "Kinetics of specific and non-specific adhesion of biological cells subjected to flow," Department of Chemistry, McGill University, Montreal, Canada, Ph.D. Thesis 1992.
- [75] J. Oblak, D. Križaj, S. Amon, A. Maček-Lebat, and D. Miklavčič, "Feasibility study for cell electroporation detection and separation by means of dielectrophoresis," *Bioelectrochemistry*, vol. 71, pp. 164-171, 2007.
- [76] R. Ananthkrishnan et al., "Modelling the structural response of an eukaryotic cell in the optical stretcher," *Current Science*, vol. 88, no. 9, pp. 1434-1440, May 2005.
- [77] M. Diez-Silva, M. Dao, J. Han, C-T. Lim, and S. Suresh, "Shape and biomechanical characteristics of human red blood cells in health and disease," *MRS Bulletin*, vol. 35, pp. 382-388, May 2010.
- [78] S. Haltiwanger, "The electrical properties of cancer cells," <http://www.royalrife.com/haltiwanger1.pdf>, Accessed April 7, 2011, Monograph.
- [79] F. Lin and E.C. Butcher, "T cell chemotaxis in a simple microfluidic device," *Lab Chip*, vol. 6, pp. 1462-1469, 2006.
- [80] M.J. Brown, J.A. Hallam, E. Colucci-Guyon, and S. Shaw, "Rigidity of circulating lymphocytes is primarily conferred by vimentin intermediate filaments," *Journal of Immunology*, vol. 166, pp. 6640-6646, 2001.
- [81] J. Li et al., "Activated T lymphocytes migrate toward the cathode of DC electric fields in microfluidic devices," *Lab Chip*, vol. 11, pp. 1298-1304, 2011.
- [82] B. Alberts et al., "The cytoskeleton and cell behavior," in *Molecular biology of the cell*, 4th edition. New York: Garland Science, 2002, ch. 16.
- [83] C.T. Lim, E.H. Zhou, and S.T. Quek, "Mechanical models for living cells - a review," *Journal of Biomechanics*, vol. 39, pp. 195-216, 2006.
- [84] T. Tharmalingham, H. Ghebeh, T. Wuerz, and M. Butler, "Pluronic enhances the robustness and reduces the cell attachment of mammalian cells," *Molecular Biotechnology*, vol. 39, pp. 167-177, 2008.
- [85] P.K. Wong, W. Tan, and C.-M. Ho, "Cell relaxation after electrodeformation: effect of latrunculin A on cytoskeletal actin," *Journal of Biomechanics*, vol. 38, pp. 529-535, 2005.

- [86] R. Li and G.G. Gunderson, "Beyond polymer polarity: how the cytoskeleton builds a polarized cell," *Nature Reviews Molecular Cell Biology*, vol. 9, pp. 860-873, November 2008.
- [87] L.A. MacQueen, M.D. Buschmann, and M.R. Wertheimer, "Mechanical properties of mammalian cells in suspension measured by electro-deformation," *Journal of Micromechanics and Microengineering*, vol. 20, 065007, 2010.
- [88] G.W. Schmid-Schönbein, K.-L. P. Sung, H. Tozeren, R. Skalak, and S. Chien, "Passive mechanical properties of human leukocytes," *Biophysical Journal*, vol. 36, no. 1, pp. 243-256, 1981.
- [89] S. Suresh, "Biomechanics and biophysics of cancer cells," *Acta Biomater.*, vol. 3, pp. 413-438, 2007.
- [90] S. Suresh et al., "Connections between single-cell biomechanics and human disease states: gastrointestinal cancer and malaria," *Acta Biomater.*, vol. 1, pp. 15-30, 2005.
- [91] S. Iyer, R.M. Gaikwad, V. Subba-Rao, C.D. Woodworth, and I. Sokolov, "Atomic force microscopy detects differences in the surface brush of normal and cancerous cells," *Nature Nanotechnology Letters*, vol. 4, pp. 389-393, 2009.
- [92] K. Porter, D. Prescott, and J. Faye, "Changes in surface morphology of Chinese Hamster Ovary cells during the cell cycle," *The Journal of Cell Biology*, vol. 57, pp. 815-836, 1973.
- [93] M. Nikkhah, J.S. Strobl, E.M. Schmelz, and M. Agah, "Evaluation of the influence of growth medium composition on cell elasticity," *Journal of Biomechanics*, vol. 44, pp. 762-766, 2011.
- [94] S. Leporatti et al., "Cytomechanical and topological investigation of MCF-7 cells by scanning force microscopy," *Nanotechnology*, vol. 20, 055103, 2009.
- [95] Q. Li, G.Y.H. Lee, C.N. Ong, and C.T. Lim, "AFM indentation study of breast cancer cells," *Biochemical and Biophysical Research Communications*, vol. 374, pp. 609-613, 2008.
- [96] X. Cai et al., "Connection between biomechanics and cytoskeleton structure of lymphocyte and Jurkat cells: an AFM study," *Micron*, vol. 41, pp. 257-262, 2010.
- [97] M. Hu, J. Wang, H. Zhao, S. Dong, and J. Cai, "Nanostructure and nanomechanics analysis of lymphocyte using AFM: From resting, activated to apoptosis," *Journal of Biomechanics*, vol. 42, pp. 1513-1519, 2009.
- [98] S.M. Mijailovich, M. Kojic, M. Zivkovic, B. Fabry, and J.J. Fredberg, "A finite element model of cell deformation during magnetic bead twisting," *Journal of Applied Physiology*, vol. 93, pp. 1429-1436, June 2002.
- [99] K. Kasza et al., "The cell as a material," *Current Opinion in Cell Biology*, vol. 19, pp. 101-107, 2007.
- [100] R.M. Hochmuth, "Micropipette aspiration of living cells," *Journal of Biomechanics*, vol. 33, pp. 15-22, 2000.
- [101] J. Guck et al., "The optical stretcher; a novel laser tool to micromanipulate cells," *Biophysical Journal*, vol. 81, pp. 767-784, 2001.
- [102] S. Huang, H. Bow, M. Diez-Silva, and J. Han, "Applying a microfluidic deformability cytometry to measure stiffness of malaria-infected red blood cells at body and febrile

- temperatures," in *MicroTAS 2010*, Groningen, Netherlands, 2010, pp. 259-261.
- [103] D.R. Gossett, H.T.K. Tse, S. Lee, A.T. Clark, and D. Di Carlo, "Deformability cytometry: high-throughput, continuous measurement of cell mechanical properties in extensional flow," in *MicroTAS 2010*, Groningen, Netherlands, 2010, pp. 1382-1384.
- [104] K. Cheung, S. Gawad, and P. Renaud, "Microfluidic impedance spectroscopy flow cytometer: particle size calibration," *17th IEEE International Conference on Micro Electro Mechanical Systems*, pp. 343-346, 2004, Proceedings: IEEE Microelectromechanical systems workshop.
- [105] D. Holmes and H. Morgan, "Single cell impedance cytometry for identification and counting of CD4 T-cells in human blood using impedance labels," *Analytical Chemistry*, vol. 82, pp. 1455-1461, 2010.
- [106] T. Sun and H. Morgan, "Single-cell microfluidic impedance cytometry: a review," *Microfluidics and Nanofluidics*, vol. 8, no. 4, pp. 423-443, 2010.
- [107] K.C. Cheung et al., "Microfluidic impedance-based flow cytometry," *Cytometry Part A*, vol. 77A, no. 7, pp. 648-666, 2010.
- [108] G.B. Salieb-Beugelaar, G. Simone, A. Arora, A. Philippi, and A. Manz, "Latest developments in microfluidic cell biology and analysis systems," *Analytical Chemistry*, vol. 82, no. 12, pp. 4848-4864, 2010.
- [109] M. Leslie, "The power of one," *Science*, vol. 331, pp. 24-26, January 11 2011.
- [110] S.L. Stott et al., "Isolation of circulating tumor cells using a microvortex-generating herringbone chip," *Proceedings of the National Academy of Sciences*, vol. 107, no. 43, pp. 18392-18397, October 26 2010.
- [111] R. Lin, J.L. Prieto, J.S. Fisher, and A.P. Lee, "High frequency cell encapsulation utilizing novel on-demand droplet generation scheme and impedance-based detection," in *MicroTAS 2010*, Groningen, Netherlands, 2010, pp. 2135-2137.
- [112] H.P. Schwan, "Linear and nonlinear electrode polarization and biological materials," *Annals of Biomedical Eng.*, vol. 20, pp. 269-288, 1992.
- [113] S. Olson, "Charge transport in molecular junctions and microfluidic devices," Department of Physics, University of Alberta, Edmonton, Alberta, M.Sc. Thesis 2010.
- [114] D.I. Kim et al., "Microfluidic chip for electrical measurement of single cell deformability," in *MicroTAS 2009*, Jeju, South Korea, 2009, pp. 1796-1798.
- [115] J. Chen et al., "A microfluidic device for simultaneous electrical and mechanical measurements on single cells," *Biomicrofluidics*, vol. 5, 014113, 2011.
- [116] R. Pethig, "Dielectrophoresis: status of the theory, technology, and applications," *Biomicrofluidics*, vol. 4, 022811, 2010.
- [117] T.L. Mahaworasilpa, H.G.L. Coster, and E.P. George, "Forces on biological cells due to applied alternating (AC) electric fields. I. dielectrophoresis," *Biochimica et Biophysica Acta*, vol. 1193, pp. 118-126, 1994.
- [118] I. Guido, M.S. Jaeger, and C. Duschl, "Cell deformation by dielectrophoretic fields," in *World Congress on Medical Physics and Biomedical Engineering, IFMBE Proceedings*, vol. 25/1, Munich, Germany, September 7-12, 2009, pp. 21-24.
- [119] S.F. Romanuik et al., "All electronic detection and actuation of single biological cells for lab-on-a-chip applications," in *Proc. IEEE Sensors*, vol. 1, 2008, pp. 634-637.

- [120] S.F. Romanuik, "A microflow cytometer with simultaneous dielectrophoretic actuation for the optical assay and capacitive cytometry of individual fluid suspended bioparticles," Electrical and Computer Engineering, University of Manitoba, Winnipeg, Manitoba, Canada, M.Sc. Thesis 2009.
- [121] H.-J. Butt, K. Graf, and M. Kappl, *Physics and chemistry of interfaces.*: Wiley-VCH, 2003.
- [122] T. Honegger, K. Berton, E. Picard, and D. Peyrade, "Determination of Clausius-Mossotti factors and surface capacitances for colloidal particles," *Applied Physics Letters*, vol. 98, 181906, 2011.
- [123] M. Nikolic-Jaric, G.A. Ferrier, D.J. Thomson, G.E. Bridges, and M.R. Freeman, "Dielectric response of particles in flowing media: the effect of shear-induced rotation on the variation in particle polarizability," *Physical Review E*, 2011.
- [124] G. Jeffery, "The motion of ellipsoidal particles immersed in a viscous fluid," *Proceedings of the Royal Society of London A - Mathematical, Physical & Engineering Sciences*, vol. 102, no. 715, pp. 161-179, November 1922.
- [125] E.C. Anderson, D.F. Peterson, and R.A. Tobey, "Density invariance of cultured Chinese hamster ovary cells with stage of the mitotic cycle," *Biophysical Journal*, vol. 10, pp. 630-645, 1970.
- [126] L.S. Munteanu and A. Dinu, "Fractionation of granulocytes from whole human blood by centrifugation, practical hints," *Romanian Journal of Biophysics*, vol. 14, no. 1-4, pp. 53-58, 2004.
- [127] M. Godin, A.K. Bryan, T.P. Burg, K. Babcock, and S.R. Manalis, "Measuring the mass, density, and size of particles and cells using a suspended microchannel resonator," *Applied Physics Letters*, vol. 91, 123121, 2007.
- [128] R. Pethig and G.H. Markx, "Applications of dielectrophoresis in biotechnology," *Trends Biotechnol.*, vol. 15, pp. 426-432, 1997.
- [129] A. Ramos, H. Morgan, N.G. Green, and A. Castellanos, "AC electrokinetics: a review of forces in microelectrode structures," *J. Phys. D: Appl. Phys.*, vol. 31, pp. 2338-2353, 1998.
- [130] A. Castellanos, A. Ramos, A. González, N.G. Green, and H. Morgan, "Electrohydrodynamics and dielectrophoresis in microsystems: scaling laws," *Journal of Physics D: Applied Physics*, vol. 36, no. 20, pp. 2584-2597, 2003.
- [131] J. Voldman, "Electrical forces for microscale cell manipulation," *Annual Review Biomedical Engineering*, vol. 8, pp. 425-454, 2006.
- [132] J. Cao, P. Cheng, and F.-J. Hong, "Applications of electrokinetics and Joule heating effects in microfluidic chips: A review," *Science in China Series E - Technological Sciences*, vol. 52, no. 12, pp. 3477-3490, 2009.
- [133] L.D. Landau and E.M. Lifshitz, *Course of Theoretical Physics.*: Pergamon Press, Oxford, 1959, vol. 7.
- [134] T.Y. Tsong, "Electroporation of cell membranes," *Biophysical Journal*, vol. 60, pp. 297-306, August 1991.
- [135] J.C. Weaver and Y.A. Chizmadzhev, "Theory of electroporation: A review," *Bioelectrochemistry and Bioenergetics*, vol. 41, no. 2, pp. 135-160, December 1996.

- [136] D. Miklavčič and T. Kotnik, "Electroporation for electrochemotherapy and gene therapy," in *Bioelectromagnetic Medicine*, Rosch P.J. and Markov M.S., Eds. New York, United States: Marcel Dekker, Inc., 2004, ch. 40, pp. 637-656.
- [137] S. Movahed and D. Li, "Microfluidics cell electroporation," *Microfluidics and Nanofluidics*, vol. 10, pp. 703-734, 2011.
- [138] H. Pauly and H.P. Schwan, "Über die impedanz einer suspension von kugelförmigen teilchen mit einer schale," *Z. Naturforsch.*, vol. 14B, pp. 125-131, 1959.
- [139] T. Kotnik and D. Miklavčič, "Second-order model of membrane electric field induced by alternating external electric fields," *IEEE Transactions on Biomedical Engineering*, vol. 47, no. 8, pp. 1074-1081, 2000.
- [140] C. Grosse and H.P. Schwan, "Cellular membrane potentials induced by alternating fields," *Biophysical Journal*, vol. 63, pp. 1632-1642, 1992.
- [141] H.-Y. Wang and C. Lu, "Electroporation of mammalian cells in a microfluidic channel with geometric variation," *Anal. Chem.*, vol. 78, pp. 5158-5164, 2006.
- [142] E. Salimi, "Nanosecond pulse electroporation of biological cells: the effect of membrane dielectric relaxation," Electrical and Computer Engineering, University of Manitoba, Winnipeg, Manitoba, M.Sc. Thesis 2011.
- [143] E. Salimi, G.E. Bridges, and D.J. Thomson, "The effect of dielectric relaxation in nanosecond pulse electroporation of biological cells," in *Proc. ANTEM-AMEREM 2010*, Ottawa, Canada, July 5-9, 2010.
- [144] N.G. Green, A. Ramos, A. Gonzalez, A. Castellanos, and H. Morgan, "Electrothermally induced fluid flow on microelectrodes," *Journal of Electrostatics*, vol. 53, pp. 71-87, 2001.
- [145] C. Meinhart, D. Wang, and K. Turner, "Measurement of AC electrokinetic flows," *Biomedical Microdevices*, vol. 5, no. 2, pp. 139-145, 2003.
- [146] D.F. Chen and H. Du, "Simulation studies on electrothermal fluid flow induced in a dielectrophoretic microelectrode system," *Journal of Micromechanics and Microengineering*, vol. 16, pp. 2411-2419, 2006.
- [147] B.G. Hawkins and B.J. Kirby, "Effects of electrothermal flow on particle deflection and trapping in insulating (electrodeless) dielectrophoresis devices," in *MicroTAS 2010*, Groningen, The Netherlands, 2010, pp. 1757-1759.
- [148] M.L.Y. Sin, V. Gau, J.C. Liao, and P.K. Wong, "Electrothermal fluid manipulation of high-conductivity samples for laboratory automation applications," *JALA Charlottesville Va.*, vol. 15, no. 6, pp. 426-432, December 31, 2010.
- [149] K.-F. Han, C.M. Butler, L.-C. Shen, H.Y. He, and M.A. Harris, "High-frequency, complex dielectric permittivity of saline solution at elevated temperatures," *IEEE Transactions on Geoscience and Remote Sensing*, vol. 29, no. 1, pp. 48-56, January 1991.
- [150] S.J. Williams, P. Chamarthy, and S.T. Wereley, "Comparison of experiments and simulation of Joule heating in AC electrokinetic chips," *Journal of Fluids Engineering*, vol. 132, p. 021103, 2010.
- [151] M. Lian, N. Islam, and J. Wu, "AC electrothermal manipulation of conductive fluids and particles for lab-chip applications," *IET Nanobiotechnol.*, vol. 1, no. 3, pp. 36-43,

- 2007.
- [152] E. Stern et al., "Importance of the Debye screening length on nanowire field effect transistor sensors," *Nano Letters*, vol. 7, no. 11, pp. 3405-3409, November 2007.
- [153] V. Studer, A. Pépin, Y. Chen, and A. Ajdari, "An integrated AC electrokinetic pump in a microfluidic loop for fast and tunable flow control," *Analyst*, vol. 129, pp. 944-949, 2004.
- [154] S.F. Romanuik et al., "Dielectrophoretic actuation and simultaneous detection of individual bioparticles," in *Advances in biomedical sensing, measurements, instrumentation, and systems*, A. Lay-Ekuakille and S.C. Mukhopadhyay, Eds.: Springer Verlag, 2010, vol. 55, pp. 106-126.
- [155] M. Nikolic-Jaric et al., "Uncertainty in flow impedance measurements arising from shear-induced rotation," in *MicroTAS 2010*, Groningen, Netherlands, 2010, pp. 1340-1342.
- [156] S. Rzeszowski et al., "Inductive detection of 4.5 μm superparamagnetic beads in a microfluidic device," in *Proc. ANTEM-AMEREM 2010*, Ottawa, Canada, July 5-9, 2010.
- [157] S. Rzeszowski, University of Manitoba, Winnipeg, Manitoba, M.Sc. Thesis 2011.
- [158] M. Nikolic-Jaric et al., "All-electronic deformability cytometry for markerless differentiation of cancer cells," in *MicroTAS 2011*, Seattle, USA, 2011 (Submitted).
- [159] D.K. Cheng, *Field and wave electromagnetics - 2nd edition*. Reading, Massachusetts, USA: Addison-Wesley Publishing Company, 1992.
- [160] G.G. Raju, *Dielectrics in electric fields*: Marcel Dekker, Inc., 2003.
- [161] R.K. Nagle and E.B. Saff, *Fundamentals of differential equations and boundary value problems*: Addison-Wesley Publishing Company, Inc., 1993.
- [162] K. Sunley, "The adaptation of Chinese Hamster Ovary cells to hypothermic temperatures increases yields of monomeric recombinant interferon-beta," Department of Microbiology, University of Manitoba, Winnipeg, Manitoba, Ph.D. Thesis 2009.
- [163] F. Lin, "A microfluidics-based method for analyzing leukocyte migration to chemoattractant gradients," in *Methods in Enzymology*, M.H. Tracy and J.H. Damon, Eds.: Academic Press, 2009, vol. 461, ch. 15, pp. 333-347.
- [164] C.A. Reznikoff, D.W. Brankow, and C. Heidelberger, "Establishment and characterization of a cloned line of C3H mouse embryo cells sensitive to postconfluence inhibition of division," *Cancer Research*, vol. 33, pp. 3231-3238, December 1973.
- [165] S.E. Egan et al., "Expression of H-ras correlates with metastatic potential: evidence for direct regulation of the metastatic phenotype in 10T1/2 and NIH 3T3 cells," *Molecular and Cellular Biology*, vol. 7, no. 2, pp. 830-837, February 1987.
- [166] D.N. Chadee, C.P. Peltier, and J.R. Davie, "Histone H1S-3 phosphorylation in Ha-ras oncogene-transformed mouse fibroblasts," *Oncogene*, vol. 21, pp. 8397-8403, 2002.
- [167] K.L. Dunn, P.S. Espino, B. Drobic, S. He, and J.R. Davie, "The Ras-MAPK signal transduction pathway, cancer and chromatin remodeling," *Biochemistry and Cell Biology*, vol. 83, no. 1, pp. 1-14, February 2005.
- [168] R. Freshney, *Culture of animal cells: a manual of basic technique*. New York: Alan R.

Liss, Inc., 1987.

- [169] M. Nikolic-Jaric et al., "All-electronic deformability cytometry for markerless differentiation of cancer cells," in *MicroTAS 2011*, Seattle, USA, 2011 (Accepted).